

universität ulm

Universität Ulm

Institut für theoretische Physik

Hyperpolarised Naphthalene and Levitated Optomechanics for Fundamental Tests of Physics

Dissertation zur Erlangung des Doktorgrades Dr. rer. nat. an der Fakultät für Naturwissenschaften der Universität Ulm

vorgelegt von

Marit Ottilie Eva Steiner

aus Berlin, Germany

2026

Dissertation

Titel: Hyperpolarised Naphthalene and Levitated Optomechanics for Fundamental Tests of Physics

Tag der Promotion: 27.08.2026

Dekan: Prof. Dr. Kay-E. Gottschalk
Erstgutachter: Prof. Dr. Martin B. Plenio
Zweitgutachter: Prof. Dr. Benjamin Stickler

Acknowledgements

First, I would like to thank my supervisor, Martin B. Plenio. I joined his group even before the start of my Bachelor's thesis, and he and Susana Huelga supported me through every stage of my academic journey until the completion of my PhD. I am grateful for the many opportunities he gave me throughout these years.

A very special thank you goes to Julen S. Pedernales, who introduced me to the field of levitated particles, a field that I grew to love. He always had immeasurable patience and an open ear, whether for discussing physics, offering advice, or simply having a chat. I could not have asked for a better mentor and I wish him all the best on his new journey at Delft University.

I would also like to thank Gerlinde Walliser for always going the extra mile and for helping me navigate the bureaucratic maze of university life. Naturally, I would like to thank everyone in the group. The scientific curiosity that always filled our corridor helped me to never lose motivation, while the memorable moments outside the office, from Christmas parties and barbecues to group dinners, made these years unforgettable.

I am also grateful for the opportunity to serve on the doctoral representatives council (ProKo). It allowed me to gain valuable insight into how the university works behind the scenes and taught me far more about science policy and university governance than I ever expected to learn. I hope that I was able to leave a positive footprint at the university, however small.

To my parents, thank you for your unconditional support throughout my studies and my PhD. Your encouragement and the curiosity for the natural sciences that you nurtured from an early age laid the foundation for everything that followed.

Finally, to my soon-to-be husband, Max: thank you for your endless patience, your unwavering support and the countless snacks that somehow always appeared exactly when they were needed most. Especially, thank you for listening to my endless stories about physics over dinner.

The final months of writing this thesis coincide with an eventful time in my life and completing this PhD would not have been possible without the flexibility and support of many people. Whether by offering practical help, proofreading chapters at short notice or showing encouragement, you made it possible for me to finish this thesis when it mattered most.

Abstract

Levitated nanoparticles, free from the clamping losses and decoherence channels imposed by mechanical support, offer a growing versatile platform for precision sensing and tests of fundamental physics at increasingly larger masses. This thesis follows complementary directions based on this platform: the coupling of optically controllable nuclear spin ensembles to the mechanical and rotational degrees of freedom of levitated solids, and the identification of decoherence mechanisms that limit levitated systems in tests of macroscopic quantum superpositions.

In the first part, we study levitated solids doped with non-permanent, optically addressable electron spins, with pentacene-doped naphthalene as a prime example, whose nuclear spins can be hyperpolarised using dynamic nuclear polarisation techniques to over 80 % at cryogenic temperatures, with lifetimes extending over weeks. Exploiting the homogeneous spin distribution and absence of a preferred nuclear quantisation axis in such materials, we design a multi-spin Stern-Gerlach interferometry protocol that circumvents key limitations of colour centres in nanodiamonds like NV centres, and use it to place improved bounds on objective collapse models. We further show that the unconstrained rotation available to levitated particles enables magic angle spinning at frequencies beyond current NMR standards, and propose a protocol for reading out spin ensemble polarisation directly from the particle's mechanical motion. Building on the same hyperpolarisation mechanism, we propose experiments to observe the nuclear Einstein-de Haas effect, using the hyperpolarised bath of nuclei as a reservoir for angular momentum. Furthermore, we propose a protocol to investigate the nuclear Barnett effect in the solid state, using the MHz-scale rotation rates accessible to levitated particles. We find that the proposed Stern-Gerlach interferometer could improve upon existing bounds on collapse-model parameters and that the nuclear Einstein-de Haas and Barnett effects could be observable using near-term experimental technology, within parameter ranges already accessible to the community.

In the second part, we turn to a central obstacle facing proposals for gravitationally induced entanglement (GIE) between levitated masses, namely the conducting and magnetic shields required to suppress direct electromagnetic coupling. We show that residual Casimir and magnetic-dipole interactions between the particles and the shield, averaged over run-to-run positional and orientational fluctuations of the experimental set-up, generate decoherence, and that the shield can itself mediate spurious entanglement between the particles that might mimic a genuine gravitational-entanglement signature. From this, we derive quantitative stability thresholds considerably stricter than previously assumed.

List of Publications

Parts of this thesis are based on or taken from the following publications that were published before this thesis:

[1] **Marit O. E. Steiner**, Julen S. Pedernales, Martin B. Plenio
Optically Hyperpolarized Materials for Levitated Optomechanics
Quantum (9), 1928. (2025).
Copyright (2025) The Authors. Published under the CC BY 4.0 license (https://creativecommons.org/licenses/by/4.0).

[2] Jan Bulling, **Marit O. E. Steiner**, Julen S. Pedernales, Martin B. Plenio
Stability Thresholds for Gravitationally Induced Entanglement in Shielded Setups
arXiv:2604.22593. (2026).
Copyright (2025) The Authors. Published under the CC BY 4.0 license (https://creativecommons.org/licenses/by/4.0).

Contents

1 Introduction **1**

I Preliminaries **7**

2 An Introduction to Levitated Systems **9**
2.1 Trapping mechanisms 9
2.2 Unavoidable sources of decoherence 14

3 Fundamental Physics Phenomena **23**
3.1 The Continuous Spontaneous Localisation Model 23
3.1.1 The CSL Model 24
3.1.2 Experimental Tests of the CSL Model 26
3.1.3 Connection to Other Collapse Models 27
3.2 Quantum Signatures of Gravity and Gravitationally Induced Entanglement 29
3.2.1 Is Gravity Quantum? 30
3.2.2 A Tabletop Experiment for Gravitationally Induced Entanglement 33
3.3 The Einstein-de Haas and Barnett Effect 36

4 Optically Hyperpolarised Materials **39**
4.1 Dynamic Nuclear Polarisation Leveraging Photo-Excited Triplet States 40
4.2 Pentacene-doped Naphthalene 43

II Optically Hyperpolarised Materials for Levitated Optomechanics **47**

5 Introduction **49**

6 Naphthalene – A Material For Levitation **51**
6.1 Hyperpolarisation 51
6.2 Magic Angle Spinning 52
6.3 Sublimation 56

7 Naphthalene in a Stern-Gerlach Type Interferometer **59**
7.1 Advantages of Naphthalene for Stern-Gerlach type interferometry 60
7.2 Time Evolution in a Magnetic Trap 61
7.3 Test of the CSL Model 69
7.3.1 Modified Protocol 74
7.3.2 Evaluation of $\langle\hat{M}\rangle(T_{\text{tot}})/\langle\hat{M}\rangle(0)$ 77
7.3.3 Bounds on the Parameter Space of the CSL Model 78
7.4 Measurement Schemes 81
7.5 Pulsed Control in the Presence of Magic-Angle Spinning 83
7.6 Possible Noise Sources 85

8 Test of the Nuclear Einstein-de Haas and Barnett Effect **93**
8.1 The Einstein-de Haas Effect 93
8.2 Test of the Nuclear Barnett Effect 97

III Stability Thresholds for Gravitationally Induced Entanglement in Shielded Setups **101**

9 Introduction **103**

10 The Setup **105**
10.1 Casimir interactions 107
10.2 Magnetic interactions 108
10.3 Electrostatic interactions 110
10.4 Gravitational interactions 111

11 Variations in the experimental geometry **113**
11.1 Gaussian states 115
11.1.1 Variations in the shield positioning 118
11.1.2 Variations in the position of the detectors and traps 119
11.2 Two-level cat-states 120
11.2.1 Variations in the shield positioning 120
11.2.2 Variations in the position of the detectors and traps 122
11.3 Continuous cat-states 122

12 Trap stability **125**
12.1 Quasi-static limit 125
12.2 Markovian limit 128

13 Quantum shield **131**
13.1 Decoherence effects of a quantum shield 133
13.2 Non-gravitationally mediated entanglement 135

14 Experimental implications **139**

IV Discussion **141**

Appendices **149**

A Naphthalene in a Stern-Gerlach Type Interferometer 149
A.1 Spin Dynamics in a Quadrupole Magnetic Field 149
A.2 Decoherence Between κ^{th} and κ'^{th} Wave Packet 150
A.3 Expectation Value of $\langle \hat{M} \rangle$ 153
A.4 $\pi/2$ Pulse in Dicke Basis 154
A.5 Expectation Value of $\langle \hat{M} \rangle$, Modified Protocol 156
A.6 Analysis of Wave Functions Structure 159
A.7 Possible Noise Sources - Spin Flips 162
B The Nuclear Einstein-de Haas and Barnett Effect with Levitated Nanoparticles 163
B.1 Friction 163
B.2 Friction Torque of a Rotating Ellipsoid in Gas 165
B.3 Rotation Under Confinement 166
B.4 Statistical Rotational Uncertainty 182
B.5 Mechanical Back Action of Nuclear Spin Relaxation 182
B.6 Commutator of Dipole-Dipole Hamiltonian with Angular Momentum 184
B.7 Magnetization in Magnetic Field Gradient 188
B.8 Magnetization of a Rotating Particle 189
B.9 Alternative Materials 190
C Stability Thresholds for Gravitationally Induced Entanglement in Shielded Setups 192
C.1 Size and Thickness of the Shield 192
C.2 Gravitational and Non-Gravitational Interactions 194
C.3 Gaussian States 200
C.4 Cat-States 205

Bibliography **213**

1 Introduction

Levitodynamics has emerged over the past decade as one of the most promising platforms for probing the quantum behaviour of mesoscopic systems [3, 4]. The idea of trapping small particles in vacuum, pioneered by Ashkin more than fifty years ago [5], has evolved from early demonstrations of optical manipulation into a sophisticated quantum technology. The first proposals for cooling the centre of mass motional degrees of freedom of levitated nanoparticles appeared about 15 years ago [6–8] and the field has since advanced rapidly to the point where motional ground-state cooling has been experimentally realised [9–11]. This achievement marks the beginning of an era in which levitated systems operate as genuine quantum platforms, combining ultralow mechanical dissipation, precise control over centre-of-mass and rotational degrees of freedom [12–14] and the ability to spin at frequencies limited only by the tensile strength of the material [15–17]. In contrast to clamped optomechanical systems [18], levitated particles are free from mechanical clamping or suspension, giving them exceptional isolation properties that make them ideal for precision sensing and tests of fundamental physics.

This thesis pushes the capabilities of levitodynamics into new territory along two distinct but complementary lines of research. The first introduces optically hyperpolarised organic crystals, materials whose nuclear spins are prepared in a highly non-equilibrium, macroscopically polarised state, as a new class of materials for levitation, proposed here for the first time. Combined with the exceptional isolation levitation provides, this opens the door to fundamental tests of quantum mechanics that were previously out of reach: tests of the linearity of quantum mechanics and the first observation of nuclear spin–rotation coupling via the Einstein-de Haas and Barnett effects. The second turns to gravitationally induced entanglement: the possibility that two massive particles become entangled purely through gravity. This thesis identifies and bounds a central obstacle to realising such a test: the shields needed to suppress electromagnetic interactions to isolate the gravitational signal turn out to introduce noise and even mediate entanglement of their own.

Hyperpolarised Materials for Fundamental Tests of Physics

The Stern-Gerlach experiment showed that a particle's spin can be coupled to its centre-of-mass motion through a spin-dependent force, splitting a beam of atoms according to their internal spin state. Using this spin-dependent splitting and

recombination to form a closed interferometric loop gives a Stern-Gerlach interferometer, which has since been realised with atoms [19]. A number of proposals have suggested extending this idea to massive, levitated nanoparticles as a means of preparing massive superpositions in position and hence testing the linearity of quantum mechanics. A key ingredient in many of these schemes is an internal spin degree of freedom that couples to the centre-of-mass motion through spin-dependent forces [20–23]. Diamond nanoparticles hosting nitrogen-vacancy (NV) colour centres have attracted considerable attention in this context [24–26], offering a route towards Stern-Gerlach-type matter-wave interferometry [27–29]. However, diamond opens up several noise channels that can severely limit interferometric coherence. For instance, the negatively charged NV centre induces an electric dipole moment in an otherwise charge-neutral nanodiamond, rendering it susceptible to stray electric fields [29, 30], while residual electronic impurities, P1 centres in the bulk and dangling bonds at the surface, introduce further decoherence channels that may render interferometry experiments impractical [31]. These limitations motivate the search for alternative spin-bearing materials that offer coherent quantum control without the associated noise.

This thesis proposes optically hyperpolarised molecular crystals as an alternative. The idea is to use a dopant molecule, which is briefly excited into a spin-polarised state, and to transfer its polarisation to the surrounding nuclear spins, before decaying back to a non-magnetically active ground state. The result is a crystal whose nuclear spins carry a large, artificially created polarisation, without the crystal ever containing a permanent, magnetically active impurity. Pentacene-doped naphthalene, the prime example studied in this thesis, illustrates the principle well. Pentacene molecules embedded in a naphthalene crystal can be optically excited into a triplet state that is itself strongly spin-polarised: through a process known as dynamical nuclear polarisation, this polarisation is transferred, using microwave driving of the electron spin, to the nuclear spins, reaching levels exceeding 80 % [32–38]. Crucially, pentacene's ground state is a singlet, so once the triplet state has decayed, none of the noise channels associated with a permanently paramagnetic defect remain. The nuclei's polarisation is furthermore remarkably long-lived, with lifetimes exceeding 920 h at cryogenic temperatures and 500 mT [36], evidence that the host crystal is essentially free of magnetic impurities that would otherwise cause it to decay.

The large collective nuclear-spin polarisation of hyperpolarised naphthalene makes it well suited to a kind of Stern-Gerlach protocol: rather than relying on a single embedded spin, as with an NV centre, the interferometer is driven by the combined strength of many nuclear spins distributed throughout the crystal. A single nuclear spin couples far more weakly than an electron spin to the mechanical motion, roughly three orders of magnitude, but the nuclear spin density in a naphthalene crystal carries so many polarised nuclei that the collective coupling, and hence the achievable superposition size, can exceed what a single electron spin allows. Because these spins have no preferred quantisation axis, unlike a single NV

centre, whose spin is pinned along a fixed crystallographic axis, the particle is not destabilised by internal torques as it moves through the interferometer, improving the visibility of the resulting interference pattern.

Quantum mechanics, in its standard formulation, places no limit on the size of a system that can be prepared in a superposition, and yet macroscopic objects are never observed in such states. This has motivated a family of collapse models, which modify the Schrödinger equation by adding a stochastic, nonlinear term whose strength grows with the mass of the system and its spatial delocalisation: for microscopic systems the added term is negligible and standard quantum mechanics is recovered, but for sufficiently large or massive systems it comes to dominate, causing the wavefunction to collapse spontaneously onto a definite outcome without invoking an observer or a measurement. The described interferometer is sensitive to precisely such kinds of deviation from standard quantum mechanics, most notably to the spontaneous, random collapse predicted by collapse models such as the Continuous Spontaneous Localisation (CSL) model [39].

Beyond interferometry, levitated particles can be rotated at MHz frequencies [40–42], far higher than any mechanically spun bulk sample can achieve. This opens the door to performing magic-angle spinning, a technique from solid-state NMR in which a sample is rotated at a specific angle to average out orientation-dependent interactions and sharpen spectral lines, in a levitated setup. Doing so would extend solid-state NMR into an entirely new regime.

This same ability to control a levitated particle's rotational degrees of freedom, combined with its nuclear polarisation, also opens a distinct class of phenomena, arising from the coupling between nuclear-spin angular momentum and rigid-body rotation. The Einstein-de Haas effect, the induction of mechanical rotation by a change in magnetisation [43], and its reciprocal, the Barnett effect, the induction of magnetisation by mechanical rotation [44], were both anticipated by Richardson [45] and first experimentally demonstrated in the electronic-spin regime a century ago. Recent work has extended the Einstein-de Haas effect to the level of single electron spins [46], but the nuclear-spin regime remains almost entirely unexplored. Signatures of the nuclear Barnett effect have been reported in liquids [47] and Barnett-induced effective magnetic fields have been measured in solids via resonance shifts [48–50], yet neither the nuclear Einstein-de Haas effect nor the direct detection of Barnett-induced nuclear magnetisation in a solid has been achieved. This thesis shows that the combination of optical hyperpolarisation and levitodynamics provides exactly the ingredients required: hyperpolarisation creates a large reservoir of nuclear angular momentum, whilst levitation grants access to free rotation and MHz rotation frequencies, making it an ideal candidate for tests of the spin-rotational coupling between nuclei and their host body.

Gravitationally Induced Entanglement in Shielded Setups

Levitated particles are, in the context of quantum experiments, unusually massive objects, and it is precisely this mass that opens a qualitatively different frontier: the quantum nature of gravity itself. Despite the remarkable success of quantum field theory in describing the electromagnetic, weak and strong interactions, a complete quantum theory of gravity remains elusive. A low-energy route towards probing the quantum character of gravity was envisioned by Feynman as a gedankenexperiment nearly seventy years ago [51] and subsequently formalised in the quantum information community [52, 53]: if two massive particles, each prepared in a spatial superposition, become entangled through purely gravitational interaction, that interaction cannot be described by local operations and classical communication alone [54, 55].

The observation of such gravitationally induced entanglement (GIE) would thus constitute a table-top test of quantum gravity. Recent advances in the quantum control of levitated massive objects [4, 9, 56–63] and in precision measurements of gravity at short ranges [64, 65] have spurred growing theoretical and experimental interest in GIE, with proposals spanning optical traps, magnetic levitation, free fall and space-based implementations [30, 52, 66–78].

A central practical obstacle in all such experiments is the electromagnetic interactions at the micrometre separations required for a detectable gravitational coupling, typically overpowering the gravitational attraction since electrostatic, magnetostatic and Casimir forces can exceed the gravitational coupling by many orders of magnitude. A conducting or superconducting Faraday shield placed between the particles is therefore an essential component of many proposals, intended to suppress direct non-gravitational interactions whilst leaving gravity unaffected [64, 79, 80]. However, the shield is not merely a passive element. Once the particles are prepared in spatially delocalised quantum states, their Casimir and magnetic-dipole interactions with the shield generate state-dependent phase shifts that depend sensitively on the particle-shield separation. Run-to-run fluctuations in the experimental geometry therefore translate into phase fluctuations that, upon averaging over many experimental realisations, degrade the entanglement. Furthermore, when the vibrational degrees of freedom of the shield are treated quantum mechanically, they act as an mediator that can generate non-gravitational entanglement between the particles, potentially masking or mimicking the gravitational signal. The shield thus becomes a central element in the certification of GIE: any experiment aiming to demonstrate gravitationally induced entanglement must not only suppress direct electromagnetic interactions between the particles, but also quantify and bound the indirect effects introduced by the shield itself.

This thesis provides a comprehensive analysis of these requirements, deriving stability thresholds on positional and orientational fluctuations of the experimental

setup, bounding the non-gravitational entanglement the shield can mediate, and establishing the constraints these requirements impose on realistic implementations.

Outline

The thesis is organised as follows. Part I provides the necessary background, covering the physics of levitated optomechanical systems, an introduction to collapse models with emphasis on the Continuous Spontaneous Localisation model, the theoretical framework for quantum-mediated entanglement and its interpretation as a signature of quantum gravity, an introduction to the Einstein-de Haas and Barnett effects, and an overview of dynamical nuclear polarisation and optically hyperpolarisable materials.

Part II, based on [1] and [81], addresses the use of levitated hyperpolarised naphthalene for fundamental physics. It opens with an analysis of naphthalene as a levitated material, covering its hyperpolarisation, the prospects for magic-angle spinning and particle preparation via sublimation. Here we show that, with magic-angle spinning, the T_2 time can be prolonged into a range sufficient to keep coherence throughout the interferometer and that the sublimation of naphthalene essentially stops when the bulk temperature is at 100 K or lower. It then develops a multi-spin Stern-Gerlach interferometry protocol and derives possible experimental constraints on CSL collapse-model parameters, exceeding the current state of the art. Finally, it investigates the nuclear Einstein-de Haas and Barnett effects in levitated naphthalene, proposing concrete protocols for their observation and analysing the relevant noise sources, including the rotational dynamics of asymmetric particles in a diamagnetic trap. This analysis shows that both effects could become observable in the near future, and identifies explicit constraints on the relevant parameters needed to suppress noise that would otherwise obscure the signal.

Part III, based on [2], analyses the role of a conducting Faraday shield in GIE experiments with levitated nanoparticles. It quantifies how Casimir and magnetic-dipole interactions between the particles and the shield impose stability requirements on the experimental geometry, characterises the decoherence arising from the quantised vibrational modes of the shield, and bounds the non-gravitational entanglement the shield can mediate between the particles. This analysis shows that the shield introduces limitations that had so far been largely overlooked, imposing stability requirements and entanglement bounds considerably stricter than previously assumed, making the observation of gravitationally induced entanglement in shielded setups more demanding than initially thought.

Finally, Part IV discusses the results of both parts in broader context, identifies open questions, and outlines directions for future research.

Part I

Preliminaries

2 An Introduction to Levitated Systems

In this thesis, we examine a specific type of mechanical oscillator: levitated nanoparticles. To stably levitate an object, it must be placed in a potential that confines it in all three spatial dimensions and counteracts the force of gravity. While there is a wide range of levitation techniques, they can broadly be categorised into Paul traps, optical traps and magnetic traps. In this chapter, we briefly introduce Paul and optical traps for completeness, but we provide a more detailed discussion of magnetic levitation, as the focus of Part II is on diamagnetic levitation. We then turn to the decoherence mechanisms relevant to levitated systems and focus on trapping and decoherence because these two aspects are the most directly relevant to the results presented in this thesis, but they are by no means the only topics relevant to levitated particles. The field has matured along several complementary directions: the development of the experimental setup itself, including loading particles directly into high vacuum [82–84], measurement and cooling of the particle's motional, rotational and internal degrees of freedom [9, 57, 60, 61, 85], motional and rotational control of the trapped particle [12, 15, 20, 86] and coupling of the particle to external systems such as spins or superconducting circuits [26, 87–89]. These experimental advances have in turn enabled a range of applications, including the study of stochastic thermodynamics [90–93], the investigation of materials [94–97], sensing and metrology [17, 98–100] and tests of fundamental physics [64, 101–104], the latter being the application this thesis focuses on. Other aspects of the platform are discussed in more depth in [4], to which we refer the reader for a comprehensive overview of the field.

2.1 Trapping mechanisms

The Paul Trap

The Paul trap was invented by Wolfgang Paul and Helmut Steinwedel [105]. Initially developed as a mass spectrometer, it is now widely used both for mass spectrometry [106] and for trapping ions, which are promising candidates for quantum computing [107]. In the following, we outline the basic principle of a Paul trap using the example of a ring-shaped configuration.

This trap consists of a hyperbolic ring electrode and two hyperbolic end-cap electrodes, which are short-circuited and oriented with their focal points facing each

other. An oscillating voltage $U(t) = U_{\mathrm{dc}} + U_{\mathrm{ac}} \cos(\omega_{\mathrm{ac}} t)$ is applied to the ring electrode.

In this configuration, the centre-of-mass motion of a charged particle in the Paul trap can be described by the Mathieu equation [108]

$$\frac{\mathrm{d}^2 r_i}{\mathrm{d}\xi^2} + [a_{r_i} - 2q_{r_i} \cos(2\xi)] r_i = 0 \tag{2.1}$$

where $r_i \in \{x, y, z\}$ are the translational degrees of freedom, $\xi = \omega_{\mathrm{ac}} t/2$ is a dimensionless time variable, and a_{r_i}, q_{r_i} are dimensionless trapping parameters. These are given by $a_x = a_y = -a_z/2 = 8QU_{\mathrm{dc}}/(m\omega_{\mathrm{ac}}^2 r_0^2)$ and $q_x = q_y = -q_z/2 = 4QU_{\mathbf{ac}}/(m\omega_{\mathrm{ac}}^2 r_0^2)$. r_0 is a trap-specific length parameter (here the inner radius of the ring electrode), m is the mass of the particle and Q its charge. (2.1) admits both stable and unstable solutions; only the stable ones correspond to conditions that allow for stable trapping.

The trapping frequency of levitated, charged nanoparticles typically lies in the range $\Omega/(2\pi) \sim 1 - 10\,\mathrm{kHz}$ and it scales with the charge-to-mass ratio as $\Omega \propto U_{\mathrm{ac}}/\omega_{\mathrm{ac}} \times Q/m$ [4].

In addition to this slow oscillatory motion, the particle experiences a superposed small, rapid oscillation at the oscillation frequency of the voltage ω_{ac}, known as micromotion. This micromotion is typically strongly suppressed compared to the large oscillation amplitude and can often be neglected, although it is always present [108].

Moreover, voltage noise in the trap electrodes is unavoidable. While static electric fields would be less noisy, Earnshaw's theorem prohibits stable trapping using purely electrostatic fields.

The Optical Trap

Building on the pioneering work on optical traps in biophysics [5, 109] and optically trapped neutral atoms [110], the optical control of levitated nanoparticles has made significant advances [7, 111, 112]. In particular, this platform has enabled ground state cooling of the centre-of-mass motion and librational modes of nanoparticles [9, 57, 63] and the generation of ground state squeezed states [62].

In optical levitation, a highly focused laser beam is used to hold and manipulate small objects, hence the term optical tweezers. The oscillating electric field of the laser induces a dipole moment in the dielectric particle, proportional to its polarisability α: $\mathbf{p} = \alpha \mathbf{E}$. Because the focused beam's field is spatially inhomogeneous, this induced dipole experiences a net force pulling it toward the region of highest field intensity at the beam focus. The trapping potential follows directly from the

potential energy of an induced dipole in an external field,

$$U(\mathbf{r}) = -\frac{\alpha}{2}|\mathbf{E}(\mathbf{r})|^2 \tag{2.2}$$

which is minimised where the field intensity is maximal, giving rise to a stable, harmonic trap at the focus [113]. The oscillation frequency is typically in the range of $\Omega/(2\pi) \sim 10 - 300\,\mathrm{kHz}$. Motion along the optical axis scales as $\Omega_l \propto \sqrt{P}\lambda/w^3$, while motion transverse to the optical axis scales as $\Omega_t \propto \sqrt{P}/w^2$, where P is the laser power, w is the beam waist at the focal point and λ is the laser wavelength [4].

To levitate nanoparticles, high laser intensities are required to counteract gravity. However, photon absorption can significantly raise the particle's internal temperature, sometimes even causing the particles to burn [114]. In ultra-high vacuum, the particle is so well isolated that thermalisation with the environment becomes extremely slow, allowing heat to accumulate. As a result, even nanoparticles made from highly transparent materials such as silica can heat up to temperatures around 1000 K [94]. This leads to substantial thermal photon emission via black-body radiation, which introduces unavoidable noise in the particle's positional degrees of freedom.

Another major noise source in optical levitation arises from the scattering and absorption of laser photons. Each such event imparts a momentum kick to the particle, which must be continuously counteracted by either passive or active feedback cooling.

Magnetic Traps

There are different magnetic trapping mechanisms. Here we focus on two closely related ones: diamagnetic levitation and superconducting levitation. Both rely on the same underlying principle: an external, spatially inhomogeneous magnetic field $\mathbf{B}(\mathbf{r})$ induces a magnetic dipole moment in a material that opposes the applied field. This induced dipole interacts with the field it is immersed in, generating a force that pushes the material toward regions of lower field magnitude. All diamagnetic materials show this effect, though typically weakly. A superconductor in the Meissner state is the extreme limit of a diamagnet, with volume susceptibility $\chi_V = -1$, expelling the field completely from its bulk. Because the effect is so strong in this limit, the geometry can effectively be reversed: instead of a diamagnetic object being repelled from a fixed magnet, a permanent magnet can be levitated above a fixed bulk superconductor. As this work mainly revolves around diamagnetic levitation, we outline its general principle first, before treating superconducting levitation as its extreme case.

When a diamagnetic particle of volume V and susceptibility $\chi_V < 0$ is placed in an external field $\mathbf{B}(\mathbf{r})$, it acquires an induced magnetic dipole moment $\mathbf{m} = \chi_V V\,\mathbf{B}(\mathbf{r})/\mu_0$, oriented anti-parallel to $\mathbf{B}$. Because this dipole is anti-aligned

rather than aligned with the field, its interaction energy is minimised where $|\mathbf{B}|$ is smallest, so the particle is pushed toward regions of minimal field strength rather than maximal field strength, as is the case for a paramagnet or an electric dipole in an inhomogeneous electric field. The potential energy density $E(\mathbf{r})$ of the particle in a magnetic field $\mathbf{B}(\mathbf{r})$, subject to Earth's gravity, at position $\mathbf{r} = (x, y, z)$, is then

$$E(\mathbf{r}) = -\frac{\chi_V}{2\mu_0}\mathbf{B}(\mathbf{r})^2 + \rho g z, \tag{2.3}$$

where ρ is the mass density of the particle. The equilibrium position for levitation is determined by the condition $\mathbf{F}(\mathbf{r}) = -\nabla E(\mathbf{r}) = 0$, where $\mathbf{F}(\mathbf{r})$ is the force density acting on the particle. For the z-component, this yields the standard condition for diamagnetic trapping:

$$B(z_0)\left.\frac{\partial B}{\partial z}\right|_{z_0} = \mu_0 g \frac{\rho}{\chi_V}. \tag{2.4}$$

Writing the field near the trap as $B(z) = B_0 + B'z$ with $B' = \partial_z B$, Eq. (2.4) must be solved for z_0 to find the equilibrium height. The trap stiffness depends only on the field gradient $\partial_z B$, while the equilibrium position depends on both B_0 and $\partial_z B$ together. In particular, B_0 can be tuned independently to shift the equilibrium height without changing the trap stiffness. The trap frequency is given by $\Omega = B'\sqrt{|\chi_V|/(\mu_0\rho)}$, the local magnetic field at z_0 is given by $B = \mu_0 g\rho/(\chi_V B')$ and the equilibrium position is given by $z_0 = -g/\Omega^2 - B_0/B'$.

To assess the practical feasibility of this approach, we consider the specific case of levitating naphthalene, as proposed in this thesis. For naphthalene, with $\rho = 1145\ \mathrm{kg/m^3}$ and $\chi_V = -9.21 \cdot 10^{-6}$ [115], the levitation condition requires $B(\partial B/\partial z)$ to be on the order of $1500\ \mathrm{T^2/m}$, which is within experimental reach [116].

Superconducting levitation can be understood as the limiting case of diamagnetic levitation with $\chi_V \to -1$. If a superconductor such as lead is cooled below its critical temperature T_c, it enters the so-called Meissner phase, in which the superconductor expels all magnetic flux from its interior [117], behaving as a perfect diamagnet. Now, instead of levitating a superconductor, a hard magnet such as a ferromagnet can also be levitated above a superconducting surface. This phenomenon can be described using the method of mirror images: when a hard magnet is placed above the superconducting plane, it induces a mirror magnetic dipole, generating a repulsive force that counterbalances gravity. The interaction energy between the magnet and the superconducting plane is equal to half the energy of the interaction with a mirror-image dipole, of the same magnetic moment, placed at the mirrored position with reversed orientation [118]. This leads to

$$U = \frac{\mu_0 \mu^2}{64\pi z^3} + mgz, \tag{2.5}$$

where m is the mass of the particle, g is the local gravitational acceleration,

$\mu_0 = 4\pi \cdot 10^{-7}$ H/m is the vacuum permeability and μ is the magnetic moment of the hard magnet. The potential energy is minimised at $z_0 = [(3\mu_0\mu^2)/(64\pi mg)]^{1/4}$.

This description strictly holds for type-I superconductors, or for type-II superconductors operated below their lower critical field H_{c1}, where the field is fully expelled. Type-I superconductors have a single critical field $H_c(T)$: below it the material is a perfect diamagnet, and above it superconductivity is destroyed abruptly, with the field penetrating completely. Since $H_c(T)$ decreases with temperature and vanishes at T_c, only a narrow window of (typically low) fields is available, particularly if one operates close to T_c. Type-II superconductors instead have two critical fields, $H_{c1}(T)$ and $H_{c2}(T)$: below $H_{c1}(T)$ they behave just like a type-I superconductor, but between $H_{c1}(T)$ and $H_{c2}(T)$ they enter a mixed state in which magnetic flux penetrates as quantised vortices while the material in between remains superconducting. Crucially, $H_{c2}(T)$ can be orders of magnitude larger than the critical field of a typical type-I superconductor, so type-II materials tolerate much stronger fields before superconductivity breaks down, but since the vortices add additional dissipation channels, type-I superconductors are more desirable for precision measurements [99, 119–121].

Magnetically levitated particles typically exhibit low trap frequencies in the range of 0.1-1 kHz [4]. The low trap frequency leads to longer experimental time scales compared to other types of traps. Additionally, in comparison to the other two trapping methods, the cooling of the particle's degrees of freedom is less developed.

However, since diamagnetic and superconducting levitation rely solely on static magnetic fields, they avoid photon scattering (as occurs in optical traps) and RF-driven micromotion (as found in Paul traps), both of which heat the particle's degrees of freedom. Furthermore, diamagnetic objects can be levitated without any optical absorption, minimising internal heating, and there is no need to electrically charge the particles [122]. Charging is undesirable for high-precision measurements, because charged particles couple strongly to stray electric fields and patch potentials from nearby surfaces, adding another source of heating and force noise.

This makes magnetic levitation an ideal candidate for precision sensing and fundamental experiments. In this thesis, we focus on diamagnetic levitation as, unlike superconducting levitation, it requires no cryogenic cooling and works for a much broader range of materials, including organic molecular crystals such as naphthalene, which cannot be made superconducting, allowing for a simpler and more versatile experimental setup.

Major Applications

Levitated nanoparticles find application across several major areas of physics. Because they can be isolated and controlled in well-defined, tunable environments,

they are ideal for exploring non-equilibrium physics and stochastic thermodynamics at the nanoscale [92]. This same isolation, combined with the high mechanical quality factors attainable in vacuum, also makes them exceptional sensors: their applications in metrology span ultra-sensitive detection of forces, accelerations, torques and rotations [16, 95, 103, 123, 124]. It is precisely this sensitivity that has established levitodynamics as a compact, table-top platform for probing physics beyond what is currently understood [125]. Diamagnetically and optically levitated force sensors have been used to search for deviations from Newtonian gravity and evidence of dark energy fields [126, 127], to propose high-frequency gravitational-wave detection in a regime inaccessible to kilometre-scale interferometers [128] and to constrain candidate dark matter interactions through their coupling to mass [104, 129]. Of particular relevance to this thesis, one of the central ambitions of the field is to bring massive mechanical oscillators into the quantum regime, both to test the validity of quantum mechanics for genuinely macroscopic objects and to probe the elusive interface between quantum theory and gravity [54, 125]. A recent experiment demonstrating the controlled quantum delocalisation of a levitated nanoparticle's wavefunction marks a first step in this direction [130]. Also central to this thesis is the investigation of the spin-rotational coupling between a levitated nanoparticle and the nuclear spins it carries, analogous to the Einstein-de Haas and Barnett effects.

Relevance for this Thesis

Throughout this thesis, levitated particles serve as the experimental platform for probing fundamental physics, owing to the high degree of control achievable over their six mechanical degrees of freedom, their comparatively large mass and the near-term prospect of reaching quantum control over the centre-of-mass motion. In Part II, we propose using diamagnetically levitated, optically hyperpolarised nanoparticles to test collapse models and nuclear spin-mechanical coupling, introduced in Sections 3.1 and 3.3. The same considerations reappear in Part III, where superconducting and optical levitation play a central role in the gravitationally induced entanglement setup as introduced in Section 3.2.

2.2 Unavoidable sources of decoherence

While levitated systems are well isolated from their environment, they still interact with residual air molecules and thermal photons. Since these sources of noise cannot be entirely eliminated, they are referred to as unavoidable sources of decoherence.

Such interactions are typically modelled as position localisation, which predicts an exponential decay of spatial coherences. This chapter follows the work of

Schlosshauer [131,132], who uses scattering theory to derive the following equation

$$\langle \mathbf{q}' | \dot{\hat{\rho}} | \mathbf{q}'' \rangle = \frac{i}{\hbar} \langle \mathbf{q}' | [\hat{\rho}, \hat{H}] | \mathbf{q}'' \rangle - \Gamma(q' - q'') \langle \mathbf{q}' | \hat{\rho} | \mathbf{q}'' \rangle , \tag{2.6}$$

where $|\mathbf{q}\rangle$ is the three dimensional position eigenstate, $\hat{\rho}$ the system state and the Hamiltonian $\hat{H}$ describes the system's unitary time evolution. The function $\Gamma(q' - q'')$ is known as the decoherence factor and is given by

$$\Gamma(\mathbf{q}' - \mathbf{q}'') = \int_0^\infty \mathrm{d}p \, \rho(p) \, v(p) \int \frac{\mathrm{d}\mathbf{n}' \, \mathrm{d}\mathbf{n}''}{4\pi} \left(1 - e^{\frac{i}{\hbar} p (\mathbf{n}' - \mathbf{n}'') \cdot (\mathbf{q}' - \mathbf{q}'')} \right) |f(p\mathbf{n}', p\mathbf{n}'')|^2 . \tag{2.7}$$

Here, $\rho(p)$ denotes the number density of incoming particles with momentum magnitude p, $v(p)$ is their velocity and $f(p\mathbf{n}, p\mathbf{n}')$ is the elastic scattering amplitude. The unit vectors $\mathbf{n}$ and $\mathbf{n}'$ represent the directions of the incoming and outgoing particles, respectively.

This model holds under the following assumptions:

- The system and environment are initially uncorrelated, a standard prerequisite in most models of decoherence.
- The scattering process is translationally invariant with respect to the total object-environment system.
- The object's centre-of-mass remains unchanged by individual scattering events[1]
- Scattering events occur on a timescale much shorter than the intrinsic dynamical evolution of the system as governed by its self-Hamiltonian.
- The incoming particles are uniformly distributed in all directions.

These assumptions are typically valid for a massive object at rest interacting with an environment of microscopic particles. Nevertheless, this model predicts infinite heating and is therefore not energy conserving. This issue arises because it neglects momentum exchange (dragging effects). A more complete, albeit more complex, master equation is derived in [131]. However, for the scenarios where this theory is applied, low temperatures, dynamics far from equilibrium, time scales too short for the particle to thermalise with its environment and massive particles, the model presented here is sufficiently accurate. The behaviour of $\Gamma(\mathbf{q}' - \mathbf{q}'')$ changes significantly depending on the ratio between $|\mathbf{q}' - \mathbf{q}''|$ and the thermal de Broglie wavelength λ_{th} of the scattering particle as shown in the following section.

[1] This condition should be understood in the sense that the scattered particle collects which-path information, but does not change the position state of the particle. If $|\mathbf{q}\rangle$ is the position state of the particle and $|\chi_i\rangle$ the state of the incoming environmental particle, the scattering interaction therefore yields $|\mathbf{q}\rangle |\chi_0\rangle \to |\mathbf{q}\rangle |\chi(\mathbf{q})\rangle$.

The Short- and Long-Wavelength Limit

To identify the relevant regime, note that each scattered environmental particle carries a de Broglie wavelength $\lambda_{\text{th}} = 2\pi\hbar/p_0$, where p_0 denotes its characteristic momentum. Since the environment is in thermal equilibrium, we take the momentum spectrum of the incoming particles to be peaked around this value. The behaviour of $\Gamma(\mathbf{q}' - \mathbf{q}'')$ is then controlled by the dimensionless parameter $p_0|\mathbf{q}' - \mathbf{q}''|/\hbar$, comparing the spatial separation to the thermal de Broglie wavelength of the scatterers. First, we will describe the two regimes and then give concrete expressions for the introduced quantities for different physical processes.

If $p_0|\mathbf{q}' - \mathbf{q}''|/\hbar \gg 1$, we are in the short-wavelength limit: the exponential on the right-hand side of Eq. (2.7) oscillates rapidly as a function of the scattering momentum $\mathbf{p}$, and upon integration over the momentum distribution of the environmental particles it is negligible compared to the constant term of one. A physical interpretation of this result is that in the short-wavelength limit, $\lambda_{\text{th}} \ll |\mathbf{q}' - \mathbf{q}''|$, the scattered particle carries away the maximum amount of which-path information, resulting in maximal decoherence per scattering event. In this regime, $\Gamma(\mathbf{q}' - \mathbf{q}'')$ becomes independent of $|\mathbf{q}' - \mathbf{q}''|$ and approaches its maximum, which we denote as the scattering rate ξ. In the short-wavelength limit, the differential equation then becomes

$$\langle \mathbf{q}' | \, \dot{\hat{\rho}} \, | \mathbf{q}'' \rangle = \frac{i}{\hbar} \langle \mathbf{q}' | \, [\hat{\rho}, \hat{H}] \, | \mathbf{q}'' \rangle - \xi \, \langle \mathbf{q}' | \, \hat{\rho} \, | \mathbf{q}'' \rangle \, . \tag{2.8}$$

This shows that, in the limit of maximal decoherence, spatial coherences are exponentially suppressed at the rate ξ.

Conversely, if $p_0|\mathbf{q}' - \mathbf{q}''|/\hbar \ll 1$, we are in the long-wavelength limit: the exponential varies slowly over the relevant range of $\mathbf{p}$ and can be Taylor expanded up to second order, so that the resulting momentum integral can be evaluated. The linear-order term vanishes by the isotropy of the momentum distribution, leaving the quadratic term as the leading contribution, which is why Γ grows as $|\mathbf{q}' - \mathbf{q}''|^2$ in this limit. Physically, in the long-wavelength limit, $\lambda_{\text{th}} \gg |\mathbf{q}' - \mathbf{q}''|$, an individual scattering event cannot resolve the separation $|\mathbf{q}' - \mathbf{q}''|$ and thus causes significantly less decoherence compared to the short-wavelength case. As the separation increases, however, the scattering particle can resolve more which-path information. Therefore, we expect $\Gamma(\mathbf{q}' - \mathbf{q}'')$ to increase with $|\mathbf{q}' - \mathbf{q}''|$ in this limit, which matches with the intuition found from the mathematical expression. Thus, in the long-wavelength limit, the decoherence factor is given by

$$\langle \mathbf{q}' | \, \dot{\hat{\rho}} \, | \mathbf{q}'' \rangle = \frac{i}{\hbar} \langle \mathbf{q}' | \, [\hat{\rho}, \hat{H}] \, | \mathbf{q}'' \rangle - \Lambda |\mathbf{q}' - \mathbf{q}''|^2 \, \langle \mathbf{q}' | \, \hat{\rho} \, | \mathbf{q}'' \rangle \, , \tag{2.9}$$

where Λ is referred to as the scattering constant in this context.

The short- and long-wavelength limits can be modelled assuming $\Gamma(\mathbf{q}' - \mathbf{q}'')$ to

have the following form

$$\Gamma(\mathbf{q}' - \mathbf{q}'') = \xi_{\mathrm{ls}} \left(1 - e^{-\frac{|\mathbf{q}' - \mathbf{q}''|^2}{4r_{\mathrm{ld}}^2}} \right) \tag{2.10}$$

which interpolates between the two limits. Here, $\xi_{\mathrm{ls}} > 0$ with units s^{-1} is called the localisation strength or collapse rate, and $r_{\mathrm{ld}} > 0$ with units m is the localisation distance. Both parameters depend on the particular source of decoherence. As a primer, it is worth noting that the noise predicted by some collapse models has the same functional form, as will be discussed further in Section 3.1. Depending on the ratio between $|q' - q''|$ and r_{ld}, the decoherence factor as in Eq. (2.10) goes as

$$\Gamma(q' - q'') = \begin{cases} \Lambda |q' - q''|^2, & |q' - q''| \ll 2r_{\mathrm{ld}} \\ \xi_{\mathrm{ls}}, & |q' - q''| \gg 2r_{\mathrm{ld}} \end{cases}, \tag{2.11}$$

and one can identify

$$\Lambda = \xi_{\mathrm{ls}} / (4r_{\mathrm{ld}}^2) \quad \text{and} \quad \lambda_{\mathrm{th}} = 2r_{\mathrm{ld}}. \tag{2.12}$$

Decoherence Due to Scattering of Thermal Photons

Every time a photon collides with a particle, it carries some which-path information. Since there is always a photon gas present in the environment due to blackbody radiation, scattering with thermal photons is an unavoidable source of noise.

Thermal photons have a thermal wavelength given by

$$\lambda_{\mathrm{th}}^{\mathrm{bb}} = \pi^{2/3} \frac{\hbar c}{k_{\mathrm{B}} T_{\mathrm{e}}} \approx \frac{0.5 \cdot 10^{-3}}{T_{\mathrm{e}}}, \tag{2.13}$$

where k_{B} is Boltzmann's constant, c is the speed of light and T_{e} is the temperature of the environment.

The scattering constant is given by

$$\Lambda^{\mathrm{bb,sc}} = 8! \cdot \frac{8}{9\pi} R^6 c \, \mathrm{Re} \left(\frac{\varepsilon - 1}{\varepsilon + 2} \right)^2 \left(\frac{k_{\mathrm{B}} T_{\mathrm{e}}}{\hbar c} \right)^9 \zeta(9), \tag{2.14}$$

where R is the radius of the system particle, ε is its dielectric constant and $\zeta(x)$ is the Riemann zeta function.

At this point, it is important to emphasise the strong dependence of Λ on both the particle's radius and the temperature of the photon gas.

Decoherence Due to Absorption and Emission of Thermal Photons

Thermal photons can not only scatter off the particle but also be absorbed. Additionally, the particle itself may emit photons due to its own blackbody radiation. The scattering constants for absorption and emission are formally identical, but the temperature entering the expression differs: it is the bulk temperature of the macroscopic particle in one case and that of the environment in the other.

The scattering constant for both absorption and emission is given by

$$\Lambda^{\mathrm{bb,e/a}} = \frac{16\pi^5 c R^3}{189} \left(\frac{k_\mathrm{B} T_\mathrm{i/e}}{\hbar c}\right)^6 \mathrm{Im}\left(\frac{\varepsilon - 1}{\varepsilon + 2}\right), \tag{2.15}$$

where $T_\mathrm{i/e}$ denotes either the internal temperature of the particle or the temperature of the surrounding photon gas.

In the regimes considered in this work, $\Lambda^{\mathrm{bb,e}}$ will typically dominate over the other two sources of decoherence.

The different scaling between scattering and absorption of photons arises from two independent factors. First, scattering is a second-order process in the induced dipole: the scattered power is proportional to $|f(p\mathbf{n}', p\mathbf{n}'')|^2 \propto R^6$, whereas absorption is a first-order dissipative process, proportional to $|f(p\mathbf{n}', p\mathbf{n}'')|^2 \propto R^3$ directly, since it only requires the lossy part of the linear response. Second, the frequency dependence of the two cross sections differs: Rayleigh scattering scales as $|f(p\mathbf{n}', p\mathbf{n}'')|^2 \propto \omega^4$, while absorption scales only linearly, $|f(p\mathbf{n}', p\mathbf{n}'')|^2 \propto \omega$. Upon integrating each cross section over the thermal photon spectrum, the extra ω^3 in the scattering cross section translates into an extra $T_\mathrm{i/e}^3$. Combined, these two independent factors of three account for the $R^6 T_\mathrm{e}^9$ scaling of scattering versus the $R^3 T_\mathrm{i/e}^6$ scaling of absorption and emission.

Decoherence Due to Scattering of Air Molecules

Even in ultra-high vacuum, residual air molecules may still scatter off the system. Their thermal wavelength is given by

$$\lambda_\mathrm{th}^\mathrm{air} = \frac{2\pi\hbar}{\sqrt{2\pi m_\mathrm{g} k_\mathrm{B} T_\mathrm{e}}} \approx \frac{1.2 \cdot 10^{-9}}{\sqrt{T_\mathrm{e}}}, \tag{2.16}$$

where $m_\mathrm{g} \approx 2\,\mathrm{u}$ is the mass of air molecules, approximated as two atomic mass units.

The corresponding scattering constant is

$$\Lambda^\mathrm{air} = \frac{4\pi m_\mathrm{g} \overline{v}_\mathrm{g} P R^2}{3\hbar^2}, \tag{2.17}$$

where $\overline{v}_{\mathrm{g}} = \sqrt{\frac{8k_{\mathrm{B}}T_{\mathrm{e}}}{\pi m_{\mathrm{g}}}}$ is the mean velocity of the gas molecules.

Since $\lambda_{\mathrm{th}}^{\mathrm{air}}$ is typically very small, we operate in the short-wavelength limit, and the resulting decoherence is quite strong.

To minimise such decoherence, a common requirement is to avoid collisions with air molecules altogether. This can be achieved by ensuring that the duration of one experimental run, T_{tot}, is so short that the probability of a collision remains negligible:

$$P = 1 - e^{-\gamma_{\mathrm{g}} T_{\mathrm{tot}}/3} \ll 1, \tag{2.18}$$

where γ_{g} is the collision frequency

$$\gamma_{\mathrm{g}} = \frac{8\pi P R^2}{m_{\mathrm{g}} \overline{v}_{\mathrm{g}}}. \tag{2.19}$$

Note that Λ^{air} and γ_{g} are directly related:

$$\Lambda^{\mathrm{air}} = \frac{(m_{\mathrm{g}} \overline{v}_{\mathrm{g}})^2}{6\hbar^2}\, \gamma_{\mathrm{g}}, \tag{2.20}$$

so that γ_{g} is simply the bare rate at which air molecules collide with the particle, while Λ^{air} is this same rate weighted by the squared momentum transfer per collision (in units of $\hbar$). This is consistent with the general picture that the decoherence strength is set by the collision rate multiplied by how much positional information each collision resolves. Note that γ_g is, up to a numerical factor on the order of one, identical to ξ as defined in Eq. (2.12).

Connection to Quantum Brownian Motion

The equation in Eq. (2.9) is of Lindblad form and can be written as

$$\dot{\hat{\rho}} = \frac{i}{\hbar}[\hat{\rho}, \hat{H}] - \sum_{i \in \{x,y,z\}} \Lambda[\hat{x}_i, [\hat{x}_i, \hat{\rho}]]. \tag{2.21}$$

Here, $\hat{x}_i$ denotes the corresponding position operators in x, y and z directions. This equation is well known from the theory of quantum Brownian motion and describes pure momentum diffusion (heating) [133, 134]. In particular, the kinetic energy grows linearly according to

$$\frac{d}{dt}\langle \hat{\mathbf{p}}^2 \rangle = 6\Lambda\hbar^2, \tag{2.22}$$

so that the dynamics is neither energy conserving nor thermalising. To obtain equilibration towards a thermal Gibbs state, one must additionally include a

dissipative (friction) term. In quantum Brownian motion, the standard master equation is given by

$$\dot{\hat{\rho}} = \frac{i}{\hbar}[\hat{\rho}, \hat{H}] - \sum_{i\in\{x,y,z\}} \left[\frac{i\gamma}{2\hbar}[\hat{x}_i, \{\hat{p}_i, \hat{\rho}\}] + \frac{D_{pp}}{\hbar^2}[\hat{x}_i, [\hat{x}_i, \hat{\rho}]] + \frac{D_{xp}}{\hbar^2}[\hat{p}_i, [\hat{p}_i, \hat{\rho}]] \right], \quad (2.23)$$

where γ, D_{pp} and D_{xp} are bath-specific constants. In this section, we will follow closely the argumentation in [135]. The anticommutator term generates friction, while the diffusion terms inject noise into the system. Thermalisation emerges from the balance between dissipation and fluctuations. The diffusion and friction coefficients are related through a fluctuation-dissipation relation, such that the stationary state is thermal.

In the weak-coupling, short-term regime $t \ll \gamma^{-1}$, the friction term can be neglected while still describing the short-time decoherence phenomena associated with quantum Brownian motion. This is in agreement with assumptions three and five when deriving the collisional-diffusion based derivation of the master equation given above: Assumption three (the object's centre-of-mass is unchanged by an individual scattering event, i.e. no recoil) is the statement that a single collision does not transfer enough momentum to appreciably alter the system's own state. Dissipation is inherently a cumulative effect: it only becomes visible once the system's momentum distribution has been measurably reshaped by the accumulation of many collisions. If each individual collision is assumed recoil-free, the leading-order equation has no mechanism to track that reshaping, so it produces pure dephasing (which only requires the collision to imprint which-path phase information, not to move the object) with no relaxation channel. Assumption five (incoming particles isotropically distributed) removes the complementary piece of the friction mechanism. Physically, friction arises from a Doppler-type asymmetry: an object moving through the gas encounters more head-on collisions on its leading face than its trailing face, and this anisotropic collision rate is what produces a net drag force. Assuming an isotropic incident flux is equivalent to evaluating the collision rate as though the system were at rest, i.e. dropping this velocity-dependent correction.

The double commutator in $\hat{p}$ is a purely quantum phenomenon needed to guarantee the positivity of Eq. (2.23) in the presence of friction at short times and ultra-low temperatures of the bath. Typically, D_{xp} is strongly suppressed with respect to the momentum diffusion term D_{pp} and, even more, its experimental verification is quite involved. As state in [135], the quantum correction term is only the dominating contribution for $t \lesssim \hbar/(k_{\mathrm{B}}T_{\mathrm{bath}}) \approx (7 \cdot 10^{-12}\,\mathrm{K\,s})/T_{\mathrm{bath}}$. Hence, for all practical purposes, we will neglect the $[\hat{p}, [\hat{p}, \hat{\rho}]]$ term, which leaves us with the pure momentum diffusing master equation $\dot{\hat{\rho}} = i[\hat{\rho}, \hat{H}]/\hbar - \sum_{i\in\{x,y,z\}} D_{pp}[\hat{x}_i, [\hat{x}_i, \hat{\rho}]]/\hbar^2$.

Relevance for this Thesis

The decoherence framework derived in this section directly determines the sensitivity of the Stern-Gerlach-type interferometer with levitated, hyperpolarised naphthalene developed in Chapter 7. Ultimately, this environmental noise budget is what weighs against the noise predicted by collapse models, which are introduced in Section 3.1. Only when this environmental noise is under control, any excess decoherence can be interpreted as evidence for, or against, a collapse-induced mechanism such as CSL.

3 Fundamental Physics Phenomena

This chapter introduces three phenomena that this thesis sets out to investigate: the loss of coherence predicted by collapse models, the entanglement gravity may be able to mediate between two masses and the coupling between nuclear spin and mechanical rotation captured by the nuclear Einstein-de Haas and Barnett effects. Each links a microscopic quantum property to a macroscopically observable signature and each motivates an experimental proposal developed in Part II and Part III, for which the levitated platforms introduced in Chapter 2 provide a natural setting.

3.1 The Continuous Spontaneous Localisation Model

Although the laws of quantum physics have been thoroughly confirmed for light particles such as electrons and massless particles such as photons, it remains an open question whether quantum mechanics also applies in the macroscopic realm. Since quantum effects are not observed in everyday life, the question arises whether this is simply because macroscopic objects are coupled strongly to their environment, causing them to decohere quickly and lose the ability to exhibit quantum behaviour. In this case, it would merely be a matter of developing the technical expertise to prepare a heavy particle in a quantum state such as a cat state and maintain the coherence for some time.

Alternatively, there are several theories that modify standard quantum mechanics and fundamentally prevent heavy objects from maintaining coherent states, such as collapse models. If these are correct, quantum mechanical effects would be strongly and fundamentally suppressed on macroscopic scales. The most direct such test is matter-wave interferometry: by coherently splitting and recombining the wave packet of an increasingly large and massive object, one directly probes whether the quantum superposition principle continues to hold at ever larger scales, or whether it breaks down as collapse models predict [132, 136, 137]. Although the physics community has succeeded in performing interferometry with increasingly large molecules, up to about 170,000 atomic mass units [138], these alternative theories have not yet been definitively ruled out.

Collapse models were originally motivated by the measurement problem: in standard quantum mechanics, the collapse of the wavefunction upon measurement is postulated ad hoc rather than following from unitary Schrödinger evolution, and the theory offers no fundamental criterion for when a system should be treated

as "classical enough" to collapse. Collapse models resolve this by modifying the Schrödinger equation itself, adding stochastic, nonlinear terms that induce spontaneous, mass-dependent localisation: microscopic quantum phenomena are left essentially untouched, while macroscopic superpositions decay rapidly, recovering classical behaviour without an observer-dependent measurement postulate. Several such models have been proposed, differing mainly in the physical mechanism assumed to drive the collapse, from the phenomenological, discrete localisations of the Ghirardi-Rimini-Weber (GRW) model [139], to gravitationally motivated collapse mechanisms such as the Diósi-Penrose model [140, 141]. In this chapter, we focus on the Continuous Spontaneous Localisation (CSL) model [142, 143], which replaces the discontinuous jumps of GRW with a continuous stochastic process, and which is, to date, one of the most extensively studied and tested collapse models [39, 144]. After a brief summary of the derivation of the model, an overview of different types of experimental tests is presented.

3.1.1 The CSL Model

In the CSL model, a stochastic term which is nonlinear in the state $\hat{\rho}$ is added to the Schrödinger equation. This term acts like a measurement with unknown outcome, therefore destroying the coherence of the quantum state. In order to reflect the well-verified phenomenology of quantum mechanics, this term is proportional to the mass of the object, going to zero for $m \to 0$. The strength of this noise-like term contains two phenomenological constants which have to be bounded by experimental evidence.

The dynamical equation for the wavefunction is stochastic and given by

$$\begin{aligned} \mathrm{d}\left|\psi_t\right\rangle = \Big[&-\frac{i}{\hbar}\hat{H}\mathrm{d}t + \frac{\sqrt{\lambda_{\mathrm{CSL}}}}{m_0}\int \mathrm{d}\mathbf{x}\hat{N}_t(\mathbf{x})\mathrm{d}W_t(\mathbf{x}) \\ &- \frac{\lambda_{\mathrm{CSL}}}{2m_0^2}\int \mathrm{d}\mathbf{x}\int \mathrm{d}\mathbf{y} g(\mathbf{x}-\mathbf{y})\hat{N}_t(\mathbf{x})\hat{N}_t(\mathbf{y})\,\mathrm{d}t\Big]\left|\psi_t\right\rangle . \end{aligned} \tag{3.1}$$

$\hat{H}$ is the Hamiltonian describing the quantum mechanical dynamics, $W_t(\mathbf{x})$ is a Wiener process and m_0 is a reference mass, typically taken to be equal to that of a nucleon. Furthermore, the equation depends on two parameters λ_{CSL} and r_{CSL} that are unknown and have to be determined experimentally. $g(\mathbf{x}-\mathbf{y}) = \exp(-(\mathbf{x}-\mathbf{y})^2/4r_{\mathrm{CSL}}^2)$ is the spatial kernel of the white noise field $w_t(\mathbf{x}) = \mathrm{d}W_t(\mathbf{x})/\mathrm{d}t$. The noise field has zero average and its correlation function is given by

$$\mathbb{E}[w_t(\mathbf{x})w_s(\mathbf{y})] = g(\mathbf{x}-\mathbf{y})\delta(t-s). \tag{3.2}$$

Furthermore, $\hat{N}_t(\mathbf{x}) = \hat{M}(\mathbf{x}) - \langle\psi_t|\,\hat{M}(\mathbf{x})\,|\psi_t\rangle$, where $\hat{M}(\mathbf{x}) = \sum_j m_j \hat{a}_j^\dagger(\mathbf{x})\hat{a}_j(\mathbf{x})$ is the mass density operator. Note that $\hat{N}_t(\mathbf{x})$ depends explicitly on the expectation value $\langle\psi_t|\,\hat{M}(\mathbf{x})\,|\psi_t\rangle$, which is itself a functional of the state $|\psi_t\rangle$ being evolved. It

is precisely this state-dependence that makes Eq. (3.1) nonlinear in $|\psi_t\rangle$. The form of $\hat{M}$ guarantees a collapse in the position basis and the function $g(\mathbf{x}-\mathbf{y})$ in the last summand of Eq. (3.1) smears the position of the massive particles. As the CSL model acts on the position degrees of freedom, the position basis is the basis of choice. The effective master equation describing the dynamics of a state evolving under the CSL model can be found by taking the average $\rho(t) = \mathbb{E}[|\psi_t\rangle\langle\psi_t|]$ and is given by [143–146]

$$\langle \mathbf{q}' | \, \dot{\hat{\rho}} \, | \mathbf{q}'' \rangle = \frac{i}{\hbar} \langle \mathbf{q}' | \, [\hat{\rho}, \hat{H}] \, | \mathbf{q}'' \rangle - \Gamma_{\mathrm{CSL}}(\mathbf{q}' - \mathbf{q}'') \langle \mathbf{q}' | \, \hat{\rho} \, | \mathbf{q}'' \rangle \, . \tag{3.3}$$

Here, $|q\rangle$ is the position state of the centre-of-mass motion of a rigid, solid-state particle. The decoherence rate $\Gamma_{\mathrm{CSL}}(\mathbf{q}' - \mathbf{q}'')$ is given by

$$\Gamma_{\mathrm{CSL}}(\mathbf{q}' - \mathbf{q}'') = \lambda_{\mathrm{CSL}} \frac{r_{\mathrm{CSL}}^3}{\pi^{3/2} m_0^2} \int \mathrm{d}\mathbf{k} |\tilde{\rho}_M(\mathbf{k})|^2 e^{-k^2 r_{\mathrm{CSL}}^2} \left(1 - e^{-\frac{(\mathbf{q}' - \mathbf{q}'')^2}{4 r_{\mathrm{CSL}}^2}} \right) \tag{3.4}$$

and depends on the Fourier transform of the mass density $\tilde{\rho}_M(\mathbf{k})$ and geometry of the particle. r_{CSL} has units of distance and gives the length scale on which the CSL model acts, while λ_{CSL} has units of inverse time and can be interpreted as a collapse rate. The original Ghirardi-Rimini-Weber (GRW) model [139], which predates CSL and is itself parameter-free, corresponds, within the CSL parametrisation, to $\lambda_{\mathrm{CSL}} = 10^{-17}\,\mathrm{s}^{-1}$ at $r_{\mathrm{CSL}} = 10^{-7}\,\mathrm{m}$. Later, Adler considered larger sets of values [147], $\lambda_{\mathrm{CSL}} = 10^{-8\pm2}\,\mathrm{s}^{-1}$ for $r_{\mathrm{CSL}} = 10^{-7}\,\mathrm{m}$, and $\lambda_{\mathrm{CSL}} = 10^{-6\pm2}\,\mathrm{s}^{-1}$ for $r_{\mathrm{CSL}} = 10^{-6}\,\mathrm{m}$. Adler's central estimate is roughly nine orders of magnitude larger than the value corresponding to the GRW model, illustrating dramatically how the two proposals differ in the strength of collapse they predict. The values proposed by Adler have since been ruled out by multiple experiments, including tests with ultracold nanomechanical cantilevers [148] and with a levitated micro-oscillator at room temperature [149]. $\int \mathrm{d}\mathbf{k} |\tilde{\rho}_M(\mathbf{k})|^2 \exp(-k^2 r_{\mathrm{CSL}}^2)$ can be calculated for different geometries [146]. For a spherical particle of radius r with homogeneous mass density, $\Gamma_{\mathrm{CSL}}(\mathbf{q}' - \mathbf{q}'')$ is given by

$$\Gamma_{\mathrm{CSL}}(\mathbf{q}' - \mathbf{q}'') = \xi \left(1 - e^{-\frac{(\mathbf{q}' - \mathbf{q}'')^2}{4 r_{\mathrm{CSL}}^2}} \right), \tag{3.5}$$

with

$$\xi = \frac{m^2}{m_0^2} \lambda_{\mathrm{CSL}} f\left(\frac{r}{r_{\mathrm{CSL}}} \right) \quad \text{and} \quad f(x) = \frac{6}{x^4} \left[1 - \frac{2}{x^2} + \left(1 + \frac{2}{x^2} \right) e^{-x^2} \right] \tag{3.6}$$

Equation Eq. (3.3) indicates that the collapse model suppresses the coherence between different position eigenstates. The coherence between spatial points $(\mathbf{q}', \mathbf{q}'')$ that are further away from each other decays faster than that between closer

points. In the limit $|\mathbf{q}' - \mathbf{q}''| \ll r_{\mathrm{CSL}}$, the decay rate of the coherences tends to $\xi(\mathbf{q}' - \mathbf{q}'')^2/(4r_{\mathrm{CSL}}^2)$, while between points that are far away from each other, the decay rate converges to ξ, which constitutes an upper limit of $\Gamma_{\mathrm{CSL}}(\mathbf{q}' - \mathbf{q}'')$. This is precisely the same short- and long-wavelength behaviour encountered in Section 2.2: just as r_{ld} set the crossover scale between the saturating, maximal-decoherence regime and the quadratically growing regime there, r_{CSL} plays the analogous role here, with ξ taking the place of the localisation strength.

3.1.2 Experimental Tests of the CSL Model

Eq. (3.3) leads to experimentally testable deviations from standard quantum mechanics. Over the last two decades, a variety of experiments has put bounds on the CSL parameter space, characterised by the collapse rate λ_{CSL} and localisation length r_{CSL}. The original GRW values remain viable, while the stronger collapse rates proposed by Adler are excluded already.

Matter-Wave Interferometry

Matter-wave interferometry provides the most direct test of CSL because it tests the suerposition principle and hence the linearity of quantum mechanics. The protocol proposed in Section 3.1.3 also belongs to this class of interferometric tests, probing the coherence of spatial superpositions.

The strongest current interferometric bounds come from the Vienna group led by Markus Arndt, especially Kapitza-Dirac-Talbot-Lau (KDTL) interferometry with large organic molecules. These experiments demonstrate interference for particles with masses above 10^4 atomic units and already exclude large parts of the CSL parameter space [150, 151]. Theoretical analyses show that these bounds hold even for generalised versions of CSL, including dissipative and coloured-noise variants [150, 152], which are discussed later in this chapter.

Centre-Of-Mass Diffusion

The CSL model predicts momentum diffusion and heating, even in the absence of a bath. Mechanical systems with ultra-low noise can therefore test CSL without having to create spatial superpositions. Important platforms include clamped systems, levitated nanoparticles, torsion balances and optomechanical oscillators.

These experiments search for unexplained heating attributable to CSL noise. The approach became especially powerful with cryogenic optomechanics and ultra-high vacuum systems [153]. Rotational optomechanics has also been proposed as a particularly sensitive probe for CSL induces angular diffusion [154, 155].

Gravitational-Wave Detectors

Large-scale precision detectors such as LIGO and LISA Pathfinder are extremely sensitive to tiny stochastic forces and therefore provide strong indirect tests of CSL-induced diffusion. Analyses by Carlesso, Bassi and collaborators showed that noise measurements from these detectors significantly tightens the allowed CSL parameter space. In particular, LISA Pathfinder established some of the strongest bounds available before recent X-ray experiments [156].

Spontaneous X-Ray Emission Experiments

One of the most powerful constraints on CSL arises from spontaneous radiation. Since the CSL noise continuously perturbs charged particles, electrons should emit weak spontaneous X-rays in a otherwise quiet environment. Searches for this effect have placed stringent limits on CSL parameters. Early constraints came from analyses of IGEX data, while more recent limits were obtained using germanium detector experiments such as the Majorana Demonstrator [157]. The same spontaneous-emission technique has also been used to test the Diósi-Penrose gravity-related collapse model, which is discussed in the following section: a dedicated experiment at the INFN Gran Sasso underground laboratory searched for the X-rays this model predicts and found none at the expected rate, ruling out the natural, parameter-free version of the Diósi-Penrose model by about three orders of magnitude in the relevant length scale [158].

3.1.3 Connection to Other Collapse Models

Next to the CSL model, there are many more collapse models. Some of them are closely related to the CSL model, as their underlying stochastic master equations are of the same form.

The Diósi-Penrose model

The Diósi-Penrose (DP) model connects wavefunction collapse with gravitational effects. The idea was first proposed by Diósi, who investigated how gravitational fluctuations could influence the dynamics of quantum systems [140, 159]. Later, through a different line of reasoning, Roger Penrose independently derived an estimate for the collapse time of a quantum superposition induced by gravity, where both Diósi's and Penrose's considerations rest on treating gravity as classical. Remarkably, his estimate coincides with Diósi's result up to an unimportant numerical factor, which motivated the name Diósi-Penrose model. An important distinction between the two approaches, however, is that Diósi formulated an explicit dynamical equation describing the collapse process, whereas Penrose

adopted a more conservative standpoint and proposed only an estimate for the lifetime of a superposition [141].

The DP model can be related to the CSL model by replacing the spatial kernel $g(\mathbf{x}-\mathbf{y}) \sim \exp(-(\mathbf{x}-\mathbf{y})^2/4r_{\mathrm{CSL}}^2)$ by $g(\mathbf{x}-\mathbf{y}) \sim |\mathbf{x}-\mathbf{y}|^{-1}$, which scales like the Newtonian potential. The resulting equation is given by

$$\begin{aligned} \mathrm{d}\,|\psi_t\rangle = \Big[&-\frac{i}{\hbar}\hat{H}\mathrm{d}t + \sqrt{\frac{G}{\hbar}}\int \mathrm{d}\mathbf{x}\hat{N}_t(\mathbf{x})\mathrm{d}W_t(\mathbf{x}) \\ &- \frac{G}{2\hbar}\int \mathrm{d}\mathbf{x}\int \mathrm{d}\mathbf{y}\frac{\hat{N}_t(\mathbf{x})\hat{N}_t(\mathbf{y})}{|\mathbf{x}-\mathbf{y}|}\,\mathrm{d}t\Big]\,|\psi_t\rangle \end{aligned} \tag{3.7}$$

with $\mathbb{E}[w_t(\mathbf{x})w_s(\mathbf{y})] = \delta(t-s)/|\mathbf{x}-\mathbf{y}|$ and where G is the gravitational constant. While there are different proposals for how to model the mass density operator $\hat{M}(\mathbf{x})$, which must be chosen such that the associated Newtonian self-gravitational energy remains finite. Otherwise Eq. (3.7) is singular for point-like mass distributions and thus ill-defined. One typical choice is a Gaussian-smeared mass density, which introduces a free parameter R_0, often taken to be the nuclear radius, and which in either case must be constrained experimentally.

Coloured and Dissipative CSL Model

The Coloured Continuous Spontaneous Localisation (cCSL) model is a modification of the standard CSL framework. As in ordinary CSL, it assumes that wavefunction collapse is a real physical process driven by a universal stochastic noise field [160, 161]. The key difference in the cCSL model is that the noise is coloured rather than perfectly white: it possesses a finite correlation time and therefore exhibits a non-flat frequency spectrum. This can be implemented by defining the noise correlations as

$$\mathbb{E}[w_t(\mathbf{x})w_s(\mathbf{y})] = g(\mathbf{x}-\mathbf{y})f(t-s) \tag{3.8}$$

where $f(t-s)$ encodes the temporal correlations of the background noise, introducing a frequency-dependent structure.

The Dissipative Continuous Spontaneous Localisation (dCSL) model addresses a key limitation of the CSL framework, namely its lack of energy conservation. In standard CSL, the continuous action of the noise leads to an unbounded increase in energy. The dCSL model resolves this issue by replacing the original noise field with a thermal noise field and introducing momentum-dependent operators. As a result, the energy no longer increases indefinitely but instead relaxes to a finite asymptotic value determined by a new parameter T [152].

An extensive comparison of the CSL model and its various extensions is provided in [150], along with an analysis of the extent to which experimental tests of CSL can constrain or inform its generalisations.

Relevance for this Thesis

The CSL model, and the broader family of collapse theories it represents, is the fundamental theory that the Stern-Gerlach type interferometer proposed in Chapter 7 is designed to test. The environmental decoherence budget established in Chapter 2 sets the noise floor against which any additional, CSL-induced decoherence must be distinguished. The interferometric loss of visibility is used in Chapter 7 to translate a measured (or absent) signal into constraints on λ_{CSL} and r_{CSL}.

3.2 Quantum Signatures of Gravity and Gravitationally Induced Entanglement

Quantum mechanics and general relativity constitute the two fundamental theoretical frameworks of modern physics, which work in two very different regimes. Quantum theory successfully describes the behaviour of matter and interactions at microscopic scales, while general relativity provides an accurate description of gravitation and the large-scale structure of spacetime. Despite their empirical success within their respective domains, the two theories are incompatible. Reconciling quantum mechanics with gravity therefore remains one of the central open problems in modern-day-physics.

Gravity is most commonly described classically through Einstein's general theory of relativity, where gravitation is not treated as a force acting within spacetime, but rather as a manifestation of spacetime curvature itself. The spacetime geometry is determined by the Einstein field equations

$$G_{\mu\nu} = \frac{8\pi G}{c^4} T_{\mu\nu} \tag{3.9}$$

where G is the gravitational constant and c is the speed of light. The Einstein field equations relate the Einstein tensor $G_{\mu\nu}$ to the classical stress-energy tensor $T_{\mu\nu}$. In contrast, the electromagnetic, weak and strong forces are described within the framework of quantum field theory, in which physical interactions are mediated by quantised fields. Quantising the gravitational field in a similar manner has not been successful as the standard approach to renormalisation fails [162, 163].

This conceptual asymmetry between quantum matter and classical spacetime gives rise to several difficulties. The question remains whether these considerations are purely academic or whether one can manufacture an experiment that actually requires a quantum-gravity theory. Feynman proposed in 1957 at the Chapel Hill

conference a gedankenexperiment, where he considered a massive object placed in a spatial quantum superposition, such that each branch of the superposition corresponded to a distinct gravitational field configuration. He argued that if quantum mechanics applies universally, then a nearby test mass will be attracted by each branch of the massive object and thus go into a superposition itself. Otherwise, if gravity is sourced only by the expectation value of the mass distribution, the test mass would respond to a single, averaged classical field rather than becoming entangled with the source. In that case, the joint evolution of source and test mass could no longer be described by a linear, unitary map on their combined Hilbert space [164]. This thought experiment provided one of the earliest conceptual motivations for treating gravity as a quantum entity rather than a fundamentally classical interaction and was later explicitly connected to gravitational entanglement generation in the quantum information [52, 66, 67, 165].

The following sections introduce the conceptual foundations of such experiments and discuss how gravitationally induced entanglement may serve as a witness of non-classical gravitational interactions.

3.2.1 Is Gravity Quantum?

One of the central questions in modern theoretical physics is whether gravity is fundamentally classical or quantum in nature. While the other fundamental interactions are successfully described within the framework of quantum field theory, gravity is still described by the classical theory of general relativity.

A commonly studied intermediate framework between classical general relativity and a full quantum theory of gravity is semiclassical gravity. In this approach, spacetime itself remains classical, while matter fields are treated quantum mechanically. To couple the two, the stress-energy tensor is promoted to an operator $\hat{T}_{\mu\nu}$ (in contrast to its classical counterpart $T_{\mu\nu}$ in Eq. (3.9)) and the classical Einstein field equations are modified such that the spacetime curvature is sourced by the expectation value of the quantum stress-energy tensor,

$$G_{\mu\nu} = \frac{8\pi G}{c^4}\langle\hat{T}_{\mu\nu}\rangle \tag{3.10}$$

where $\langle\hat{T}_{\mu\nu}\rangle$ denotes the expectation value of the stress-energy operator in a quantum state. Semiclassical gravity has been successfully applied in several contexts, including quantum field theory in curved spacetime, Hawking radiation and cosmological particle creation [166]. It is therefore worth asking which phenomena, if observed, would be incompatible with this framework and would thus constitute genuine evidence that gravity must be quantised. In particular, a classical spacetime sourced only by expectation values may not consistently describe individual measurement outcomes before averaging or the generation of gravitationally induced entanglement [167]. These issues have motivated the development of a

quantum theory of gravity.

A full quantum theory of gravity seeks to quantise spacetime and the gravitational interaction itself [167]. Among the most extensively studied approaches are string theory [168] and loop quantum gravity [169]. In addition to these fundamental approaches, low-energy descriptions of gravity provide a framework for studying quantum gravitational effects at energies far below the Planck scale [54]. Within this approach, gravity is treated as a quantum field theory valid as an effective low-energy description, despite its nonrenormalisability at high energies. Effective field theory methods are particularly important in discussions of experimentally accessible quantum gravity signatures like levitated particles.

An alternative perspective is provided by gravitationally motivated collapse models, which, instead of modifying gravity, modify quantum mechanics [39, 141, 159]. In these models, the Schrödinger equation is modified such that sufficiently massive or spatially separated superpositions collapse into definite classical states. As discussed in the previous chapter, one influential proposal was developed by Penrose, who argued that superpositions of different spacetime geometries may possess an intrinsic instability associated with gravitational self-energy [141]. Related ideas were independently developed by Diósi [159].

Determining what it would mean for gravity itself to be "quantum" or "classical" is not just an experimental, but also a conceptual challenge. When discussing this question, we will focus on the quantum informational point of view, rather than the field theoretical viewpoint.

One promising avenue for probing quantum aspects of gravity is through gravitationally induced entanglement (GIE) experiments, which were already motivated at the beginning of this chapter. These experiments aim to test whether gravity can mediate entanglement between two quantum systems and thereby reveal whether the gravitational interaction itself possesses quantum properties.

The conceptual basis of GIE experiments originates from quantum information theory. It is well established that entanglement cannot be generated through local operations and classical communication (LOCC) alone [55, 170]. In other words, if two systems become entangled, some form of non-classical information transfer must have occurred. Consequently, if gravity is the only interaction between two massive quantum systems, the observation of entanglement in an initially separable state would imply that gravity is capable of transmitting quantum information and therefore cannot be described by a purely classical communication channel [66, 67, 171–174].

This conclusion has important implications for competing theories of gravity. In particular, the detection of GIE would strongly support approaches in which spacetime itself exhibits quantum properties, as expected in many candidate theories of quantum gravity. At the same time, it has been argued that it would constrain alternative models in which gravity remains fundamentally classical like the Kafri-

Taylor-Milburn classical-channel model [165] or Oppenheim's postquantum theory of classical gravity [175]. More generally, the argument has been used to claim that a local classical gravitational field cannot generate entanglement, since LOCC processes are incapable of doing so [170, 172, 174].

This conclusion should, however, be treated with some caution. First, some semi-classical gravity models are known to permit superluminal signalling, and a signalling channel can in principle mimic quantum correlations without any genuinely quantum mediator. Detecting GIE would therefore not unambiguously rule out models of this kind [176]. Second, and more surprisingly, at least one of the classical models listed above may not be so easily excluded either: Trillo and Navascués recently showed that the Diósi-Penrose model, despite treating gravity as fundamentally classical, can generate entanglement between two masses whenever the parameters of the experimental setup and the free constant R_0 of the Diósi-Penrose model are chosen appropriately [177]. Whether comparable loopholes exist for other models, to our knowledge, is still an open question. Some authors have further argued that GIE experiments do not necessarily probe genuinely quantum properties of the gravitational field [178–181]. Observing GIE would still imply that gravity is capable of mediating non-LOCC dynamics, but translating this into a clean verdict on any specific model requires care, and remains an active area of debate. In this work, we restrict ourselves to the question of whether gravity can mediate non-LOCC dynamics, and leave the broader implications for future work [182–184].

It is further worth noting that entanglement generation is not the only feature out of reach for LOCC channels: more general inequalities have been proposed that witness the non-LOCC nature of a dynamical map without necessarily relying on the generation of entanglement [69]. These extensions still probe the same underlying question as GIE experiments but widen the space of observable signatures beyond entanglement alone. A conceptually different route towards testing the quantum nature of gravity is the direct search for gravitons, rather than probing gravity's classicality indirectly through correlations between massive test particles. Despite the breakdown of standard renormalisation techniques as mentioned in the beginning of this chapter, an effective quantum field theory of gravity can still be formulated at low energies [185]. In this regime, the graviton is defined as a quantised excitation around a flat background spacetime. Attempting to detect such excitations directly, rather than inferring their existence from entanglement or LOCC-violation, offers a complementary strategy to the GIE-based tests discussed above. In the past, the detection of such particles seemed far beyond current experimental capabilities [186]. Nevertheless, recent work has proposed an experimental analogue of the photoelectric effect for gravitons [187], whose authors argue brings the search for gravitons closer to experimental feasibility. Nevertheless, it has been argued that a classical gravitational field could reproduce signals of such kind and therefore may not unambiguously distinguish a quantised gravitational field from a classical one [188, 189].

Furthermore, if quantum mechanics were to experience non-linear corrections at mesoscopic scales, even a tiny residual non-gravitational quantum interaction between the two masses could give rise to entangling dynamics that mimic the signature of GIE [190]. This stresses the importance of testing the linearity of quantum mechanics at mesoscopic scales before any statements about the nature of gravity can be made.

3.2.2 A Tabletop Experiment for Gravitationally Induced Entanglement

Particularly noteworthy is the subfield of levitated optomechanics, which was introduced in Chapter 2, where the mechanical degrees of freedom belong to objects suspended in vacuum. This promises a high degree of environmental isolation by avoiding direct mechanical clamping or suspension and enabling, in principle, large delocalisation. In light of these opportunities, many proposals have been made for inducing gravitationally induced entanglement using levitated particles. In this section, we outline the foundation on which many of these proposals are based.

Consider two masses levitated such that their centres of mass are separated by a distance $2L$ along some axis x. Next, we prepare each of these masses in a coherent spatial superposition, where the two localisations are separated by a distance Δx. The delocalisation can have any orientation relative to x, but we restrict ourselves to the situation where the delocalisation is parallel to x, as shown in Fig. 3.1. In Part III, other configurations will be investigated as well.

Each particle is in a state sometimes referred to as a Schrödinger-cat-like state, as it represents a superposition of two macroscopically distinct states. In an experiment, such a state could be prepared using an ancillary system, such as a spin that couples to the centre-of-mass motion of the object, for example through the presence of a magnetic-field gradient, or through a nonlinear potential such as a double-well potential. The combined state can be written as

$$|\psi\rangle(0) = \frac{1}{\mathcal{N}}\left(|\psi_A^L\rangle + |\psi_A^R\rangle\right) \otimes \left(|\psi_B^L\rangle + |\psi_B^R\rangle\right) \tag{3.11}$$

where $\mathcal{N}$ is a normalisation constant.

We now assume that the particles interact only through their mutual gravitational interaction, whose potential in the low-energy regime is described by

$$\hat{H}_{\text{Gravity}} = -\frac{GM_AM_B}{|2L + \hat{x}_B - \hat{x}_A|}, \tag{3.12}$$

where $\hat{x}_A$ and $\hat{x}_B$ describe the positions of the particles as displacements from their equilibrium positions, M_A and M_B are the masses of the two particles and G is the gravitational constant. After a time t, relative phases build up and the

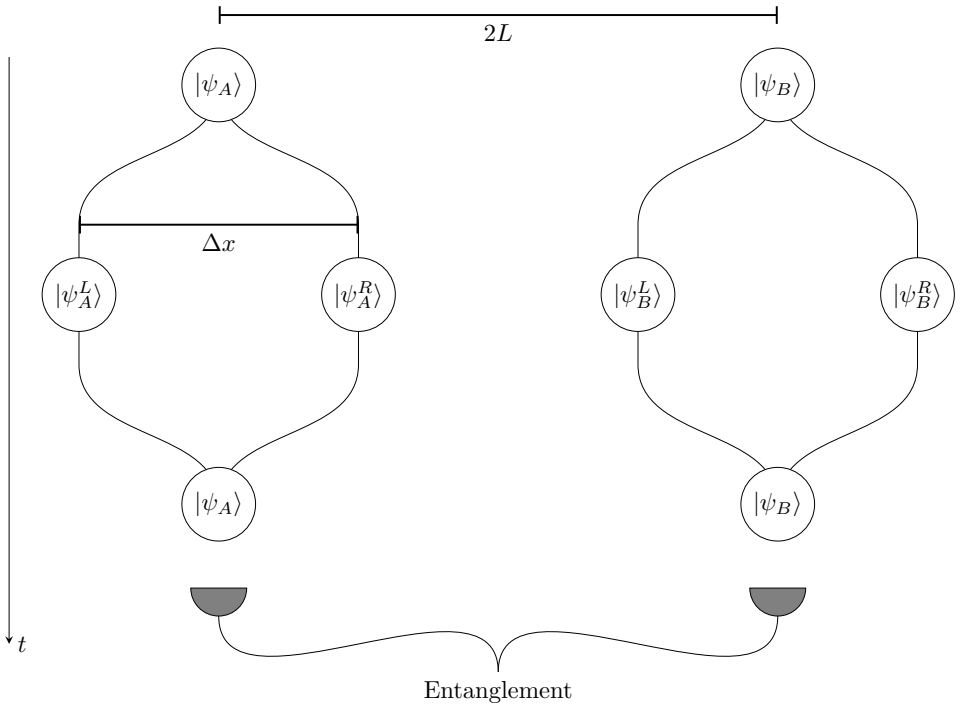


Figure 3.1: Sketch of a GIE test, where the two interacting bodies A and B are prepared in a spatial superposition. The gravitational interaction induces relative phases in the components of the superpositions $\left|\psi_{A/B}^{L/R}\right\rangle$, leading to the generation of entanglement between the bodies after a time t. The distance between the two bodies is $2L$, and the spatial width of the superposition is Δx.

state is given by

$$|\psi\rangle(t) = \frac{1}{2}\big(e^{i\phi_{LL}}\left|\psi_A^L\psi_B^L\right\rangle + e^{i\phi_{LR}}\left|\psi_A^L\psi_B^R\right\rangle + e^{i\phi_{RL}}\left|\psi_A^R\psi_B^L\right\rangle + e^{i\phi_{RR}}\left|\psi_A^R\psi_B^R\right\rangle\big). \tag{3.13}$$

with

$$\phi_{LL} = \phi_{RR} = \frac{GM_AM_B}{2\hbar L}t, \quad \phi_{LR} = \frac{GM_AM_B}{\hbar(2L-\Delta x)}t, \quad \text{and}$$
$$\phi_{RL} = \frac{GM_AM_B}{\hbar(2L+\Delta x)}t. \tag{3.14}$$

In general, this is an entangled state, and we can use the logarithmic negativity to quantify the amount of entanglement. The logarithmic negativity is given by

$$E_N(\rho) = \log_2 ||\rho^{\Gamma_B}||_1, \tag{3.15}$$

where $||\cdot||_1$ denotes the trace norm and ρ^{Γ_B} represents the density matrix of the composite system partially transposed with respect to subsystem B. Under the assumption that $\left\langle\psi_{A/B}^L\middle|\psi_{A/B}^R\right\rangle \approx 0$, one finds

$$E_N(\rho) = \log_2\left(1 + |\sin(\phi/2)|\right), \qquad \text{with} \qquad \phi = \phi_{RL} + \phi_{LR} - 2\phi_{LL}. \tag{3.16}$$

In the limit $\Delta x \ll 2L$, ϕ simplifies to

$$\phi \approx \frac{2GM_AM_Bt}{\hbar(2L)^3}\Delta x^2. \tag{3.17}$$

The same analysis can also be performed for Gaussian initial states, as shown in [74].

In order to guarantee that gravity is the only interaction capable of entangling the two particles, it is often proposed to use a Faraday shield to suppress electromagnetic interactions between them. In Part III, further intricacies of this setup, including interactions between the particles and the shield as well as potential challenges arising from such interactions, are investigated.

Relevance for this Thesis

The gravitationally induced entanglement protocol sketched out in this chapter is the basis of the experimental scenario investigated in Part III. This chapter further contextualises this proposal, as what conclusions the physics community can draw from the presence (or absence) of GIE about the quantum nature of gravity remains a matter of active debate.

3.3 The Einstein-de Haas and Barnett Effect

Magnetisation and mechanical rotation are both forms of angular momentum, and angular momentum must be conserved. This simple principle links a magnetic property, the alignment of spins, to a mechanical one, the rotation of a macroscopic body, through what is known as spin-rotation coupling.

This connection is best illustrated with the Einstein-de Haas effect: an external field aligns the spins in a body. If the magnetic field is then reversed, the spins realign in the opposite direction, changing their total angular momentum, and this change can only be conserved by setting the body itself rotating. The Barnett effect is the counterpart: rotating a magnetic material causes the spins to align with the rotation axis. Remarkably, both effects were established within months of each other in 1915 [43, 44], following a 1908 prediction by Owen Richardson [45] that magnetising a ferromagnet should induce it to rotate. This chapter introduces both effects and their observation across a range of platforms.

The Einstein-de Haas Effect

The effect was first demonstrated in 1915 by Albert Einstein and Wander Johannes de Haas [43], more than a decade before the microscopic, spin-based understanding of the coupling described above was known.

In the original experiment, a ferromagnetic rod, for example a piece of iron, was suspended by a thin wire, allowing it to rotate. A coil surrounding the rod generated an alternating magnetic field, causing the magnetisation within the rod to reverse as the field changed direction. Each time the field changed direction, the magnetisation within the ferromagnet switches as well. Since angular momentum must be conserved, these reversals induced a mechanical rotation of the rod. When the frequency of the alternating field was tuned appropriately, the rotational displacement amplitude was amplified, making it possible to measure the rotation. This demonstrated the intrinsic connection between the magnetisation of a body and its mechanical angular momentum, decades before the discovery of electron spin provided a microscopic explanation.

The gyromagnetic ratio γ of the electron, defined as the ratio of its magnetic moment μ to its angular momentum L, can be directly measured using the Einstein-de Haas effect. This makes the effect a powerful tool for characterising the magnetic properties of different materials.

Interestingly, the original 1915 measurement itself became a point of historical controversy. Einstein and de Haas inferred an effective g-factor close to one, which at the time was seen as a confirmation of the classical picture of magnetism: if magnetisation arises purely from electrons circulating in classical orbits, also known as Ampère's molecular currents, then the ratio of magnetic moment to orbital

angular momentum is expected to equal exactly $g = 1$. Later, more careful experiments instead converged on values close to $g \approx 2$. This discrepancy, known as the gyromagnetic anomaly, was not fully explained until the discovery of electron spin and the Dirac equation in 1928, which predicted a spin g-factor of exactly 2 in the non-relativistic limit. Measurements by Scott on a pure iron ellipsoid yielded $g' = 1.919 \pm 0.002$ [191], implying that roughly 96 % of the angular momentum responsible for ferromagnetism in iron originates from electron spin, with the remainder being attributed to an orbital contribution. The Einstein-de Haas effect therefore not only demonstrated the spin origin of magnetism, but historically served as one of the few macroscopic, mechanical probes capable of distinguishing spin from orbital angular momentum.

Over the years, the Einstein-de Haas effect has been observed in a variety of materials [192], as well as at the quantum level using individual electron spins in single-molecule magnets [46].

More recently, the Einstein-de Haas effect has further attracted renewed interest in the context of levitated nanoparticles. Since a levitated particle is mechanically unclamped, it responds to spin-rotation coupling with negligible dissipation, making it an attractive platform to probe this effect. Rusconi et al. predicted that the same gyromagnetic coupling underlying the Einstein-de Haas effect can stabilise a non-rotating single-domain ferromagnetic nanoparticle against Earnshaw's theorem when levitated in a static magnetic field [41]. This gyroscopic behaviour has recently been experimentally confirmed by observing the coupling between librational modes of a non-spinning ferromagnet levitated in a superconducting trap [193]. In a related direction, Vinante et al. used the torque generated in a levitated ferromagnet to surpass the standard energy-resolution limit of torque sensing [194], while Fast et al. employed the frequency dependence of the Einstein-de Haas torque as a nanomechanical spectroscopic probe of magnetic resonance [195]. At the single-spin level, a scheme coupling a single-molecule magnet to a carbon-nanotube mechanical resonator has been proposed and partially realised, in which conservation of angular momentum during magnetisation reversal excites quantised phonon modes and suppresses quantum tunnelling of the magnetisation [46]. These developments illustrate that levitated and nanomechanical systems, the platforms considered throughout this thesis, are natural candidates for extending the Einstein-de Haas effect into regimes inaccessible to the original bulk experiment, including, ultimately, the single-nuclear-spin level.

The Barnett Effect

The counterpart of the Einstein-de Haas effect is known as the Barnett effect, named after Samuel Barnett, who discovered it in 1915 [44, 196]. Barnett found that a rotating ferromagnetic object with angular velocity $\vec{\omega}_r$, in the absence of an external magnetic field, produces the same magnetisation as if it were subjected

to an effective magnetic field

$$\vec{B}_{\mathrm{bar}} = \frac{\vec{\omega}_r}{\gamma}, \tag{3.18}$$

where γ is the gyromagnetic ratio.

Similar to the Einstein-de Haas effect, the Barnett effect has been observed in a range of materials. Beyond bulk ferromagnets, spin-rotation coupling analogous to the Barnett effect has also been observed for individual electron spins associated with nitrogen-vacancy (NV) centres in diamond, where physical rotation of the host crystal generates an effective pseudo-magnetic (Barnett) field acting on the NV electron spin. This pseudo-field has been directly measured in diamonds spun at up to 200,000 rpm [50], and has recently been extended to NV centres in an optically levitated, rotating nanodiamond in high vacuum [89]. Beyond magnetic systems, the same spin-rotation coupling has been predicted to generate a mechanical spin current and spin accumulation in non-magnetic conductors under rotation [197, 198], demonstrating that the Barnett mechanism extends well beyond the ferromagnetic case originally considered by Barnett.

Nevertheless, the nuclear Barnett effect remains more elusive. Since the induced magnetisation scales with the gyromagnetic ratio, the nuclear Barnett effect is approximately $1.5 \cdot 10^{-3}$ times weaker than its electronic counterpart. The nuclear Barnett effect has been successfully observed in liquids [47], but has not yet been demonstrated in solid-state systems.

Detecting the nuclear Barnett or Einstein-de Haas effect in a solid is made difficult not only by the small nuclear gyromagnetic ratio but also by the comparatively small equilibrium nuclear spin polarisation at accessible temperatures and fields. A dense, highly polarised nuclear spin ensemble, such as the hyperpolarised nuclear spin baths obtained via optically detected dynamic nuclear polarisation discussed in the previous chapter, would substantially enhance the expected mechanical or magnetic signal, suggesting hyperpolarisation as a promising route towards finally observing these nuclear effects in the solid state.

Relevance for this Thesis

The spin-rotation coupling discussed in this chapter is the physical mechanism underlying the nuclear Einstein-de Haas and Barnett effects, whose investigation is the topic of Chapter 8 and Section 8.2. Two missing ingredients are what finally make these effects observable: the optically hyperpolarised nuclear spin ensemble discussed in Chapter 4, which provides a dense reservoir of nuclear angular momentum, and the mechanically unclamped levitated platform introduced in Chapter 2, which allows this angular momentum to be converted into rotation.

4 Optically Hyperpolarised Materials

In this thesis, the prospect of leveraging the spin degrees of freedom within levitated particles to test fundamental principles of physics is examined. In this context, a family of polycyclic aromatic hydrocarbons (PAHs) will play an essential role. In their molecular ground state, the electronic configuration corresponds to a singlet state, S_0, which is not paramagnetic. Upon photoexcitation, the electronic state can be promoted to the S_1 state, which is also a singlet. From there, the system can either decay directly back to the S_0 state or, with some probability, undergo intersystem crossing via spin-orbit coupling to a long-lived intermediate triplet state. Due to zero-field splitting (ZFS), the triplet sublevels T_0 and $T_\pm$ are non-degenerate, even in the absence of a magnetic field. The application of an external magnetic field further lifts the degeneracy between T_+ and T_-. As the spin-orbit coupling that drives intersystem crossing is itself anisotropic, the relative occupation of the three sublevels depends on the orientation of the magnetic field relative to the molecular axes and, when the field is applied along the molecular quantisation axis, the population of one of the three sublevels is strongly favoured. By tuning a microwave field into resonance between the populated sublevel and another, an effective two-level system can be realised, which constitutes a molecular qubit. Nevertheless, the spin order after photo-excitation depends on the strength and direction of the external magnetic field. Therefore, a matrix such as a host crystal in which the molecules can be built in and in which the quantisation axes are aligned is crucial.

By embedding molecular qubits into such host crystals, it becomes possible to hyperpolarise their nuclear spin environment using dynamic nuclear polarisation (DNP). There is a wide variety of protocols which can achieve this, like Nuclear Orientation via Electron Spin Locking (NOVEL) [199, 200], the Integrated Solid Effect (ISE) [201] or PulsePol [202].

Here, the NOVEL pulse sequence will be examined more closely in a two-spin example to understand how the DNP sequences work, even though more advanced sequences such as PulsePol are more robust against detunings and control errors.

4.1 Dynamic Nuclear Polarisation Leveraging Photo-Excited Triplet States

Quantum Mechanical Description of the Triplet State

A triplet state is described by the spin-1 operators $\hat{S}_{i,1}$:

$$\hat{S}_{x,1} = \frac{1}{\sqrt{2}} \begin{pmatrix} 0 & 1 & 0 \\ 1 & 0 & 1 \\ 0 & 1 & 0 \end{pmatrix}, \quad \hat{S}_{y,1} = \frac{1}{\sqrt{2}i} \begin{pmatrix} 0 & 1 & 0 \\ -1 & 0 & 1 \\ 0 & -1 & 0 \end{pmatrix}, \quad \hat{S}_{z,1} = \begin{pmatrix} 1 & 0 & 0 \\ 0 & 0 & 0 \\ 0 & 0 & -1 \end{pmatrix}. \tag{4.1}$$

In the presence of a magnetic field $\mathbf{B}$, the Hamiltonian of the triplet state takes the form

$$\hat{H} = D\left(\hat{S}_{z,1}^2 - \tfrac{1}{3}S(S+1)\right) + E\left(\hat{S}_{x,1}^2 - \hat{S}_{y,1}^2\right) + \gamma_e \mathbf{B} \cdot \hat{\mathbf{S}}_1. \tag{4.2}$$

The first two terms represent the zero-field splitting, which lifts the degeneracy between the $|0\rangle$ and $|\pm1\rangle$ states, leading to a splitting of the three sublevels. The last term corresponds to the Zeeman interaction with the external field. Here, $S = 1$ is the total spin of the triplet state, γ_e is the electron gyromagnetic ratio and D and E are the axial and rhombic zero-field-splitting parameters, respectively. D quantifies the splitting of spin sublevels along the molecule's principal magnetic axis, lifting the degeneracy between $|0\rangle$ and $|\pm1\rangle$. E quantifies the deviation from axial symmetry: it couples $|+1\rangle$ and $|-1\rangle$, so that the true eigenstates become the symmetric and antisymmetric combinations $(|+1\rangle \pm |-1\rangle)/\sqrt{2}$, split by $2E$; since $|E| \ll D$, this splitting is often considered negligible. Once an external field is applied, the Zeeman interaction dominates over the second term and is used to further lift the degeneracy between $|\pm1\rangle$. For pentacene, one finds $D = 1381(2\pi)\,\mathrm{MHz}$ and $E = -42(2\pi)\,\mathrm{MHz}$ [203].

When the population is predominantly concentrated in one sublevel, and a microwave drive near resonance is used to connect this sublevel to another, the system can be approximated as an effective two-level system. In this case, the dynamics are governed by spin-$\frac{1}{2}$ operators $\hat{S}_i = \hat{\sigma}_i/2$, where $\hat{\sigma}_i$ denote the Pauli matrices. The corresponding operators read:

$$\hat{S}_x = \frac{1}{2} \begin{pmatrix} 0 & 1 \\ 1 & 0 \end{pmatrix}, \quad \hat{S}_y = \frac{1}{2i} \begin{pmatrix} 0 & 1 \\ -1 & 0 \end{pmatrix}, \quad \hat{S}_z = \frac{1}{2} \begin{pmatrix} 1 & 0 \\ 0 & -1 \end{pmatrix}. \tag{4.3}$$

The Hamiltonian of this reduced system under the influence of the microwave drive is

$$\hat{H}(t) = \omega_S \hat{S}_z + 2\Omega(t)\cos(\omega_{\mathrm{mw}} t + \varphi)\hat{S}_x, \tag{4.4}$$

where $\omega_S = D \pm \gamma_e B$ is the transition frequency between the $|0\rangle$ and $|\pm 1\rangle$ sublevels, with the $+$ and $-$ signs corresponding to the $|0\rangle \leftrightarrow |+1\rangle$ and $|0\rangle \leftrightarrow |-1\rangle$ transitions, respectively. ω_{mw} is the microwave frequency and φ is the microwave phase. The Rabi frequency $\Omega(t)$ equals Ω when the drive is on and vanishes otherwise. Here, the magnetic field is chosen as $\mathbf{B} = B\mathbf{e}_z$, parallel to the quantisation axis of the qubit. Transforming into the rotating frame with respect to $\omega_S \hat{S}_z$ and applying the rotating-wave approximation yields

$$\hat{H}^{\mathrm{int}} = \Omega \left(\cos(\varphi)\hat{S}_x + \sin(\varphi)\hat{S}_y \right), \tag{4.5}$$

where only resonant contributions are retained ($\omega_S = \omega_{\mathrm{mw}}$); the counter-rotating terms oscillating at frequencies of order $\omega_S + \omega_{\mathrm{mw}} \approx 2\omega_S$ have been dropped, which is justified provided $\Omega \ll \omega_S$, so that these fast oscillations average to zero over the much slower timescale $1/\Omega$ set by the coherent Rabi dynamics. Both $\hat{S}_x$ and $\hat{S}_y$ mediate transitions between the ground state $|\downarrow\rangle$ and the excited state $|\uparrow\rangle$.

The corresponding time-evolution operator is

$$\hat{U}(t) = e^{-i\hat{H}^{\mathrm{int}}t} = \begin{pmatrix} \cos\left(\frac{\Omega t}{2}\right) & -ie^{-i\varphi}\sin\left(\frac{\Omega t}{2}\right) \\ -ie^{i\varphi}\sin\left(\frac{\Omega t}{2}\right) & \cos\left(\frac{\Omega t}{2}\right) \end{pmatrix}. \tag{4.6}$$

After a duration $t = \pi/\Omega$, the populations are fully inverted, while the phase φ determines the relative phase imprinted on the state. Throughout this thesis, an α-pulse around the x- (y-) axis refers to a pulse of duration α/Ω with $\varphi = 0$ ($\varphi = \pi/2$).

In the case of a detuned microwave field, the effective Hamiltonian becomes

$$\hat{H}^{\mathrm{int}} = \Delta\omega\, \hat{S}_z + \Omega \left(\cos(\varphi)\hat{S}_x + \sin(\varphi)\hat{S}_y \right), \tag{4.7}$$

with $\Delta\omega = \omega_S - \omega_{\mathrm{mw}}$. The time-evolution operator is then

$$\hat{U}(t) = e^{-i\hat{H}^{\mathrm{int}}t} = \begin{pmatrix} \cos\left(\frac{\tilde{\Omega}t}{2}\right) - i\frac{\Delta\omega}{\tilde{\Omega}}\sin\left(\frac{\tilde{\Omega}t}{2}\right) & -ie^{-i\varphi}\frac{\Omega}{\tilde{\Omega}}\sin\left(\frac{\tilde{\Omega}t}{2}\right) \\ -ie^{i\varphi}\frac{\Omega}{\tilde{\Omega}}\sin\left(\frac{\tilde{\Omega}t}{2}\right) & \cos\left(\frac{\tilde{\Omega}t}{2}\right) + i\frac{\Delta\omega}{\tilde{\Omega}}\sin\left(\frac{\tilde{\Omega}t}{2}\right) \end{pmatrix}, \tag{4.8}$$

where the effective Rabi frequency is defined as $\tilde{\Omega} = \sqrt{\Delta\omega^2 + \Omega^2}$. For strong driving ($\Omega \gg |\Delta\omega|$), the effect of detuning becomes negligible, and the system dynamics approach the resonant case.

Hyperpolarisation of a Nuclear Spin Bath

In the simplest case, the electron spin couples to a single nuclear spin. The Hamiltonian of the system is

$$\hat{H} = \omega_S \hat{S}_z + \omega_I \hat{I}_z + \hat{\mathbf{S}} A \hat{\mathbf{I}} + 2\Omega(t)\hat{S}_x \cos(\omega_{\mathrm{mw}} t + \varphi), \tag{4.9}$$

where $\omega_I = \gamma_p B$ is the nuclear Larmor frequency, $\hat{\mathbf{I}}$ denotes the spin-1/2 operators of the nuclear spin, and the hyperfine interaction is described by $\hat{\mathbf{S}} A \hat{\mathbf{I}}$.

For distant nuclear spins, which is typically the case considered in this work, the hyperfine interaction is dominated by magnetic dipole-dipole coupling,

$$\hat{H}_{\mathrm{dd}} = \hat{\mathbf{S}} A \hat{\mathbf{I}} = -\frac{\mu_0 \gamma_e \gamma_p \hbar}{4\pi r^3} \left[3(\hat{\mathbf{S}} \cdot \mathbf{n})(\hat{\mathbf{I}} \cdot \mathbf{n}) - \hat{\mathbf{S}} \cdot \hat{\mathbf{I}} \right], \tag{4.10}$$

where $\mathbf{n} = \mathbf{r}/r$ is the unit vector along the internuclear axis and r is the distance between the electron and nuclear spin.

This Hamiltonian enables polarisation transfer from the electron to the nuclear spin, provided that a suitable pulse sequence is applied. As an illustrative example, we consider the NOVEL sequence.

NOVEL consists of an initial $\pi/2$ pulse applied to the electron spin, followed by a phase-locked microwave drive ($\varphi = 0$) with $\Omega = \omega_I$. In the rotating frame with respect to $\omega_S \hat{S}_z$, the spin operators transform as

$$\begin{aligned} \hat{S}_x(t) &= \cos(\omega_S t)\, \hat{S}_x - \sin(\omega_S t)\, \hat{S}_y, \\ \hat{S}_y(t) &= \cos(\omega_S t)\, \hat{S}_y + \sin(\omega_S t)\, \hat{S}_x, \\ \hat{S}_z(t) &= \hat{S}_z. \end{aligned} \tag{4.11}$$

After discarding the rapidly oscillating terms and assuming resonant driving, the effective Hamiltonian becomes

$$\hat{H}^{\mathrm{int}} = \omega_I \hat{I}_z + \hat{S}_z \left(a_\perp \hat{I}_x + a_\parallel \hat{I}_z \right) + \Omega \hat{S}_x, \tag{4.12}$$

where the coordinate frame is chosen such that the dipole-dipole term involving $\hat{S}_z \hat{I}_y$ vanishes. Here, $a_\parallel$ is the usual secular dipolar shift along z, while $a_\perp$ is the transverse coupling that will drive the electron-nuclear polarisation transfer once the Hartmann-Hahn condition $\Omega = \omega_I$ is imposed below (if $a_\parallel \ll \omega_I$). $a_\parallel$ and $a_\perp$ are given by

$$a_\parallel = -\frac{\mu_0 \gamma_e \gamma_p \hbar}{4\pi r^3} \left(3\cos^2\theta - 1 \right), \tag{4.13}$$

$$a_\perp = -\frac{3\mu_0 \gamma_e \gamma_p \hbar}{4\pi r^3} \sin\theta \cos\theta, \tag{4.14}$$

The initial $\pi/2$ pulse rotates the operators as $\hat{S}_z \rightarrow -\hat{S}_x$ and $\hat{S}_x \rightarrow \hat{S}_z$. The Hamiltonian then reads

$$\hat{H}^{\text{int}} = \omega_I \hat{I}_z - \hat{S}_x \left(a_\perp \hat{I}_x + a_\parallel \hat{I}_z \right) + \Omega \hat{S}_z. \tag{4.15}$$

Moving into another rotating frame with respect to $\omega_I \hat{I}_z + \Omega \hat{S}_z$, neglecting fast-rotating terms, and enforcing $\Omega = \omega_I$, the so-called Hartmann-Hahn condition, yields the effective Hamiltonian

$$\hat{H}_{\text{NOVEL}} = -\frac{a_\perp}{2} \left(\hat{S}_x \hat{I}_x + \hat{S}_y \hat{I}_y \right). \tag{4.16}$$

This approximation holds as long as $a_\perp \ll \omega_I$.

By expressing $\hat{H}_{\text{NOVEL}}$ in terms of the spin ladder operators $\hat{S}_\pm = \hat{S}_x \pm i\hat{S}_y$, one obtains

$$\hat{H}_{\text{NOVEL}} = -\frac{a_\perp}{4} \left(\hat{S}_+ \hat{I}_- + \hat{S}_- \hat{I}_+ \right). \tag{4.17}$$

This Hamiltonian acts only on the two-dimensional subspace spanned by $\{|\uparrow\downarrow\rangle, |\downarrow\uparrow\rangle\}$. Assuming the electron spin is fully polarised while the nuclear spin is initially in a mixed state, the polarisation is transferred after $t = \pi/(a_\perp/2)$. At this point, the electron spin becomes fully mixed, while the nuclear spin is fully polarised. Through spin-diffusion processes, this polarisation spreads to neighbouring nuclear spins in the lattice. Reinitialising the electron spin and repeating the process leads to a gradual build-up of nuclear spin polarisation throughout the crystal.

Relevance for this Thesis

The optically induced dynamic nuclear polarisation mechanism described in this section, worked out here for the NOVEL sequence as an illustrative example, is the method by which the nuclear spin bath used throughout Part II would be hyperpolarised in practice. The highly polarised nuclear ensemble it produces is what enables the coherent nuclear spin dynamics exploited to design the Stern-Gerlach-type interferometer in Chapter 7 and is the missing ingredient for rendering the nuclear Einstein-de Haas effect observable as discussed in Chapter 8.

4.2 Pentacene-doped Naphthalene

One example of optically hyperpolarisable materials is pentacene-doped naphthalene. Naphthalene is the simplest of the polycyclic aromatic hydrocarbons, consisting of two fused benzene rings as shown in Fig. 4.1. At room temperature, it forms a white, crystalline solid held together by van der Waals forces. It has a distinct, pungent odour, and, while it is best known as the main ingredi-

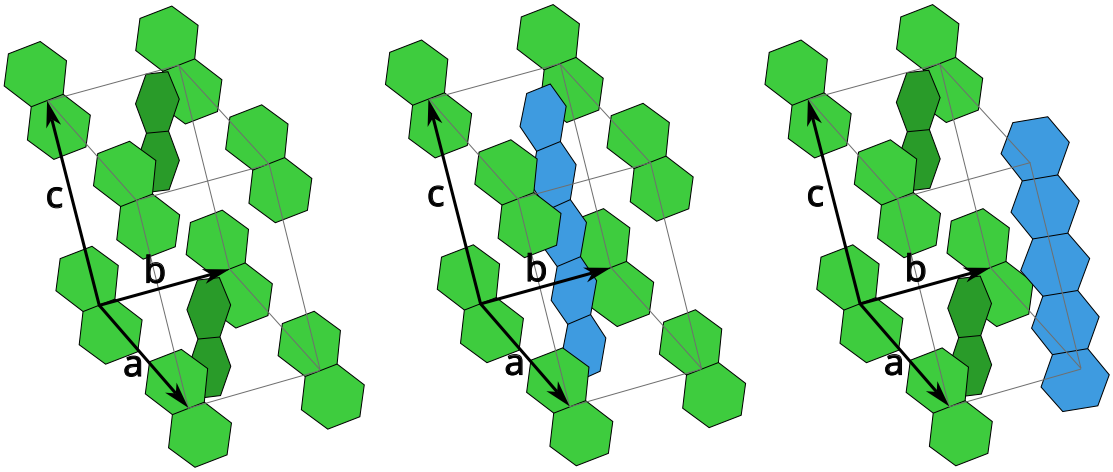


Figure 4.1: Structure of the naphthalene crystal on the left and the two possible sites of pentacene molecules in the naphthalene host crystal. This figure was inspired by Figure 1.2 in [207].

ent of mothballs, its usage is wide-ranging [204–206]. Naphthalene can be doped with pentacene, another polycyclic aromatic hydrocarbon, where each pentacene molecule substitutes two naphthalene molecules without perturbing the lattice. Pentacene-doped naphthalene has gained attention in the nuclear magnetic resonance community due to its large nuclear spin polarisability. When doped with pentacene, the spins of the hydrogen atoms in naphthalene can be polarised [32–36] to over 80 % even in a macroscopic crystal. Hyperpolarised naphthalene is used as a filter in neutron scattering [37] and as a means to enhance sensitivity in nuclear magnetic resonance [38].

The crystal structure of naphthalene is monoclinic, with two molecules in the primitive cell: one centred at $(0, 0, 0)$ and the other at $(1/2,\ 1/2,\ 0)$. The dimensions of the primitive cell are $a = 8.235\,\text{Å}$, $b = 6.003\,\text{Å}$ and $c = 8.658\,\text{Å}$, with an angle $\beta = 122°55'$ between a and c, while b is perpendicular to the other two axes [208].

The position and orientation of pentacene molecules in naphthalene host crystals were determined by [203] using electron spin echo techniques. Each pentacene molecule replaces two naphthalene molecules without significantly disturbing the lattice. The two possible substitution sites are $(0, 0,\ -1/2)$ and $(1/2,\ 1/2,\ -1/2)$. In both cases, the long molecular x-axis, which also serves as the main quantisation axis of the pentacene electron spin, lies in the ac-plane of the unit cell and is tilted by 10° with respect to the crystalline c-axis. The molecular z-axes of the two possible orientations differ by an angle of 47°. The crystalline structure of naphthalene and the two possible sites of individual pentacene molecules within the crystal are shown in Fig. 4.1.

Furthermore, naphthalene exhibits interesting optical and magnetic properties.

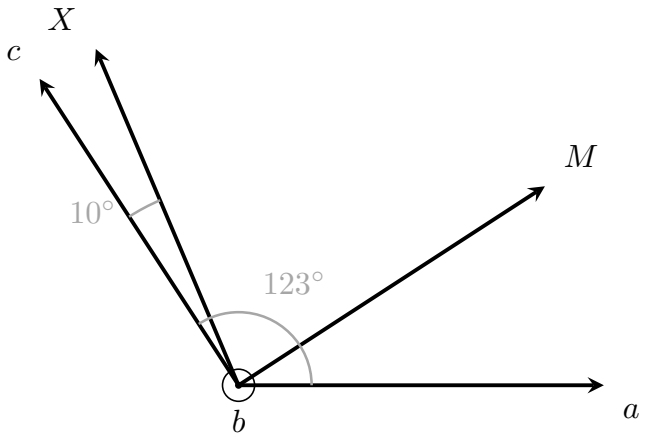


Figure 4.2: Here, the directions of the optical axes as well as the quantisation axes of the pentacene molecule with respect to the unit cell are shown. The naphthalene crystal is anisotropic and has three optical axes along b, c and M, where M is perpendicular to b and c. X indicates the direction at which the naphthalene long molecular axis points, which is also the main quantisation axis. The unit vectors are: $a : (1, 0, 0), b : (0, 1, 0), c : (-0.545, 0, 0.839), X : (-0.391, 0, 0.921), M : (0.839, 0, 0.545)$.

Because the crystal is highly anisotropic, it has three optical axes along b, c and M, where M is perpendicular to both b and c. In the principal coordinate system of the crystal, the magnetic susceptibility tensor along the M, b and c axes is

$$\chi_V = -\mathrm{diag}(17.8, 7.9, 4.4) \cdot 10^{-6}. \tag{4.18}$$

The corresponding refractive indices along these axes are [209]

$$n = \mathrm{diag}(1.441,\ 1.775,\ 1.932). \tag{4.19}$$

In Fig. 4.2, the directions of the three principal axes of naphthalene with respect to the crystal unit cell, as well as the orientation of the long molecular pentacene axes, are illustrated.

The naphthalene-pentacene system is particularly successful when it comes to hyperpolarisation. Remarkably, even in macroscopic samples, the nuclear spins of the hydrogen atoms in naphthalene crystals can be polarised to levels exceeding 80 %, with ultra-long decay times surpassing 920 h at 25 K [32–36].

Relevance for this Thesis

Pentacene-doped naphthalene is the material system used throughout Part II as a prime example of an optically hyperpolarisable material. The crystallographic and magnetic properties summarised in this section are the quantities on which the rest of the thesis relies. Together with the diamagnetic trapping condition introduced in Chapter 2, this section builds the basis for the material-specific analysis throughout Part II.

Part II

Optically Hyperpolarised Materials for Levitated Optomechanics

5 Introduction

Among the materials considered for levitation experiments, diamond nanoparticles hosting nitrogen-vacancy (NV) colour centres have attracted particular interest [24–26], providing an internal spin degree of freedom that couples to the centre-of-mass motion through spin-dependent forces [20–23] and offering a route towards Stern-Gerlach-type matter-wave interferometry [27–29]. However, the negatively charged NV centre and residual electronic impurities introduce significant noise channels [29–31], motivating the search for alternative spin-bearing materials.

This part investigates pentacene-doped naphthalene, a prime example of optically hyperpolarised materials, as such an alternative, where the polarising electron spin is only an intermediate one and so avoids the persistent noise channels that limit NV centres (see Chapters 4 and 6). The resulting polarisation levels exceeding 80 % and lifetimes above 920 h at cryogenic temperatures [32–36] suggest a very clean and highly favourable environment for coherent quantum experiments.

Building on these properties, this part develops three main research directions. First, levitation of hyperpolarised naphthalene is shown to enable nuclear magnetic resonance experiments in entirely new parameter regimes. In conventional solid-state NMR, magic-angle spinning rotates the sample rapidly at 54.74° relative to the external magnetic field. This averages out anisotropic interactions, narrowing spectral lines and extending the transverse coherence time T_2 [210]. State-of-the-art rotors reach spinning frequencies of order 100 kHz, but mechanical stress ultimately limits them. Levitated particles have no such limit: free from any mechanical clamping or suspension, they can in principle spin orders of magnitude faster, limited only by the tensile strength of the material itself [15, 211–213]. This opens an unexplored regime for solid-state NMR spectroscopy. Second, a multi-spin matter-wave interferometry protocol exploiting the large collective nuclear-spin polarisation, as well as a displacement-based measurement scheme of the particle's magnetic moment, is presented. In contrast to colour-centre-based approaches, the homogeneous spin distribution throughout the crystal and the absence of a preferred quantisation axis suppress unwanted torques acting on the particle during the interferometric sequence, improving visibility and stability. A radio-frequency pulse scheme for coherent control of the nuclear ensemble in a levitated geometry is introduced alongside a measurement scheme for detecting nuclear-spin polarisation through magnetisation-induced displacements. From the expected interferometer output, constraints on CSL collapse-model parameters are derived and compared with existing experimental bounds, demonstrating

the competitive sensitivity offered by this platform. Third, the expected coupling between nuclear-spin angular momentum and rigid-body rotation is exploited to propose concrete protocols for the first direct observation of the nuclear Einstein-de Haas and Barnett effects. Optical hyperpolarisation aligns the nuclear spins, transforming the nuclear-spin ensemble into a macroscopic angular-momentum reservoir capable of generating measurable rigid-body rotation via the Einstein-de Haas effect. Conversely, the fast rotation frequencies accessible in levitated systems produce Barnett-induced nuclear polarisation large enough to detect. In the first case, optical readout is used to measure the rotation, while in the latter case, the same displacement-based measurement as developed for the interferometry readout is employed, whose sensitivity is governed by the long longitudinal relaxation time T_1 rather than the short transverse coherence time T_2, representing a qualitative advantage over conventional solid-state NMR approaches. A detailed analysis of noise sources, including the rotational dynamics of asymmetric particles in a diamagnetic trap, establishes the feasibility of both observations.

The part is organised as follows. Chapter 6 analyses the suitability of naphthalene as a host crystal, covering hyperpolarisation, magic-angle spinning prospects and sublimation as a potential limitation. Chapter 7 develops the multi-spin Stern-Gerlach interferometry protocol, derives CSL bounds, introduces a magnetisation-induced displacement measurement scheme and characterises the relevant noise sources. Chapter 8 investigates the nuclear Einstein-de Haas effect, including the rotational dynamics of asymmetric particles in a diamagnetic trap. Finally, in the same chapter, the Barnett-induced nuclear polarisation at levitation frequencies and a adapted measurement scheme, as introduced in Chapter 7, is analysed.

Chapter 6 and Chapter 7 are in large parts based on [1], published under the CC BY 4.0 license

6 Naphthalene – A Material For Levitation

This chapter is in large parts based on [1], published under the CC BY 4.0 license.

As introduced in Section 4.2, pentacene-doped naphthalene combines a simple, robust crystal host with exceptional nuclear-spin hyperpolarisability. Here we examine what this means specifically for a levitated particle: the hyperpolarisation protocol under trapping conditions, the prospects for magic-angle spinning at unprecedented rotation frequencies and the sublimation limits on bulk temperature.

6.1 Hyperpolarisation

As described in Chapter 4, optical excitation of pentacene into its triplet state, followed by resonant microwave driving, transfers electron spin polarisation to the surrounding nuclear spin bath via dipole-dipole coupling. For a levitated particle, two further considerations are important: the sensitivity of this mechanism to the alignment of the crystal within the trap, and the fate of the electron spin once the polarisation transfer is complete.

It is noteworthy that the optical excitation of the electron spin in pentacene requires a good alignment of the pentacene molecule with the external magnetic field. Nevertheless, a few degrees of deviation from perfect alignment is admissible, as this results in only a few percent loss of the polarisation of the pentacene electron spin. However, for larger deviations, the achievable polarisation drops quickly. For a more detailed analysis, we refer the reader to Ref. [203]. The alignment might be achieved by suitable trapping conditions. Alternatively, it has been shown that instead of orientating the crystal in the magnetic field, the pentacene molecule can be modified with polarising agents such as thiophene. Thiophene-modified pentacene exhibits a sharper and stronger electron spin resonance spectrum compared to unmodified pentacene. Moreover, the triplet electron distribution is more isotropic without loss of triplet polarisation, making it more robust to deviations from the ideal orientation in the external magnetic field [214].

The transfer of electron spin polarisation from the pentacene molecule to the nuclear spin ensemble can be accomplished by the application of a suitable microwave drive (or a sequence of pulses) that brings the electron spin into resonance with the nuclear spin lattice, described in Section 4.1. However, the eigenfrequency of the electron spin depends on the spatial orientation of the pentacene molecule with respect to the external magnetic field and thus this will also require a good alignment between the magnetic field and the pentacene molecule. In this case, the

effect of imperfect alignments might be mitigated by using pulse sequences that exhibit robustness against detuning errors such as sweep schemes [33] or robust pulse sequences such as PulsePol [202].

The triplet state of pentacene has a lifetime of order of tens of microseconds, which is sufficiently long to allow for the transfer of polarisation to the nuclear spin-lattice. After the transfer, the electron quickly decays back to form a singlet ground state, which does not interact magnetically with its environment. differentiates pentacene-doped naphthalene from persistent embedded spins, such as colour centres in diamond, where the colour centre can also be used as a source of polarisation of the nuclear spin-lattice. However, in contrast to pentacene-doped naphthalene, persistent electronic spins used for polarisation remain magnetically active, typically in the form of a ground-state triplet. This leads to undesired interactions with the spin-lattice and possible environmental fields even after the polarisation transfer has been completed, turning into an unwanted source of decoherence and dissipation. In contrast, the short lifetime of the photo-excited triplet states in pentacene allows the opening of a channel for polarisation transfer that is subsequently closed, thus removing an important source of dissipation, and resulting in unmatched nuclear polarisation lifetimes. Given the $\sim$920 h T_1 times and $>$80 % polarisation established in [36], in a nanoparticle of 70 nm radius, with just one or two embedded pentacenes, even higher polarisation levels can be expected.

As will be discussed in the next chapter, the ability to polarise the nuclear spins in naphthalene offers a promising alternative to create macroscopic superpositions, diverging from the conventional use of single electron spins like NV centres in diamond. Despite the electron spin's higher gyromagnetic ratio, the collective strength of naphthalene's hydrogen spins, numbering around $6 \cdot 10^7$ in a particle with 70 nm radius, surpasses that of an individual electron spin by more than 4 orders of magnitude.

6.2 Magic Angle Spinning

While the longitudinal relaxation time T_1 is very long, the coherence time of each nuclear spin is constrained by the, generally much shorter, T_2 time. For each nuclear spin, the main source of decoherence is provided by its interaction with the rest of the nuclear spin lattice, which constitutes its immediate environment. Thus, to achieve extended coherence times, it would be desirable to suppress the inter-nuclear spin interactions. A technique, well known in the field of nuclear magnetic resonance spectroscopy, that can achieve this is that of magic angle spinning (MAS), which is routinely used in solid-state NMR to increase the T_2 time of spins in a crystal by suppressing their dipole-dipole interaction. The technique works by rotating the probe sufficiently fast around an axis that is tilted with respect to the direction of the magnetic field by a specific angle of

$\arccos\left(1/\sqrt{3}\right) \approx 54.74°$, referred to as the magic angle [210]. The achievable T_2 time is approximately determined by the rotation frequency ν_{MAS} and is given by [215]

$$T_2 \approx \frac{\nu_{\mathrm{MAS}}}{\pi G d_{\mathrm{rss}}^2}, \tag{6.1}$$

where d_{rss} is the effective dipolar coupling. The effective dipolar coupling experienced by a given proton j can be written as $d_{\mathrm{rss,j}} = (\sum_{k\neq j} d_{j,k}^2)^{1/2}$, where $d_{j,k}$ is the dipolar coupling between the j^{th} and k^{th} spin. G is a geometric factor given by the structure of the lattice, with a value that can range between 0.04 and 0.11 [215]. While the exact value for the naphthalene crystal is not known, for our calculations we will use the maximum value of $G = 0.11$, leading to the most conservative estimations of the T_2 time. To estimate d_{rss}, we first compute the inter-nuclear dipolar coupling strength

$$d_{j,k} = \frac{\mu_0 \gamma_H^2 \hbar}{4\pi |\vec{r}_{jk}|^3}(1 - 3\cos^2\theta_{jk}) \tag{6.2}$$

between a nuclear spin j and all the spins k in its lattice cell as well as in the first-neighbour cells, and use it to compute $d_{rss,j}$. We then average this value over all the spins j within a lattice cell. Here, $\gamma_H \approx (2\pi)42.576\,\mathrm{MHz/T}$ is the gyromagnetic ratio of the hydrogen nucleus, $\vec{r}_{jk}$ is the vector joining the spins j and k, and θ_{jk} is the angle formed by the magnetic field and the vector $\vec{r}_{jk}$. We take the positions of the hydrogen atoms in naphthalene from X-ray scattering data [216]. The computation yields $d_{\mathrm{rss}} \approx (2\pi)8.1\,\mathrm{kHz}$, resulting in the following relation between the achievable T_2 time and the rotation frequency of the crystal

$$T_2 \approx 4.4\,\nu_{\mathrm{MAS}} \cdot 10^{-8}\,\mathrm{s}. \tag{6.3}$$

Thanks to their inherent rotational freedom, nanoparticles levitated in a vacuum offer an unprecedented opportunity for MAS with rotational frequencies well beyond the state of the art [217] in solid-state NMR. The most advanced rotation methods in this field typically operate at frequencies on the order of 100 kHz, with the largest demonstrated rotation frequencies being on the order of 200 kHz [218]. This is achieved by pneumatic techniques, which employ compressed air to spin an air-bearing rotor containing the sample of interest. In contrast, levitated nano- and microparticles, exploit the transfer of angular momentum from circularly polarised light to the rotational degrees of freedom of the particle. This transfer can occur through photon absorption, or due to the birefringence or geometric anisotropy of the particles [217, 219]. Exploiting this mechanism, microparticles levitated in a vacuum can attain rotational frequencies up to the MHz range [211, 212] while a nanoparticle can achieve frequencies as high as GHz [15, 213]. Notably, naphthalene crystals exhibit strong birefringence with three optical axes, with refractive indices along these axes measured at 1.442, 1.775, and 1.932 respectively [209], surpassing even the birefringence of vaterite [115]. This suggests that under sim-

ilar conditions, naphthalene could achieve rotational frequencies as high as those observed in the rotation of vaterite [211] or potentially higher.

Nevertheless, the ultimate rotation frequencies achievable with any material are constrained by the yield strength of the material. The maximal rotation frequency a sphere of naphthalene can survive before breaking is given by

$$\nu_{\max} = \frac{1}{2\pi}\sqrt{\frac{\sigma_{\mathrm{UTS}}}{r^2\rho}} \tag{6.4}$$

where $\sigma_{\mathrm{UTS}} = 49\,\mathrm{MPa}$ is its ultimate tensile strength [220, 221]. For example, for a 70 nm naphthalene particle with a density of $\rho = 1145\ \mathrm{kg/m^3}$ we find $\nu_{\max} = 470\,\mathrm{MHz}$, which suggests that nuclear spins in naphthalene can reach coherence times of $T_2 \approx 20$ s. As will be discussed in the next section, this exceeds by several orders of magnitude the required coherence times to perform matter-wave interferometry using nuclear spins.

An important aspect that could limit the achievable rotation frequencies is the absorption of photons coming from the laser used to induce the rotation. An excessive degree of heating of the internal temperature of the particle will have implications for the sublimation rate, as discussed in the next section, and for the intensity of the emitted black body radiation, which can result in excessive decoherence and could be detrimental for interferometric applications. It is, however, noteworthy to mention that in contrast to the optically levitated setups where rotation has been demonstrated, here we are proposing a protocol where the nanoparticle is magnetically levitated and the laser is used only for a short time to induce the desired rotations. The short duration of the laser pulse together with the high degree of purity attainable in the production of naphthalene crystals, which results in low absorption rates, leads us to expect heating rates below those observed in optical traps with other materials. In the following, we make a back-of-the-envelope estimation of the expected heating and conclude that, while the increase in internal temperature may not be negligible, it does not impede achieving the required rotation frequencies.

The rotation frequency ν_{MAS} obeys the differential equation

$$I\dot{\nu}_{\mathrm{MAS}} = \tau_{\mathrm{opt}} - \tau_{\mathrm{drag}}, \tag{6.5}$$

where I is the moment of inertia, τ_{opt} is the light-induced torque, and τ_{drag} is the damping torque due to viscous interaction of the rotating nanoparticle with the surrounding gas molecules. τ_{drag} is proportional to $\nu_{\mathrm{MAS}}P$, with P the pressure of the gas, and the maximal rotation frequency is reached, as soon as $\tau_{\mathrm{opt}} = \tau_{\mathrm{drag}}$ [15]. At frequencies much lower than this maximum, one can safely assume that $\tau_{opt} \gg \tau_{drag}$, and thus that the rotation frequency increases linearly in time as $\nu_{MAS} = (\tau_{opt}/I)t$.

For a nanoparticle that is significantly smaller than the wavelength of the incident

light, the optical torque due to the birefringence of the particle is given by [219]

$$\tau_{\mathbf{opt}} = \frac{\epsilon_0 V}{2} \operatorname{Re}[(\chi \mathbf{E}^*) \times \mathbf{E}] + \frac{\epsilon_0 k^3 V^2}{12\pi} \operatorname{Im}[(\chi^2 \mathbf{E}^*) \times \mathbf{E} - (\chi \mathbf{E}^*) \times (\chi \mathbf{E})], \quad (6.6)$$

where V is the volume of the particle, and $k = 2\pi/\lambda_L$ is the wave number of the laser. χ is the orientation-dependent polarisability tensor, which for an anisotropic, ellipsoidal particle is diagonal in a frame coinciding with its principal axes. In that frame, it is determined by the diagonal elements [222]

$$\chi_j = 3\frac{\epsilon_j - 1}{\epsilon_j + 2}. \quad (6.7)$$

Here, $\epsilon_j = n_j^2$ is the relative permittivity along the j^{th} principal axis, and $\mathbf{E}$ is the possibly complex amplitude of the electric field $\mathbf{E}(t) = \mathbf{E}\exp(-i\omega t)$. Notably, for an isotropic material, the torque is zero. To compute the torque, the complex contribution to χ will be neglected, as the absorption of naphthalene in the visible range is minimal. If the naphthalene is orientated such that the principal axes of n align with the lab frame, n is given by $n = \operatorname{diag}(1.442, 1.932, 1.775)$. The largest torque is achieved with circularly polarised light travelling along the z axis, namely $\mathbf{E} = E_0/\sqrt{2}(1, \exp(i\pi/2), 0)$. For a spherical naphthalene particle of radius r, with moment of inertia $I = 2/5\, mr^2$ and a laser with wavelength λ_L, we find

$$\nu_{\text{MAS}} = a\frac{r}{\lambda_L^3}\mathcal{I}t\,, \quad (6.8)$$

where $a = 8.15 \cdot 10^{-11}\,\text{m}^4/(\text{Ws}^2)$ is a constant, $\mathcal{I} = c\epsilon_0|E_0|^2/2$ is the intensity of the laser and t the time the particle is exposed to the laser light.

We now proceed to estimate the amount of heating expected as a function of the rotation frequency. If heat losses due to other mechanisms like black body radiation are neglected, the heating rate is given by [223]

$$mc_m(T)\dot{T} = 8\pi^2\mathcal{I}\frac{r^3}{\lambda_L}\operatorname{Im}\left[\frac{\epsilon - 1}{\epsilon + 2}\right], \quad (6.9)$$

where $c_m(T)$ is the temperature-dependent specific heat capacity in units of J/(kgK). This differential equation can be solved by the technique of separation of variables. Plugging Eq. (6.8) in we get

$$\int_{T_i}^{T_f} c_m(T)\,\mathrm{d}T = 6\pi\nu_{\text{MAS}}\frac{\lambda_L^2}{a\,r\,\rho}\operatorname{Im}\left[\frac{\epsilon - 1}{\epsilon + 2}\right]. \quad (6.10)$$

Remarkably, the expression is independent of the employed laser intensity, as the heating rate is proportional to the laser intensity while the duration of the laser pulse is inversely proportional to it. We compute specific values for the expected

temperature increase, using data from Ref. [224] to model the temperature dependence of the heat capacity of naphthalene. To find $\epsilon = n^2$, we assume that the real part of n is given by the average over the two axes involved in the rotation, therefore $\mathrm{Re}(n) = 1.687$. On the other hand, we calculate an upper bound to the imaginary part of n from one of the main absorption peaks of naphthalene in the optical range, which is found at 470 nm and shows an absorbance of $\alpha = 5 \cdot 10^{-4}\,\mathrm{cm}^{-1}$ [225]. α is related to the imaginary part of the refraction index via $\mathrm{Im}(n) = \alpha c/(2\omega)$, where ω is the frequency of the light. We therefore find $\mathrm{Im}(n_{\mathrm{naph}}) = 1.175 \cdot 10^{-8}$. In the neighbourhood of this peak, the absorption is expected to be even lower [226]. A pentacene concentration of $c_{\mathrm{pen}} = 10^{-7}\,\mathrm{mol/mol}$ would allow for multiple pentacene molecules within a spherical naphthalene crystal of 70 nm. If the effective absorption index is estimated via linear mixing, it is given by $\mathrm{Im}(n_{\mathrm{eff}}) = n_{\mathrm{naph}}(1 - c_{\mathrm{pen}}) + n_{\mathrm{pen}}c_{\mathrm{pen}})$. For the individual pentacene molecules to have a significant effect, the absorption coefficient would need to be on the order of 10^{-1}.While solid-state pentacene exhibits strong absorption near its electronic transitions at around 600 nm, the absorption of single pentacene molecules decreases rapidly. As there are no quantitative measurements of pentacene's absorption coefficient in the blue spectral range, we refer to the work of Faltermeier et al. [227], where the extinction coefficient of pentacene is not resolvable for wavelengths shorter than 400 nm. Based on this, we conclude that the absorption of pentacene molecules can be neglected. Naturally, in experiments, the frequency of the employed laser should be suitably placed outside any absorption line width of both naphthalene and pentacene, to minimise the internal heating of the particle. With these considerations we use $n = 1.687 + i\,1.175 \cdot 10^{-8}$ as an upper bound. While this estimate is based on rough calculations, the true absorption coefficient of this hybrid system would need to be determined experimentally.

Putting everything together, we find that, for example, to achieve a T_2 time of 1 s, a spinning frequency of 23 MHz is required. For a particle with 70 nm radius that was initially prepared at an internal temperature of 5 K this would result in its temperature increasing up to not more than 11 K when being accelerated to this frequency by using 500 nm light.

6.3 Sublimation

Because naphthalene is a van der Waals crystal, the question arises as to whether, at the low pressures necessary to conduct matter-wave interferometry experiments, sublimation events may occur that are detrimental to the coherence of the experiment. Each time a molecule of naphthalene evaporates from the crystal, departing with some momentum $\vec{p}$, it induces a recoil on the levitated particle, that constitutes a form of noise on its mechanical degrees of freedom. Moreover, each evaporated naphthalene molecule carries into the environment information on the

position and the velocity of the naphthalene crystal, which may also destroy the desired interference pattern. In particular, for situations where the de Broglie wavelength of the sublimated molecule is shorter than the spatial superposition of the interferometer, a single molecule loss could be enough to resolve the position of the naphthalene particle and in turn destroy the interference. Thus, we would like to estimate the rate at which naphthalene molecules detach from the bulk of the crystal and restrict each of our experimental runs to times for which the probability of a single naphthalene molecule evaporating is negligible. We assume that the rate at which particles detach from the crystal depends only on the internal temperature of the crystal, and follow the argument presented by Tennakone and Peiris to find this rate [228].

Let us consider a bulk sphere of naphthalene with radius r, levitated in a completely evacuated container. Over time, some of the naphthalene will evaporate until the pressure in the chamber is the same as the vapour pressure p_n of naphthalene, at which point, an equilibrium is reached between the rate of particles that leave the crystal and those that are deposited onto it. Following statistical physics considerations, one can estimate the rate at which, at a pressure of p_n, naphthalene molecules in the gas collide with the bulk sphere of radius r. This is given by

$$\dot{N} = \frac{4\pi r^2 p_{\mathrm{n}}}{\sqrt{2\pi m_{\mathrm{N}} k_B T}}, \tag{6.11}$$

where $m_{\mathrm{N}} = 128\,\mathrm{a.m.u.} = 2.1{\cdot}10^{-25}\,\mathrm{kg}$ is the mass of a single naphthalene molecule and T is its temperature, which is also the temperature of the bulk, as the situation is described at equilibrium. If all incident particles were to get deposited onto the surface of the naphthalene nanoparticle, Eq. (6.11) would also constitute the rate at which naphthalene molecules sublimate from the crystal. While this is not true in general, Eq. (6.11) provides an upper bound to the real rate of sublimation and allows us to make a conservative estimation of the available time before a single molecule escapes (or gets deposited onto) the crystal, as a function of its temperature and size.

The relation between the vapor pressure of naphthalene and its temperature is found to be well described by the equation [229]

$$\ln \frac{p_n}{p_0} = \left(1 - \frac{T_0/K}{T/K}\right) \exp\left(\sum_{i=0}^{n} A_i (T/K)^i\right), \tag{6.12}$$

where the parameters A_i are to be experimentally fit, and p_0 is the vapor pressure at an arbitrarily chosen temperature T_0. As a reference, we use the values at room temperature, $p_0 = 13.08$ Pa and $T_0 = 300$ K. As for the parameters A_i, the values $\{A_0 = 3.272310, A_1 = -2.663498 \cdot 10^{-4}, A_2 = -2.929123 \cdot 10^{-9}\}$ for the first three orders provide a good fit in the temperature range from 150 K to the triple point at 353.37 K [229].

With this, we can compute that, for example, at room temperature the emission rate of naphthalene molecules from a particle of 70 nm is $\dot{N} \approx 10^{10}$ s^{-1} which would limit the duration of a single experimental run to 10^{-10} s. This naturally rules out any option of performing interferometry experiments without cooling the internal temperature of the naphthalene nanoparticle. However, this rate exhibits a dramatic dependence on temperature. At 150 K, which is the lowest temperature for which Eq. (6.12) provides a reliable value, the emission frequency is $\dot{N} = 40$ s^{-1}, extending the available time for each experimental run to several milliseconds.

Moreover, for matter-wave interferometry experiments, internal temperatures on the order of a few Kelvin will be required to reduce noise coming from the emission of black body radiation, as will be explained in the next section. At these temperatures, sublimation rates are expected to be even lower by orders of magnitude. Thus, we do not expect sublimation to be a factor limiting the coherence of matter-wave interferometry experiments with naphthalene.

On the other hand, any experiment will consist of a statistically significant number of runs that allow the reconstruction of the observables of interest. Thus, while one could guarantee that on a single experimental run, no naphthalene molecules are sublimated, it is to be expected that the total experimental time will extend over periods where the emission rate of naphthalene particles is not negligible. This could lead to a drift of the mass of the particle as the experiment progresses. To understand the extent of this mass variation, we compute the rate of change of the total mass of a naphthalene particle of radius r relative to its initial mass M_0. From Eq. (6.11) we see that, at pressures below the vaporization pressure, the rate of mass loss is upper bounded by

$$\frac{d}{dt}\left(\frac{M}{M_0}\right) = -\sqrt{\frac{m_N}{2\pi k_B T}}\frac{3p_N}{\rho\, r}, \tag{6.13}$$

where $\rho = 1.145 \cdot 10^3$ kg/m^3 is the density of naphthalene. For a particle of 70 nm, at a temperature of 150 K, this results in a relative mass that varies in time as $M/M_0 = 1 - 1.8 \cdot 10^{-10} t$, which suggests that even on a time scale of hours the mass of the nanoparticle would not change beyond its 7th significant digit. We, thus, do not expect this to affect the experiment.

7 Naphthalene in a Stern-Gerlach Type Interferometer

This chapter is in large parts based on [1], CC BY 4.0 license.

This chapter describes the dynamics of a diamagnetic particle containing N embedded nuclear spins in the presence of a magnetic field gradient. The magnetic field gradient induces a harmonic confinement of the centre of mass of the diamagnetic particle and, at the same time, its interaction with the spin system leads to forces whose strength and direction depend on the state of the spin ensemble. These forces can be used to manipulate the motion of the particle and in particular to expand its position variance and enhance its sensitivity to external perturbations [74, 230, 231]. We introduce a protocol based on microwave pulses that manipulates precisely the state of the spin ensemble, allowing us to engineer dynamics that involve a rapid expansion of the centre of mass wave packet and its subsequent reversal. Probing the coherence of such expand-and-recombine dynamics, which can be done through the measurement of the spin state at the end of the protocol, allows us to test the linearity of quantum mechanics at the scales of the employed particle mass and the reached size of the wave function. This constitutes an instance of a matter-wave interferometry protocol, that is, an interferometer that harnesses the wave character of matter. The novelty with respect to other matter-wave interferometry protocols based on spin-dependent forces is the presence of multiple spins, which boosts the spread of the wave function, resulting in shorter experimental times and therefore increased robustness to several sources of noise. We discuss the scaling of the different figures of merit with the number of spins N. Moreover, we explore the intricacies of the protocol, propose a way to measure the spin state through the position of the nanoparticle, and analyse the resilience of the protocol against various sources of noise.

The following chapters are organised as follows: Section 7.1 analyses why nuclear spin ensembles in naphthalene offer a robust alternative to single electron-spin platforms such as NV centres: their high density allows the large number of spins to outperform a single electron spin in collective force, while their homogeneous distribution and the absence of zero-field splitting avoid the unwanted rotations that afflict single-spin systems. Section 7.2 derives the Hamiltonian governing the coupled centre-of-mass and spin dynamics of a naphthalene particle in a diamagnetic trap, constructing a Stern-Gerlach type interferometer. Section 7.3 turns this protocol into a quantitative test of the CSL collapse model, showing that a naive readout of the collective magnetic moment fails to exploit the large number of spins, and proposes a modified pulse sequence that restores this scaling. It

further establishes bounds on the CSL parameters λ_{CSL} and r_{CSL} attainable with the modified protocol, showing that it can exclude previously untested regions of parameter space, including the values proposed by GRW. Section 7.4 addresses how the nuclear spin polarisation $\langle \hat{M} \rangle$ can actually be measured, showing that the spin-motion coupling maps the collective magnetisation onto a displacement of the nanoparticle's centre of mass with sufficient precision to resolve the effect of the CSL model, and discussing the photo-excited triplet state of the embedded pentacene molecule as an alternative optical readout, before addressing how imperfect and fluctuating initial polarisation can be compensated for. Section 7.5 examines how magic-angle spinning affects the delivery of the microwave pulses, showing that fast enough spinning decouples the spin dynamics from the rotation itself, though the spatial extent of the particle and the delocalisation of the wave packet broaden the spin resonance and demand composite or chirped pulse schemes to drive the full ensemble uniformly. Section 7.6 assesses the dominant noise sources acting on the interferometer and derives the experimental conditions, temperature, pressure, and field gradient, required to keep their effects subdominant to the CSL signal.

7.1 Advantages of Naphthalene for Stern-Gerlach type interferometry

Nuclear spins in naphthalene present a promising pathway for creating macroscopic superpositions of the nanoparticle in position space. While current proposals for Stern-Gerlach-type macroscopic interferometers often rely on single electron spins, such as NV centres in diamond [232,233], here we argue that the use of nuclear spin ensembles presents an intriguing alternative. Although the gyromagnetic ratio of an electron spin is roughly three orders of magnitude higher than that of a nuclear spin, the collective strength of approximately $6 \cdot 10^7$ polarised hydrogen spins in a 70 nm naphthalene particle exceeds that of an individual electron spin in the same magnetic field gradient.

Furthermore, the homogeneous distribution of nuclear spins within naphthalene presents a distinct advantage over systems reliant on single electron spins. In traditional setups, precise positioning of the spin on the nanoparticle's centre of mass is necessary to prevent undesired rotations of the entire particle. However, in naphthalene, the evenly dispersed nuclear spins exert a collective force that acts uniformly on the nanoparticle, avoiding undesired rotational effects.

On the other hand, particles containing embedded spins with zero-field splitting, such as the NV centre in diamond, are prone to additional unwanted rotations. For particles with a zero-field splitting the axis of quantization is not determined by the direction of the external magnetic field but rather by the spin direction that diagonalises the zero-field Hamiltonian. When this quantization axis deviates

Table 7.1: Material constants of naphthalene.

χ_V (CGS)	χ_V (SI)	ρ in kg/m^3	σ_{UTS} in MPa	H density in 1/m^3
$-7.33 \cdot 10^{-7}$	$-9.21 \cdot 10^{-6}$	1145	49	$4.3 \cdot 10^{28}$

from the direction of the magnetic field, it tries to realign, exerting a force that induces a torque on the particle. This presents a challenge for experiments leveraging spin-dependent forces for the generation of spatial superposition. Matter-wave interferometry experiments will generally require preparing the spin in a superposition of states $|\uparrow\rangle$ and $|\downarrow\rangle$. Thus, even in the case of a perfect alignment of the NV axis with the magnetic field, one of the superposed states will be aligned parallel to the magnetic field, while the other will be in an anti-parallel orientation. In this configuration, any small deviations from this perfect alignment between the NV axis and the magnetic field will induce torques dependent on the spin state, which will eventually lead to entanglement between spin and rotational degrees of freedom. In contrast, nuclear spin-$\frac{1}{2}$ systems lack such splitting. Any potential zero-field splitting observed in the nuclear spins of naphthalene arises from dipole-dipole interactions among nuclear spins, which in our setup are suppressed by the implementation of magic-angle spinning. Moreover, the rapid rotation of the nanoparticle contributes to the stabilisation of its rotational degrees of freedom, akin to magnetic tops, increasing the robustness of the setup against unwanted torques and rotations [234, 235].

7.2 Time Evolution in a Magnetic Trap

In this section, we analyse the dynamics of a hyperpolarised naphthalene sphere confined within a diamagnetic trap. Diamagnetic levitation exploits the fact that diamagnetic materials are repelled by magnetic fields, naturally tending toward regions of minimal magnetic field strength. The potential energy density $E(\vec{r})$ of a particle in a magnetic field $\vec{B}(\vec{r})$ and subject to earth's gravity, at position $\vec{r} = (x, y, z)$, is given by

$$E(\vec{r}) = -\frac{\chi_V}{2\mu_0}\vec{B}(\vec{r})^2 + \rho g x, \tag{7.1}$$

where $\mu_0 = 4\pi \cdot 10^{-7}$ H/m is the vacuum permeability, χ_V is the volume magnetic susceptibility, ρ is the mass density of the particle, and g is the gravitational acceleration. Here, and throughout the rest of the manuscript, the coordinate frame is chosen such that gravity points in the x-direction. The equilibrium position for levitation is determined by the condition $\vec{F}(\vec{r}) = -\nabla E(\vec{r}) = 0$, where $\vec{F}(\vec{r})$ is the force density acting on the particle. For the x-component, this leads to the

standard levitation condition for diamagnetic trapping:

$$B_0 \frac{\partial B}{\partial x} = \mu_0 g \frac{\rho}{\chi_V}. \tag{7.2}$$

For naphthalene, with $\rho = 1145\ \mathrm{kg/m^3}$ and $\chi_V = -9.21 \cdot 10^{-6}$ [115], the condition requires $B(\partial B/\partial x)$ to be on the order of $1500\ \mathrm{T^2/m}$, which is within experimental feasibility [116]. Furthermore we would like to point out that the static contribution of the magnetic field is determining the equilibrium position of the levitated particle, while the gradient determines the trap frequency. In principle, other levitation methods for naphthalene could be considered. These include charging the particle and trapping it in a Paul trap, utilising its spin angular momentum to stably levitate it in a static magnetic field [41], or potentially, hyperpolarising the nuclear spin lattice and using the Meissner effect to levitate it above a superconductor. In this work, we focus solely on diamagnetic levitation and leave the exploration of alternative methods for future investigations.

The Hamiltonian describing the centre-of-mass motion and spin dynamics of a naphthalene nanoparticle of mass m containing N nuclear spins, each with gyromagnetic ratio γ_p, and embedded in a magnetic field gradient of the form $\vec{B}(x) = (B'x + B_0)\hat{k}$, with $\hat{k}$ a unit vector in the z direction, can be expressed as

$$\hat{H} = \frac{\hat{p}^2}{2m} - \frac{\chi_V V (B_0 + B'\hat{x})^2}{2\mu_0} + \frac{\hbar}{2}\gamma_p (B_0 + B'\hat{x}) \sum_{n=1}^{N} \hat{\sigma}_z^{(n)}. \tag{7.3}$$

Under the coordinate transformation $x \to x - \frac{B_0}{B'}$, and a suitable rearranging of the terms, the Hamiltonian can be rewritten as

$$\hat{H} = \frac{\hat{p}^2}{2m} + \frac{m\Omega^2}{2}\left(\hat{x} + \chi \sum_{n=1}^{N} \hat{\sigma}_z^{(n)}\right)^2 - \eta \left(\sum_{n=1}^{N} \hat{\sigma}_z^{(n)}\right)^2, \tag{7.4}$$

where we have introduced the parameters

$$\Omega \equiv \sqrt{\frac{|\chi_V|}{\rho\mu_0}} B', \qquad \chi \equiv \frac{\hbar\gamma_p\mu_0}{2|\chi_V|VB'} \quad \text{and} \quad \eta \equiv \frac{\hbar^2\gamma_p^2\mu_0}{8|\chi_V|V}. \tag{7.5}$$

In this form, it becomes clear that the centre of mass oscillates with frequency Ω around an equilibrium position that is displaced from the origin by an amount $x_{\mathrm{eq}} = -\chi \sum_{n=1}^{N} \hat{\sigma}_z^{(n)}$. This equilibrium position depends on the state of the spin ensemble. We would like to point out that the trap frequency Ω solely depends on material constants and the magnetic field gradient. With the values provided in Table 7.1, we find $\Omega \approx 0.08\,\mathrm{m/(Ts)} \cdot B'$ and therefore trap frequencies on the order of tens to hundreds of Hertz for gradients in the range of $10^3 - 10^4\,\mathrm{T/m}$. The magnetic field assumed here is, of course, not a physical field as it does not satisfy

with Maxwell's equations, which require that $\vec{\nabla} \cdot \vec{B} = 0$. Therefore, a physical fields needs at least another contribution along the y axis. In Appendix A.1 we discuss why this contribution can be neglected.

For clarity, we will presume that the spin ensemble is initially fully polarised—any implications of imperfect polarisation are discussed in Section 7.4. Hence we can assume that all spins are initially arranged in their lowest energy state, aligning uniformly in a single direction. Subsequently, we apply a $\pi/2$-pulse, mapping each spin into a superposition of spin up and spin down. The precision with which such a pulse can be delivered to all the spins in the ensemble is discussed in Section 7.5. Assuming that the centre-of-mass motion is prepared in a thermal state $\hat{\rho}_{\mathrm{th}}$, the resulting state of the combined system is given by

$$\hat{\rho} = \hat{\rho}_{\mathrm{th}} \otimes \frac{1}{2^N} \sum_{\kappa,\kappa'=0}^{N} \sqrt{\binom{N}{\kappa}\binom{N}{\kappa'}} \left|\kappa\right\rangle \left\langle\kappa'\right| , \tag{7.6}$$

where $|\kappa\rangle$ is the κ^{th} Dicke state, defined as the linear combination of all spin states with κ spins up

$$\sqrt{\binom{N}{\kappa}} \left|\kappa\right\rangle = \left|\uparrow^{\otimes\kappa}\downarrow^{\otimes N-\kappa}\right\rangle + \text{permutations.} \tag{7.7}$$

Hamiltonian (7.4) preserves the Dicke state, as this is an eigenstate of the operator $\sum_{n=1}^{N} \sigma_z^{(n)}$, and thus, of the Hamiltonian. Therefore, provided that the initial state is contained in the subspace spanned by the Dicke states, the state of the system at any time t can be expressed in terms of Dicke states as

$$\hat{\rho}(t) = \frac{1}{2^N} \sum_{\kappa,\kappa'=0}^{N} \sqrt{\binom{N}{\kappa}\binom{N}{\kappa'}} \hat{\rho}_{\kappa,\kappa'}(t) \otimes \left|\kappa\right\rangle \left\langle\kappa'\right| . \tag{7.8}$$

In the following, we want to find a differential equation describing the time evolution of the spatial components of the density matrix $\hat{\rho}_{\kappa,\kappa'}(t)$. The time evolution of $\hat{\rho}(t)$ is given by von Neumann's equation $\dot{\hat{\rho}} = -\frac{i}{\hbar}[\hat{H}, \hat{\rho}]$ and with Ansatz 7.8, we find

$$\dot{\hat{\rho}}_{\kappa,\kappa'} = -\frac{i}{\hbar} \left\{ \hat{H}_\kappa \hat{\rho}_{\kappa,\kappa'} - \hat{\rho}_{\kappa,\kappa'} \hat{H}_{\kappa'} + \eta_{\kappa,\kappa'} \hat{\rho}_{\kappa,\kappa'} \right\} \tag{7.9}$$

with

$$\hat{H}_\kappa \equiv \frac{\hat{p}^2}{2m} + \frac{m\Omega^2}{2} [\hat{x} + (2\kappa - N)\chi]^2 \tag{7.10}$$

and

$$\eta_{\kappa,\kappa'} \equiv \eta \left[(2\kappa' - N)^2 - (2\kappa - N)^2 \right], \tag{7.11}$$

and which has the solution

$$\hat{\rho}_{\kappa,\kappa'}(t) = e^{-\frac{i}{\hbar}\hat{H}_\kappa t} \hat{\rho}_{\kappa,\kappa'}(0) e^{\frac{i}{\hbar}\hat{H}_{\kappa'} t} e^{-\frac{i}{\hbar}\eta_{\kappa,\kappa'} t}. \tag{7.12}$$

The evolution of the initial state in Eq. (7.6) can be described as follows. At first, the mechanical and spin degrees of freedom are in a product state, however, as the evolution progresses the initial centre-of-mass wave packet splits into $N+1$ trajectories, each correlated with one of the Dicke states, which are parametrised by $\kappa \in [0, N]$. All trajectories follow a harmonic motion, albeit each oscillating around a different equilibrium position. Thus to each Dicke state, we can associate an equilibrium position $x_{\mathrm{eq},\kappa} = (2\kappa - N)\chi$. It is not difficult to show that at any given time, one will find the $N+1$ wave packets evenly distributed along dimension x with the nearest-neighbour spacing given by $2\chi \sin^2(\Omega t/2)$.

The specific shape of each trajectory associated with a Dicke state κ depends on the initial position of the particle. If the particle is cooled while the spins are fully polarised, that is, when the spin ensemble is in the Dicke state $\kappa = N$—then the particle will be prepared in the ground state (or a low temperature thermal state) at the corresponding equilibrium position, $x_{\mathrm{eq},N}$. As a result, after the first $\pi/2$ pulse, the trajectory corresponding to $\kappa = N$ will remain centred around its equilibrium position, while the other trajectories, associated with $\kappa < N$, will begin to oscillate with amplitudes that grow with the distance to their equilibrium positions. Not all trajectories are equally likely, however. According to state (7.6) the probability of the spin ensemble being in Dicke state κ is given by $p_\kappa = \binom{N}{\kappa} 2^{-N}$. Therefore, it is desirable for the trajectory corresponding to $\kappa = N/2$ which is the most probable to remain near equilibrium, while the less probable trajectories fan out symmetrically to the left and right, as depicted in Fig. 7.1. This would ease the requirement for maintaining a linear magnetic field gradient across the region where the particle is most likely to be found.

To realize this configuration, we propose continuously driving the nuclear spins with a Rabi frequency Ω_{M} that is higher than the oscillation frequency of the mechanical oscillator Ω. The effective potential experienced by the particle can then be described by a harmonic oscillator whose centre is given by $w(t) = N\chi \cos(\Omega_{\mathrm{M}} t)$, such that the differential equation governing the centre-of-mass position $q(t)$ of the particle reads $m\ddot{q}(t) + m\Omega^2 \big[q(t) - w(t)\big] = 0$. We assume that the particle has already settled into its long-time behaviour, described by the particular solution $q(t) = N\chi\,\Omega^2/(\Omega^2 - \Omega_{\mathrm{M}}^2)\cos(\Omega_{\mathrm{M}} t)$, which is referred to as micromotion. The amplitude of the micromotion is given by $|N\chi\,\Omega^2/(\Omega^2 - \Omega_{\mathrm{M}}^2)| \approx |N\chi\,\Omega^2/\Omega_{\mathrm{M}}^2|$ for $\Omega^2 \ll \Omega_{\mathrm{M}}^2$. Using the parameters listed in Table 7.1, we find $N\chi\,\Omega^2/\Omega_{\mathrm{M}}^2 \approx (0.53\,\mathrm{m^2 s^{-2}/T}) \cdot B'/\Omega_{\mathrm{M}}^2$. For a gradient of 10^4 T/m and a Rabi frequency of 100 kHz

we find a resulting oscillation amplitude of approximately 13 nm respectively. To start the interferometry protocol, the driving field is first turned off, and the sequence of pulses described above is applied. If this is done at an arbitrary time, the particle may already possess some initial momentum or displacement within the trap. In that case, its resulting motion will be the sum of two contributions: the motion induced by the pulse sequence for an initially stationary and centred particle, and the free motion corresponding to its initial state in the absence of any pulses. Let us consider the case when the particle is maximally displaced at the moment of starting the protocol, and hence, has no momentum. In this case, it oscillates in the mechanical trap with an amplitude as discussed above and frequency Ω. This implies that the trajectories spread over a spatial extent that is larger than the ideal case by 13 nm, depending on the applied Rabi frequency. For a gradient of 10^4 T/m, the variation of the magnetic field across this space is now larger by 0.26 mT. Alternatively, if the drive stops when the particle is at the trap centre, it has a maximum momentum $p(0) = mN\chi\Omega^2/\Omega_{\mathrm{M}}$, corresponding to an oscillation amplitude of $p(0)/(m\Omega) = 6.6/\Omega_{\mathrm{M}}$. For $\Omega_{\mathrm{M}} = 100$ kHz, this adds to each trajectory oscillations with amplitude 10 μm, which results in an additional field variation of 0.2 T. This requirement may be demanding, but timing the drive to stop at maximum displacement and using the largest possible Rabi frequency should, in principle, suffice to keep the particle within the linear gradient region.

In this regime, the nuclear spins become effectively decoupled from the oscillation mode, and the particle will settle near the equilibrium position corresponding to $|\kappa = N/2\rangle$, with a deviation of about 10 nm. While continuous spin driving may induce polarisation loss through T_2 relaxation, the associated timescale is expected to be on the order of seconds under magic-angle spinning. The thermalisation time is highly dependent on the specific realization of the experiment, but should remain shorter than this timescale to avoid significant losses in polarisation.

Shortly after stopping the drive, the initial $\pi/2$ pulse can be applied, or equivalently, the drive could be stopped when the spins have rotated by a suitable angle corresponding to a $\pi/2$ rotation with respect to their initial state. With this modification, the trajectories would evolve as depicted in Fig. 7.1. The drive can either be applied while hyperpolarising the spin ensemble during polarisation within the trap, or, if the particle is hyperpolarised outside the trap, the drive can be applied immediately after placing the particle in the trap.

The variance in the position of the centre of mass at a given time t can be computed to be

$$\langle \Delta x \rangle^2 = \langle \Delta x_{\mathrm{th}} \rangle^2 + \left(2\chi \sin^2(\Omega t/2)\sqrt{N} \right)^2 , \tag{7.13}$$

where $\langle \Delta x_{\mathrm{th}} \rangle$ is the position variance of the initial thermal state. Equation (7.13) shows the enhancement that can be achieved in the expansion of the centre-of-mass wave function from a larger number of spins. In comparison to matter-wave interferometry based on a single electron spin, such as an NV-centre in a diamond

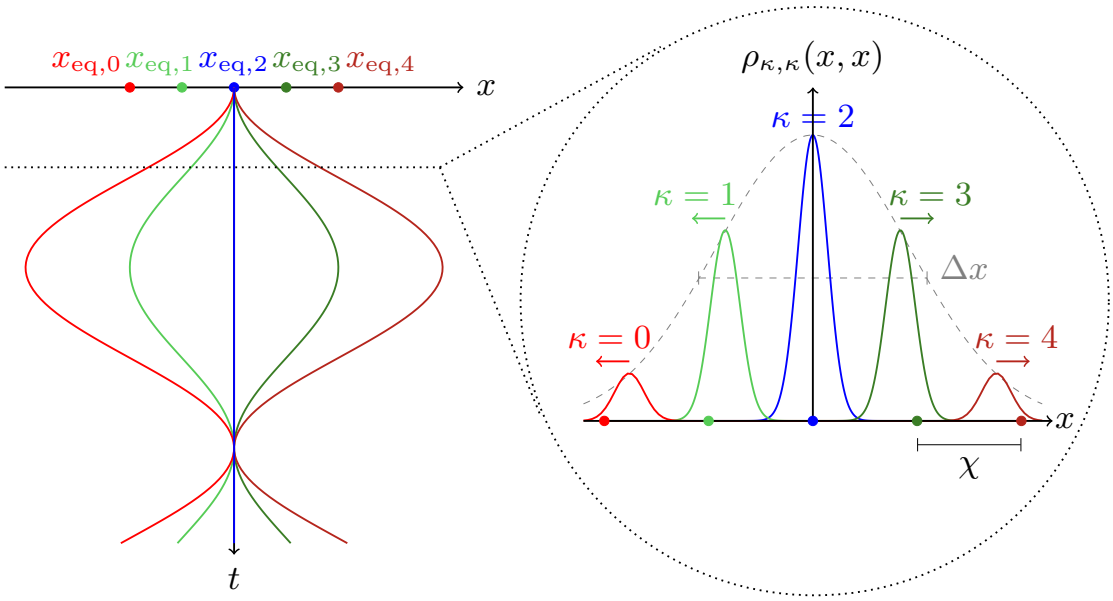


Figure 7.1: Here, the time evolution of the κ wave packets in a magnetic field gradient is displayed. The κ^{th} wave packet oscillates around the equilibrium position $x_{\mathrm{eq},\kappa}$, as depicted on the left. After a full period of $2\pi/\Omega$, all trajectories meet again in the centre of the trap. The equilibrium positions $x_{\mathrm{eq},\kappa} = (2\kappa - N)\chi$ are spaced by χ. If the initial spin state is given by Eq. (7.6), the wave packets corresponding to κ are in a superposition, as depicted on the right. The Gaussians are displaced by $x_{\mathrm{eq},\kappa}[1 - \cos(\Omega t)]$ and enclosed in an envelope that follows a binomial distribution. The width of the envelope is given by Eq. (7.13).

nanoparticle, we observe an enhancement factor of

$$\sqrt{(\langle\Delta x\rangle^2 - \langle\Delta x_{\mathrm{th}}\rangle^2)/(\langle\Delta x\rangle^{(NV)} - \langle\Delta x_{\mathrm{th}}\rangle^2)} \approx 1.5 \cdot 10^{-3}\sqrt{N}. \tag{7.14}$$

Here, the factor of $1.5 \cdot 10^{-3}$ originates from the ratio between the gyromagnetic ratios of the hydrogen and electronic spins. A naphthalene nanoparticle with a radius 100 nm contains approximately 10^8 nuclear spins, resulting in a 15-fold enhancement of the achievable variance at any given time over that achievable with a single electron spin. For the parameters in Table 7.2 a), one can achieve an expansion of the wave packet of $\langle\Delta x\rangle^2 - \langle\Delta x_{\mathrm{th}}\rangle^2 = (167\,\mathrm{nm})^2$ after just 0.5 ms, a position variance that is larger than its radius.

For matter-wave interferometry with spin-dependent forces, it is often desirable to revert the expansion of the wavepacket and return the system to its initial state where spin and mechanical degrees of freedom are decoupled from each other. Then the coherence of the process can be tested through a measurement of the spin system, certifying also the spatial coherence of the superposition achieved

Table 7.2: Overview of some critical specifications of the protocol for different sets of parameters. The parameters are chosen in such a way, that $\phi = 0$ and an interference fringe can be resolved. It was assumed that the only noise acting on the state where spontaneous collapses with $\lambda_{\mathrm{CSL}} = 10^{-16}$ and $r_{\mathrm{CSL}} = 10^{-7}$. While the proposed field gradients are challenging, they are in principle within experimental feasibility [116, 237].

	r [nm]	N	$B'[\frac{\mathrm{T}}{\mathrm{m}}]$	T_{tot} [ms]	χ[m]	$\frac{\langle \hat{M} \rangle(T_{\mathrm{tot}})}{\langle \hat{M} \rangle(0)}$	$\frac{\Omega}{4\lambda}$	Δx_{dis} [m]	P_{flip}	$T_{\mathrm{i,max}}$ [K]
a)	44	$1.5 \cdot 10^7$	10^4	7.8	$5.4 \cdot 10^{-10}$	0.956	0.4	$6.6 \cdot 10^{-4}$	0.04	4
b)	44	$1.5 \cdot 10^7$	10^3	78	$5.4 \cdot 10^{-9}$	0.65	0.1	$56 \cdot 10^{-3}$	0.3	4
c)	105	$2.1 \cdot 10^8$	10^5	0.77	$4 \cdot 10^{-12}$	0.61	4.3	$6.5 \cdot 10^{-4}$	0.05	9

during the protocol. For the setup described in this section, this decoupling occurs without additional intervention at times that are natural multiples of the trap period, a time at which all the trajectories return simultaneously to their initial position, see Fig. 7.1. Nevertheless, with a suitable manipulation of the spin state, this decoupling can be achieved at times shorter than a single period of the trap, in this way reducing the influence of detrimental sources of noise [236]. While this also reduces the size of the prepared superposition, it allows us to adjust the protocol to the available coherence time.

First, one lets the wave function spread for a time $t_1 < \pi/\Omega$—if the expansion time is larger than half of an oscillation period, then the fastest way to decouple the spin and centre-of-mass motion is to leave the system complete one full period. At this time, a microwave π-pulse is applied on the spins, causing them to flip their state, which for the Dicke states translates into the transformation $\kappa \to N - \kappa$. This reverts the force acting on each of the Dicke states, slowing down the expansion of the position variance and eventually leading to its compression, see Fig. (7.2). A second π-pulse is required to guarantee that all the superposed wavepackets overlap not only in position but also in momentum. The spacing between the first and second π-pulses depends on the initial spreading time t_1 and is given by

$$t_2(t_1) = \frac{2}{\Omega} \arcsin\left(\frac{\sin(\Omega t_1)}{\sqrt{5 - 4\cos(\Omega t_1)}} \right). \tag{7.15}$$

Finally, waiting for a time t_1 after the second π-pulse, all trajectories recombine and the position and spin degrees of freedom are decoupled again. Thus, for such a protocol the total time is $T_{\mathrm{tot}}(t_1) = 2t_1 + t_2(t_1)$.

While at the end of the protocol, all the superposed trajectories overlap and the spin and motion decouple, the state of the system is not the same as that at the beginning of the protocol, because each trajectory has followed a different path in phase space and therefore acquired a different phase. The phase picked up by

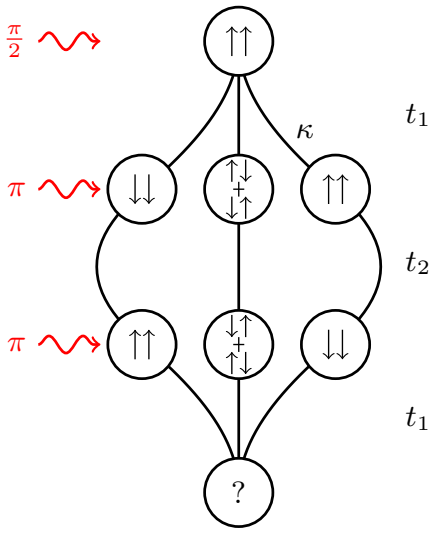


Figure 7.2: Protocol for rapid expansion and recombination of the wave function of the centre-of-mass motion in naphthalene. A hyperpolarised particle is placed in a magnetic gradient, forming a harmonic trap. Then a $\pi/2$ pulse is applied. The spin state is now a superposition of the $N+1$ possible Dicke state. Depending on the spin state, the particle travels along another trajectory and the wave function expands for a time t_1. By applying two well-timed π pulses spaced by t_2, all trajectories recombine after another time t_1. The trajectories are denoted by $\kappa \in [0, N]$. To better illustrate the intrinsic dynamics of the protocol, we consider an initial particle position at $\kappa = N/2$ rather than at the equilibrium position $\kappa = N$. In this case, the centre of the wave packet remains stationary.

each trajectory κ, sometimes referred to as the geometric phase, is given by

$$\phi_\kappa = (2\kappa - N)^2[(\chi/2x_0)^2 \sin(\Omega t_1) + \frac{\eta}{\hbar} T_{\text{tot}}] \tag{7.16}$$

where $x_0 = \sqrt{\hbar/(2m\Omega)}$ is the width of the ground state. A detailed derivation of this phase is given in Appendix A.2. Note that the phase is the same for trajectories that are symmetric about the origin, that is, for trajectories $\kappa = 0$ and $\kappa = N$, for trajectories $\kappa = 1$ and $\kappa = N - 1$, and so on. Finally, provided that the whole process is coherent, at the end of the protocol, the system is found in a state of the form $\hat{\rho} = \hat{\rho}_{\text{th}} \otimes |\psi_{\text{f}}\rangle \langle\psi_{\text{f}}|$ with

$$|\psi_{\text{f}}\rangle = \frac{1}{2^{N/2}} \sum_{\kappa=0}^{N} \sqrt{\binom{N}{\kappa}} e^{-i\phi_\kappa} |\kappa\rangle \, . \tag{7.17}$$

Due to the different phases picked up by each Dicke state, the spin ensemble at the end of the protocol is in general entangled. We emphasize that the proposed protocol remains valid regardless of whether the initial state is in the ground state or in a thermal state. This robustness is a general feature of Stern-Gerlach-type experiments and stems from the fact that the spin and motional degrees of freedom decouple at the end of the protocol [27, 28].

A breakdown of the linearity of quantum mechanics on the scales at which the protocol is performed would manifest as a deviation of the final state from that in Eq. (7.17). This remains true even in cases where the thermal variance is large and dominates the total variance of the interferometer, since the spin degrees of freedom are sensitive to decoherence acting on each pure state that contributes to the mixed state.

Conversely, experimental verification of the final state in Eq. (7.17) would constitute proof of the validity of quantum mechanics at such scales. To provide a more quantitative account of such a possibility, in the next section, we compute the evolution of the system in the presence of, arguably, the most widely analysed model of wavefunction collapse at macroscopic scales, namely, the Continuous Spontaneous Localization (CSL) model.

7.3 Test of the CSL Model

Motivated by the aspiration to provide a unified framework to describe micro/quantum systems and macro/classical systems and to solve the so-called measurement problem in quantum mechanics, collapse models postulate modifications to the Schrödinger equation [39]. These modifications are, typically, in the form of non-linear and stochastic extensions, whose effects manifest for systems of large mass and states of wide spatial delocalisation. In contrast, for small masses and well-

localized systems, these modifications are negligible, and spontaneous collapse models converge to the standard Schrödinger equation. In this sense, they provide a framework to describe a progressive breakdown of the linearity of quantum mechanics with increasing system mass. Generally, the effect of these modifications is to induce spontaneous collapses of the wavefunction onto spatially well-localized states. The Continuous Spontaneous localisation (CSL) model is perhaps the most general and widely studied of the collapse models. It postulates a localisation of the wavefunction in position space which depends on two free parameters, λ_{CSL} and r_{CSL}. λ_{CSL} has units of s^{-1} and relates to the frequency of the collapses, while r_{CSL} has units of m and relates to the length scale of the localisation. The dynamics of the CSL model at the level of the density matrix, that is, after averaging over a large number of stochastically occurring collapses, is given, in coordinate representation, by [39, 142, 143]

$$\dot{\rho}(q', q'') = -\frac{i}{\hbar}\langle q'|\,[\hat{H}, \hat{\rho}]\,|q''\rangle - \xi\left(1 - e^{-\frac{(q'-q'')^2}{4r_{\mathrm{CSL}}^2}}\right)\rho(q', q''), \tag{7.18}$$

where $\rho(q', q'') = \langle q'|\,\hat{\rho}\,|q''\rangle$ with $|q\rangle$ the position eigenstate, and ξ is a coefficient that depends on the free parameters λ_{CSL} and r_{CSL}, the mass and the shape of the system. For a spherical particle of radius r and mass m, ξ is given by [146]

$$\xi = \frac{m^2}{m_0^2}\lambda_{\mathrm{CSL}} f\left(\frac{r}{r_{\mathrm{CSL}}}\right) \quad \text{with} \quad f(x) = \frac{6}{x^4}\left[1 - \frac{2}{x^2} + \left(1 + \frac{2}{x^2}\right)e^{-x^2}\right], \tag{7.19}$$

and m_0 is a reference mass, typically, taken to be the mass of a nucleon.

Equation 7.18 indicates that the effect of the collapse model is to suppress the coherence between different position eigenstates. The coherence between spatial points (q', q'') that are further away from each other decays faster than that between closer points. In the limit $|q' - q''| \ll r_{\mathrm{CSL}}$, the decay rate of the coherences tends to $\xi(q' - q'')^2/(4r_{\mathrm{CSL}}^2)$, while between points that are far away from each other, the decay rate converges to ξ.

Our goal is to use the interferometric protocol introduced in the previous section to provide bounds for the values that the free parameters of the CSL model, λ_{CSL} and r_{CSL}, can take. To that end, we compute the state of the spin ensemble at the end of the protocol in the presence of the CSL model and determine how it differs from that of the noise-free case in Eq. (7.17)

It is noteworthy that the presence of CSL noise does not distort the trajectories that each Dicke state follows, but only the coherence between them. Thus, at the end of the protocol, all the trajectories overlap, as in the noise-free case, and the system is in a separable state of the form $\hat{\rho} = \hat{\rho}_{\mathrm{CM}} \otimes \hat{\rho}_{\mathrm{S}}$, where $\hat{\rho}_{\mathrm{CM}}$ denotes the centre-of-mass state and $\hat{\rho}_{\mathrm{S}}$ that of the spin ensemble. Nevertheless, the loss of

coherence between the different trajectories manifests as a reduction of the purity of the spin state, which can be computed to be

$$\hat{\rho}_{\rm S} = \frac{1}{2^N} \sum_{\kappa,\kappa'=0}^{N} \sqrt{\binom{N}{\kappa}\binom{N}{\kappa'}} e^{-i(\phi_\kappa - \phi_{\kappa'})} e^{-\Lambda_{\kappa,\kappa'}} \left|\kappa\right\rangle \left\langle\kappa'\right|, \tag{7.20}$$

where the relative phase ϕ_κ was introduced in Eq. (7.16) and

$$\Lambda_{\kappa,\kappa'} = \xi \int_0^{T_{\rm tot}} (1 - e^{-\frac{[\mathcal{X}_\kappa(t') - \mathcal{X}_{\kappa'}(t')]^2}{4r_{\rm CSL}^2}}) \, {\rm d}t', \tag{7.21}$$

as shown in Appendix A.2. Here, $\mathcal{X}_\kappa(t) = \chi \, {\rm Re}[\zeta_\kappa(t)]$ is the classical trajectory of the $\kappa^{\rm th}$ wave packet and is given in Eq. (A.14). Since $\zeta_\kappa(t)$ is linear in κ, the decoherence rate between the $\kappa^{\rm th}$ and $\kappa'^{\rm th}$ trajectories is proportional to $(\kappa - \kappa')^2$.

For matter-wave interferometers with a single spin, the standard procedure is to apply a $\pi/2$-pulse on the spin at the end of the protocol, and then measure the magnetic moment of the spin $(1/2)\hbar\gamma\sigma_z$. In the absence of noise, the pulse returns the spin to the initial state $|\uparrow\rangle$, and the expectation value of σ_z is thus found to be one. A loss of coherence, for example, due to the presence of CSL noise, is then manifested as a reduction of the expectation value. Thus the expectation value of the magnetic moment of the spin accounts for the amount of noise observed by the system. The natural extension of such a protocol for the multi-spin case that we consider here is the application of a $\pi/2$-pulse to each of the spins in the ensemble and the subsequent measurement of the total magnetic moment of the nanoparticle

$$\hat{M} = \frac{\hbar}{2}\gamma_p \sum_{n=1}^{N} \hat{\sigma}_z^{(n)}, \tag{7.22}$$

with $\hat{\sigma}_z^{(n)}$ the z Pauli operator acting on the $n^{\rm th}$ spin. However, as we explain below, this will turn out not to be an optimal strategy.

As shown in Appendix A.3, the expectation value of $\hat{M}$ after applying a $\pi/2$-pulse on all the spins at the end of the protocol, can be computed to be

$$\frac{\langle\hat{M}\rangle(T_{\rm tot})}{\langle\hat{M}\rangle(0)} = e^{-\gamma(T_{\rm tot})} \cos^{N-1}(4\phi), \tag{7.23}$$

with $\gamma(T_{\rm tot}) = \Lambda_{\kappa,\kappa\pm1}(T_{\rm tot})$ and $\phi = \phi_\kappa/(2\kappa - N)^2 = (\chi/2x_0)^2 \sin(\Omega t_1) + \eta T_{\rm tot}/\hbar$. As discussed, $\Lambda_{\kappa,\kappa'}$ is proportional to $(\kappa - \kappa')^2$, and therefore $\gamma(T_{\rm tot})$ is independent of κ. Assuming that the distance between nearest neighbour trajectories is much smaller than $r_{\rm CSL}$, which is not a particularly restrictive assumption, $\gamma(T_{\rm tot})$ has a closed form, although lengthy, solution which is given in Appendix A.3.

Expression (7.23) presents two notable drawbacks. Firstly, it fails to exploit the

presence of multiple spins, resulting in a decay due to CSL noise that remains independent of the number of spins. Consequently, the sensitivity of the protocol mirrors that of the single-spin scenario, neglecting the potential enhancement from multiple spins and only leveraging decoherence between nearest-neighbour trajectories. This limitation stems from the nature of the operator $\hat{M}$, and can easily be understood under the following logic. The measurement of operator $\hat{M}$ after a collective $\pi/2$-pulse is equivalent to taking the expectation value of operator $(\hbar/2)\gamma_p \sum_{n=1}^{N} \hat{\sigma}_x^{(n)}$ over state (7.20). Given that the $\hat{\sigma}_x^{(n)}$ operators, responsible for individual spin flips, induce transitions of the form $\hat{\sigma}_x^{(n)} |\kappa\rangle \rightarrow \{|\kappa - 1\rangle, |\kappa + 1\rangle\}$, only coherences between nearest-neighbor Dicke states contribute to the expectation value of $\hat{M}$.

Secondly, the presence of the term $\cos^{N-1}(4\phi)$ in Eq. (7.23) poses another challenge. This term arises from the relative phase accumulation among different trajectories and restricts the duration of the protocol to times that guarantee the condition $\phi = n\pi$, where n is an integer. Any deviations from this condition result in the rapid vanishing of the expectation value of $\hat{M}$, regardless of the presence of CSL noise. Given that even the smallest nanoparticles harbor millions of nuclear spins, as indicated in Table (7.2), minor deviations $\Delta\phi$ from $n\pi$ could prove detrimental. A rough estimate suggests that, since $\cos^N(n\pi + \Delta\phi) \approx 1 - N(\Delta\phi)^2/2 + \cdots$, determining ϕ with a precision below $1/\sqrt{N}$ radians is required. Nonetheless, with sufficient precision, one can always adjust the parameters and vary t_1 to meet this criterion. One example would be to set $t_1 = \pi/\Omega$. Then, t_2 would be zero and the total time is $T_{\text{tot}} = 2\pi/\Omega$. $\phi = l\pi$ then holds true for

$$B' = \frac{\hbar\gamma_p^2}{lV}\sqrt{\frac{\mu_0^3\rho}{|\chi_V|^3}}, \tag{7.24}$$

where l is an integer. In general, the experiment can be conducted faster by finding the values of t_1 that meet the required conditions for a given set of system parameters.

We note that the variance of $\hat{M}$ does not provide a significant advantage. Since the variance is determined through single-shot measurements of $\hat{M}$, we normalize the quantity by $\langle\hat{M}\rangle(0)^2$ to enable a fair comparison between $\langle\hat{M}\rangle$ and $\langle\Delta\hat{M}\rangle^2 = \langle\hat{M}^2\rangle - \langle\hat{M}\rangle^2$. Analogous to Appendix A.3, one can find $\langle\Delta\hat{M}\rangle^2$ to be

$$\begin{aligned}\frac{\langle\Delta\hat{M}\rangle^2(T_{\text{tot}})}{\langle\hat{M}\rangle^2(0)} =& \frac{1}{2N}\left[1 - e^{-4\gamma}\cos^N(8\phi)\right] + \frac{1}{2}\big[1 - 2e^{-2\gamma}\cos^{2N-2}(4\phi) \\ &+ e^{-4\gamma}\cos^{N-2}(8\phi)\big].\end{aligned} \tag{7.25}$$

Notably, for large N, the term in the first line is suppressed. The rest is independent of N, therefore this observable does not show an improvement compared to Eq. (7.23). At this point, the argument of $\gamma = \gamma(T_{\text{tot}})$ was omitted for readability.

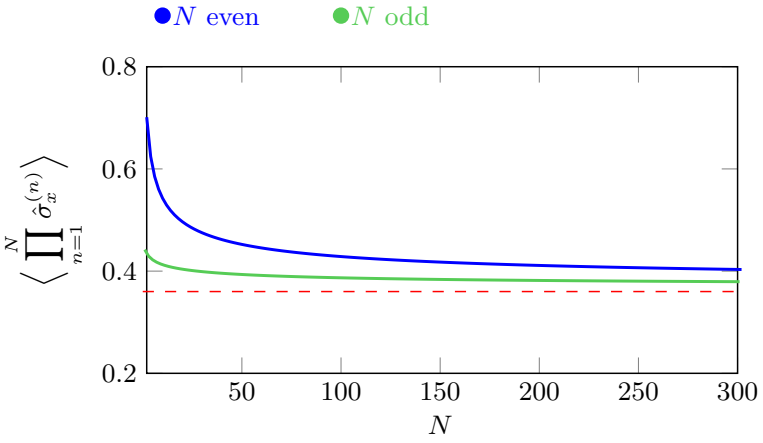


Figure 7.3: $\left\langle \prod_{n=1}^{N} \hat{\sigma}_x^{(n)} \right\rangle$ for an arbitrary set of system parameters and protocol duration. $\left\langle \prod_{n=1}^{N} \hat{\sigma}_x^{(n)} \right\rangle$ is greater for even values of N and smaller for odd ones. This discrepancy arises from the fact that for even N, there exists a trajectory $\tilde{\kappa} = N/2$ for which $\tilde{\kappa} = N - \tilde{\kappa}$ and thus $\Lambda_{N/2,N/2} = 0$, a condition not satisfied for odd N. Moreover, this term carries the greatest weight in the sum of Eq. (7.26). For large N, the difference between odd and even N diminishes as expected and $\left\langle \prod_{n=1}^{N} \hat{\sigma}_x^{(n)} \right\rangle$ approaches the bound given by $\exp(-\xi T_{\text{tot}})$, which is depicted in red.

A more suitable observable for mitigating the impact of relative phases and harnessing the collective behaviour of multiple spins is given by $\propto \prod_{n=1}^{N} \hat{\sigma}_x^{(n)}$. This observable induces the transition $\prod_{n=1}^{N} \hat{\sigma}_x^{(n)} |\kappa\rangle = |N - \kappa\rangle$ between Dicke states. Notably, the two connected states accumulate the same relative phase throughout the protocol, that is $\phi_\kappa = \phi_{N-\kappa}$, effectively eliminating from the expectation value the dependence on the geometric phase ϕ. Furthermore, the decay rate now relies on the total number of spins, as contributions to the expectation value stem not only from nearest-neighbour coherences. This can be computed as:

$$\left\langle \prod_{n=1}^{N} \hat{\sigma}_x^{(n)} \right\rangle = \frac{1}{2^N} \sum_{\kappa=0}^{N} \binom{N}{\kappa} e^{-\Lambda_{\kappa,N-\kappa}} . \tag{7.26}$$

Figure (7.3) shows how Eq. (7.26) behaves with increasing N for an arbitrary set of system parameters and protocol duration. Notice that as $\Lambda_{\kappa,\kappa'}$ is bounded from below by ξT_{tot}, the expectation value $\langle \prod_{n=1}^{N} \hat{\sigma}_x^{(n)} \rangle$ at time T_{tot} converges to the value $\exp(-\xi\, T_{\text{tot}})$ as N increases.

However, measuring such an observable presents greater challenges compared to measuring the magnetic moment of the nanoparticle. One way to do so would be to apply a global π-pulse on the spin ensemble that is controlled on the state of an ancillary qubit, that is, $U_{\text{c}} = |0\rangle\langle 0|_a \otimes \prod_{n=1}^{N} \hat{\sigma}_x^{(n)} + |1\rangle\langle 1|_a \otimes \mathcal{I}_{2^N}$, where subscript

$_a$ indicates the operators acting on the ancillary qubit, and $\mathcal{I}_{2^N}$ is the identity operator on the Hilbert space of the N spin ensemble. The expectation value of $\prod_{n=1}^{N} \hat{\sigma}_x^{(n)}$ can then be retrieved by measuring the off-diagonal element of the density matrix of the ancillary qubit $\langle |0\rangle\langle 1| \rangle_a$. Implementing such a controlled gate, however, may prove challenging in practice as it requires generating and maintaining coherence between the ancillary qubit and the N-spin ensemble for the duration of the readout. One could argue that were such an operation available to the experimentalist, they could instead use it to prepare an initial state that is a superposition of the two more distant Dicke states, $|0\rangle_a \otimes |\kappa = 0\rangle + |1\rangle_a \otimes |\kappa = N\rangle$, and in this way maximise the achievable position variance of the interferometer. Notice, however, that such a strategy would require maintaining the coherence between the ancilla and the spin ensemble for the duration of the experiment, while the use of such a gate only during readout may be significantly less challenging.

7.3.1 Modified Protocol

Given the challenges faced by the standard matter-wave interferometry protocol when attempting to utilise the collective behaviour of multiple spins, as highlighted above, here, we propose a modified version thereof. This adaptation aims to effectively leverage the presence of numerous spins while still relying on the measurement of the total magnetic moment of the nanoparticle, thus, circumventing the need for measuring correlations between the spins. The modified protocol is depicted in Fig. 7.4 for the minimal case of 2 spins (3 Dicke states). In essence, the introduced modification is the application of additional $\pi/2$-pulses, which has the effect of multiplying the number of trajectories. The detailed protocol is as follows. Initially, a $\pi/2$-pulse is applied and the wave packet splits into $N+1$ wave packets each following a different trajectory, which are numbered consecutively by $\kappa \in [0, N]$. So far, the protocol is identical to the standard one. The novelty is introduced after a time $t_1 = \pi/\Omega$, when a second $\pi/2$ pulse is applied. Each of the $N+1$ trajectories then further divides into an additional $N+1$ trajectories, numbered by $\alpha \in [0, N]$, and resulting in a total of $(N+1)^2$ trajectories that we label (κ, α). By repeating the protocol as in Fig. 7.2, we ensure that the trajectories α generated by the second $\pi/2$-pulse overlap. If another $3\pi/2$-pulse is applied at this point, these trajectories recombine into the original $N+1$ trajectories, that is, $(\kappa, \alpha) \to (\kappa)$, see Fig. 7.4. If $t_1 = \pi/\Omega - 2t_{2,1} - t_{2,2}$ is satisfied, all trajectories overlap after another time t_1, and the spin ensemble is decoupled from the motion of the nanoparticle, provided that the process is coherent. The state of the spin

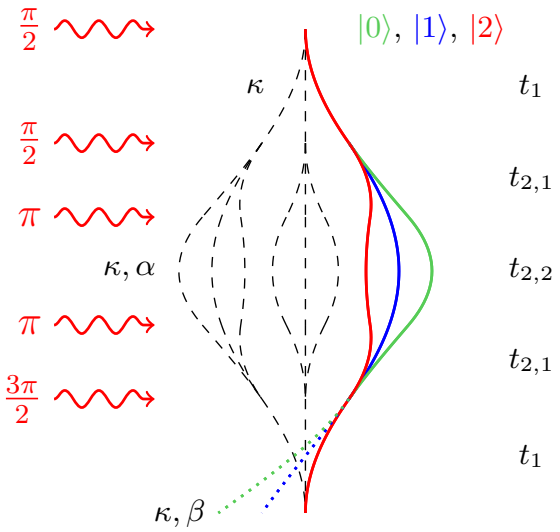


Figure 7.4: Example for the protocol to test the CSL model with two spins. A $\pi/2$ is applied in the beginning, bringing all spins into a superposition of up and down. Depending on the spin state, the particle starts oscillating around d_κ, the wave function expands in space. Here, the trajectory the particle takes if all spins are pointing up, in this case $\kappa = 2$, is highlighted. After half a period at $t_1 = \pi/\Omega$, a second $\pi/2$ pulse is applied and each trajectory again splits up into $N + 1$ trajectories. Each of the trajectories is denoted by α. For the $\kappa = 2$ branch, the different spin states of the α^{th} trajectory are colour-coded. The times are given by $t_1 = \pi/\Omega - 2t_{2,1} - t_{2,2}$, and $t_{2,2}$ as in Eq. (7.15). In the unitary case, the particle continues traveling on the κ^{th} trajectory and all paths meet after another time t_1 in the origin with zero momentum. In the presence of noise, the coherence between the α^{th} trajectories breaks down. This decoherence is mapped on the spin state when the α^{th} trajectories meet. Therefore, there are also small contributions to Dicke states different from κ after the $3\pi/2$ pulse is applied. The $N+1$ trajectories on the κth branch after the $3\pi/2$ pulse are denoted with β.

ensemble at the end of the protocol is given by

$$\hat{\rho}_{\mathrm{S}} = \frac{1}{2^N} \sum_{\kappa,\kappa'=0}^{N} \sum_{\alpha,\alpha'=0}^{N} \sum_{\beta,\beta'=0}^{N} \sqrt{\binom{N}{\kappa}} \sqrt{\binom{N}{\kappa'}} \left(\frac{\pi}{2}\right)^{\otimes N}_{\kappa,\alpha} \left(\frac{3\pi}{2}\right)^{\otimes N}_{\alpha,\beta} \left(\frac{\pi}{2}\right)^{\otimes N}_{\alpha',\kappa'} \left(\frac{3\pi}{2}\right)^{\otimes N}_{\beta',\alpha'} \times e^{-i(\phi_{\kappa,\alpha,\beta}(T_{\mathrm{tot}}) - \phi_{\kappa',\alpha',\beta'}(T_{\mathrm{tot}}))} \operatorname{tr}\{\hat{\rho}_{\kappa,\kappa\prime,\alpha,\alpha',\beta,\beta'}(T_{\mathrm{tot}})\} |\beta\rangle \langle\beta'| , \tag{7.27}$$

where $(\pi/2)^{\otimes N}_{\kappa,\alpha}$ and $(3\pi/2)^{\otimes N}_{\kappa,\alpha}$ are the matrix elements in Dicke basis of the $\pi/2$- and the $3\pi/2$-pulse, respectively, whose explicit expression is provided in Appendix A.4. Provided the process was unitary, only the elements with $\{\beta, \beta'\} = \{\kappa, \kappa'\}$ survive and, furthermore, we find

$$\operatorname{tr}\{\hat{\rho}_{\kappa,\kappa\prime,\alpha,\alpha',\beta,\beta'}(T_{\mathrm{tot}})\} = \operatorname{tr}\left\{\hat{D}(x)\hat{\rho}_0\hat{D}^{\dagger}(x')\right\}, \tag{7.28}$$

where $x = \frac{\chi}{2x_0}\zeta_{\kappa,\alpha,\beta}(T_{\mathrm{tot}})$ is used as the argument in the displacement operator $\hat{D}(x) = \exp\left(x\hat{a}^{\dagger} - x^*\hat{a}\right)$ and $\zeta_{\kappa,\alpha,\beta}(t)$ are the classical trajectories. These, together with the geometric phase picked up by each of them, $\phi_{\kappa,\alpha,\beta}$, are given in Appendix A.5. $\hat{\rho}_0$ is the initial state of the mechanical degree of freedom. For the pulse timings described before, $\zeta_{\kappa,\alpha,\kappa}(T_{\mathrm{tot}}) = 0$ and Eq. (7.28) reduces to 1. On the other hand, the system parameters can be chosen to guarantee that $\phi_{\kappa,\alpha,\beta} = l\pi$, with l an integer, which is the case for the examples given in Table 7.1. Under these conditions, we recover $\hat{\rho}_{\mathrm{S}} = 2^{-N}\sum_{\kappa,\kappa'=0}^{N}\sqrt{\binom{N}{\kappa}\binom{N}{\kappa'}}\,|\kappa\rangle\langle\kappa'|$. Thus, in this noiseless case, after applying a $\pi/2$-pulse and measuring $\hat{M}$, we find $\langle\hat{M}\rangle(T_{\mathrm{tot}}) = \langle\hat{M}\rangle(0)$, as expected.

Now, we need to understand how the expectation value of $\hat{M}$ at the end of the protocol deviates from $\langle\hat{M}\rangle(0)$ in the presence of CSL noise. When CSL noise acts on the system the coherences between the different (κ, α) paths decay at different rates. This decoherence manifests on $\langle\hat{M}\rangle$ in two ways: first, the loss of coherence between the (κ, α) and $(\kappa \pm 1, \alpha')$ trajectories results in the decoherence between the κ^{th} and $\kappa \pm 1^{\mathrm{th}}$ trajectories. This enhances the loss of coherence between neighbouring trajectories at the end of the protocol, which is picked up by the expectation value of $\hat{M}$. An intuitive way to convince oneself why this scheme is so effective is that the $\pi/2$ and $3\pi/2$ pulses do not induce just a transition $\kappa \to \kappa \pm 1$, but also higher-order transitions. Second, the loss of coherence between trajectories (κ, α) and (κ, α') prevents the successful completion of the transformation $(\kappa, \alpha) \to (\kappa)$ after the third $3\pi/2$-pulse. The spin state does not return perfectly to the κ^{th} Dicke state but to a superposition of Dicke states, inducing a transformation of trajectories of the form $(\kappa, \alpha) \to (\kappa, \beta)$. Therefore, not all trajectories overlap at the end of the protocol and, thus, the spin and mechanical degrees of freedom do not become separable. This, however, is not detrimental as it enhances the decoherence due to the CSL noise on the spin ensemble, making it more easily detectable. The full expression of the state of the spin ensemble at the end of the protocol in the presence of CSL noise is given in Appendix A.5.

A second advantage of the modified protocol is that it allows us to tune the spatial maximal delocalisation of the wave function by varying t_1, which we define as

$$\Delta x(t)^2 = \sum_{\kappa,\alpha=0}^{N} \chi^2_{\kappa,\alpha}(t)\, P(\kappa,\alpha). \tag{7.29}$$

$P(\kappa,\alpha)$ is the probability for the $(\kappa,\alpha)^{\text{th}}$ trajectory being realised and is given by

$$P(\kappa,\alpha) = \binom{N}{\kappa} \left(\left(\frac{\pi}{2}\right)^{\otimes N}_{\kappa,\alpha} \right)^2 . \tag{7.30}$$

$\chi^2_{\kappa,\alpha}(t)$ is the corresponding trajectory, which is of the form $\chi^2_{\kappa,\alpha}(t) = c_\kappa(t)\kappa + c_\alpha(t)\alpha$. In Appendix A.6, we find $\Delta x(t)^2 = c_\kappa^2 \frac{N}{4} + c_\alpha^2 \frac{N+N^2}{8}$. While we do not have a rigorous proof of this relation, it agrees perfectly with all numerical tests we have performed. As long as the terms proportional to c_κ dominate, the wave function retains a Gaussian shape. When this is no longer the case, the wave function begins to develop two distinct, widely separated peaks. In general, we look to remain within the Gaussian regime of the interferometer in order to guarantee that most of the trajectories occur in a region where the magnetic field gradient remains linear.

As an example, for $r = 44\,\text{nm}$, $t_1\Omega = 3.1$, $\Omega t_{2,1} = 0.0022$, and $\Omega t_{2,2} = 0.0044$, we find at the time of maximal delocalisation: $\chi_{\kappa,\alpha}(t_1 + t_{2,1} + t_{2,2}/2) = 5.2 \cdot 10^{-6}\kappa + 1.3 \cdot 10^{-11}\alpha$. A particle of this size contains approximately $1.5 \cdot 10^7$ hydrogen nuclear spins. The wave function remains Gaussian, and we find that its standard deviation spreads over a variation of the magnetic field of $\Delta B = B'\Delta x = 10.4\,\text{mT}$. Moreover, if the magnetic field gradient remains constant over a range of 100 mT, then more than 99.99% of all trajectories stay within the linear region at all times. Another possible parameter set is $r = 105\,\text{nm}$, $\Omega t_1 = 3$, $\Omega t_{2,1} = 0.03$, and $\Omega t_{2,2} = 0.061$. For these values, we obtain $\chi_{\kappa,\alpha}(t_1 + t_{2,1} + t_{2,2}/2) = 3.9 \cdot 10^{-7}\kappa + 1.8 \cdot 10^{-10}\alpha$. Such a particle contains around $2.1 \cdot 10^8$ hydrogen spins. The wave function remains Gaussian, and its width spread over a magnetic field variation of $\Delta B = 14\,\text{mT}$. These parameter sets are given in Table 7.2.

7.3.2 Evaluation of $\langle\hat{M}\rangle(T_{\text{tot}})/\langle\hat{M}\rangle(0)$

Now we have to evaluate the expectation value of $\hat{M}$ in the presence of the CSL model. Unfortunately, $\langle\hat{M}\rangle(T_{\text{tot}})/\langle\hat{M}\rangle(0)$ has no closed form expression and needs to be evaluated numerically. Moreover, its numerical evaluation becomes increasingly hard with a growing number of spins N. Our simulations are limited to values of $N \approx 200$. In Fig. 7.5 we plot the value $\langle\hat{M}\rangle(T_{\text{tot}})/\langle\hat{M}\rangle(0)$ as a function of $(\chi/r_{\text{CSL}L})N$. Even though the numerical results clearly suggest that $\langle\hat{M}\rangle(T_{\text{tot}})/\langle\hat{M}\rangle(0)$ is a function of $(\chi/r_{\text{CSL}L})N$, we have been unable to prove

this analytically. To explore the full range of the function we combine curves corresponding to different values of χ where for each curve N ranges from 10 to 250. It is evident that the expectation value of $\hat{M}$ now depends on the number of spins as desired, and can, thus, outperform the sensitivity of a single spin interferometer. It is noteworthy to mention, that this observable is lower bounded by $\langle\hat{M}\rangle(T_{\text{tot}})/\langle\hat{M}\rangle(0) \geq \exp(-\xi\, T_{\text{tot}})$, with the bound corresponding to the case where the coherence between any pair of Dicke states decays at the maximum decay rate, that is, at ξ. We observe that as $(\chi/r_{\text{CSL}L})N$ grows, the magnetic moment of the nanoparticle approaches this limit. This lower bound can be used to restrict the values that the free parameters of the CSL model can take. For instance, if a given experiment measures at the end of the protocol a magnetisation $\langle\hat{M}\rangle_{\text{exp}}$, an upper bound on ξ is given by

$$\xi < \frac{\ln \langle\hat{M}\rangle_{\text{exp}}}{T_{\text{tot}}}\,, \tag{7.31}$$

as any larger value of ξ would result in stronger decoherence and therefore a lower value of $\langle\hat{M}\rangle$ at the end of the protocol. As ξ depends on r_{CSL} and λ_{CSL}, they can be bounded by measuring $\langle\hat{M}\rangle_{\text{exp}}$.

7.3.3 Bounds on the Parameter Space of the CSL Model

In Fig. 7.6, the parameter space of the CSL model is shown, marking the areas already excluded by various other experiments. In the same figure, we show the areas that could, in principle, be excluded by our protocol if operated with the set of parameters in Table 7.2 (a). Based on this analysis, the parameters proposed by GRW could be potentially excluded. Comparable bounds could be achieved with the other two parameter sets in Table 7.2. However, achieving complete exclusion of the parameter space would likely necessitate significantly longer experimental times or heavier particles. For comparison, we also show a dark blue line delineating the region corresponding to the *"minimal" protocol* introduced in Section 7.2, in which the multi-spin character of the interferometer is not exploited. It is evident that the modified interferometric scheme, incorporating an additional sequence of control pulses, substantially enhances the achievable bounds on the CSL model. In particular, it may enable the demonstration of more stringent constraints than those reported in previous experimental efforts.

The question arises as to whether the scheme can be further enhanced by adding additional $\pi/2$ and $3\pi/2$ pulses. This would, on the one hand, increase the duration of the interferometric protocol as well as the maximal width of the delocalisation of the wave function, both of which would increase the sensitivity to possible collapses of the wave function. However, as error sources due to the increased number of pulses would also increase, it is difficult to assess whether further improvements can be obtained and we leave the detailed analysis to future work. In

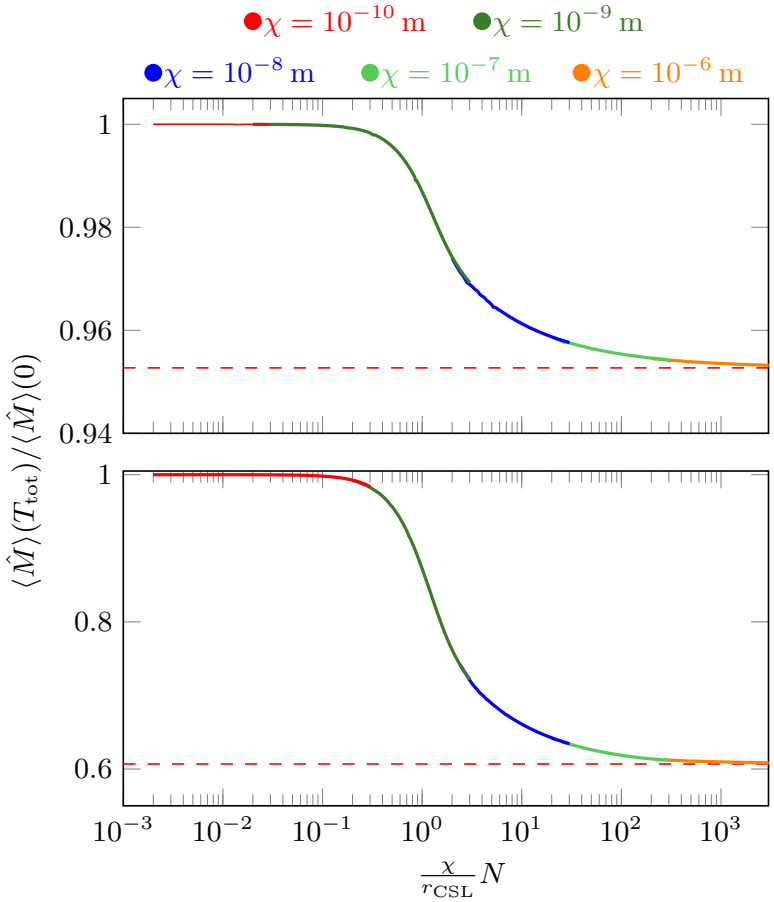


Figure 7.5: Illustration of the behaviour of $\langle\hat{M}\rangle(T_{\text{tot}})/\langle\hat{M}\rangle(0)$ for the parameters in Table 7.2 a) (upper panel) and Table 7.2 c) (lower panel) and for fixed χ. Due to limited computation times, $\langle\hat{M}\rangle(T_{\text{tot}})/\langle\hat{M}\rangle(0)$ could not be evaluated numerically for $N \approx 10^8$ as required, but only for $N < 300$. Therefore, additionally to varying N, χ was varied as this is equivalent to varying the gyromagnetic ratio of the spins. In different colours, one sees $\langle\hat{M}\rangle(T_{\text{tot}})/\langle\hat{M}\rangle(0)$ for different, fixed χ and $N \in [10, 300]$. As one can see, the plots strongly indicate that $\langle\hat{M}\rangle(T_{\text{tot}})/\langle\hat{M}\rangle(0)$ is a function of $(\chi/r_{\text{CSL}})N$. Furthermore, for $(\chi/r_{\text{CSL}})N > 10^2$, it approaches its lower limit given by $\exp(-\xi T_{\text{tot}})$ as indicated by the red, dashed line. For all parameters in Table 7.2, $(\chi/r_{\text{CSL}})N \gg 10^2$. Therefore we can assume that $\langle\hat{M}\rangle(T_{\text{tot}})/\langle\hat{M}\rangle(0)$ is very close to its lower bound.

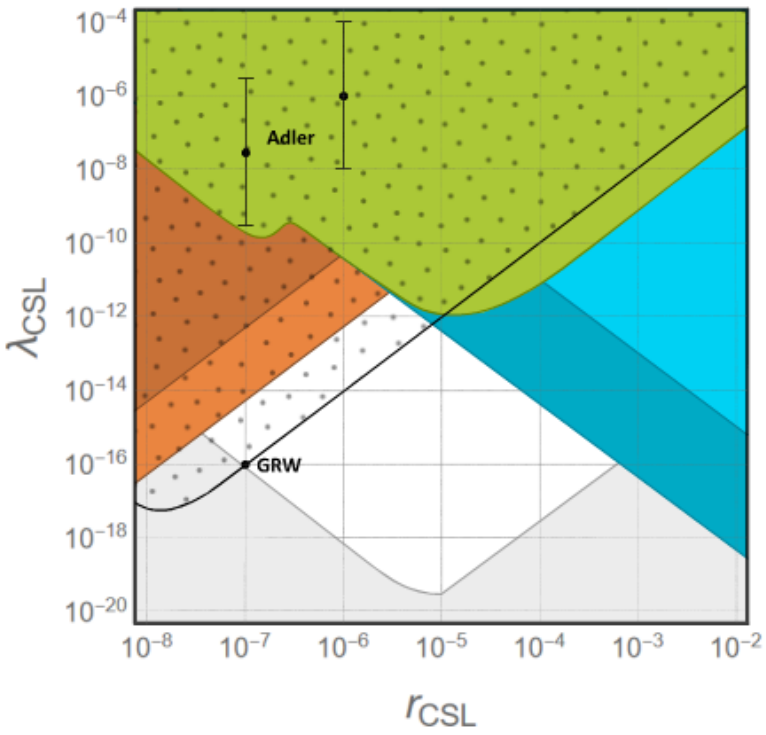


Figure 7.6: Exclusion plot of the parameter space of the CSL model, with λ_{CSL} in the vertical axis and r_{CSL} in the horizontal one. Various experimentally excluded areas are depicted: the green area corresponds to cantilever-based experiments [238], the blue region represents experiments conducted with the gravitational wave detectors LIGO and LISA Pathfinder [155, 156, 239], the brown bounds are derived from spontaneous X-ray emission tests [158, 240], while the gray area is theoretically excluded [150]. The values for λ_{CSL} and r_{CSL} proposed by Adler [147] and by Ghirardi, Rimini and Weber [139] are highlighted in black. The red line bounds the exclusions region obtained from the modified protocol (Section 7.3.1) using pentacene-doped naphthalene and the parameters listed in Table 7.2a. For comparison the dark blue line marks the border of exclusion region using the *minimal* protocol described in Fig. 7.2, under the same parameter assumptions. The modified protocol allows for the exploration of previously untested regions of the parameter space.

any case, we do not expect a significant improvement for the parameter regime investigated in this work, as $\langle\hat{M}\rangle(T_{\mathrm{tot}})/\langle\hat{M}\rangle(0)$ already approaches its lower bound with the scheme presented here.

7.4 Measurement Schemes

We now move on to the question of the measurement of $\langle\hat{M}\rangle$. One possibility could be to leverage the presence of the photo-excited triplet state of the embedded pentacene molecule and its magnetic interaction with the nuclear spin ensemble. In particular, the polarisation of the nuclear spin ensemble would have two notable effects on the pentacene molecule. On the one hand, it would shift the energy splitting between the magnetic triplet states $|+1\rangle$ and $|-1\rangle$. On the other hand, the polarisation of the spin-lattice could be transferred to the triplet state of the pentacene molecule, provided that this is prepared in a suitable initial state. Both of these effects are, in principle, measurable and proportional to the polarisation of the spin ensemble. However, they are bound to be more sensitive to the state of the spins near the pentacene molecule, while underestimating the contribution from spins sitting further from it. We thus turn to alternative measurement schemes that can be sensitive to the global nuclear spin polarisation. In particular, we propose to exploit the spin-motion coupling of the nanoparticle to map expectation values of the spin ensemble onto measurements of the centre-of-mass position.

The Hamiltonian of our system is of the form

$$\hat{H} = \hbar\Omega\hat{a}^\dagger\hat{a} + \hbar\lambda\hat{Z}(\hat{a} + \hat{a}^\dagger), \tag{7.32}$$

where $\hat{Z} = \sum_{n=1}^{N}\sigma_z^{(n)}$ is the observable of interest and $\lambda = (\gamma_p B'/2)\sqrt{\hbar/2m\Omega}$. $\langle\hat{Z}\rangle$ is directly related to $\langle\hat{M}\rangle$ by $\langle\hat{M}\rangle = \hbar/2\gamma\langle\hat{Z}\rangle$. For the particle diameters below 200 nm that we consider, it is safe to assume that the magnetic field gradient is constant across the particle. Consequently, a flip of any of the nuclear spins yields the same momentum kick which, in turn, can then be measured by the displacement. The evolution under such a Hamiltonian has an exact solution, which in the interaction picture w.r.t. $H_0 = \hbar\Omega a^\dagger a$, is given by the unitary-evolution operator

$$\hat{U} = e^{\lambda\hat{Z}[\alpha(t)\hat{a}^\dagger - \alpha^*(t)\hat{a}]}e^{i\frac{\lambda^2}{\Omega}\hat{Z}^2[t-\frac{\sin(\Omega t)}{\Omega}]}, \tag{7.33}$$

where $\alpha(t) = (1 - e^{i\Omega t})/\Omega$.

To see how such an evolution maps the operator $\hat{Z}$ onto the position, we consider the time evolution of the dimensionless position operator $\hat{X} = \hat{a} + \hat{a}^\dagger$ in the Heisenberg picture

$$\hat{X}(t) = \hat{U}^\dagger\hat{X}(0)\hat{U} = \hat{X}(0) + \frac{4\lambda\hat{Z}}{\Omega}\sin^2(\Omega t/2). \tag{7.34}$$

In this form, it becomes evident that, for any state of the spin-motion composite system, the expectation value of the $\hat{Z}$ operator can be retrieved from the expectation value of the position operator as

$$\langle \hat{Z} \rangle = \frac{\Omega}{4\lambda \sin^2(\Omega t/2)} [\, \langle \hat{X} \rangle (t) - \langle \hat{X} \rangle (0)]. \tag{7.35}$$

Here, the coefficient $\Omega/(4\lambda)$ captures the required precision in the position measurement. While this will, in general, depend on the parameters of the system, we find that the position measurement precision required to make meaningful measurements of the spin polarisation is not that great. For example, for the case of a particle of radius $r = 100$ nm and a magnetic field gradient of $B' = 10^5$ T/m, we find that $\Omega/(4\lambda) = 4.3$. This suggests that a position displacement of the ground state width, which in this example is $x_0 = 4 \cdot 10^{-10}$ m, would provide enough sensitivity to distinguish a change in $\langle \hat{M} \rangle$ of 4 units, corresponding to the change induced by four nuclear spin flips. This is quite a remarkable measurement precision, taking into account that optical position measurements of levitated nanoparticles with $\approx 10^{-10}$ m resolution have been demonstrated [10] and as low as 10^{-12} m with charged particles [241]. For an initially fully polarised particle, $\langle \hat{Z} \rangle = N$. The change in the displacement of a naphthalene crystal which is initially fully polarised is then given by

$$\Delta x_{\mathrm{dis}} = x_0 \frac{4\lambda}{\Omega} \left(1 - \frac{\langle \hat{M} \rangle (T_{\mathrm{tot}})}{\langle \hat{M} \rangle (0)} \right). \tag{7.36}$$

In Table 7.2, $\Omega/(4\lambda)$ as well as Δx_{dis} for three different examples are given.

The presence of the pentacene molecule presents an additional method to read out the position of the naphthalene particle. By probing the Zeeman splitting of the photo-excited triplet state of pentacene, which depends on the position of the particle due to the presence of the magnetic field gradient, information on the position of the particle can be retrieved. Such techniques are standard in magnetometry with NV centres [242]. In this approach, the lifetime of the photo-excited triplet state limits the achievable position measurement resolution, as this determines the linewidth the optical transition between the ground state and the excited, triplet state. In naphthalene, the lifetime of the excited triplet states is in the order of $\tau = 50\,\mu$s [33], corresponding to a line width $\Delta\omega_{\mathbf{pent}} = \tau^{-1} = (2\pi)3.1\,$kHz. Interactions with the surrounding nuclear spins would in general broaden this line width, but as magic angle spinning suppresses dipole-dipole interactions, this broadening is also suppressed in our setup. To rapidly resolve the change in displacement due to the CSL model, this should ideally induce a larger Zeeman shift than $\Delta\omega_{\mathbf{pent}}$.

For the example discussed above, with a magnetic field gradient of $B' = 10^5$ T/m, we find the following relation between position displacement Δx and the shift of

the transition frequency $\Delta\omega$ in SI units, $\Delta\omega \approx 1.8 \cdot 10^{13}\Delta x$. This suggests that a displacement of the order of the zero-point motion of the nanoparticle, which in this case, for a particle of $r = 100$ nm, is $x_0 = 7 \cdot 10^{-11}$ m, induces a frequency shift on the order of kHz, and corresponds to a magnetic field change on the order of μT. Hence, displacements a few times the zero-point motion could, in principle, be resolved with this method. To see the effect of the CSL model, for the numbers as in Table 7.2, displacements on the order of 10^{-5} m and larger would have to be resolved. This results in Zeeman shifts in the order of MHz and higher, which is well above the limit imposed by the line width.

In reality, the nuclear spins in the nanoparticle will not be fully polarised. When the nuclear spins of the nanoparticle are polarised by a percentage p, the initial magnetisation and consequently the final magnetisation too will be reduced by a factor of p. Also, the polarisation may vary from run to run. However, $\langle\hat{M}\rangle(T_{\text{tot}})/\langle\hat{M}\rangle(0)$ does not depend on the initial polarisation. Therefore, if the polarisation is measured before each run, one can compensate for variations in the initial polarisation.

7.5 Pulsed Control in the Presence of Magic-Angle Spinning

The protocol suggested in the previous subsection operates under the assumption that the particle is undergoing magic angle spinning. Due to this rotation, the magnetic field observed by the nuclear spins will in general be time-dependent, and thus, it prompts the question of whether this affects our ability to deliver with sufficient precision the microwave pulses required for the protocol. In this section, we look into answering this question.

The particle is sitting in a magnetic field $B(x) = B_0 + B'x$ that points in the z-direction and is rotating with frequency ω_{MAS} around an axis that is tilted with respect to the magnetic field by an angle $\phi_{MAS} = \arccos\big(1/\sqrt{3}\big) \approx 54.74°$. In this arrangement, a microwave pulse is applied to the system with frequency ω_{M} and Rabi frequency Ω_{M}. The Hamiltonian describing such a configuration for a given spin i is provided by

$$\hat{H} = \frac{\hbar}{2}\gamma_p\{B_0 + B'[x_0 + d\sin(\omega_{\text{MAS}}t)]\}\hat{\sigma}_z^{(i)} + \frac{\hbar}{2}\Omega_{\text{M}}\cos(\omega_{\text{M}}t)\hat{\sigma}_x^{(i)}. \tag{7.37}$$

Here, x_0 is the x coordinate of the point on the rotation axis closest to the spin and d is the distance between the spin and this point along the x-axis, as depicted in Fig. 7.7. We define the parameters $\Omega_{\text{MAS}} = \gamma_p B'd$ and $\omega_0 = \gamma_p(B_0 + B'x_0)$. Notice that the latter corresponds to the Larmor frequency of a spin sitting on the rotation axis at x_0. To elucidate the effect of the magic angle spinning on our ability to perform the desired spin rotation, we move to an interaction picture

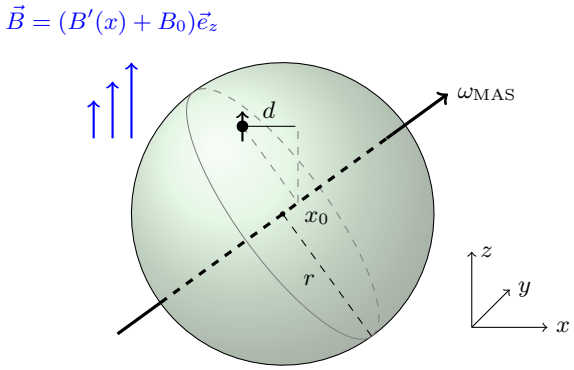


Figure 7.7: Here, a spherical nanoparticle with radius r in a magnetic field gradient is depicted. The particle rotates with ω_{MAS} around an axis that is tided with respect to the magnetic field. A spin in this particle will see an oscillating magnetic field $\vec{B}_{\mathrm{eff}} = \{B_0 + B'[x_0 + d\sin(\omega_{\mathrm{MAS}}t)]\}\vec{e}_z$. x_0 is the x coordinate of the point on the rotation axes closest to the spin and d is the distance between the spin and this point along the x-axis.

with respect to $H_0 = (\hbar/2)\Omega_{\mathrm{MAS}}\sin(\omega_{\mathrm{MAS}}t)\hat{\sigma}_z^{(i)}$, resulting in the Hamiltonian

$$\hat{H}_{\mathrm{int}} = \frac{\hbar}{2}\omega_0\hat{\sigma}_z + \frac{\hbar}{2}\Omega_{\mathrm{M}}\cos(\omega_{\mathrm{M}}t)\Big(e^{-i\frac{\Omega_{\mathrm{MAS}}}{\omega_{\mathrm{MAS}}}\cos(\omega_{\mathrm{MAS}}t)}\sigma_-^{(i)} + e^{i\frac{\Omega_{\mathrm{MAS}}}{\omega_{\mathrm{MAS}}}\cos(\omega_{\mathrm{MAS}}t)}\sigma_+^{(i)}\Big). \tag{7.38}$$

We identify that the required regime to suppress the effect of magic angle spinning is given by $\omega_{\mathrm{MAS}} \gg \Omega_{\mathrm{MAS}}$, where we recover the Hamiltonian corresponding to a static spin with energy splitting ω_0 that is driven at frequency ω_{M}, that is $\hat{H}_{\mathrm{int}} = \hbar/2(\omega_0\hat{\sigma}_z + \Omega_{\mathrm{M}}\cos(\omega_{\mathrm{M}})\hat{\sigma}_x)$. Thus, in this regime, all spins in the body of the naphthalene nanoparticle behave as if they were sitting on the rotation axis, with each spin taking the position on the axis that is the closest to its actual position in the crystal. Since d cannot be larger than the radius of the particle, assuming a spherical particle of radius r, an upper bound on Ω_{MAS} is given by $\Omega_{\mathrm{MAS,max}} = \gamma_p B' r$. For the parameters given in Table 7.2 c), we find $\Omega_{\mathrm{MAS,max}} \lessapprox (2\pi)1.2\,\mathrm{MHz}$, which is several orders of magnitude below the rotation frequencies on the order of hundreds of MHz considered in our protocol to attain efficient magic angle spinning. We, thus, do not expect the rotation of the particle to impose limitations on our ability to deliver the required spin rotation pulses.

However, since the body has a spatial extent in the direction of the magnetic field gradient and the rotation axis is not orthogonal to the magnetic field gradient, not all spins on the axis will have the same energy splitting. Notice that the rotation axis could be arranged to lie in the $y-z$ plane, therefore, giving all the spins on the axis the same x coordinate. However, this would not solve the problem, as any magnetic field exhibiting a gradient along the x direction would also have to exhibit a gradient along the y direction to satisfy the Maxwell equations. For a particle

with a radius 70 nm that sits in a magnetic field gradient of $B' = 5 \cdot 10^4$ T/m, a magnetic field variation from one end of the axis to the other of $\Delta B = 7 \cdot 10^{-4}$ T will occur, assuming that the rotation axis is fully contained in the $x - z$ plane. Thus, the energy splittings of the spins sitting on the axis are contained in a frequency band of width $\Delta\omega_{\text{particle}} = (2\pi)30$ kHz. As radio frequency pulses on hydrogen can achieve Rabi frequencies above 100 kHz$\gg \Delta\omega_{\text{particle}}$, composite pulse techniques (see e.g. Ref. [243, 244]) offer a potential path to compensate for detunings and Rabi frequency errors that are up to approximately half of the Rabi frequency.

During the protocol, the delocalisation of the centre-of-mass wavepacket will further broaden the resonance peak of the spin ensemble. In the modified protocol, the pulses are applied while the position state's width is given by Eq. (7.13). When neglecting the position variance of the initial state, the width is given by $\langle\Delta x\rangle \approx 2\chi\sqrt{N}$, where χ represents the spacing between the equilibrium positions around which the different trajectories oscillate, and is defined in Eq. (7.5). The frequency band associated with a given position width is $\Delta\omega_{\text{wp}} = \gamma_p\langle\Delta x\rangle B'$. As χ is inversely proportional to B', $\Delta\omega_{\text{wp}}$ is independent of the magnetic field gradient, and only depends on system constants and the size of the particle. In particular, one finds $\Delta\omega_{\text{wp}} = (2\pi)2r^{-3/2} \cdot 10^{-4}$. For a particle with $r = 45$ nm, the spectrum width is approximately $\Delta\omega_{\text{wp}} \approx 20$ MHz. We would like to point out that composite pulses alone will not suffice to compensate for such detunings. Other potential approaches might involve the use of chirped pulses, which can implement broadband rotations [245]. Modified schemes of the protocol that momentarily turn off the magnetic-field gradient during the duration of the pulses could also provide a viable means to efficiently apply the required spin rotations to the entire spin ensemble. While this aspect is crucial to the protocol, the detailed design of such pulses is considered beyond the scope of this work and will be presented elsewhere.

7.6 Possible Noise Sources

In this section, we analyse some of the most relevant sources of noise acting on the interferometer without being exhaustive. A more complete analysis will be required for concrete experimental setups.

Coherence Time of the Nuclear Spins

As already discussed, for the T_1 time of nuclear spins in naphthalene, with approximately 920 h at 25 K [32–36], and the short timescales of the proposed interferometry protocols (< 1 ms), even for the large number of nuclear spins in the considered nanoparticles, $N = 10^6 - 10^8$, the probability that at least one

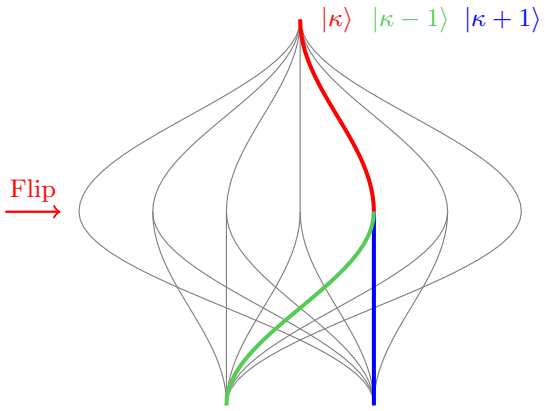


Figure 7.8: An example of the simplest case of the interferometric protocol without π pulses involves the trajectories recombining at the centre after a total time of $T_{\text{tot}} = 2\pi/\Omega$. If a T_1 flip occurs during the protocol, for all states except $\kappa = 0$ and $\kappa = N$, the κ^{th} Dicke state transitions into an incoherent superposition of $|\kappa+1\rangle$ and $|\kappa-1\rangle$. Consequently, the trajectories split into an incoherent superposition of two trajectories oscillating around the $\kappa+1^{\text{th}}$ and $\kappa-1^{\text{th}}$ equilibrium points, respectively. Thus, the trajectories will recombine at two different points. In phase space, the maximum distance between these two points is given by $|\Delta\zeta| = 4\chi/x_0$, as shown in Appendix A.7.

of the spins in the ensemble flips during the protocol is small. However, as in the proposed experiment with its rapid rotation, the T_1 time may turn out to be shortened somewhat and it is therefore pertinent to analyse the effect of stochastic spin flips on the performance of the protocol.

When a spin flips, it changes the equilibrium position around which each state of the spin ensemble is oscillating due to the presence of the magnetic field gradient. For a joint eigenstate of all the individual $\sigma_z^{(i)}$ operators, e.g. $|\uparrow\uparrow\downarrow\uparrow\cdots\rangle$, the equilibrium position will jump to the right or the left depending on whether the spin involved in the rotation undergoes a spin flip from $|\downarrow\rangle$ to $|\uparrow\rangle$ or the opposite. Since the trajectories of the interferometer are associated with Dicke states, and Dickes states are superpositions of spin states with the same number of spin up, we expect that all trajectories, except for $\kappa = 0$ and $\kappa = N$, will split into an incoherent superposition of two trajectories in the event of a spin flip. As a consequence, trajectories do not recombine in a single point, as would be the case in the noise-free scenario. Instead, two recombination points emerge, one to the left and one to the right of the original recombination point, such that half of the trajectories recombine on one of these points and half on the other. In Fig. 7.8, this process is depicted for a six-spin case. In Appendix A.7, an analytical derivation of this phenomenon is provided. For each additional spin flip, the number of

recombination points is doubled, such that if two spin flips occur then trajectories recombine in 4 different points, and so on. The result of this process is that at the end of the protocol spins and motion will not end up in a product state. This contributes to the loss of purity of the spin ensemble upon tracing the mechanical degrees of freedom, and is, therefore, not desirable.

While an exhaustive numerical simulation of this form of noise is unattainable for any realistic number of spins, it is useful to calculate the spatial spread of the recombination points to understand how much decoherence can be expected from such stochastic spin flips. If the recombination points are spread over a length scale that is below the zero-point motion of the nanoparticle, then one can expect the spin and motion to be almost separable, and the induced decoherence to be small. In general, the distance between the recombination points will depend on the parameters of the system and the instant at which the spin-flip occurs. For the protocol described in this work, the maximal distance between the two recombination points in dimensionless position space is given by

$$|\Delta\zeta| = \frac{4\chi}{x_0}, \tag{7.39}$$

corresponding to the case where the flip happens while the wave packet is maximally expanded. χ is the spacing between the spin-dependent equilibrium points around which the trajectories oscillate and is given in Eq. (7.5). For the parameters as in Table 7.2, χ/x_0 will be in the order of 0.1-1. Moreover, T_1 flips could be even more destructive if the flip happens in between the $\pi/2$ and $3\pi/2$ pulses in the modified protocol, as the fanned-out trajectories will not recombine in one point anymore. Although the full extent of decoherence induced by an individual spin flip is not accurately quantifiable at this point, we aim to operate in a regime where such flips are highly improbable.

Assuming that the spin-flips occur independently from each other, at a rate given by N/T_1, and follow a Poisson distribution, the probability that during an experimental run of duration T_{tot}, at least one spin flips is given by

$$P_{\text{flip}} = 1 - \exp\left\{-\frac{T_{\text{tot}}}{T_1} \cdot N\right\}. \tag{7.40}$$

With the parameters in Table 7.2 b), the run time of the protocol to test the CSL model is given by $T_{\text{tot}} = 78\,\text{ms}$. The total number of nuclear spins is $N = 1.5 \cdot 10^7$. We then find that the probability for at least one spin to flip is 30 %. By increasing the magnetic field gradient, the protocol can be conducted faster and this probability reduced. For the parameters in Table 7.2 a), T_{tot} is given by 7.8 ms, and the total number of spins is $1.5 \cdot 10^7$. For these values, the probability for one or more spin flips is reduced to 4 %. These values might be further reduced if the experiment is conducted with the bulk temperature of the naphthalene nanoparticle below 25 K, as required to avoid other forms of noise such as that

coming from black body radiation.

Regarding the T_2 time of the nuclear spins, we refer the reader to Section 6.2, where we describe the use of magic angle spinning. By rotating the particle sufficiently fast around an axis tilted by the magic angle with respect to the magnetic field, T_2 times of hundreds of milliseconds or even seconds can be achieved. For example, if the particle is rotating at a frequency of 23 MHz, a T_2 time of 1 s can be expected. To check to what extent T_2 processes can be tolerated, we describe them using the Lindblad equation

$$\hat{\rho} = -\frac{i}{\hbar}[\hat{H}, \hat{\rho}] + \frac{\Gamma}{2}\sum_{n=1}^{N}\left(\hat{\sigma}_z^{(n)}\hat{\rho}\hat{\sigma}_z^{(n)} - \hat{\rho}\right) \tag{7.41}$$

where $\Gamma = T_2^{-1}$. Since the Hamiltonian in Eq. (7.4) commutes with the Lindbladian, the two processes can be described independently. Pure dephasing can also be described using Kraus operators

$$\hat{M}_0 = e^{-\frac{\Gamma}{2}t}\mathbf{1}\,, \quad \hat{M}_1 = \sqrt{1-e^{\Gamma t}}\,\frac{\mathbf{1}+\hat{\sigma}_\mathbf{z}}{2}\,, \quad \hat{M}_2 = \sqrt{1-e^{\Gamma t}}\,\frac{\mathbf{1}-\hat{\sigma}_\mathbf{z}}{2}. \tag{7.42}$$

Pure dephasing of N spins can therefore be written as

$$\mathcal{S}[\hat{\rho}, t] = \sum_{i_1,\ldots,i_N=0}^{2} M_{i_1}\otimes\ldots\otimes M_{i_N}\hat{\rho}M_{i_1}^\dagger\otimes\ldots\otimes M_{i_N}^\dagger\,. \tag{7.43}$$

Bringing everything together, we find for the full-time evolution under Eq. (7.41)

$$\hat{\rho}(t+\Delta t) = \mathcal{M}_{\mathrm{dp}}[\hat{\rho}, \Delta t] = \hat{U}(\Delta t)\mathcal{S}[\hat{\rho}, \Delta t]\hat{U}^\dagger(\Delta t) \tag{7.44}$$

where $\hat{U}$ is given by $\exp\Big[-(i/\hbar)\,\hat{H}\,\Delta t\Big]$.

Nevertheless, the pulses do not commute with $S[\hat{\rho}, t]$. We will look at a minimal version of the protocol as in Fig. 7.4 for simplicity, where $t_1 = \pi/\Omega, 2t_{2,1} = 2\pi/\Omega$ and $t_{2,2} = 0$. Therefore, the full-time evolution of the protocol is given by

$$\begin{aligned}
&\hat{\rho}\left(\frac{\pi}{\Omega}\right) = \mathcal{M}_{\mathrm{dp}}\left[\hat{\rho}_0, \frac{\pi}{\Omega}\right]\,, \quad \hat{\rho}\left(\frac{3\pi}{\Omega}\right) = \mathcal{M}_{\mathrm{dp}}\left[U_{\pi/2}^{\otimes N}\hat{\rho}\left(\frac{\pi}{\Omega}\right)U_{\pi/2}^{\dagger\otimes N}, \frac{2\pi}{\Omega}\right]\,,\\
&\hat{\rho}\left(\frac{4\pi}{\Omega} = T_{\mathrm{tot}}\right) = \mathcal{M}_{\mathrm{dp}}\left[U_{3\pi/2}^{\otimes N}\hat{\rho}\left(\frac{3\pi}{\Omega}\right)U_{3\pi/2}^{\dagger\otimes N}, \frac{\pi}{\Omega}\right]\,,
\end{aligned} \tag{7.45}$$

where $\hat{\rho}_0$ is as in Eq. (7.6). The average magnetisation is then given by $\langle\hat{M}(T_{\mathrm{tot}})\rangle = \mathrm{tr}\{\hat{M}U_{\pi/2}^{\otimes N}\hat{\rho}(T_{\mathrm{tot}})U_{\pi/2}^{\dagger\otimes N}\}$. While we did not find an analytical expression for $\langle\hat{M}(T_{\mathrm{tot}})\rangle$,

we evaluated it explicitly for $N \in [2, 20]$. In all cases, we found

$$\frac{\langle \hat{M}(T_{\mathrm{tot}})\rangle}{\langle \hat{M}(0)\rangle} = \frac{1}{2}\Big(e^{-4\Gamma T_{\mathrm{tot}}} - e^{-4\Gamma T_{\mathrm{tot}} - 64\left(\frac{1}{2}+\bar{n}\right)\left(\frac{\chi}{x_0}\right)^2} + e^{-2\Gamma T_{\mathrm{tot}}} + e^{-2\Gamma T_{\mathrm{tot}} - 64\left(\frac{1}{2}+\bar{n}\right)\left(\frac{\chi}{x_0}\right)^2}\Big), \tag{7.46}$$

where $\bar{n}$ is the mean occupation number of the initial thermal position state. For our choice of parameters, χ/x_0 is on the order of one. Also, in general, $\bar{n}$ can be very large, so we assume $(1/2 + \bar{n})(\chi/x_0)^2 \gg 1$. Under this assumption, $\langle \hat{M}(T_{\mathrm{tot}})\rangle/\langle \hat{M}(0)\rangle$ becomes

$$\frac{\langle \hat{M}(T_{\mathrm{tot}})\rangle}{\langle \hat{M}(0)\rangle} = \frac{1}{2}\left(e^{-4\Gamma T_{\mathrm{tot}}} + e^{-2\Gamma T_{\mathrm{tot}}}\right) \tag{7.47}$$

which also constitutes a lower bound on $\langle \hat{M}(T_{\mathrm{tot}})\rangle/\langle \hat{M}(0)\rangle$. For $T_{\mathrm{tot}} = 1\,\mathrm{ms}$ and $\Gamma^{-1} = T_2 = 1\,\mathrm{s}$, we find $\langle \hat{M}(T_{\mathrm{tot}})\rangle/\langle \hat{M}(0)\rangle \approx 0.997$.

Collisions with Air Molecules

Since no experiment can be conducted in a perfect vacuum, there will always be some gas molecules that might collide with the nanoparticle. For a spherical particle in an ideal gas containing gas particles of mass m_g, temperature T_g, and pressure P, the collision frequency is given by

$$\gamma_g = \frac{8\pi P r^2}{m_g \overline{v}_g}, \tag{7.48}$$

where $\overline{v}_g = \sqrt{8 k_{\mathrm{B}} T_g/(\pi m_g)}$ is the mean velocity of the gas molecules. We assume cryogenic temperatures of $T_g = 4\,\mathrm{K}$ and a gas composition that is mainly dominated by H_2 molecules with $m_g = 2\,\mathrm{a.m.u.}$ We are interested in the probability of finding no collision, as, in general, a single collision would be enough to destroy the visibility of the interferometer. For $P = 5 \cdot 10^{-11}\,\mathrm{P}$ and the parameters as in Table 7.2 b), the probability of having no collisions with air molecules is $\exp(-\gamma_g T_{\mathrm{tot}}/3) \approx 0.91$. For the parameter set as in Table 7.2 a) and c), a pressure of $P = 5 \cdot 10^{-10}$ Pa suffices to ensure, that the probability of no collisions happening are higher than 90 %. Notice that gas pressures as low as 10^{-16} Pa have been demonstrated [246]. Therefore, the conditions to guarantee no collisions with air molecules, while demanding, are, in principle, achievable.

Black Body Radiation

Another possible noise source is induced by thermal photons that are either scattered or emitted by the nanoparticle. Just as the noise induced by the CSL model, the noise due to black body radiation is well described by a master equation of the form [131]

$$\begin{aligned}\dot{\rho}(q',q'') = &-\frac{i}{\hbar}\langle q'|\,[\hat{H},\hat{\rho}]\,|q''\rangle \\ &-\xi_{bb}\left(1-e^{-\frac{(q'-q'')^2}{4r_{\mathrm{bb}}^2}}\rho(q',q'')\right).\end{aligned} \tag{7.49}$$

Here, r_{bb} is called the localisation distance, and ξ_{bb} represents the localisation strength. Both parameters depend on the specific decoherence process. The localisation distance of thermal photons is related to the thermal wavelength by $r_{\mathrm{bb}} = \lambda_{\mathrm{th}}/2$ [132]. Therefore, for thermal photons, we find $r_{\mathrm{bb}} = \pi^{2/3}\hbar c(2k_B T_{b/e})$, where $T_{b/e}$ is the temperature of the bulk and environment, respectively. For scattered photons, the localisation strength is given by [131, 132]

$$\frac{\xi_{\mathrm{bb,sc}}}{4r_{\mathrm{bb}}^2} = \frac{8!\ 8\zeta(9)c\ r^6}{9\pi}\left(\frac{k_B T_e}{\hbar c}\right)^9 \mathrm{Re}\left[\frac{\epsilon-1}{\epsilon+2}\right]^2. \tag{7.50}$$

Here, $\zeta(x)$ is the Riemann function. For the absorption and emission of thermal photons, the localisation strength is given by

$$\frac{\xi_{\mathrm{bb,em/ab}}}{4r_{\mathrm{bb}}^2} = \frac{16\pi^5 c\ r^3}{189}\left(\frac{k_B T_{b/e}}{\hbar c}\right)^6 \mathrm{Im}\left[\frac{\epsilon-1}{\epsilon+2}\right]. \tag{7.51}$$

Here, ϵ is the dielectric constant of naphthalene in the spectrum range of the thermal photons. Due to the lack of available data, we assumed a conservative value of $\epsilon = 1.1 + 0.15i$. For $r_{\mathrm{bb}} \gg (q'-q'')$, the noise term approaches $\xi_{\mathrm{bb,sc}}(q'-q'')^2/(4r_{\mathrm{bb}}^2)$, while for $r_{\mathrm{bb}} \ll (q'-q'')$, it saturates to $\xi_{\mathrm{bb,sc}}$. In any case, both limits are upper bounds for all q', q''. At 4 K, we find $r_{\mathrm{bb}} \approx 0.5\,\mathrm{mm}$ which, in general, is neither significantly larger nor smaller than the delocalisation of the particle in our interferometric protocol. Nonetheless, we will consider $\xi_{\mathrm{bb,sc}}$ as an upper bound for this analysis. To ensure that the noise induced by possible spontaneous collapses is greater than the noise induced by interactions with thermal photons, one must ensure $\xi_{\mathrm{bb}} = \xi_{\mathrm{bb,sc}} + \xi_{\mathrm{bb,em}} + \xi_{\mathrm{bb,ab}} < \xi$, where ξ is the localisation strength of the CSL model as in Eq. (7.18). For a particle of $r = 100\,\mathrm{nm}$ and at cryogenic temperatures, the noise due to emission and absorption dominates over the noise induced by the scattering of thermal photons, as one can easily convince oneself. Thus, it is justified to only ensure that $\xi_{\mathrm{bb,em}} + \xi_{\mathrm{bb,ab}} = 2\xi_{\mathrm{bb,em/ab}} < \xi$. In Table 7.2, the maximum internal or bulk temperature that can be tolerated to ensure $\xi_{\mathrm{bb}} < \xi$ for different parameters is shown. Note, that ξ_{bb} already represents

an upper limit for the noise induced by thermal photons; hence, it may be possible to tolerate slightly higher temperatures.

8 Test of the Nuclear Einstein-de Haas and Barnett Effect

Having introduced the Einstein-de Haas and Barnett effects in Section 3.3, the properties of hyperpolarised naphthalene in Chapter 4 and its behaviour under diamagnetic levitation in Chapter 6, we now combine these ingredients to propose a test of the nuclear analogue of the Einstein-de Haas effect with a levitated, hyperpolarised naphthalene particle. Whereas the classic effect relies on electronic magnetic moments, here the angular momentum reservoir is instead formed by a hyperpolarised nuclear spin ensemble. This chapter develops the theoretical description of this proposal: we specify the trapping and field configuration, derive the resulting particle rotation from angular momentum conservation, and estimate the achievable angular velocity for realistic particle sizes and polarisations. We then discuss a variety of noise sources and experimental constraints and outline the conditions under which the effect could be observed.

The second proposal addresses the nuclear Barnett effect, the inverse process by which mechanical rotation of the particle induces a nuclear magnetisation. We show how the resulting magnetisation can be read out via the spin-motion coupling protocol of [1], in which a magnetic-field gradient converts the nuclear polarisation into a measurable centre-of-mass oscillation. Since hyperpolarisation is not required for this measurement, we further comment on the suitability of alternative levitated materials such as diamond and silica.

8.1 The Einstein-de Haas Effect

To probe the nuclear Einstein-de Haas effect, we consider a hyperpolarised naphthalene particle diamagnetically levitated in a quadrupole magnetic field $\mathbf{B} = \big(B'_x x, B'_y y, B'_z z + B_0\big)$, where Maxwell's equations require $\nabla \cdot \mathbf{B} = 0$. The offset field B_0 is chosen such that the diamagnetic force balances gravity, $B_0 \partial B/\partial z = \mu_0 g \rho/(\chi_V)$, where ρ is the mass density, χ_V is the volume susceptibility, g is the gravitational acceleration and μ_0 is the vacuum permeability.

For naphthalene ($\chi_V \approx 10^{-5}$, $\rho = 1145\,\mathrm{kg/m^3}$), this yields $B_0 B'_z = 1411\,\mathrm{T^2/m}$. For the particle sizes and field gradients considered below, this implies $B_0 \gg B'_x x, B'_y y, B'_z z$ throughout the particle volume. The magnetic field experienced by the nuclei is therefore essentially set by the offset field at a magnitude of order 1 T. Moreover, the dipolar coupling between hydrogen nuclear spins in naphthalene is

only in the kHz-range [1], while even mT-scale offset fields yield Larmor frequencies exceeding $100 \cdot (2\pi)$ kHz. Hence, the Zeeman interaction dominates the nuclear spin Hamiltonian and defines the quantisation axis along which the hyperpolarised spins align.

When the hyperpolarisation is allowed to relax on the spin-lattice relaxation timescale, T_1, the nuclear spin angular momentum changes. In the absence of appreciable external torques, conservation of angular momentum requires a compensating transfer to mechanical degrees of freedom. This transfer eventually produces rigid-body rotation of the particle, in direct analogy with the electronic Einstein-de Haas effect. The rotation of the levitated birefringent particle could be detected via polarisation analysis of a probe beam transmitted through or scattered by the particle. A birefringent particle acts as a rotating wave retarder, continuously modulating the polarisation state of a probe beam. After a polarising beam splitter, a balanced detector records a signal oscillating at twice the mechanical rotation frequency [95, 211, 247, 248]. Alternatively, scattered light collected off-axis carries the same intensity modulation due to the orientation-dependent scattering cross-section, and can be detected with a single photodetector behind a fixed polariser [249].

The experimental sequence proceeds as follows: (i) Hyperpolarise the proton ensemble. (ii) Move the particle to a chosen B_0 where T_1 is short enough to permit relaxation within a practical timescale. (iii) Record the initial angular velocity of the particle prior to spin relaxation to determine the thermal baseline present at the start of that run. (iv) Allow the spin polarisation to relax on the spin-lattice relaxation timescale T_1. (v) Detect the resulting change in angular velocity of the particle.

In the following, we examine several details and intricacies of this proposal. For a given T_1 time, the angular momentum of the nuclear spins decays as $S(t) = S(0)\,\exp(-t/T_1)$, and, in the absence of coupling to the environment, the angular momentum of the nanoparticle increases at the same rate,

$$L(t) = L(0) + S(0)\left(1 - e^{-\frac{t}{T_1}}\right). \tag{8.1}$$

This corresponds to a time-dependent torque

$$\tau = \mathrm{d}L/\mathrm{d}t = \frac{S(0)}{T_1} e^{-t/T_1}. \tag{8.2}$$

The spin-lattice relaxation time T_1 decreases with decreasing magnetic fields [250]. This could be achieved by charging the particle and moving it in space to a low-field regime by applying a constant electric field along z. The required charges and electric fields are analysed in Appendix B.3 to be $\sim 300\,\mathrm{V/m}$ for a sphere of 100 nm radius carrying one elementary charge. We envisage that the electric field

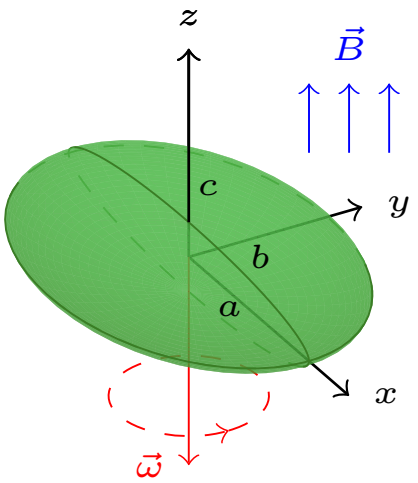


Figure 8.1: The naphthalene particle is modelled as an ellipsoid with major and minor semi-axes a and b, where the short semi-axis is aligned with the constant magnetic field B_0. Due to the finite T_1 relaxation time of the nuclear spins, the particle begins to rotate about the field axis, transferring the lost nuclear spin angular momentum into rigid-body rotation.

is applied parallel to the z axis, which coincides with the rotation axis, to ensure that it does not constrain the particle's azimuthal rotation. From Fig. 3 of [250], T_1 at 77 K begins to drop below ∼10 mT. Extrapolating this field dependence, which follows approximately $T_1 \propto B_0^2$ consistent with librational relaxation in the slow-motion regime [251], to 1 mT yields $T_1 \approx 5$ min at 77 K. Since the particle in our proposal operates at ∼100 K, T_1 will be shorter than this estimate. Crucially, at 1 mT the proton Larmor frequency is $\omega_L/(2\pi) = \gamma_H B_0/(2\pi) \approx 42.6$ kHz, still well above the inter-spin dipolar coupling of $\sim 1 - 10$ kHz in naphthalene [1], so the Zeeman interaction continues to dominate and non-secular processes remain suppressed.

The particle's angular velocity depends sensitively on its geometry. Although the shape of micrometre-sized naphthalene particles is not well characterised, larger crystals tend to form flakes. We therefore model the particle as an ellipsoid with semi-axes $c < a, b$. The resulting angular velocity follows from $\mathbf{S} = I\boldsymbol{\omega}$, where the inertia tensor of an ellipsoid of mass m is $\mathbf{I} = \frac{m}{5}\mathrm{diag}\,(b^2 + c^2, a^2 + c^2, a^2 + b^2)$. The angular velocity therefore depends on the particle orientation within the trap.

This orientation is determined by the anisotropic magnetic susceptibility, which aligns the axis with the largest (least negative) susceptibility along the magnetic field direction to minimise the magnetic energy as shown in Appendix B.3. For naphthalene, $\boldsymbol{\chi}_V = -\mathrm{diag}(17.8, 7.9, 4.4)\cdot 10^{-6}$ [209]. The susceptibility and inertia

principal axes need not coincide, while shape-induced corrections to the susceptibility can be neglected as discussed Appendix B.3. For a conservative estimate, we assume rotation about the axis of maximum moment of inertia, which minimises ω. For $c < a, b$, this corresponds to the orientation shown in Fig. 8.1.

For an initially polarised spin ensemble, the nuclear spins carry an angular momentum $S(0) = N\hbar p/2$, where p is the polarisation fraction and $N = \rho_N V$ is the number of spins. Here, $\rho_N = 4.2 \cdot 10^{28}\mathrm{m}^{-3}$ is the hydrogen spin density and $V = 4\pi abc/3$ is the ellipsoid volume. Although polarisations of up to 80 % have been demonstrated [37], we conservatively assume $p = 10\,\%$.

As the nuclear spins relax, their angular momentum is transferred to the rotational motion of the crystal, yielding a final angular velocity

$$\omega = \frac{S(0)}{I_z} = \frac{9.9 \cdot 10^{-9} p}{a^2 + b^2}. \tag{8.3}$$

For semi-axes $a = 150\,\mathrm{nm}$ and $b = 100\,\mathrm{nm}$, this gives $\omega \approx 4.8 \cdot (2\pi)\,\mathrm{kHz}$.

Possible Noise Sources

Several effects can obscure the mechanical rotation induced by the nuclear Einstein-de Haas effect. First, residual gas pressure gives rise to rotational friction. In the low-Mach-number regime relevant here, the drag torque is linear in the angular velocity and in the background gas pressure. It therefore reduces the final rotation speed if the spin relaxation time is long compared to the damping time. However, already at moderate vacuum pressures, the damping rate becomes sufficiently small that gas friction does not fundamentally limit the observation as shown in Appendix B.1. The expected angular velocity for a given size and environmental pressure is given in Fig. 4.

Second, the rotational degree of freedom may be confined by anisotropies of the particle or of the trapping fields. Such confinement can arise from the anisotropic magnetic susceptibility of naphthalene in an asymmetric quadrupole field, or from residual electric fields acting on a charged or polarisable particle. The Einstein-de Haas signal can be observed provided the angular momentum transfer occurs faster than the restoring torque can trap the particle, and provided the rotational energy gained from the spin ensemble exceeds the confinement barrier. These conditions are most favourable for small particles, short nuclear relaxation times and trapping fields of the form $B'_x = B'_y = -B'_z/2$.

Unwanted coupling to other rotational axes might arise when the particle does not rotate about its major or minor principal axis of the moment of inertia, that is, when an intermediate axis becomes aligned with the z-axis. This misalignment can occur for two reasons: first, the principal axes of the particle's body do not necessarily coincide with those of its magnetic susceptibility or dielectric tensor,

which governs the particle's orientation in the trap. Second, if a surface charge is used to translate the particle into a region of low magnetic field by applying an electric field, an off-centre charge distribution can exert a torque that rotates the particle to a new equilibrium orientation within the trap. Rotation about the intermediate principal axis represents the more unfavourable case, and in Appendix B.3 it is shown that this scenario can cause the rotation axis to flip due to the tennis racket effect. Concrete bounds on the experimental parameters are derived there. To avoid these effects, either spherical particles or particles prepared such that the first or third principal axis is aligned with the rotation axis should be used. If an electronic surface charge causes the particle to settle into an unfavourable equilibrium orientation, the particle can be discharged and recharged until it settles into a more suitable one [252].

Finally, the finite temperature of the nanoparticle leads to a statistical uncertainty in its initial rotational state. If the particle is in thermal equilibrium, an upper bound for this uncertainty is given by the Boltzmann distribution. As shown in Appendix B.4, the ratio between the statistical uncertainty $\Delta\omega\sqrt{k_B T/I}$ and the maximum angular velocity $\omega = S/I$ the particle can acquire via the Einstein-de Haas effect is given by $\omega/\Delta\omega \approx 58400 \cdot p\sqrt{r/T}$. For a $r = 100\,\mathrm{nm}$ sphere with $10\,\%$ nuclear spin polarisation and at $100\,\mathrm{K}$, it is approximately 0.2. One could boost the signal by using a larger particle, cooling the environment, or cooling the rotational degrees of freedom. Note that the competing preference for small particles to mitigate azimuthal confinement and for large particles to overcome the statistical uncertainty $\Delta\omega > \omega$ can be met simultaneously over a wide range of parameters, since short nuclear relaxation times T_1 allow larger particles to escape azimuthal confinement. The optimal parameters heavily depend on the details of the experiment. In any case, $\Delta\omega > \omega$ does not fundamentally prevent the effect from being observed but does increase the number of measurement runs that are required to resolve the rotation.

Furthermore, the flip of a nucleus might induce a torque due to the interaction with the gradient of the trapping magnetic field. As we show in Appendix B.5, under typical conditions these torques do not contribute to the rotation of the particle on average, but may increase the statistical rotational uncertainty. However, this effect does not impose a constraint for the parameters considered in this work. In Appendix B.5, we give a conservative upper bound on r to ensure that the rotational energy gained by the Einstein-de Haas effect is larger than the spread introduced by the mechanical back action with B.

8.2 Test of the Nuclear Barnett Effect

A rotating ferromagnetic object at frequency $\boldsymbol{\omega}_r$, in the absence of a magnetic field, produces the same magnetisation as when the object is subjected to a magnetic field $\mathbf{B}_{\mathrm{bar}} = \boldsymbol{\omega}_r/\gamma$, where γ is the gyromagnetic ratio. In levitated setups, materials

can be spun until they can no longer withstand the induced lattice strain. This capability makes it natural to consider whether this platform is suitable for testing the nuclear Barnett effect in solids.

In thermal equilibrium, the total magnetic moment of a nuclear spin ensemble follows from the Boltzmann distribution,

$$M = N m_0 \tanh\left(\frac{\hbar \gamma_p B}{2 k_\mathrm{B} T}\right), \tag{8.4}$$

where $m_0 = \hbar\gamma_p/2$ is the magnetisation of a fully polarised spin and $\Delta E = \hbar\gamma_p B$ is the Zeeman splitting. This expression follows from the thermal occupation ratio $P_\uparrow/P_\downarrow = \exp(-\Delta E/k_\mathrm{B}T)$.

As before, we approximate the magnetic field as $\mathbf{B}_0 \approx B_0 \mathbf{e}_z$. Rotating with angular velocity $\boldsymbol{\omega}_r = \omega_r \mathbf{e}_z$, the thermal magnetisation is

$$M = N m_0 \tanh\left[\frac{\hbar(\gamma_p B_0 + \omega_r)}{2 k_\mathrm{B} T}\right]. \tag{8.5}$$

This configuration may be realised by exploiting the particle's strong birefringence to optically rotate it: the laser propagation direction is aligned with $\mathbf{e}_z$, which also determines the particle's rotation axis.

To verify that the enhanced magnetisation originates from the nuclear Barnett effect, the spin polarisation must be measured independently. We employ the spin-readout protocol proposed in [1], in which a magnetic-field gradient couples the particle's centre-of-mass motion to its collective nuclear spin. A π pulse displaces the equilibrium position of the particle in the magnetic trapping potential and induces mechanical oscillations whose amplitude is proportional to $\langle\hat{\Sigma}_z\rangle = \langle\Sigma_{n=1}^{N} \hat{\sigma}_z^{(n)}\rangle$, namely

$$\langle\hat{X}\rangle(t) = \langle\hat{X}\rangle(0) + \frac{4\lambda}{\Omega}\langle\hat{\Sigma}_z\rangle \sin^2(\Omega t/2), \tag{8.6}$$

allowing the nuclear magnetisation $M = m_0\langle\hat{\Sigma}_z\rangle$ to be inferred directly from the particle's motion. Here, $\Omega = \sqrt{|\chi_V|/(\mu_0\rho)}B'$ is the trap frequency and $\lambda = \gamma_p B' x_0$ is the coupling between the magnetic moment of the spin and the centre-of-mass motion.

To ensure that the nuclear spins remain inverted throughout the measurement, the magnetic field must be sufficiently large that $T_1 \gg \Omega^{-1}$. For a 100 nm naphthalene sphere in a field gradient of $B' = 10^3\,\mathrm{T/m}$, the mechanical oscillation frequency is $\Omega = 8.8 \cdot (2\pi)\,\mathrm{Hz}$, assuming motion along the axis with the smallest diamagnetic response, $\chi_V = -4.4 \times 10^{-6}$. According to [250], a field of $B_0 = 100\,\mathrm{mT}$ at room temperature yields a T_1 time of several minutes, while at 77 K a field of only $\sim 10\,\mathrm{mT}$ is sufficient to achieve T_1 times of hundreds of minutes.

As shown in Appendix B.7, the net magnetisation in a quadrupole trap generally depends on both the particle shape and its orientation within the trap. However, for moderate temperatures, ellipsoidal particles and magnetic fields satisfying

$$\frac{\hbar(\gamma_p B_0 + \omega_r)}{2k_\mathrm{B}T} \ll 1, \tag{8.7}$$

the total magnetic moment can be linearised, yielding

$$\mathbf{M} = N m_0 \frac{\hbar}{2k_\mathrm{B}T} \left(\gamma_p \mathbf{B}_0 + \boldsymbol{\omega}_r\right). \tag{8.8}$$

Taking both $\mathbf{B}_0$ and $\boldsymbol{\omega}_r$ along the z axis, the oscillation amplitude induced by the spin-readout protocol of [1] becomes

$$x_\mathrm{amp}(\omega_r) = N x_0 \frac{2\lambda}{\Omega} \frac{\hbar(\gamma_p B_0 + \omega_r)}{k_\mathrm{B}T}. \tag{8.9}$$

Note that the B_0-dependent contribution can be eliminated by a differential measurement: subtracting the oscillation amplitude measured at rest ($\omega_r = 0$) from that measured during rotation yields

$$x_\mathrm{amp}(\omega_r) - x_\mathrm{amp}(0) = N x_0 \frac{2\lambda}{\Omega} \frac{\hbar\omega_r}{k_\mathrm{B}T}, \tag{8.10}$$

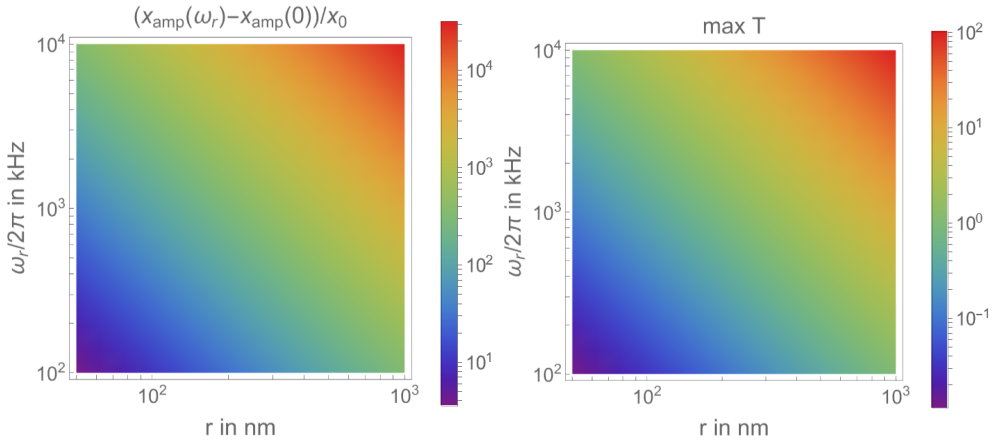
which depends only on the rotation frequency ω_r and is independent of B_0. This quantity is shown in units of x_0 in Fig. 8.2a.

Once the centre-of-mass motion and optical readout noise are sufficiently suppressed, the remaining intrinsic limit is spin-projection noise. For an ensemble of N weakly polarised spin-1/2 nuclei, the equilibrium fluctuation in $\hat{\Sigma}_z$ is $\delta\Sigma_z = \sqrt{N}/2$, which produces a mechanical noise floor $x_\mathrm{noise} = 2\lambda\sqrt{N}/\Omega$.

The Barnett-induced signal scales as Np_B, where $p_B = \hbar\omega_r/(2k_\mathrm{B}T)$ is the single-spin Barnett polarisation, giving a single-shot signal-to-noise ratio (SNR) $\mathrm{SNR} = \sqrt{N}\, p_B$. One hence needs $n_\mathrm{avg} = (Np_B^2)^{-1}$ repetitions to reach an SNR of 1. In Fig. 8.2b, the maximal bulk temperature T to ensure $n_\mathrm{avg} < 1$ for different values of r and ω_r is shown.

The centre-of-mass oscillations induced by the spin-readout protocol are detectable optically: the scattered light from the levitated particle provides a position signal which is used to resolve sub-μm length scales [253].

For the Barnett-induced displacement to be resolvable, the oscillation amplitude $x_\mathrm{amp}(\omega_r) - x_\mathrm{amp}(0)$ must exceed the thermal width of the centre-of-mass wave packet. In thermal equilibrium, this width is $\Delta x_\mathrm{th} = x_0\sqrt{2k_\mathrm{B}T/(\hbar\Omega)} = [2.2 \cdot 10^6\, \sqrt{\mathrm{T/(mK)}}] \cdot \sqrt{T/B'}x_0 \approx 6.9 \cdot 10^5 x_0$ at $T = 100\,\mathrm{K}$ and $B' = 10^3\,\mathrm{T/m}$. Hence, a moderate pre-cooling of the particle's centre-of-mass motion is necessary.



(a) (b)

Figure 8.2: In (a), the difference in oscillation amplitude for a rotating naphthalene nanosphere is shown as a function of its radius and rotation frequency, in units of x_0, for $T = 100\,\mathrm{K}$ and $B' = 10^3\,\mathrm{T/m}$. In (b), the maximal bulk temperature T to ensure $n_{\mathrm{avg}} < 1$ is shown. To prevent the particle from breaking due to rotational strain, the condition $\omega_{\mathrm{r}} < \omega_{\mathrm{max}} = \sqrt{\sigma_{\mathrm{UTS}}/(r^2\rho)}$ must be satisfied, where $\sigma_{\mathrm{UTS}} = 49\,\mathrm{MPa}$ is the ultimate tensile strength. For the parameter regime considered, this condition is fulfilled.

As hyperpolarisation is not required for observing the Barnett effect, other levitated materials, such as diamond and silica, may also be suitable candidates, as discussed in Appendix B.9.

Part III

Stability Thresholds for Gravitationally Induced Entanglement in Shielded Setups

9 Introduction

Having established the theoretical foundations and experimental landscape of gravitationally induced entanglement (GIE) in Section 3.2, here attention turns to a quantitative analysis of the practical obstacles that any levitated nanoparticle implementation must overcome.

Recall that the central idea behind GIE experiments is to prepare two massive particles in spatially delocalised quantum states and to observe entanglement generated solely through their gravitational interaction. As argued in Chapter 3.2, such an observation would imply that the gravitational field cannot be described by local operations and classical communication (LOCC) alone [54, 55]. Levitated nanoparticles are a particularly promising platform for this purpose, combining excellent environmental isolation with precise control over motional quantum states, both essential given the extreme weakness of the gravitational coupling at laboratory scales. A central practical challenge, however, is that the same micrometer-scale separations required to make the gravitational interaction measurable also expose the particles to short-range electromagnetic forces, electrostatic, magnetostatic and Casimir, that can easily dominate over gravity. The standard remedy is to place a thin conducting or superconducting shield between the particles, suppressing electromagnetic cross-talk while leaving gravity unaffected [64, 79, 80]. This introduces a new set of complications. Casimir and magnetic-dipole forces between each particle and the shield shift the particle's equilibrium position and imprint a local phase on each component of its spatial superposition, since different parts of the wavefunction experience different particle-shield separations. Unavoidable run-to-run fluctuations in particle positions, shield placement and measurement device alignment then translate into shot-to-shot phase variations that, when averaged over many experimental repetitions, manifest as dephasing and degrade the GIE.

This chapter provides a quantitative analysis of these effects for levitated nanoparticle implementations. Stochastic forces acting on the setup are modelled and bounds on the tolerable fluctuations in the relative positioning of the trapping potentials, the shield and the detectors are derived. Both Casimir and magnetic-dipole interactions between the particles and the shield are treated, for both squeezed Gaussian states and Schrödinger-cat states. Noise arising from the quantised vibrational modes of the shield is further analysed, and the spurious, non-gravitational entanglement the shield can mediate is bounded. Although the analysis is tailored to the levitated nanoparticle platform, the results are in principle transferable to a broader class of implementations, including free-fall and

space-based proposals.

The chapter is organised as follows. Chapter 10 describes the class of setups considered and characterises the relevant interactions between the particles and the shield and between the particles themselves. Chapter 11 examines run-to-run positional and orientational fluctuations and quantifies how they suppress achievable GIE, deriving bounds on tolerable fluctuations for both state families. Chapter 12 analyses trapping-potential fluctuations, which induce noise even in the absence of particle-shield interactions, and determines the corresponding stability thresholds. Chapter 13 treats the shield as a quantum mechanical object, quantifies the resulting noise as a function of its temperature and geometry, and bounds the entanglement it can mediate. Finally, Chapter 14 summarises the experimental implications.

This part of the thesis is in large parts based on [2], published under the CC BY 4.0 license.

10 The Setup

In this analysis, we consider an idealized model of the GIE experiment, abstracting away implementation-specific details. The schematics are presented in Fig. 10.1(a). The setup consists of two spherical particles, labeled A and B, which are separated by a fixed centre-to-centre distance $2L$. We introduce a local coordinate system $(x, y, z)_{A/B}$ for each particle and denote the laboratory frame by the primed coordinates (x', y', z'). After letting the particles interact gravitationally, their state is read-out by two detectors. In order to suppress non-gravitational interactions, a circular shield of radius r_s and thickness d_s is placed symmetrically midway between the particles, with its surface lying in the $y'z'$-plane.

We consider both, silica and superconducting lead particles with a radius of $R = 10\mu$m, corresponding to masses in the range $M \approx 1 \times 10^{-11}$kg to 5×10^{-11}kg. Superconducting lead particles, which are strongly diamagnetic and typically magnetically levitated, serve as a representative example of regimes in which particle–shield interactions are dominated by induced magnetic dipole moments. In contrast, in the absence of magnetic trapping, e.g., in free-falling or space-based implementations, weakly diamagnetic silica particles serve as a representative example of regimes in which particle–shield interactions are dominated by Casimir forces.

Table 10.1: **Set of parameters** We consider silica particles ($\rho_{\mathrm{SiO_2}} = 2650\mathrm{kg/m^3}$) in free-fall and space-based implementations and superconducting lead particles ($\rho_{\mathrm{Pb}} = 11340\mathrm{kg/m^3}$) levitated magnetically (with a static trapping field $B_{\mathrm{trap}} = 250\mu$T). Both particles are chosen to have a radius of $R = 10\mu$m for better comparability, as the relevant interactions Eq. (10.1) and Eq. (10.2) depend on the radius. In principle, Silica particles could also be magnetically levitated with a static trapping field or $B_{\mathrm{trap}} \simeq 20$mT.

Particle properties				
Material	Mass M / kg	ε_r	χ_V	Dominant interaction
Silica (SiO_2)	1.11×10^{-11}	3.9	-1.4×10^{-5}	Casimir forces
Lead (Pb)	4.75×10^{-11}	∞	-1	Induced magnetic dipoles
Experimental parameters			**Shield properties**	
L	Δx	Δy	Radius r_s	Thickness d_s
$20\,\mu$m	50 nm	10^{-3} nm	1 cm	$2\,\mu$m

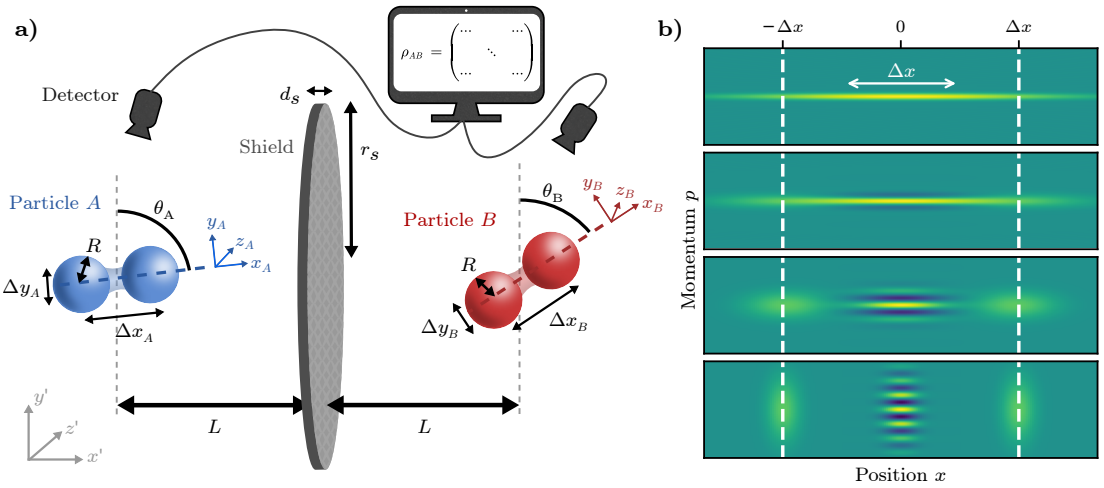


Figure 10.1: **Setup and initial states. a,** Schematic illustration of an idealized setup for gravitationally induced entanglement (GIE) experiments considered in this work. Two particles A and B of radius R are prepared in spatially delocalized quantum states and positioned at a fixed centre-to-centre separation $2L$. A circular shield of thickness d_s and radius r_s is placed midway between the particles to suppress unwanted electromagnetic crosstalk while preserving the gravitational coupling. The angles $\theta_{A/B}$ indicate the orientation of each particle's principal delocalization axis (here without loss of generality the x-direction) and the shield. Two detectors measure the state of the particles after a gravitational interaction. **b,** Wigner phase-space representation of the family of delocalized states with fixed standard deviation Δx used in this work, ranging from squeezed Gaussian states **(top)** to symmetric superpositions of two displaced squeezed states **(bottom)**, illustrating the continuous interpolation up to idealized orthonormal cat-states representable in a truncated 2-dimensional Hilbert space.

The particles are prepared in spatially delocalized pure quantum states of their centre-of-mass motion. We consider squeezed Gaussian states and Schrödinger-cat-like superpositions, characterized by position uncertainties $\Delta x_{A/B}$ and $\Delta y_{A/B}$ defined along the axes of each particle's local coordinate frame. Without loss of generality, we take $\Delta x \gg \Delta y$, thereby identifying the local x axis as the principal delocalization direction. In the lab frame, the orientation of the initial state is parameterized by a single angle $\theta_{A/B} \in [0, \pi)$, corresponding to rotations of the state about the z-axis. The delocalization direction is thus confined to the $x'y'$-plane, while any z'-component is neglected. This restriction is well justified in the regime $\Delta z \lesssim \Delta y \ll \Delta x$. Moreover, displacements along the z-axis parallel to the shield do not significantly affect the relevant geometries, provided that $\Delta z \ll r_s$ and the particles remain sufficiently far from the shield boundaries.

A fully general treatment with arbitrary spatial spreads and orientations would require the inclusion of all three Euler angles. However, such an extension does not provide additional physical insight in the regime of interest and is therefore not pursued.

For electrostatic and Casimir screening, a conducting Faraday shield is used, which may be fabricated from copper [80], gold-coated substrates [254] or graphene [255]. On the other hand, magnetic interactions require superconducting Meissner shielding, for example based on superconducting type-II Niobium.

Since all relevant interactions differ fundamentally in range and strength, the required shield dimensions depend on the dominant interaction, as discussed in detail in the subsequent sections. In practice, however, the minimum shield thickness is set by mechanical rigidity and fabrication constraints, which impose a larger thickness than that required by the shielding performance. In the following, we assume a thickness of $d_s = 2\mu$m, which is sufficient to shield all undesired electromagnetic interactions.

We focus on two geometries commonly discussed in GIE proposals: In the *parallel configuration* ($\theta_{A/B} = 0$), the principal delocalization axes of the two particles are parallel to each other and to the shield surface. In the *linear orientation* ($\theta_{A/B} = \pi/2$), the delocalization axes of both particles coincide, forming a single line perpendicular to the shield. As discussed later, the choice between these configurations has important consequences for the robustness of entanglement generation in presence of shield-induced noise.

10.1 Casimir interactions

At surface-to-surface separations below a few hundred micrometers, short-range Casimir forces [256] constitute an important source of non-gravitational interactions between the particles. Neglecting finite-frequency penetration of electromagnetic fields into the material, mutual particle–particle interactions can be efficiently suppressed by inserting a conductive Faraday shield of radius $r_s \gtrsim 50\mu$m and thickness $d_s \gtrsim 0.3 \times$nm, as estimated in Appendix C.1 and summarized in Table 1. In practice, however, the finite optical skin depth imposes a more stringent lower bound on the thickness of around $d_s \approx 20$nm [257].

Casimir interactions between each particle and the shield must nevertheless be taken into account. Closed-form expressions for this potential in the sphere-plane geometry are not available for arbitrary separations. Analytic results exist only in the limiting cases of short and large separations, corresponding to the proximity-force approximation (PFA) valid for small surface-to-surface separations $L - R \ll R$, and the large-separation limit (LSL), valid in the opposite regime $L \gg R$. In this work, we operate in an intermediate regime where neither limit is valid. We therefore employ the proximity-force approximation, which overestimates the

actual Casimir strength for the parameters in Table 10.1 by a factor of ≈ 2.4 and thus provides a conservative upper bound on decoherence effects, as discussed in Appendix C.2. In the sphere-plane geometry, it is given by [258, 259]

$$V_{\mathrm{PFA}} = -\frac{\hbar c \pi^3 R}{720(L - R - d_s/2)^2}\,\varphi(\varepsilon_r) \tag{10.1}$$

where $L-R-d_s/2$ is the surface-to-surface separation of the sphere and the plane. The factor $\varphi(\varepsilon_r)$ accounts for dielectric properties of the particles as a function of the relative permittivity ε_r and is given by $\varphi(\varepsilon_r) = (\varepsilon_r-1)/(\varepsilon_r+1)\chi(\varepsilon_r)$ with $\chi(\varepsilon_r)$ being a tabulated function [260]. In particular, $\chi(\varepsilon_r \to \infty) \to 1$, $\chi(\varepsilon_r = 1) \approx 0.46$ and $\chi(\varepsilon_{r,\,\mathrm{SiO_2}}) \approx 0.5$. Finite temperature corrections to the Casimir interaction exists but are negligible for temperatures $T \ll \hbar c/(k_B L) \approx 100\mathrm{K}$ [261].

10.2 Magnetic interactions

In addition to Casimir forces, induced magnetic dipole moments arising from external magnetic fields, e.g. the magnetic trapping potential, introduce an additional source of non-gravitational coupling between the particles in the form of magnetic dipole-dipole interactions. These can quickly become dominant over the gravitational interaction and thus also need to be suppressed. Magnetic interactions are however only weakly shielded by a conducting Faraday shield and therefore require explicit consideration. Furthermore, the relevance of these interactions depends crucially on the particle material and differ quantitatively between the silica particles and the superconducting lead particles considered in this work. For a spherical particle of radius R and volume magnetic susceptibility χ_V, an external magnetic field $\mathbf{B}$ induces a magnetic dipole moment $\mathbf{m} = 4\pi R^3 \chi_V \mathbf{B}/[\mu_0(3+\chi_V)]$ [262], where μ_0 is the vacuum permeability. Silica is weakly diamagnetic with $\chi_{V,\,\mathrm{SiO_2}} \approx -1.4 \times 10^{-5}$ [263], whereas superconducting lead behaves as a perfect diamagnet with $\chi_V = -1$.

Requiring the magnetic dipole-dipole interaction to remain smaller than gravitational coupling imposes an upper bound on the admissible external magnetic field. As shown in Appendix C.1, this condition yields $B \lesssim 71\mu\mathrm{T}$ for silica particles, which is on par with Earth's magnetic field. For superconducting lead particles, the bound is significantly more stringent with $B \lesssim 2.83\,\mathrm{nT}$. The screening of magnetic dipole-dipole interactions between the particles and of external magnetic fields is therefore necessary.

Besides the Earth's magnetic field, additional fields may arise from the trapping mechanism itself. For diamagnetically levitated particles, static magnetic fields are required to levitate, following

$$B\partial_x B = \frac{g\rho\mu_0}{\chi_V},$$

where $g = 9.81\text{m/s}^2$. To levitate superconducting lead with magnetic gradients of $\partial_x B \sim 10^2 - 10^3\text{T/m}$ [116] requires a static magnetic field of $B_{\text{trap}} \sim 0.1 - 1\,\text{mT}$. For the less diamagnetic silica, however, higher gradients of $\partial_x B \sim 10^4 - 10^5\text{T/m}$ [264] with static magnetic fields of $B_{\text{trap}} \sim 20 - 200\text{mT}$ are sufficient [1].

When the magnetic moments are aligned, the dipole-dipole interaction is proportional to $3\cos^2\phi - 1$, where ϕ is the angle between the dipole orientation and the interparticle separation vector. It vanishes at $\phi \approx 54.7°$, the magic angle. However, achieving this configuration would require precise control of the applied field direction, particularly for the superconducting lead particle, as well as of the experimental geometry. Moreover, such cancellation is impossible for dipole components induced by uncontrolled stray fields.

An alternative approach is to modulate the induced dipoles in time, for instance via modulation of the trapping fields, such that the interaction averages to zero over a cycle. While this dynamical averaging suppresses the controlled dipole-dipole coupling, it again leaves contributions from uncontrolled stray fields unaffected. We therefore do not pursue this mechanism further and instead focus on suppression via magnetic shielding.

One option is using high-permeability materials, such as Mu-metals with a permeability of $\mu_r \sim 10^5$ [263, 265]. While such materials may suffice to screen weak magnetic interactions, they are generally ineffective in shielding strong couplings, like for magnetically levitated particles, where we assume a static trapping magnetic field of $B_{\text{trap}} = 250\mu\text{T}$ is required. For such regimes, Meissner shielding using a type-II superconductor is required. Niobium ($T_c \approx 10\text{K}$) with a London-penetration depth of $\lambda_L \approx 40\text{nm}$ [266] would sufficiently suppress magnetic couplings at a thickness of $d_s \gtrsim 455\,\text{nm}$, as seen in Appendix C.1.

However, introducing a magnetic shield, whether based on high-permeability materials or superconductors, inevitably leads to additional particle–shield interactions, analogous to the Casimir forces discussed previously. The interaction potential from a magnetic dipole and its mirror dipole in the superconducting shield is given by

$$V_{\text{mag. Dipole}} = -\frac{|\mathbf{m}|^2\mu_0}{32\pi(L - d_s/2)^3}\frac{\mu_r - 1}{\mu_r + 1}\left(1 + \cos^2\phi\right) \tag{10.2}$$

for a shield with magnetic permeability μ_r, where ϕ is the angle between the magnetic dipole moment and the shield's normal. For the parameters in Table 10.1 and $B_{\text{trap}} = 250\mu\text{T}$, these interactions between magnetically trapped superconducting lead particles and the shield exceed the corresponding Casimir interactions by a factor of 10^4 and the direct gravitational particle–particle coupling by 10^9. For

[1] In the absence of gravity, a diamagnetic particle can be trapped at $B = 0$, for example at the centre of an ideal anti-Helmholtz configuration. In this case, the induced response is purely quadrupolar, leading to comparatively weaker interactions with the shield. In terrestrial experiments, however, gravity is unavoidable and shifts the equilibrium position away from the field zero, thereby inducing a finite dipolar contribution.

silica magnetically levitated in $B_{\rm trap} \lesssim 20\text{mT}$, Casimir interactions with the shield still dominate over magnetic dipole interactions.

10.3 Electrostatic interactions

Electrostatic forces pose a further challenge for GIE experiments due to the large disparity between electromagnetic and gravitational interaction strengths. If the particles carry a net charge q, direct Coulomb interactions would easily dominate over gravity, unless effectively shielded. Even for a single elementary charge $q = e$ on each particle, suppressing Coulomb couplings to below the gravitational interaction would require a Faraday shield of radius $r_s \gtrsim 66\,\text{cm}$ and thickness $d_s \gtrsim 20\,\text{nm}$, as estimated in Appendix C.1. Such a large shield would support low-frequency vibrational modes that are thermally populated even at low temperatures and couple to the particles, thereby introducing additional noise, as discussed in Sec. 13. We therefore strongly advocate operating with electrically neutral particles.

However, even in the absence of a net charge, couplings can arise from permanent or induced electric dipoles. The particles may possess intrinsic dipole moments due to lattice or surface inhomogeneities [267] on the order of $p \sim eR$ (e.g. $p \approx 10^{-2} e\text{cm}$ in micrometer silica particles [102]). Moreover, stray electric fields $\mathbf{E}$ can induce dipole moments as $\mathbf{p} = 4\pi\varepsilon_0(\varepsilon_r - 1)/(\varepsilon_r + 2)R^3\mathbf{E}$. Particularly relevant sources of stray fields are spatially varying electrostatic patch potentials on the shield's surface. These arise from crystal defects, mechanical stress, or surface contamination and typically exhibit voltage variations $V_{\rm Patch} \sim 1 - 100\text{mV}$ [268, 269] over length scales $\ell_{\rm Patch} \sim 100\text{nm}$. Such potentials generate electric fields of magnitude $E \sim V_{\rm Patch}\ell_{\rm Patch}/L^2 \approx 10^{-1} - 10^2\text{V/m}$ which can induce dipole moments $p \approx 10^{-5} - 10^{-3} e\text{cm}$ in the particles. Shielding all these dipolar interactions between the two particles to below the gravitational coupling requires a more modest shield size with radius $r_s \gtrsim 1\text{mm}$ and thickness $d_s \gtrsim 0.05\,\text{nm}$, as estimated in Appendix C.1 and summarized in Table 1. In practice, the optical skin depth of the shielding material as well as rigidity and fabrication methods give a stricter lower bound on the thickness than the physical shielding.

Each dipole also interacts with the conducting shield, resulting in an interaction potential given by

$$V_{\text{elec. Dipole}} = -\frac{|\mathbf{p}|^2}{32\pi\varepsilon_0(L - d_s/2)^3}\left(1 + \cos^2\phi\right),$$

where ϕ again denotes the angle between the dipole orientation and the shield's normal. For the parameters listed in Table 10.1, the dipole-induced particle–shield interaction is weaker than the corresponding Casimir interaction by a factor ranging from $\sim 10^{-6}$ to $\sim 10^{0}$ and weaker than magnetic dipole interactions

by $\sim 10^{-10} - 10^{-4}$ (depending on the magnitude of the induced electric dipole moment). Thus, we only consider Casimir- and magnetic dipole induced effects in the following. The decoherence induced by electric dipole interactions, however, could be analyzed in the same way as in Sec. 11 and Sec. 13.

10.4 Gravitational interactions

The gravitational interaction between the two particles is described by a Newtonian potential, as we operate in the nonrelativistic, low-energy regime

$$\hat{H}_{\text{Gravity}} = -\frac{GM_AM_B}{|\hat{d}_{AB}|}, \tag{10.3}$$

where $\hat{d}_{AB} = \sqrt{(\hat{x}'_A - \hat{x}'_B)^2 + (\hat{y}'_A - \hat{y}'_B)^2}$ denotes the canonically quantized distance operator between the centres of mass of the two particles. Provided that the delocalization of each particle is small compared to their separation, i.e., $\Delta x, \Delta y \ll L$, the potential in Eq. (10.3) can be expanded up to second order in $\hat{x}$ and $\hat{y}$. As shown in Appendix C.2, this expansion yields bilinear coupling terms of the form $\propto x_A x_B$ and $\propto y_A y_B$, which constitute the origin of gravitationally induced entanglement in this model [74].

Gravitational interactions between the particles and the shield are neglected in this work, as they are several orders of magnitude weaker than all other particle–shield interactions discussed before.

Beyond mutual interaction between the particles, sources of external gravitational fields, ranging from the Earth and nearby celestial bodies to moving massive objects in the laboratory and its surroundings, can influence the phase evolution of the delocalized state. Since the spatial superpositions must be maintained in a fixed configuration with respect to the experimental screen, they generally acquire relative phases due to these external gravitational accelerations.

In particular, the dominant contributions originate from the Sun and the Moon, with effective accelerations of approximately $g_{\text{Sun}} \approx 6 \times 10^{-4}\, g$ and $g_{\text{Moon}} \approx 3.3 \times 10^{-6}\, g$, while contributions from other planets are typically at the level of $10^{-8}\, g$ or smaller. In the worst-case configuration, this leads to a relative phase accumulation rate given by

$$\Gamma = \frac{2\Delta x M g_{\text{Sun}}}{\hbar}$$

for a particle of mass M. For the parameters in Table 10.1, we find $\Gamma \approx 10^{13} - 10^{14}$Hz. Such large phase evolution rates impose stringent requirements on the timing precision of the experiment, as well as on the accurate knowledge of the relative orientation between the experimental setup and the Sun.

In principle, this contribution could be reduced by using a test mass to measure the

total acceleration arising from the combined gravitational influence of the Earth, the Sun and other bodies and subsequently aligning the principal delocalisation axis orthogonal to this total acceleration vector. At the same time, the shield imposes an additional alignment constraint, as its normal vector must be aligned accordingly with the delocalization axis, depending on whether the parallel or linear orientation is prepared. This introduces a nontrivial geometrical constraint on the experimental design, where the shield has to co-rotate with the changing total acceleration vector.

While the severity of this effect is reduced for smaller test masses, it remains non-negligible and must be accounted for. More generally, it is worth noting that even in exceptionally quiet underground environments or close to the first Lagrange point, residual random accelerations are typically of the order of $10^{-8}\mathrm{m/s^2}/\sqrt{\mathrm{Hz}}$ at 1Hz [270, 271], providing an additional background contribution that limits phase stability.

11 Variations in the experimental geometry

In the lab frame, all relevant objects – the two local potentials, the two measuring devices and the shield – may undergo stochastic displacements and rotations relative to their desired position and orientation. We model these fluctuations by independent Gaussian variables $\xi_i \sim \mathcal{N}(0, \Delta\xi^2)$. These fluctuations may or may not be correlated across different objects, depending on the specifics of the experimental configuration. In the following, we describe the state of the system in the detector frame, which defines the operational frame in which the density matrix is reconstructed. It is useful to distinguish two qualitatively different types of stochasticity:

a) Uncertainty in initial state
In this case, randomness enters exclusively through the initial state, while the time evolution is governed by the same Hamiltonian and therefore identical for all realizations. The dynamics is therefore described by a single unitary channel acting on a classical mixture

$$\rho(t) = U(t) \left(\int \mathrm{d}\xi \, p(\xi) \, |\psi(\xi)\rangle\langle\psi(\xi)| \right) U^\dagger(t).$$

As a consequence, no additional decoherence is generated during the evolution; any loss of purity is solely inherited from the initial state.

b) Run-to-run variation of the setup
Here, fluctuations in the experimental arrangement lead to different dynamics in each run, resulting in an ensemble-averaged state at time t,

$$\rho(t) = \int \mathrm{d}\xi \, p(\xi) \, U_\xi(t) \rho_0 U_\xi^\dagger(t), \tag{11.1}$$

where $U_\xi(t) = \exp\left[-i\hat{H}(\xi)t/\hbar\right]$. The dynamics is thus described by a convex mixture of unitary channels and gives rise to decoherence.

We consider two experimentally relevant instances that lead to two different forms of noise, both visualized in Fig. 11.1(b):

1. *Shield variations:* The two detectors and two traps are all fixed to the lab frame, while the shield undergoes stochastic displacements $\xi^{(L)}_{\mathrm{Shield}}$ and rotations $\xi^{(\theta)}_{\mathrm{Shield}}$ that affect the Hamiltonian observed by the particles in each realization $H(\xi)$.

2. *Detector variations:* Each trapping potential is rigidly attached to its local detector, but, the distance and orientation of each detector relative to the shield and to each other fluctuates. In this case each detector observes a different fluctuation of the shield's position and orientation, $\xi^{(L)}_{A/B} \sim \mathcal{N}(0, \Delta L^2)$ and $\xi^{(\theta)}_{A/B} \sim \mathcal{N}(0, \Delta\theta^2)$, respectively, where the fluctuations are, in general, uncorrelated across the two detectors. Such a situation may be found, for example, where the same elements are used for trapping and for detection, or when the detector always measures displacements with respect to the equilibrium position of the trap.

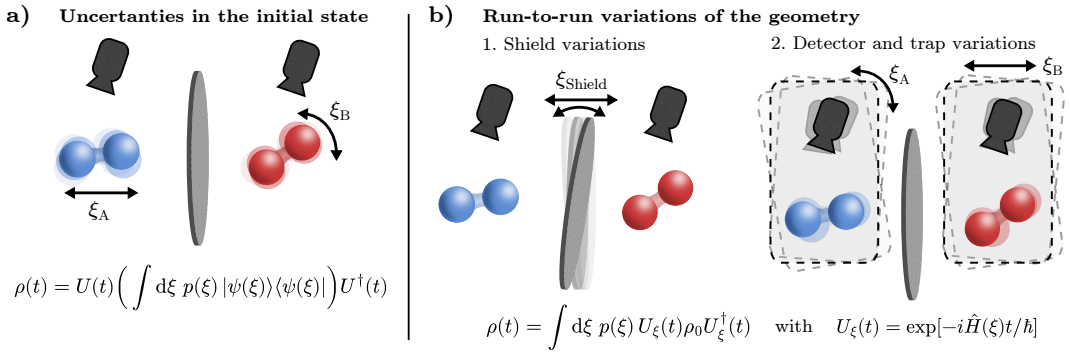


Figure 11.1: **Geometry variations a,** Uncertainty in the preparation of the initial state. The initial state $\rho(0) = \int d\xi\, p(x)\, |\psi(t)\rangle\langle\psi(t)|$ is mixed. The time evolution does not generate additional decoherence and any loss of purity is solely inherited from the initial state. **b,** Run-to-run variations of the setup. The varying geometry results in run-dependent time evolution operators $U_\xi(t)$ which generate, after averaging over ξ, decoherence even if the initial state ρ_0 is pure. We distinguish the two experimentally relevant cases of distance $\xi^{(L)}$ and orientation $\xi^{(\theta)}$ variations in the orientation and placement of the *1. shield* and *2. detectors/traps* discussed in the text.

We note that, although both, initial-state uncertainty and run-to-run variations of the experimental arrangement, induce fluctuations in the particle–shield separation, they are not equivalent, and lead to qualitatively different forms of noise. The case where the trapping potentials fluctuate relative to the detectors leads to decoherence also in the absence of particle–shield interactions and is discussed separately in Sec. 12.

For small spatial delocalisations $\Delta x, \Delta y \ll L$ as well as small geometric variations $\Delta L \ll L$ and $\Delta\theta \ll L/\Delta x$, it is well justified to expand the Hamiltonian $\hat{H}(\xi)$ up to second order in the position operators and in the stochastic parameters ξ. The explicit form of these expansions is given in Appendices C.2 and C.2.

For the parameter regimes and electrically neutral particles considered here, coherence loss is dominated by Casimir and magnetic dipole interactions of each

particle with the shield. Fluctuations in the gravitational coupling are therefore negligible. While an analytical justification is provided in Appendix C.2, this approximation has also been verified numerically.

In the following, we neglect the trapping potential in the Hamiltonian during the entanglement generation step, i.e. setting $\omega = 0$. During the preparation and detection stage in the GIE protocols, a trap may however still be employed. For evolution times $t \lesssim 2\pi/\omega$ the harmonic confinement does not significantly modify the dynamics, while its omission considerably simplifies the analysis. Moreover, the bounds on admissible setup variations derived below remain largely unaffected by the inclusion of a weak trapping potential; numerical results indicate that they become slightly more stringent.

11.1 Gaussian states

We consider squeezed Gaussian states delocalised along the x-direction and y-direction, modelled as harmonic oscillator modes with position widths Δx and Δy. Gaussian states are fully characterised by their first and second moments, given by the displacement vector $\mathbf{d} = \langle \mathbf{r} \rangle$ and the second-moment matrix $V_{ij} = \frac{1}{2}\langle r_i r_j + r_j r_i \rangle$, where $\mathbf{r} = (X_1, P_1, \ldots, X_n, P_n)^\intercal$ collects the quadratures. The covariance matrix is then defined as $\sigma = V - \mathbf{d}\mathbf{d}^\intercal$. For convenience, we introduce dimensionless quadratures $X_i \equiv \hat{x}_i/x_0$ and $P_i \equiv \hat{p}_i/p_0$ for some x_0 and $p_0 = \hbar/x_0$ such that $[X_i, P_j] = i\delta_{ij}$. These satisfy the uncertainty relation $\Delta X_i \Delta P_i \geq \frac{1}{2}$. Initially, all modes m are in a thermal state

$$\mathbf{d}(0) = 0 \qquad \text{and} \tag{11.2}$$

$$V(0) = \bigoplus_{\substack{m=\{X_A,X_B,\\ Y_A,Y_B\}}} (1+2\bar{n}_m)\mathrm{diag}\left(\Delta m^2, \Delta P_m^2\right), \tag{11.3}$$

where $\bar{n}_m$ denotes the mean thermal occupation of mode m. The initial state is pure when $\bar{n}_m = 0$ for all m. We always take $\bar{n}_y = 0$ in the following.

Under a quadratic Hamiltonian $\hat{H} = \frac{1}{2}\mathbf{r}^\intercal G \mathbf{r} + \mathbf{g}^\intercal \mathbf{r}$, Gaussianity is preserved at all times. The time evolution of $V(t)$ and $\mathbf{d}(t)$ follows from the Heisenberg equations of motion and are shown in Appendix C.3. For each realization $\xi(t)$, the system evolves to a different Gaussian state, such that the ensemble-average covariance matrix is given by

$$\bar{\sigma}(t) = \langle V(t) \rangle_\xi - \langle \mathbf{d}(t) \rangle_\xi \langle \mathbf{d}(t) \rangle_\xi^\intercal . \tag{11.4}$$

Equivalently, this can be expressed as

$$\bar{\sigma}(t) = \langle \sigma(t) \rangle_\xi + \mathrm{Cov}_\xi[\mathbf{d}(t)],$$

where $\mathrm{Cov}_\xi[\mathbf{d}] = \langle \mathbf{d}\mathbf{d}^\intercal \rangle_\xi - \langle \mathbf{d} \rangle_\xi \langle \mathbf{d} \rangle_\xi^\intercal$ represents the covariance of the fluctuating mean displacements. This expression highlights that averaging only over specific realizations of $\sigma_\xi(t)$ would underestimate the total variance of the averaged state: random shifts of the mean displacement increase the overall variance, even if each realization $\sigma_\xi(t)$ exhibits the same intrinsic quantum noise.

To quantify entanglement between two subsystems with m and n modes, we use the logarithmic negativity [272], which for Gaussian states is given by

$$E_N = \sum_{j=1}^{m+n} \max\{0, -\log_2(2\nu_j)\}. \tag{11.5}$$

Here, ν_j are the $m+n$ symplectic eigenvalues of the covariance matrix σ^Γ of the partially transposed state, obtained by applying the phase space transformation $p_i \mapsto -p_i$ to σ for all the modes i in one subsystem [273].

We first analyse entanglement generation in the presence of only gravitational interaction and no variations of the setup, providing a baseline for comparison with the case where Casimir and magnetic dipole interactions together with setup fluctuations are included. By expanding the gravitational Hamiltonian to second order in the particle position operators [74], we obtain the entanglement rate $\Gamma_{\text{ent.}} = \partial_t E_N|_{t\to 0}$ as in Appendix C.3 for $\theta_A = \theta_B \equiv \theta$ as

$$\begin{aligned}\Gamma_{\text{ent.}} =& \frac{\lambda \Delta X_A \Delta X_B x_0^2}{\hbar \log 2} \left|2\sin^2\theta - \cos^2\theta\right| \\ &+ \frac{\lambda \Delta Y_A \Delta Y_B x_0^2}{\hbar \log 2} \left|2\cos^2\theta - \sin^2\theta\right|,\end{aligned} \tag{11.6}$$

with the gravitational coupling strength $\lambda = GM_AM_B/(4L^3)$. For $\Delta X \gg \Delta Y$, this rate is maximised for $\theta = \pi/2$, when the delocalisation axis is oriented perpendicular to the shield in the linear orientation and exceeds the parallel configuration by a factor of 2. This behaviour is expected: in this configuration, the spatial delocalisation maximizes the spread between the shortest and longest interparticle separations sampled by the wavefunction. As a result, the gravitational interaction generates the largest differential phase accumulation across the support of the state, leading to a faster buildup of non-local correlations.

In the following, we study the effect on entanglement generation of random variations in the setup geometry. Note that, after averaging over the classical fluctuations, the resulting state is in general no longer guaranteed to be Gaussian. Higher order cumulants become non-vanishing and the averaged state has to be written perturbatively as $\rho = \rho_G + \Delta\rho$, where ρ_G denotes the Gaussian state described by the covariance matrix $\bar{\sigma}$. The trace-norm $\|\Delta\rho\|_1$ is bounded in Appendix C.3 and scales in the variations $\Delta\xi$ as $\|\Delta\rho\|_1 \sim \Delta\xi^2 \|\rho_G\|_1 + \mathcal{O}(\Delta\xi^4)$. The deviation of the logarithmic negativity satisfies $\Delta E_N = |E_N(\rho_G) - E_N(\rho)| \leq \left\|\Delta\rho^\Gamma\right\|_1 / \left\|\rho_G^\Gamma\right\|_1$,

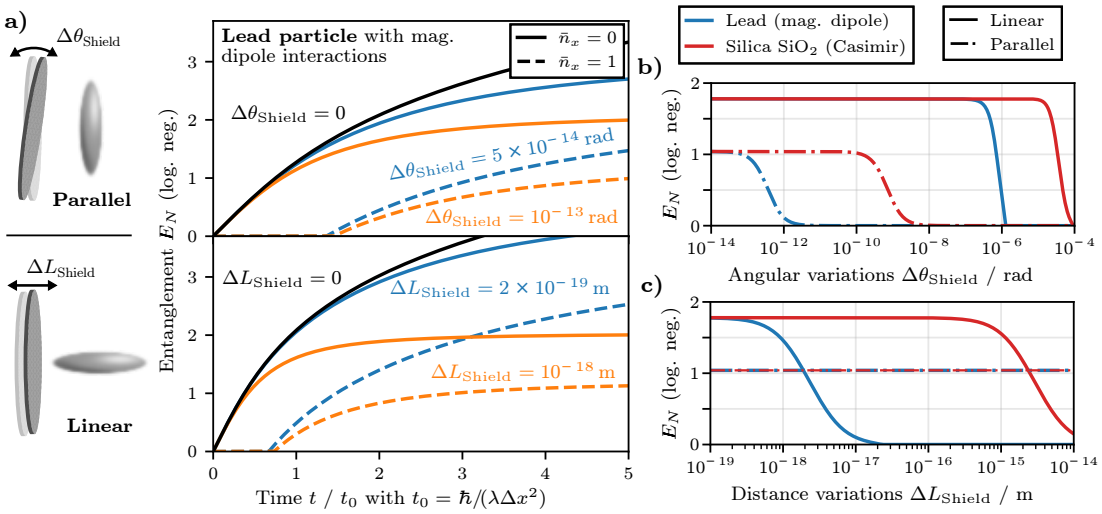


Figure 11.2: **Entanglement between Gaussian squeezed states subject to *shield variations (see Fig. 11.1(b)1.)*** **a,** Time evolution of the logarithmic negativity E_N for Gaussian wave packets in the presence of particle–shield magnetic dipolar interactions in the parallel ($\theta = 0$, **top**) and linear ($\theta = \pi/2$, **bottom**) orientation. The parallel configuration is illustrated with run-to-run angular fluctuations of the shield orientation, while the linear orientation is shown with variations in the lateral shield placement. The principal x-mode is initially in a thermal state with occupation number $\bar{n}_x$. Time is expressed in units of $t_0 = \hbar/(\lambda\Delta x)$ with the gravitational coupling strength $\lambda = GM_AM_B/(4L^3)$, corresponding to $t_0 \approx 164$ms for silica particles and $t_0 \approx 9$ms for superconducting lead particles with the parameters of Table 10.1. For times $t/t_0 \lesssim \Delta x\Delta p/\hbar$, the entanglement grows linear as $E_N \propto t/t_0$ [30]. **b,** Logarithmic negativity at $t = t_0\pi/4$ as a function of angular variations $\Delta\theta_{\text{Shield}}$. For lead particles in the linear configuration, the small but non-zero transverse y-mode has a visible effect on the stability, explaining the distinct look compared to other curves. **c,** Logarithmic negativity at the same time as a function of distance variations ΔL_{Shield}.

where ρ^Γ is the partial transposition of a state ρ with respect to any subsystem. For small variations $\Delta\xi$, the state is therefore almost Gaussian with $\lim_{\Delta\xi\to 0}\Delta E_N = 0$, and the logarithmic negativity of ρ_G serves as a good estimator of the logarithmic negativity of ρ.

11.1.1 Variations in the shield positioning

If position and orientation of the shield fluctuate slightly from run to run, the particle–shield interaction Hamiltonian changes accordingly as

$$\hat{H}(\xi) = \hat{H}_{\text{Grav.}} + \hat{H}_{\text{Cas./mag. Dip.}}(\xi_{\text{Shield}}).$$

Expanding the Hamiltonian up to second order in both, the stochastic variables ξ_{Shield} and the position operators, allows us to analytically evolve and average the resulting state. The full expression of the expanded interaction Hamiltonians for both considered orientations are given in Appendices C.2 to C.2. The logarithmic negativity as a function of the standard deviation of the fluctuations ΔL_{Shield} and $\Delta\theta_{\text{Shield}}$ is shown in Fig. 11.2 for both pure and thermal initial states.

An initial state with thermal population $\bar{n}_x > 0$ results in a delayed onset of entanglement growth, in alignment with Ref. [274]. The entanglement generation and its sensitivity to variations depends strongly on the orientation of the states with respect to the shield.

In the parallel orientation, entanglement grows more slowly but is more robust against fluctuations in the particle–shield separation L, since all components of the delocalised wave packet acquire the same random phase. Angular variations however, rapidly suppress entanglement once $\Delta\theta_{\text{Shield}}$ exceeds approximately 10^{-9}rad for Casimir interactions between silica particles and 10^{-13} rad for superconducting lead dominated by magnetic dipole interactions.

In contrast, for the linear configuration the entanglement initially grows twice as fast and is significantly more tolerant to angular misalignment. Variations in the separation, however, suppress entanglement for fluctuations exceeding $\Delta L_{\text{Casimir}} \approx 10^{-14}$m and $\Delta L_{\text{mag. Dipole}} \approx 10^{-17}$m. The linear configuration has an additional practical limitation that persists even under ideal setup alignment. Because different parts of the spatial superposition are located at different distances from the shield, they experience substantially different Casimir or magnetic dipole potentials. The resulting energy difference $\Delta V = V(\Delta x) - V(-\Delta x)$ leads to a rapid relative phase accumulation at a rate $\Gamma \sim |\Delta V|/\hbar$. For the parameters in Table 10.1, this corresponds to 10.4GHz for a silica particle experiencing Casimir interactions and 378THz for a superconducting lead particle experiencing magnetic dipole interactions. As a consequence, the entanglement readout becomes extremely sensitive to the precise measurement time: The local phases evolve on sub-nanosecond timescales, so even small timing uncertainties translate into large phase uncertainties. Although this unitary dynamics preserves entanglement, averaging over states sampled at slightly different times, hence with different local phases, is equivalent to local dephasing and suppresses the coherences responsible for entanglement. Resolving the gravitationally induced correlations therefore requires sub-nanosecond timing control to sample the state at a well-defined relative phase.

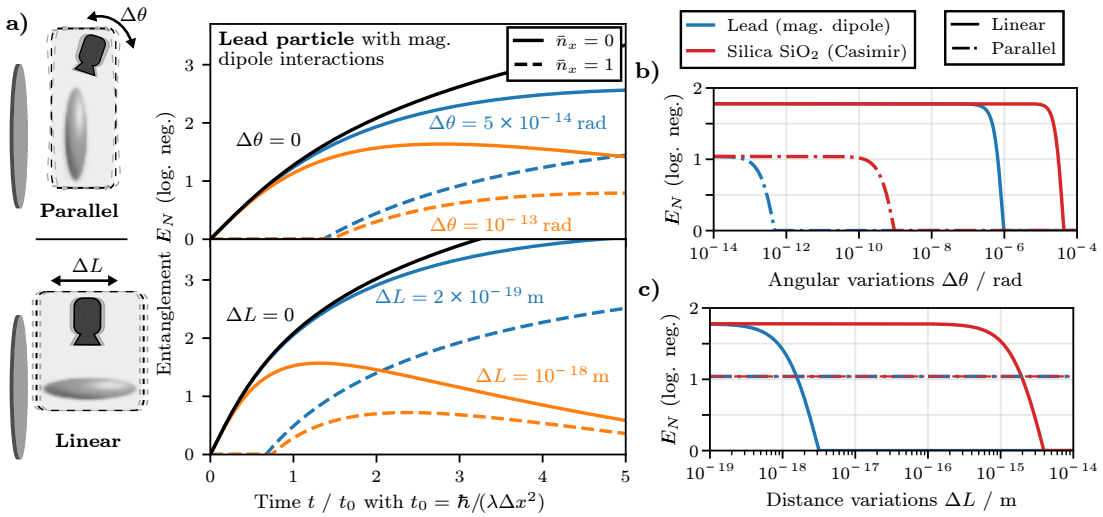


Figure 11.3: **Entanglement between Gaussian squeezed states subject to *detector and trap variations (see Fig. 11.1(b)2.)*** **a,** Time evolution of the logarithmic negativity E_N for Gaussian wave packets in presence of particle–shield magnetic dipolar interactions in the parallel (**top**) and linear (**bottom**) orientations. The parallel configuration is illustrated with angular fluctuations of the detectors over many runs, while the linear configuration is shown with variations in the detector positioning. After saturation, the entanglement decays much faster back to zero compared to the previous case. **b,** Logarithmic negativity at time $t = t_0\pi/4$ as a function of angular variations $\Delta\theta$ for both orientations and both particle types. The difference in the shape of the curves compared to Fig. 11.2 stems from the uncorrelated nature of the variations. **c,** Logarithmic negativity at the same time as a function of placement fluctuations ΔL relative to the static shield.

11.1.2 Variations in the position of the detectors and traps

Variations in the positioning of the detectors and traps relative to each other and to the shield can be modelled by including the uncorrelated local fluctuations $\xi^{(L)}_{A/B}$ and $\xi^{(\theta)}_{A/B}$ directly in the interaction Hamiltonian as

$$\hat{H}(\xi) = \hat{H}_{\text{Grav.}} + \hat{H}_{\text{Cas./mag. Dip.}}(\xi_A, \xi_B).$$

The previous case of shield variations can actually be expressed by using the same fluctuations in a correlated manner, such that $\xi^{(L)}_A = -\xi^{(L)}_B \equiv \xi^{(L)}_{\text{Shield}}$ and $\xi^{(\theta)}_A = \xi^{(\theta)}_B \equiv \xi^{(\theta)}_{\text{Shield}}$.

The resulting entanglement dynamics are shown in Fig. 11.3. Compared to the

previous case discussed above, the system is now more sensitive to fluctuations, with tolerance thresholds reducing by nearly one order of magnitude.

11.2 Two-level cat-states

The second class of initial states we investigate here are massive Schrödinger cat-states, consisting of symmetric superpositions of spatially separated states. The combined initial state of the two particles is then written as

$$|\psi_{\text{Cat}}\rangle = \frac{1}{2}\left(|\psi^{(1)}\rangle + |\psi^{(2)}\rangle\right)_A \otimes \left(|\psi^{(1)}\rangle + |\psi^{(2)}\rangle\right)_B .$$

We constrain ourselves to the regime in which the states $\left\{|\psi^{(1)}\rangle, |\psi^{(2)}\rangle\right\}$ can be approximated as orthonormal and therefore span an effective two-dimensional Hilbert space. This corresponds to the limit in which the spatial overlap $\langle\psi^{(1)}|\psi^{(2)}\rangle = 0$ vanishes due to a sufficiently large spatial separation of the wave packets. In this regime, the motional degree of freedom of each particle can be approximated by a two-level system encoding the two branches of the spatial superposition. We refer to these states as two-level cat-states.

Within this effective description, the continuous position operators can be discretised: If the delocalisation satisfies $\Delta x \gg \Delta y$, the operators reduce to $\hat{x} \to \Delta x \sigma_z$ and $\hat{y} \to 0$, where σ_z is the Pauli matrix. For general orientations $\theta_{A/B}$, the time evolution of the entanglement under the gravitational interaction is derived in Appendix C.4 and is given by

$$E_N = \log_2\left(1 + |\sin(\phi t)|\right), \tag{11.7}$$

with

$$\phi = \frac{\lambda \Delta x_A \Delta x_B}{\hbar}\left(2\sin\theta_A \sin\theta_B - \cos\theta_A \cos\theta_B\right).$$

As in the Gaussian case, entanglement growth is maximal in the linear configuration.

11.2.1 Variations in the shield positioning

Here, we again consider the stability of entanglement against fluctuations of the shield position and orientation, while all other geometries stay fixed.

The resulting stability of the entanglement between cat-states with respect to variations ΔL_{Shield} and $\Delta\theta_{\text{Shield}}$ is shown in Fig. 11.4. In addition, the first-order analytical prediction derived in Appendix C.4 is shown in gray. As before, the robustness of entanglement depends strongly on the particle orientation: In the

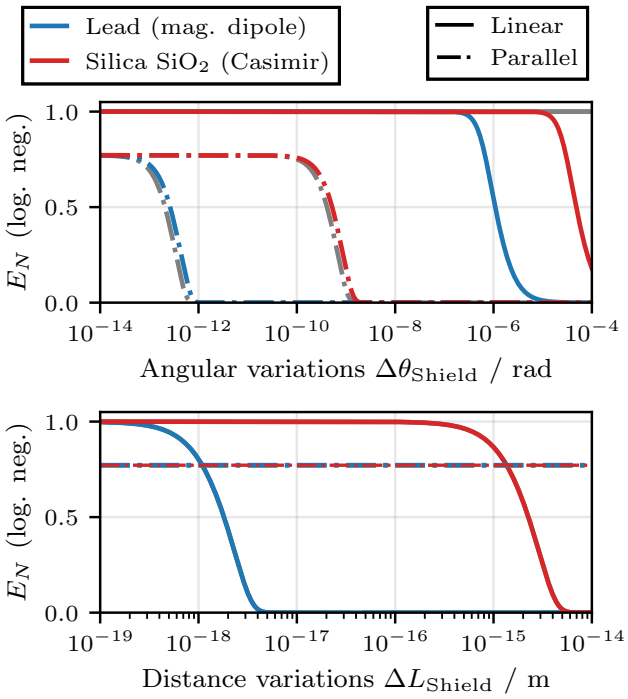


Figure 11.4: **Entanglement for two-level cat-states subject to *shield variations (see Fig. 11.1(b)1.)*** Logarithmic negativity in the parallel and linear orientation after evolution times $t = t_0\pi/4$, corresponding to $t \approx 129$ms for silica particles and $t \approx 7$ms for superconducting lead. We use the parameters from Table 10.1. **top,** Entanglement as a function of fluctuations in the shield orientation. In gray we show the first-order analytical expressions derived in Apx. C.4. **bottom,** Entanglement as a function of fluctuations in the particle–shield separation. The qualitative dependence on orientation and type of the variation closely mirrors the behaviour for Gaussian states in Fig. 11.2.

parallel configuration ($\theta = 0$), decoherence arises predominantly from angular fluctuations, whereas in the linear configuration ($\theta = \pi/2$), entanglement is sensitive to variations in the particle–shield separation.

The qualitative behaviour closely matches that observed for Gaussian states. The apparently enhanced robustness of cat states against angular fluctuations in the linear configuration is not intrinsic, but results from the inclusion of a finite transverse y-mode in the Gaussian analysis. In the limit $\Delta y \to 0$, both state classes exhibit nearly identical stability thresholds, with Gaussian states showing a marginally higher robustness.

11.2.2 Variations in the position of the detectors and traps

The effect of variations in the placement of the detectors can be treated analytically in a compact manner, as detailed in Appendix C.4. To first order in $\xi^{(j)}$ with $j \in \{L, \theta\}$, the logarithmic negativity between two identically prepared particles ($\theta_A = \theta_B \equiv \theta$ and $\Delta x_A = \Delta x_B \equiv \Delta x$), is given by

$$E_N = \max\left\{0,\, \log_2\left[e^{-\gamma^2}\left(\cosh\left(\gamma^2\right) + |\sin(\phi t)|\right)\right]\right\}, \tag{11.8}$$

with $\gamma^2 = \sum_{j\in\{L,\theta\}} (\gamma^{(j)}_{\text{Casimir}})^2 + (\gamma^{(j)}_{\text{mag. Dipole}})^2$. For Casimir-dominated particle–shield interactions, γ_{Casimir} take the form

$$\gamma^{(\theta)}_{\text{Casimir}} = \sqrt{8}\,(L - R - d_s/2)\,\eta\, t\,\Delta x\,\Delta\theta\,\cos\theta\,/\,\hbar,$$
$$\gamma^{(L)}_{\text{Casimir}} = \sqrt{72}\,\eta\, t\,\Delta x\,\Delta L\,\sin\theta\,/\,\hbar,$$

where $\eta = \hbar c\pi^3 R\varphi(\varepsilon_r)/(720(L-R-d_s/2)^4)$ denotes the Casimir coupling strength. For superconducting lead particles, where particle–shield interactions are dominated by induced magnetic dipole moments, we find

$$\gamma^{(\theta)}_{\text{mag. dipole}} = \sqrt{18}\,(L - d_s/2)\,\delta\, t\,\Delta x\,\Delta\theta\,\cos\theta\,/\,\hbar,$$
$$\gamma^{(L)}_{\text{mag. dipole}} = \sqrt{288}\,\delta\, t\,\Delta x\,\Delta L\,\sin\theta\,/\,\hbar,$$

with $\delta = 2\mu_0|\vec{m}|^2/(32\pi(L - d_s/2)^5)$.

In Fig. 11.5, we present the full numerical results and the analytical prediction from Eq. (11.8). Compared to the shield-variations shown in Fig. 11.4, the system exhibits a reduced robustness against these uncorrelated fluctuations, mimicking the results obtained for Gaussian states discussed in Sec. 11.1.

11.3 Continuous cat-states

Gaussian states and two-level cat-states form limiting cases of a continuous family of delocalised states. Establishing this connection enables a unified comparison of their entanglement generation. We consider the symmetric superposition

$$|\psi\rangle = \frac{1}{\mathcal{N}}\left(|\psi_+\rangle + |\psi_-\rangle\right)_A \otimes \left(|\psi_+\rangle + |\psi_-\rangle\right)_B \tag{11.9}$$

where each branch is a displaced squeezed state $|\psi_\pm\rangle = D(\pm\alpha)S(r)\,|0\rangle$ with the position-space representation

$$\langle x|\psi_\pm\rangle = \frac{1}{(2\pi\sigma^2)^{1/4}}\exp\left\{-\frac{(x \pm d/2)^2}{4\sigma^2}\right\}.$$

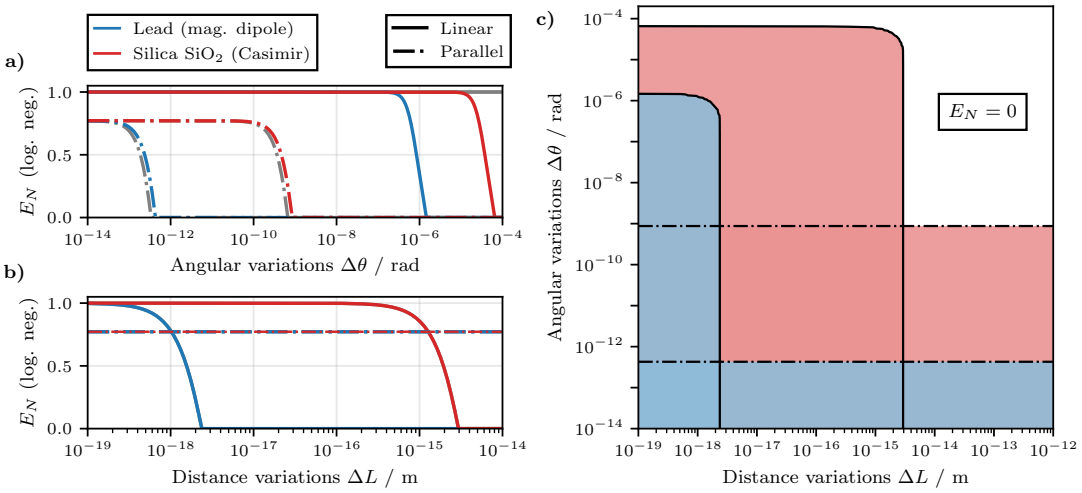


Figure 11.5: **Entanglement for two-level cat-states subject to *detector and trap variations (Fig. 11.1(b)2.)*** Logarithmic negativity in the parallel and linear orientation after evolution times $t = t_0\pi/4$. We use the parameters from Table 10.1. **a,** Entanglement as a function of angular variations with the first-order analytical expressions of Eq. (11.8) shown in gray. **b,** Entanglement as a function of fluctuations in the particle–shield separation in analogy to Fig. 11.3(c). **c,** Entanglement for combined variations $\xi^{(L)}_{A/B}$ and $\xi^{(\theta)}_{A/B}$ in both discussed orientations (black outlines) after an evolution time of $t = t_0\pi/4$. In the white region, the logarithmic negativity is zero.

Here, σ quantifies the width of each wave packet and d their spatial separation. The squeezing and displacement parameters are related by $r = -\log(\sigma/x_0)$ and a real displacement $\alpha = d/(4x_0)$ for an arbitrary scaling $\hat{x} = x_0(\hat{a} + \hat{a}^\dagger)$.
To quantitatively compare the entanglement generation of these generalised cat-states with the Gaussian and two-level limits discussed previously, we fix their position variance as

$$(\Delta x)^2 = \sigma^2 + \frac{d^2}{4(1+S)},$$

where $S = \langle\psi_+|\psi_-\rangle = \exp\{-d^2/(8\sigma^2)\}$ is the overlap between the two branches.

For $d = 0$, the state reduces to a single Gaussian wave packet with $\sigma = \Delta x$, recovering the Gaussian limit of Sec. 11.1. Conversely, for $d \to 2\Delta x$ (implying $\sigma \to 0$ and $S \to 0$), the state approaches the two-level cat-states analysed previously.

The time evolution of this state is obtained numerically in a truncated Fock basis. Ensemble averaging over the experimental parameters $\xi^{(L)}$ and $\xi^{(\theta)}$ is performed using exponentially convergent Gauss-Hermite quadratures.

As shown in Fig. 11.6 for the case of variations in detector-positioning, the en-

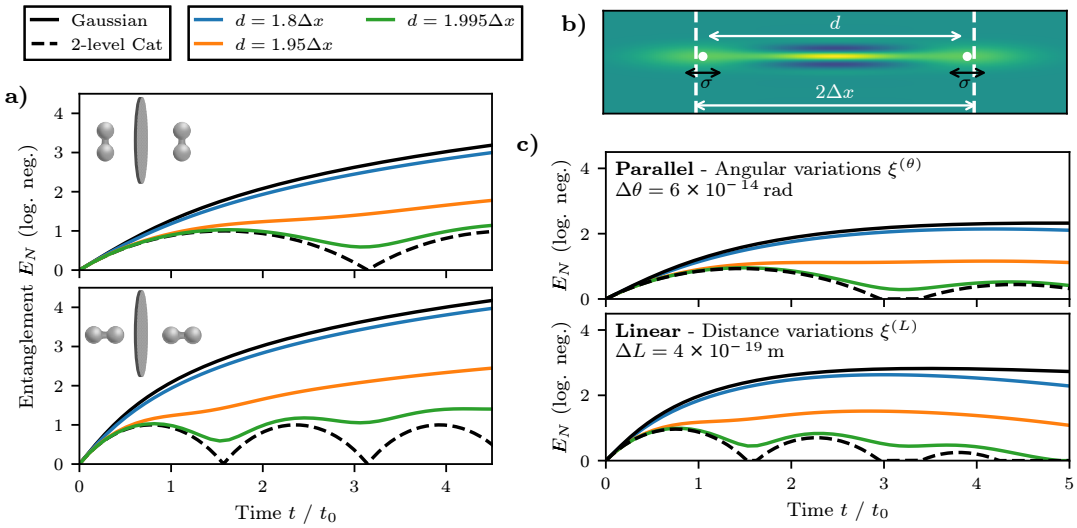


Figure 11.6: **Entanglement dynamics for continuous cat-states. a,** Logarithmic negativity E_N for continuous initial states interpolating between squeezed Gaussian states and two-level cat-states, computed numerically in a truncated Fock basis at zero temperature. Results are shown for the parallel (**top**) and linear (**bottom**) orientations with variations in detector positioning. For reference, the corresponding analytical solutions for Gaussian and two-level cat-states with identical position variance $(\Delta x)^2$ are shown in black. The initial linear growth of entanglement with rate $\Gamma_{\text{ent.}} = \partial_t E_N|_{t=0}$ is identical across the family of states; in agreement with Ref. [74]. **b,** Continuous cat-state in analogy to Eq. (11.9) with positional standard deviation Δx, where the parameter $d \in [0, 2\Delta x]$ interpolates between a fully Gaussian state ($d = 0$ and $\sigma = \Delta x$) and a two-level cat-state ($d \to 2\Delta x$ and $\sigma \to 0$). **c,** Entanglement dynamics including magnetic dipole coupling of superconducting lead particles to the shield. We show representative angular variations (parallel orientation, **top**) and separation variations (linear orientation, **bottom**), evaluated numerically using Gauss-Hermite quadratures. As in panel **a**, the behaviour interpolates continuously between the Gaussian and two-level cat-state limits.

tanglement dynamics interpolate smoothly between the Gaussian and two-level cat-state regimes. This confirms that the two classes of states are continuously connected.

12 Trap stability

We model fluctuations of the trapping potential by a stochastic force acting on each particle. The corresponding Hamiltonian is given by

$$\hat{H}_{\mathrm{Trap}} = \sum_{i=A,B} \left(\frac{1}{2} M\omega^2 \hat{x}_i^2 + \xi_i(t)\hat{x}_i \right), \tag{12.1}$$

where ω denotes the trap frequency and $\xi_i(t)$ are real-valued stochastic processes with units of force. They capture, for instance, slow drifts of the trap centre, fluctuating forces due to residual gas collisions, or attraction to the shield. Their effect is to shift the equilibrium position of the trapping potential by a distance $\xi_i^{(L)}(t) = \xi_i(t)/(M\omega^2)$. We limit ourselves to zero-mean, stationary noise that is uncorrelated across particles,

$$\langle \xi_i(t) \rangle = 0, \qquad \langle \xi_i(t)\xi_j(s) \rangle = \delta_{ij} C_i(t-s),$$

with exponentially decaying time correlations

$$C_i(\tau) = \Delta\xi^2 \, e^{-|\tau|/t_c},$$

where $\Delta\xi^2$ sets the noise strength and t_c the correlation time. Including gravitational interactions and the particle–shield couplings introduced in Sec. 10, the full Hamiltonian reads

$$\hat{H} = \sum_{i=A,B} \frac{\hat{p}_i^2}{2M} + \hat{H}_{\mathrm{Trap}} + \hat{H}_{\mathrm{Grav.}} + \hat{H}_{\mathrm{Cas./mag.\,Dip.}}. \tag{12.2}$$

12.1 Quasi-static limit

In the limit of long correlation times $t_c \gg t$, the noise correlator can be approximated as constant over the duration of a single realization of the experiment, $C_i(\tau) \simeq \Delta\xi^2$. In this regime, the stochastic force is effectively time-independent within a single experimental realization, corresponding to a static displacement of the trap centre, described by $H_{\mathrm{Trap}}(\hat{x}_i + \xi_i^{(L)})$ with $\xi_i^{(L)} \sim \mathcal{N}(0, \Delta L^2)$. The state of the system at a given time t is thus described by an ensemble of states, each evolved with randomly shifted equilibrium positions.

Expanding the Hamiltonian Eq. (12.2) to second order, the time evolution can be solved analytically within the Gaussian formalism (see Appendix C.3). The

corresponding entanglement dynamics for the parameters listed in Table 10.1 are shown in Fig. 12.1(a). At short times, the entanglement grows linearly, while

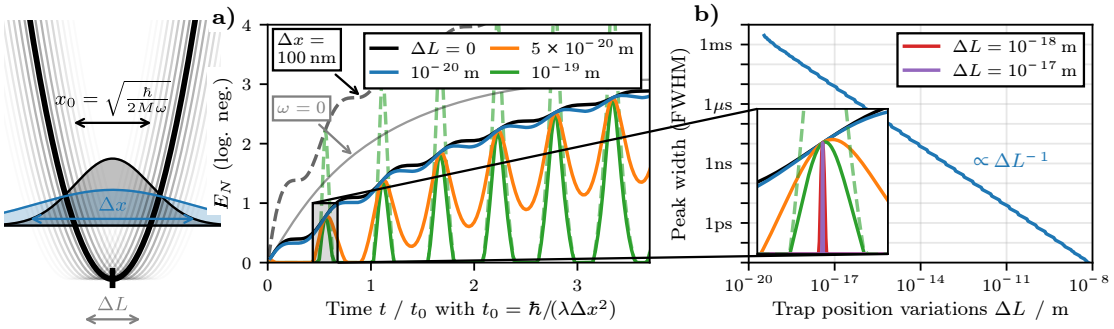


Figure 12.1: **Entanglement in the presence of quasi-static trap fluctuations. a,** Time evolution of the logarithmic negativity E_N for magnetically levitated superconducting lead particles in an harmonic trap ($\omega = 100 \times 2\pi$Hz) in the linear configuration. Time is expressed in units of $t_0 = \hbar/(\lambda \Delta x^2)$ with the gravitational coupling strength λ, corresponding to $t_0 \approx 9$ms for the superconducting lead particles shown here. Periodic oscillations arise from the harmonic motion of the trapped particles. Different run-to-run fluctuations ΔL of the trap centre are included. Nonzero entanglement is observable only near integer multiples of $T/2 = \pi/\omega'$. Continuous lines corresponds to $\Delta x = 50$nm, while dashed lines correspond to $\Delta x = 100$nm. **b,** Numerically determined peak-widths (FWHM) for different variations in seconds. We find, that FWHM $\propto 1/\Delta L$.

at later times, the dynamics exhibit periodic modulations due to the harmonic evolution of the trapped particles: For each realization, the Gaussian state rotates around the point $(x_{\text{eq}}, p_{\text{eq}}) = (\xi^{(L)}, 0)$ in phase space, with an effective frequency

$$\omega' = \sqrt{\omega^2 - \frac{\lambda + 12\delta + 6\eta}{M}},$$

where λ is the gravitational coupling strength and δ, η account for magnetic and Casimir particle–shield interactions, respectively.

In the absence of noise, all realizations follow identical unitary dynamics, and the entanglement grows monotonically in time, although the entanglement rate $\Gamma_{\text{ent.}} = \partial_t E_N$ exhibits periodic suppression while never vanishing exactly. This is reflected in the recurrent near-flat segments of the black curve in Fig. 12.1(a). This behaviour follows from $\Gamma_{\text{ent.}} \propto \Delta x^2$ [74] and from the time-dependence of the position variance

$$\Delta x(t) = \Delta x(0) \cos(\omega' t) + \frac{\Delta p(0)}{M\omega'} \sin(\omega' t).$$

For the strongly squeezed states, $\Delta x(0) \gg \Delta p(0)/(M\omega')$, the spatial width is minimised after a quarter period, $t = T/4$ with $T = 2\pi/\omega'$. At this time, the wave packet spread in position reaches $\Delta x(T/4) = \hbar/(2M\omega'\Delta x(0))$. As a consequence, the entanglement rate is large at the beginning of each cycle, strongly suppressed near odd multiples of $t = T/4$ and recovers again at later times. In contrast, weakly squeezed states exhibit significantly smaller oscillations in the entanglement rate.

In the presence of fluctuations, $\xi^{(L)} \neq 0$, the entanglement grows no longer monotonically and becomes strongly suppressed, whenever the position variance is small in the course of the time evolution. Averaging over random displacements leads to enhanced distinguishability of narrow wave packets, resulting in stronger decoherence and a corresponding reduction of entanglement. Conversely, at times $nT/2$ ($n \in \mathbb{N}$), when the position variance is maximal, the effect of displacements is minimised and the entanglement approaches the noiseless value.

In such realistic scenarios, entanglement becomes detectable only within narrow time windows centreed around multiples of $T/2$. We find that the size of these windows scales inversely with the amplitude of the fluctuations in the trap equilibrium position, i.e., $\propto 1/\Delta L$, as shown in Fig. 12.1(b).

While stronger squeezing increases the achievable entanglement, it also enhances sensitivity to positional fluctuations. Interestingly, the time window over which the entanglement remains non-zero is unaffected by the amount of squeezing and depends only on the fluctuation amplitude ΔL. Within this window, however, the maximum entanglement attained increases for more strongly squeezed states. Consider, for example, a moderate trap frequency of $\omega = 100 \times 2\pi\text{Hz}$ and the parameters from Table 10.1 for magnetically levitated lead particles, the position variance after a quarter of a period corresponds to an extremely small width $\Delta x(T/4) \sim 10^{-20}\text{m}$, which leads to an extreme sensitivity to static displacements at this point in time, with even minute variations of order $\Delta L \sim 10^{-20}\text{m}$ affecting the entanglement.

Reducing the squeezing mitigates this sensitivity but increases the entanglement generation time. The minimum required squeezing is therefore set by the available coherence time τ, the detectable entanglement threshold $E_{N,\min} \leq E_N(\tau)$, and the gravitational coupling λ. Expressed relative to the trap's ground-state width $x_0 = \sqrt{\hbar/(2M\omega)}$, the required delocalisation of the two identical particles is given by

$$\frac{\Delta x}{x_0} \geq \Delta x_{\min}\sqrt{\frac{2M\omega}{\hbar}} = \sqrt{\frac{3L_0^3\omega E_{N,\min}\log 2}{G\pi\rho\tau}} \tag{12.3}$$

where $L_0 = L/R$ and $E_N(t) \approx 2t/(t_0 \log 2)$, valid for small times $t \lesssim t_0$, was used in the last equality. For representative parameters $\tau \sim 1\text{s}$, $E_{N\min} = 10^{-2}$ and $L_0 = 1.5$ this corresponds to a squeezing parameter $r = -\log(\Delta x/x_0) \approx -8.3$, ($= 72\text{dB}$) which significantly exceeds currently achievable experimental squeezing

levels [62, 275, 276].

12.2 Markovian limit

The opposite regime of short correlation times $t_c \to 0$ corresponds to rapidly fluctuating forces. To obtain a well-defined limit, the correlator must be rescaled such that its integrated strength remains finite. We therefore write

$$C_i(\tau) = \frac{D}{t_c}\, e^{-|\tau|/t_c} \xrightarrow{t_c \to 0} 2D\delta(\tau)$$

which effectively describes Gaussian white noise with diffusion constant D.

In this limit, the dynamics reduce to a Markovian equation for the covariance matrix (see Appendix C.3),

$$\frac{\mathrm{d}\sigma}{\mathrm{d}t} = \Omega G \sigma + \sigma G^{\intercal} \Omega^{\intercal} + \mathcal{D},$$

where Ω denotes the symplectic form and G is the quadratic Hamiltonian matrix associated with Eq. (12.2). The diffusion matrix takes the form

$$\mathcal{D} = 2D \bigoplus_{i=A,B} \begin{pmatrix} 0 & 0 \\ 0 & 1 \end{pmatrix},$$

corresponding to independent momentum diffusion acting on each mode. As shown in Appendix C.3, this evolution for the covariance matrix is equivalent to the Lindblad master equation

$$\frac{\mathrm{d}\rho}{\mathrm{d}t} = -\frac{i}{\hbar}[\hat{H}, \rho] - \frac{D}{\hbar^2} \sum_{i=A,B} [\hat{x}_i, [\hat{x}_i, \rho]],$$

for the density matrix, which describes pure diffusion in position basis. Physically, this represents the action of random kicks on the particle, changing its momentum and thus translates into incoherent broadening of its phase space distribution.

The entanglement dynamics are shown in Fig. 12.2. In contrast to the quasi-static regime, the Markovian limit induces irreversible decoherence, and thus, no revivals of the entanglement are present. While the Hamiltonian coupling generates inter-particle correlations, the local diffusion process degrades these correlations, leading to a suppression of the entanglement rate. As a result, for sufficiently strong noise when the decoherence rate $\Gamma_{\text{dec.}} = D\Delta x^2/\hbar^2$ is equal to the entanglement rate $\Gamma_{\text{ent.}} \sim \lambda \Delta x^2/\hbar$, the dynamics become entanglement-breaking, preventing the buildup of non-classical correlations despite the presence of coherent interactions.

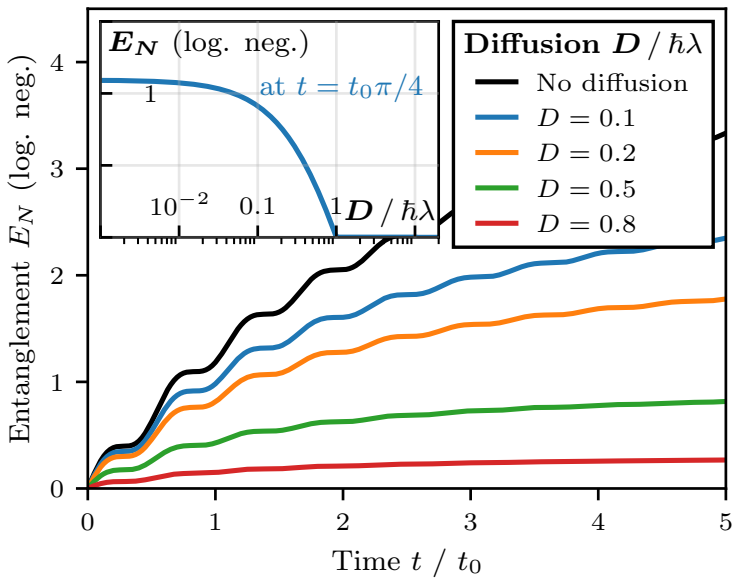


Figure 12.2: **Entanglement in the presence of Markovian trap fluctuations** Logarithmic negativity over time for different diffusion constants D. Here, D is measured in units of $\hbar\lambda$ and for $D = 1\hbar\lambda$, the entanglement rate $\Gamma_{\text{ent.}} = \partial_t E_N$ is precisely equal to the decoherence rate. Consequently, for larger diffusion, no entanglement is observable, as seen in the inset plot.

13 Quantum shield

Up to this point, the shield has been assumed to be a rigid plate with its position and orientation varying classically between runs. Accordingly, this has been captured by fluctuating Hamiltonian parameters. In the following, we now treat the shield as an explicit subsystem with its own quantum degrees of freedom coupled to those of the particles. Its modes are assumed to be thermally populated and interact with the particles through Casimir or magnetic dipole interactions, which, in general, contain both dispersive and dissipative components determined by the material response. We focus on the regime of low temperature and low material losses, where dissipative contributions are strongly suppressed and the interaction can be approximated by an effective coherent Hamiltonian term. In this regime, the shield may become entangled with the particles, thereby inducing decoherence, and additionally can also act as a coherent mediator of non-gravitational entanglement between them. Such contributions are undesirable, as they may mask gravitationally induced entanglement if comparable in strength. Since the goal of GIE experiments is to demonstrate entanglement mediated solely by gravity, any additional quantum channel would introduce a loophole in attributing the observed correlations to gravitational interaction. It is therefore important to bound non-gravitational entanglement and identify regimes ensuring genuine GIE. The mechanism of this entanglement mediation by the shield is similar in nature to previous findings of entanglement mediation by a massive object in a thermal state discussed in related contexts [30].

We describe the shield as a circular elastic plate of thickness d_s and radius r_s. Its vibrational eigenmodes can be obtained analytically and are expressed in terms of Bessel functions. Each mode is labelled by integers (k, l) with $k \in [1, \infty)$, $l \in [0, \infty)$ and their spatial profiles are denoted by $u_{kl}(r, \vartheta, t)$ with corresponding resonance frequencies ω_{kl}. Here, $r \in [0, r_s]$ and $\theta \in [0, 2\pi]$ denote the position on the shields surface in polar coordinates, while the thickness d_s is assumed to be constant everywhere, which is valid for a sufficiently thin plate. Explicit expressions are provided in Appendix C.2 and representative mode shapes are shown in Fig. 10.

Throughout the following analysis, we assume that the particle is positioned above the centre of the shield ($r_0 = 0$). Small displacements against the centre $r = r_0 \pm \xi^{(r)}$, however, do not affect the overall dynamics of the system considerably, as long as $\xi^{(r)} \ll r_s$. For realistic shields with non-uniform mass distribution, the ideal particle placement will have to be found experimentally to minimise the particle–shield interactions. We furthermore impose two conditions on the spatial

extent of the particle wave packets: (i) the delocalisation along the principal axis, Δx, is small compared to the radial length scale on which u_{kl} varies; and (ii) the delocalisation parallel to the shield, Δz, is sufficiently small so that the angular dependence of the mode can be neglected, i.e. u_{kl} may be treated as effectively constant in ϑ over the support of the wave packet.

Both conditions are well satisfied in our parameter regime, as the lowest-order modes vary only on scales set by r_s – much larger than the extent of the particles' main delocalisation. Coupling to higher-order modes is strongly suppressed and therefore does not contribute appreciably to the dynamics as seen in the following section.

Under these conditions, the mode shape can be locally linearized around the particles' positions as $u_{kl}(r,\vartheta) \approx u_{kl}(0,\vartheta_0) + r\,\partial_r u_{kl}\big|_{r=0,\vartheta=\vartheta_0}$. One can verify that the radial gradient $\partial_r u_{kl}\big|_{r=0}$ is maximal for $\vartheta_0 = 0$. Hence, we adopt this configuration to obtain a worst-case estimate on the noise induced on the particles by the dynamical shield.

Each vibrational mode behaves as an independent quantum harmonic oscillator of frequency ω_{kl} and effective mass

$$m_{\text{eff}} = \frac{m}{\pi r_s^2} \int_{\text{Shield}} r\mathrm{d}r\mathrm{d}\vartheta\, |u_{kl}(r,\vartheta)|^2,$$

where $m = \rho\pi r_s^2 d_s$ is the total mass of the shield. Quantising each mode leads to quadrature operators $\hat{q}_{kl} = \sqrt{\hbar/(2m_{\text{eff}}\omega_{kl})}(\hat{a}_{kl}^\dagger + \hat{a}_{kl})$ and $\hat{p}_{kl} = i\sqrt{\hbar m_{\text{eff}}\omega_{kl}/2}(\hat{a}_{kl}^\dagger - \hat{a}_{kl})$, whose thermal variances at temperature T fully describe the state and are given by

$$(\Delta q_{kl})^2 = \frac{\hbar}{2m_{\text{eff}}\omega_{kl}} \coth\!\left(\frac{\beta\hbar\omega_{kl}}{2}\right) \quad \text{and} \tag{13.1}$$

$$(\Delta p_{kl})^2 = \frac{m_{\text{eff}}\hbar\omega_{kl}}{2} \coth\!\left(\frac{\beta\hbar\omega_{kl}}{2}\right). \tag{13.2}$$

Here, $\beta = 1/(k_B T)$ and k_B is Boltzmann's constant. Equivalently, the thermal state of each mode can be written as

$$\rho_{\text{th},kl} = \int \mathrm{d}\alpha^2\, \frac{1}{\pi\bar{n}_{kl}} e^{-\frac{|\alpha|^2}{\bar{n}_{kl}}}\, |\alpha\rangle\langle\alpha|\,, \tag{13.3}$$

where the notation $\mathrm{d}\alpha^2 = \mathrm{d}\,\mathrm{Re}\,\alpha\,\mathrm{d}\,\mathrm{Im}\,\alpha$ is used and $\bar{n}_{kl} = 1/(\mathrm{e}^{\beta\hbar\omega_{kl}} - 1)$ is the average thermal occupation number of mode (k,l). The full state of the shield is thus given by $\rho_{\text{Shield}} = \bigotimes_{(k,l)} \rho_{\text{th},kl}$.

Two-level cat-states in front of the shield can therefore be initially described by the joint state $\rho_0 = |\psi_{\text{Cat}}\rangle\langle\psi_{\text{Cat}}| \otimes \rho_{\text{Shield}}$. The combined time evolution of particles together with the shield can be performed analytically and is provided in

Appendix C.4.

In the Gaussian-state formalism, we describe the shield modes by the quadrature set $(\{\hat{q}_{kl}, \hat{p}_{kl}\})$. The initial covariance matrix of the two particles and the shield is then given by

$$\sigma = \sigma_{\text{Particles}} \oplus \bigoplus_{(k,l)} \begin{pmatrix} (\Delta Q_{\text{kl}})^2 & 0 \\ 0 & (\Delta P_{\text{kl}})^2 \end{pmatrix}$$

where $\sigma_{\text{Particles}}$ is the covariance matrix for squeezed particles as in Sec. 11.1.

To extract the bipartite entanglement between both particles, we first must trace out the shield after the time evolution. For the cat-states, this is done by performing the usual partial trace, whereas in the Gaussian formalism, one can simply discard all covariance-matrix elements associated with the shield modes [273].

13.1 Decoherence effects of a quantum shield

We analyse the decoherence effects due to the presence of a quantum shield interacting with the particles in GIE experiments. We constrain our analysis to the parallel orientation only, as particles in the linear orientation are prone to entanglement mediated via the shield, as discussed in detail in the next section. Although the linear orientation could in principle be treated analogously, for our parameters the non-gravitationally mediated entanglement would obscure the gravitational signal, making the parallel configuration favourable for assessing gravitationally induced entanglement. To investigate the interplay between gravity and shield dynamics, we consider the Hamiltonian

$$\hat{H} = \hat{H}_{\text{Gravity}} + \hat{H}_{\text{Shield}} \tag{13.4}$$

where the shield dynamics are governed by

$$\hat{H}_{\text{Shield}} = \sum_{(k,l)} \left[\hat{H}_{kl} + \hbar\omega_{kl} \left(\hat{a}^\dagger_{kl} \hat{a}_{kl} + \tfrac{1}{2} \right) \right] \tag{13.5}$$

with $\hat{H}_{kl}$ describing the Casimir- or magnetic dipole coupling between the particles and the (k,l) vibrational mode of the shield and is presented in Appendix C.2. After linearising the mode-profile u_{kl} around the particles positions, $\hat{H}_{\text{Shield}}$ can be expanded to second order in its position operators $\{\hat{x}_A, \hat{x}_B, \hat{q}_{kl}\}$, allowing us to solve the time evolution analytically in the case of two-level cat-states, as shown in Appendix C.4.

Generally, the shield supports an infinite set of mechanical eigenmodes, however, only the lowest modes contribute considerably to shield-induced decoherences. In the high-temperature limit $\hbar\omega_{kl} \ll k_B T$, which is well-satisfied for $T \gtrsim 10^{-9}$K and

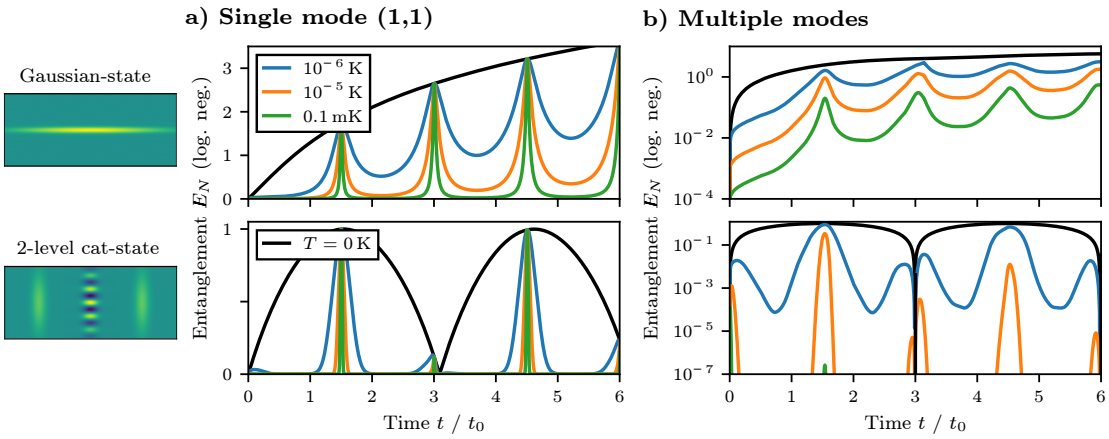


Figure 13.1: **Entanglement dynamics in a GIE setup in the presence of a quantum dynamical shield.** Results are shown for delocalised superconducting lead particles interacting with the shield via magnetic dipole interactions prepared in the parallel orientation ($\theta = 0$), for which the gravitational signal is most robust against noise. The parameters from Table 10.1 were used with a Niobium shield of size $d_s = 2\mu$m and $r_s = 1$cm. If the particle–shield couplings are dominated by Casimir interactions instead, the corresponding dynamics are shown in Fig. 12. **a,** Entanglement dynamics for Gaussian states (**top**) and two-level cat-states (**bottom**) with the shield dynamics restricted to the dominant $(1,1)$-mode only. Symmetry dictates that this mode provides the leading contribution to shield-induced decoherence in the parallel configuration. Partial revivals of gravitationally generated entanglement occur near times $t = 2\pi j/\omega_{(1,1)}$ ($j \in \mathbb{N}$), where the single mode periodically re-phases. The peak widths $\sqrt{\omega_{(1,1)}/T} \sim \sqrt{d_s/(r_s^2\, T)}$ decrease with increasing temperature. **b,** Corresponding dynamics where multiple shield modes are included (here: first 64 modes). Because the modes have incommensurate frequencies, no time exists at which all modes simultaneously return to their initial quadratures and hence, the particles never fully decouple from the shield.

typical mode frequencies $\omega \sim 50 - 200\text{s}^{-1}$, the variance of the oscillation amplitude scales as $\Delta q_{kl} \sim \omega_{kl}^{-1}$. Therefore, low-frequency modes dominate the interaction.

The resulting entanglement dynamics for two-level cat-states and Gaussian states are shown in Fig. 13.1 and Fig. 12. One can see, that the quantum shield suppresses the bipartite entanglement generated by gravity. Although a single mode would periodically decouple from the particles at times $t = 2\pi j/\omega_{kl}$ ($j \in \mathbb{N}$), the shield hosts many modes with distinct and incommensurate frequencies. Consequently, the collective shield never returns to its initial configuration and the

particles therefore never fully disentangle from the shield. This leads to the persistent degradation of gravitationally induced entanglement.

We furthermore want to stress that the dynamics and entanglement suppression is strongly dependent on the size of the shield. As $\omega_{kl} \sim d_s/r_s^2$, reducing the radius r_s or increasing the thickness d_s increases the eigenfrequencies and hence reduces the thermal fluctuations. While the minimal shield radius is limited by the suppression of direct Casimir, electrostatic or magnetic couplings, the thickness can, in principle, be increased up to $d_s \sim 2(L-R)$. The resulting entanglement after a constant time for different thicknesses d_s is shown in Fig. 13.2. This statement, however, only applies to noise induced by shield vibrations. Increasing the shield thickness may instead increase noise arising from placement variations, as a thicker shield reduces surface-to-surface distance between the shield and the particles and thus increases the relevant interactions.

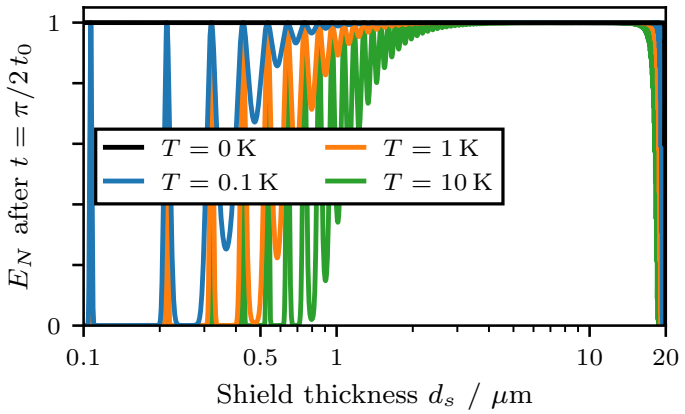


Figure 13.2: **GIE for different shield thicknesses.** Logarithmic negativity E_N after an evolution time of $t = \pi/2\,t_0$ (where $E_N(T = 0\mathrm{K}) = 1$) in the parallel orientation for different shield thicknesses d_s. Here we show silica particles interacting with a copper shield via Casimir interactions. The decoherence strongly depends on the vibrational frequencies $\omega \sim d_s$, where a higher frequency increases the stability. For $d_s \to 2(L-R) = 20\mu$m, the surface-to-surface separation between the shield and the particles becomes very small and thus Casimir interactions increase, resulting in more decoherence.

13.2 Non-gravitationally mediated entanglement

We analyse bipartite entanglement between two particles arising exclusively from their mutual Casimir or magnetic dipole coupling to the quantum shield, while gravitational interactions are completely neglected in this section. Such mediated

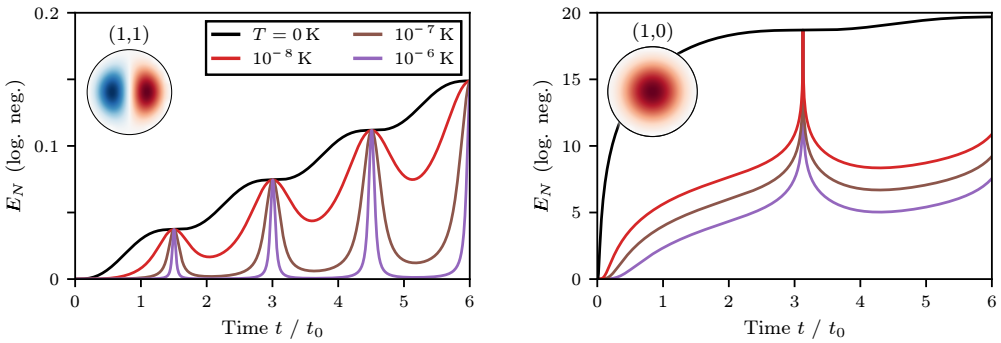


Figure 13.3: **Shield-mediated entanglement in the absence of direct particle–particle coupling.** Logarithmic negativity between two lead particles prepared in Gaussian states interacting exclusively through their common magnetic dipole coupling to the quantum shield. The dynamics are shown for different shield temperatures T and for the parameters from Table 10.1. **Left:** parallel orientation ($\theta = 0$), for which symmetry enforces that the dominant contribution arises from the $(1,1)$ vibrational mode. **Right:** linear configuration ($\theta = \pi/2$), for which the strong coupling is governed primarily by the $(1,0)$-mode, whose displacement is maximal at the shields centre. In both cases, the shield acts as an entanglement mediator, producing peaks in $E_N(t)$ of width $\sim \sqrt{\omega_{kl}/T}$ at times $t = 2\pi j/\omega_{kl}$ ($j \in \mathbb{N}$). The black curves show the zero-temperature limit. For clarity, only the dominant single mode is displayed here.

entanglement through a thermal reservoir is similar to related effects considered in Ref. [30]. The dynamics are fully governed by $\hat{H}_{\mathrm{Shield}}$ in Eq. (13.5). The induced entanglement depends sensitively on the spatial profile u_{kl} at the particles positions and on whether the particles are oriented parallel or orthogonal relative to the shield.

As discussed previously in Sec. 11, the parallel orientation ($\theta = 0$) is intrinsically robust against fluctuations in the particle–shield separation. In this case, the dominant coupling is set by the radial gradient $\partial_r u_{kl}\big|_{r=0,\vartheta=0}$, reflecting variations in the separation distance under radial displacement. It induces relative phases between components of a state delocalised parallel to the shield. The lowest mode with non-zero gradient is $(1,1)$. Its contribution leads to a weak but finite amount of shield-mediated entanglement, as shown in Fig. 13.3. The effect remains small because (i) the coupling is proportional to the gradient of the large Faraday shield rather than its absolute displacement at the centre, and (ii) the $(1,1)$-mode possesses a comparatively high resonance frequency, which suppresses its thermal amplitude and hence its gradient.

In contrast, the linear configuration ($\theta = \pi/2$) is highly sensitive to changes in the particle–shield separation. For a particle placed at the shield's centre, the $(1,0)$-

mode dominates, since its displacement attains a maximum at $r = 0$. Even at temperatures as low as 10^{-8}K, the displacement amplitude $u_{(1,0)}(r = 0)\Delta q_{(1,0)} \approx 1.4 \times 10^{-14}$m exceeds the tolerance threshold on variations in the particle–shield separation established earlier in Sec. 11. Consequently, this yields a strong coupling between the particles and the low-frequency $(1, 0)$-mode, sufficient to mediate appreciable bipartite entanglement in the absence of any direct particle–particle interaction, as shown in Fig. 13.3.

Note, that the particle–shield coupling can get worse if the particle is not perfectly positioned in the centre or if the shield is not completely homogeneous. In such cases, the fundamental mode $(1, 0)$ would also mediate small amount of additional entanglement between particles in the parallel configuration, worsen the situation discussed here.

14 Experimental implications

The analysis presented allows us to identify the dominant constraints for realistic implementations of GIE experiments. In particular, the interplay between non-gravitational interactions, geometric stability, timing precision and particle–shield couplings place strong requirements on experimentally viable platforms.

Even in the absence of interactions with the shield, slow fluctuations of the trap equilibrium position – arising, for instance, from uncontrolled external forces – can significantly constrain the recoverable entanglement, even when they occur only from run to run. In particular, such fluctuations confine non-zero entanglement to narrow time windows around the trap oscillation period, whose width decreases with increasing fluctuation amplitude. This, in turn, imposes stringent requirements on both the stability of the trapping potential and the timing precision of the measurements.

A second limitation particularly relevant for magnetically levitated systems are dominant magnetic-dipole couplings. External trapping fields induce dipole moments in the particles, which constitute a strong non-gravitational interaction between the particles as well as between the particles and a shield. As a consequence, magnetically levitated setups require extremely tight control of the experimental geometry, with tolerable variations in the relative placement and orientation of the detectors and the shield on the order of $\Delta L = 10^{-18}\,\mathrm{m}$ and $\Delta\theta = 10^{-13}\,\mathrm{rad}$, as seen in Figs. 11.2-11.5.

In other GIE implementations, like free-fall or space-based implementations, where trapping potentials are absent during the entanglement generation step, the dominant non-gravitational couplings arise from Casimir interactions of the particles with the shield or from residual electrostatic or magnetostatic fields. Geometric stability remains a major challenge, with tolerable variations of at least $\Delta L = 4 \times 10^{-15}\mathrm{m}$ and $\Delta\theta = 10^{-9}\mathrm{rad}$ required in order to preserve the gravitationally generated entanglement signal (see Figs. 11.2-11.5). These variations strongly depend on the orientation of the principal delocalisation axes of the particles and can be estimated analytically by Eq. (11.8). We find that the parallel configuration, in which the principal delocalisation axis lies parallel to the shield is considerably more stable against variations in the position. The linear configuration, where particles are oriented perpendicular to the shield, exhibits advanced stability against orientation noise. The choice of orientation therefore provides an additional degree of freedom for optimising experimental robustness.

We also find that the orientation of the experimental apparatus itself has to account for the change of the effective direction of the gravitational pull of the

Sun and other celestial bodies, which varies due to Earth's rotation. It is worth noting that, in all cases considered here, independent measurements of the relative positions between all relevant objects can be used to mitigate decoherence in post-processing. Additionally, even a perfectly static configuration can lead to decoherence if there is uncertainty in the duration of experimental evolution times.

In Chapter 13, we further investigated the role of the shield whose vibrational degrees of freedom are treated dynamically. Thermally populated vibrational modes were shown to induce decoherence via entanglement with the particles and, simultaneously, to mediate non-gravitationally induced entanglement between them, thereby potentially obscuring the gravitational signal. The resulting decoherence rates depend sensitively on the shield's geometry and size: reducing the lateral extent of the shield or increasing its thickness, substantially suppresses the coupling between vibrational modes and the particles. Modifying the shield geometry to a non-planar shield (like a concave parabolic or hollow half-spherical shield that is thin at its centre and thicker towards the edges) can simultaneously reduce static Casimir forces (as suggested by Refs. [277, 278]) and suppress vibrational amplitudes further.

Part IV

Discussion

Levitated nanoparticles, free from any mechanical suspension or clamping, combine exceptional isolation from their environment with the ability to prepare, control and read the translational and rotational degrees of freedom. This thesis exploits this property along two distinct routes to reach parameter regimes of fundamental physics that have so far been out of reach: The exceptional hyperpolarisability of pentacene-doped naphthalene opens the door to a new material platform for matter-wave interferometry and tests of spin-rotation coupling, bringing new collapse-model bounds and signatures of the nuclear Einstein-de Haas and Barnett effects within reach of near-term experiments (Part II). The second route turns to a property every levitated particle possesses regardless of its internal structure: its mass, which makes it a natural candidate for probing the quantum nature of gravity itself, provided the electromagnetic interactions that otherwise dominate at the required separations can be suppressed. The electromagnetic shielding needed to isolate a gravitational entanglement signal turns out to introduce decoherence and mediate entanglement of its own, and identifying the stability requirements any such experiment must satisfy to make this regime experimentally accessible is the central task of Part III. The following sections discuss each contribution in turn, before a shared outlook closes the chapter.

While diamond nanoparticles hosting NV centres have so far been the primary platform pursued for Stern-Gerlach-type matter-wave interferometry [27–29], the negatively charged NV centre and residual electronic impurities introduce noise channels that are difficult to eliminate [29–31]. Optically hyperpolarised organic crystals offer a compelling alternative host material for spin-based levitated optomechanics, and pentacene-doped naphthalene serves as the case study developed here. By using photo-excited electron spins only transiently, to hyperpolarise the nuclear-spin ensemble via dynamic nuclear polarisation before decaying away, this approach removes the associated decoherence channels once polarisation transfer is complete, circumventing the limitation at its root. Combined with polarisation levels exceeding 80 % and lifetimes above 920 h at cryogenic temperatures [32–36], together with the possibility to grow naphthalene crystals extraordinarily clean and the lack of dangling surface bonds, this material provides an exceptionally clean environment for coherent spin-dependent experiments.

This thesis develops three applications on this basis, each opening a regime beyond the reach of current experiments. Levitation opens the door to magic-angle spinning at frequencies no mechanically mounted rotor could sustain. In conventional solid-state NMR, magic-angle spinning extends T_2 by averaging anisotropic interactions [210], but state-of-the-art rotors are capped at frequencies of order 100 kHz by mechanical stress. Free from any mechanical contact, a levitated particle can in principle spin orders of magnitude faster, limited only by friction due to residual surrounding gas and the tensile strength of the material itself [15, 211–213], suppressing anisotropic spin interactions to a degree previously unattainable and extending nuclear spin coherence times well beyond conventional NMR.

The same platform, combined with the large collective nuclear polarisation of hyperpolarised naphthalene, paves the way for a multi-spin Stern-Gerlach interferometry protocol that avoids the torque instabilities inherent to colour-centre-based schemes. Because the nuclear spins are homogeneously distributed through the crystal with no preferential quantisation axis, the undesirable torques that plague other interferometer designs are strongly suppressed; and although the nuclear gyromagnetic ratio is orders of magnitude smaller than the electronic one, the achievable splitting grows with the collective spin as $\sqrt{N}$, so a sufficiently large polarised ensemble outweighs this disadvantage and produces position delocalisations beyond what a single electron spin could achieve. Combined with pulsed control of the nuclear ensemble and a magnetisation-induced displacement readout, this protocol could improve on existing bounds for the free parameters of collapse models such as the CSL model. The proposed readout principle, detecting a levitated particle's nuclear-spin polarisation through its displacement rather than through bulk magnetisation, is itself new, with a qualitative advantage over conventional detection: its sensitivity is governed by the long relaxation time T_1 rather than the short coherence time T_2.

Beyond interferometry, the same nuclear-spin ensemble opens the door to a different class of phenomena, arising from the coupling between nuclear-spin angular momentum and mechanical rotation. We exploit this coupling in two complementary directions. First, we identify the nuclear polarisation as a macroscopic angular-momentum reservoir, proposing a way to achieve the first direct observation of the nuclear Einstein-de Haas effect. As polarised nuclear spins relax with their characteristic T_1, they transfer their angular momentum to the lattice which is then converted into mechanical rotation due to conservation of angular momentum. Second, we show that the high rotation frequencies accessible to levitated particles induce a measurable nuclear Barnett polarisation, detectable through the same displacement-based detection scheme used already to read out the interferometer's signal. A detailed noise analysis, including the rotational dynamics of asymmetric particles in a diamagnetic trap and potential limitations such as quadrupole locking and air friction, supports the feasibility of both measurements within realistic experimental parameters.

Beyond the three protocols discussed above, the large collective nuclear spin of levitated hyperpolarised naphthalene points to further applications as a precision sensor due to the combination of a macroscopic number of polarised spins and the sensitive coupling between the nuclear spin degrees of freedom and the centre-of-mass motion. For a suitable choice of interferometer parameters, the spin state recovered at the end of the Stern-Gerlach interferometer is not simply the initial coherent spin state but a spin-squeezed state [279,280] of the form $e^{-\beta \hat{S}_z^2}|N\rangle$, where $|N\rangle$ denotes the state with all N nuclear spins polarised along the quantisation axis. Since N can reach millions of nuclear spins or more in a levitated naphthalene particle, this would constitute a spin-squeezed state at a scale far beyond what has been achieved to date. Spin-squeezed states are a well-established resource for

quantum-enhanced sensing, as they allow precision below the standard quantum limit set by an uncorrelated ensemble [281,282]. Such a squeezed nuclear ensemble could be used either to measure magnetic fields with a precision beyond that of an unsqueezed ensemble of the same size, or in dark-matter searches, since several proposals have identified precision NMR experiments as a sensitive probe of the oscillating nucleon-spin coupling induced by axion and axion-like-particle dark matter [283]. Therefore, levitated, hyperpolarised naphthalene has considerably more to offer than the three directions pursued here, and we expect this to motivate further work. Taken together, levitated hyperpolarised naphthalene emerges as a versatile platform spanning matter-wave interferometry, tests of spin-rotational coupling and high-precision metrology.

It is, moreover, only one representative of a broader class of optically polarisable materials to which this analysis largely transfers: p-dibromobenzene doped with p-dichlorobenzene [284] and p-terphenyl doped with pentacene [285], for instance, exhibit substantially lower particle losses at room temperature and may offer practical advantages depending on the application at hand. The Barnett protocol itself needs no hyperpolarisation at all and extends directly to any diamagnetic solid with sufficient nuclear spin density, such as ^{13}C-enriched nanodiamond or ^{29}Si-enriched silica. The analysis developed here provides the toolbox needed to work out the correct parameter regimes and expected sensitivity for any alternative material.

Certain limitations apply. The material properties underlying this analysis, such as the refractive index and heat capacity of naphthalene, were measured in bulk samples over restricted temperature and pressure ranges, and their behaviour in levitated nanoscale particles remains to be experimentally confirmed. This constrains the precision of the present estimates, but it also opens an unexplored opportunity: levitation itself provides a means of probing these material properties in a regime no one has yet charted.

Altogether, the results of this part make a compelling case for levitated, optically hyperpolarised organic crystals as a versatile and largely unexplored platform for quantum sensing and fundamental physics tests.

Gravitationally induced entanglement (GIE) offers a tabletop probe of the quantum nature of gravity: if two massive particles held in spatial superposition become entangled purely through their mutual gravitational attraction, that entanglement cannot arise from local operations and classical communication alone [51–53]. Advances in levitated-mass quantum control have turned this thought experiment into an active experimental target, with proposals spanning optical, magnetic, free-fall and space-based platforms [66–68]. In all of these, electromagnetic interactions at the required micrometre separations vastly exceed the gravitational signal, motivating a conducting Faraday shield placed between the particles [79,80]. However, such a shield couples to the particles via Casimir and magnetic-dipole fields, introducing relative phases. Moreover, its own vibrational modes can me-

diate entanglement of their own.

While shield-induced effects, discussed below, constitute the dominant limitation identified in this thesis, fluctuations of the trapping potential impose a separate, non-negligible constraint in trapped setups, arising even in the complete absence of any particle-shield interaction. Such fluctuations confine the recoverable entanglement to narrow windows around the trap oscillation period, whose width shrinks as the fluctuation amplitude grows, tightening the demands on both trapping-potential stability and measurement timing.

Among the shield-induced effects, magnetic dipole interactions place the most stringent limitation on magnetically levitated implementations: the trapping field induces dipole moments in the particles that couple strongly to the shield, demanding placement and orientation tolerances of order $\Delta L = 10^{-18}\,\mathrm{m}$ and $\Delta\theta = 10^{-13}\,\mathrm{rad}$, comparable to a thousandth of a proton's radius or the displacement sensitivity of kilometre-scale gravitational-wave detectors such as LIGO [286], despite arising here on a micrometre-scale tabletop experiment. Free-fall and space-based implementations, lacking a trapping potential during entanglement generation, are instead limited by residual Casimir couplings to the shield, requiring somewhat less extreme, but still demanding, tolerances of $\Delta L = 4 \times 10^{-15}\,\mathrm{m}$ and $\Delta\theta = 10^{-9}\,\mathrm{rad}$. In both cases, the orientation of the particles' delocalisation axes relative to the shield offers a means of trading positional against orientational robustness: a configuration with the delocalisation axis parallel to the shield is more robust against positional variations, while a perpendicular configuration better resists orientation noise. Furthermore, the direction of the dominant gravitational pull itself varies over the course of the experiment as the Earth rotates, an effect the apparatus orientation must account for. Independent monitoring of the relative positions can mitigate the resulting decoherence in post-processing, though timing uncertainty alone can still degrade an otherwise static configuration.

Treating the shield's vibrational modes as a genuine quantum multi-mode system, rather than a static boundary, reveals another limitation: the very element intended to suppress electromagnetic interactions between the particles can itself act as a massive mediator of entanglement [30]. Because each particle couples to the shield, this shared coupling can entangle the two particles even in the complete absence of any gravitational interaction between them, an effect that persists whether the shield's vibrational modes occupy their ground state or a thermal state. Thermally populated modes additionally decohere the particles while simultaneously mediating this non-gravitational entanglement, an effect that depends sensitively on the shield's geometry and can be suppressed by reducing its lateral extent, increasing its thickness, or departing from a planar geometry in favour of a concave or hollow shield that is thin at the centre and thicker at the edges, which also reduces static Casimir forces [277, 278]. This mechanism is distinct from surface-induced electromagnetic noise as captured by macroscopic dielectric-response frameworks [287]: whereas the latter arises even for a perfectly

fixed shield through coherent and thermally driven surface fluctuations, the decoherence identified here originates from stochastic geometric variations of the shield itself and does not rely on thermal excitation.

All limitations are captured within a single, setup-independent framework developed here, extending beyond earlier setup-specific treatments [80, 254] to apply uniformly across trapping platforms and shield geometries. Within it, the degradation of entanglement and the associated stability requirements turn out, at short times, to be identical in order of magnitude regardless of whether the particles are prepared as Schrödinger-cat states or Gaussian squeezed states, provided the position variance $(\Delta x)^2$ is matched, a result not previously established for either class of state in this context.

Several extensions of this framework suggest themselves. The shield geometry could be optimised more systematically. Furthermore, setup-specific analyses could be conducted by replacing the simplified mode treatment used here by a realistic phonon spectral density obtained from the true material dispersion and three-dimensional shield geometry used in the specific experiment, which would rely heavily on numerics. The present analysis also omits patch charges: static, spatially varying surface potentials arising from adsorbates, grain boundaries, or polycrystalline structure are a well-documented source of anomalous electric-field noise and spurious forces in ion-trap and Casimir-force experiments [288], and an equivalent treatment for the shield considered here would establish whether patch-charge-induced forces on the particles impose tolerances beyond those already derived from the idealised vibrational and Casimir couplings. A further direction is to search for initial states intrinsically more robust to the placement and orientation variances identified above, rather than accepting the stability requirements derived here for Gaussian squeezed and Schrödinger-cat states. Finally, translating the setup-independent bounds derived in this part into specifications for one concrete experimental proposal, incorporating realistic values for seismic and acoustic noise, stray electromagnetic fields and shield material properties, would complement the general toolbox developed here and connect directly to ongoing efforts to design GIE experiments.

In sum, these results establish quantitative bounds on the placement precision, angular stability, measurement timing, temperature and shield geometry that any GIE experiment employing electromagnetic shielding must satisfy, regardless of the specific trapping platform chosen. The shield, introduced to suppress unwanted electromagnetic interactions, must itself be characterised and controlled with extreme care before an observed entanglement signal can be attributed to gravity, and magnetically levitated implementations face the most stringent obstacles among the platforms considered. The general toolbox developed here for evaluating shield-induced decoherence and spurious entanglement applies to any GIE proposal, independent of the specific choice of trap, shield material or particle state.

A few caveats remain. The bounds derived here isolate the geometric and vibrational contributions of the shield and do not incorporate the intrinsic, temperature-dependent electromagnetic surface noise captured by dielectric-response frameworks [287]. A complete assessment of any realistic setup will need to combine both mechanisms. Likewise, achieving the sub-attometre and sub-nanoradian tolerances identified for magnetically levitated and free-fall implementations, respectively, will require dedicated advances in metrology and active stabilisation beyond what has been demonstrated to date. Taken together, the results of this part give a clear roadmap of the control an experimentalist needs to exert over the setup in order to certify GIE.

Overall, the two directions pursued in this thesis point beyond their individual results to a broader development: levitated optomechanics is maturing from a tool for demonstrating quantum control of a single mechanical mode into a versatile platform for fundamental physics. Engineering the internal degrees of freedom of a levitated particle, as with the hyperpolarised nuclear-spin ensemble of naphthalene, and rigorously characterising the auxiliary structures, such as electromagnetic shields, needed to isolate a signal of interest, are both necessary steps along this trajectory. The concepts and tools developed in this thesis contribute concretely to the development of the field and bring tests of collapse models, spin-rotation coupling and the quantum nature of gravity a step closer to experimental reach.

Appendices

A Naphthalene in a Stern-Gerlach Type Interferometer

A.1 Spin Dynamics in a Quadrupole Magnetic Field

While we assumed a magnetic field of the form $\vec{B} = (B'\hat{x} + B_0)\vec{k}$ in the main text, where $\vec{k}$ defines the quantisation axis of the spins. This field does not satisfy Maxwell's equations which dictate that the magnetic field has to be free of divergences, namely $\nabla \cdot \vec{B} = 0$. This requires at least one other component perpendicular to $\vec{k}$. One simple variant that fulfills Maxwell's equations is given by the 2D quadrupole field $\vec{B} = (-B'\hat{z}, 0, B'\hat{x} + B_0)$. This field provides a confinement in one additional dimension and could, in principle, induce spin transitions. The corresponding Hamiltonian of this configuration is given by

$$\begin{aligned}\hat{H} =& \frac{\hat{p}_z^2 + \hat{p}_x^2}{2m} - \frac{\chi_V V}{2\mu_0}\left[(B'\hat{z})^2 + (B'\hat{x})^2\right] + \frac{\hbar}{2}B'\gamma_p \sum_{n=1}^{N}\left(-\hat{z}\hat{\sigma}_x^{(n)} + \hat{x}\hat{\sigma}_z^{(n)}\right) \\ &+ \frac{\hbar}{2}B_0\gamma_p \sum_{n=1}^{N}\hat{\sigma}_z^{(n)}. \end{aligned} \tag{A.1}$$

By switching to ladder operators defined by $\hat{x}_i = \sqrt{\hbar/(2m\omega)}(\hat{a}_i^\dagger + \hat{a}_i), \hat{p}_i = i\sqrt{\hbar m\omega/2}(\hat{a}_i^\dagger - \hat{a}_i)$, the Hamiltonian can be rewritten to find

$$\begin{aligned}\hat{H} =& \hbar\Omega(\hat{a}_z^\dagger\hat{a}_z + \hat{a}_x^\dagger\hat{a}_x) + \frac{\hbar}{2}\Gamma\left[-(\hat{a}_z^\dagger + \hat{a}_z)\sum_{n=1}^{N}\hat{\sigma}_x^{(n)} + (\hat{a}_x^\dagger + \hat{a}_x)\sum_{n=1}^{N}\hat{\sigma}_z^{(n)}\right] \\ &+ \frac{\hbar}{2}\omega_0\sum_{n=1}^{N}\hat{\sigma}_z^{(n)} \end{aligned} \tag{A.2}$$

where we defined

$$\Omega = \sqrt{\frac{|\chi_V|}{\rho\mu_0}}B', \quad \Gamma = \gamma_p B'\sqrt{\frac{\hbar}{2m\omega}} \quad \text{and} \quad \omega_0 = \gamma_p B_0. \tag{A.3}$$

Here, Ω is the mode frequency, and Γ the coupling strength between the modes and the spins. We write the Pauli matrices in spin-ladder operators as $\hat{\sigma}_x = \hat{\sigma}_+ + \hat{\sigma}_-$ and by switching into a rotating picture with respect to $\hbar\Omega(\hat{a}_z^\dagger\hat{a}_z + \hat{a}_x^\dagger\hat{a}_x) + \frac{\hbar}{2}\omega_0\sum_{n=1}^{N}\hat{\sigma}_z^{(n)}$

we find

$$\hat{H}^I_{\rm int} = \frac{\hbar}{2}\Gamma\sum_{n=1}^{N}\big[-(\hat{a}_z^\dagger e^{i\Omega t}+\hat{a}_z e^{-i\Omega t})(\hat{\sigma}_+^{(n)}e^{i\omega_0 t}+\sigma_-^{(n)}e^{-i\omega_0 t}) \\ +(\hat{a}_x^\dagger e^{i\Omega t}+\hat{a}_x e^{-i\Omega t})\hat{\sigma}_z^{(n)}\big]$$

For $B' = 10^4\mathrm{T/m}$, the trap frequency is given by $\Omega = 130(2\pi)\,\mathrm{Hz}$. For a particle of 100 nm radius, the coupling strength is given by $\Gamma = 50(2\pi)\,\mathrm{Hz}$. As the eigenfrequency of the nuclear spins is given by $\omega_0 = \gamma_p B_0$, already at a magnetic field of $B_0 = 1$ mT, $\omega_0 = 43(2\pi)\,\mathrm{kHz}$, ensuring that the spins are far detuned from Ω. Thus, in most experimentally relevant configurations, we have that $\omega_0 \gg \{\Gamma, \Omega\}$, and we can safely discard terms rotating at frequencies $\omega_0 \pm \Omega \gg \Gamma$

$$\hat{H} = \hbar\Omega(\hat{a}_z^\dagger\hat{a}_z + \hat{a}_x^\dagger\hat{a}_x) + \frac{\hbar}{2}\Gamma(\hat{a}_x^\dagger + \hat{a}_x)\sum_{n=1}^{N}\hat{\sigma}_z^{(n)} + \frac{\hbar}{2}\omega_0\sum_{n=1}^{N}\hat{\sigma}_z^{(n)}. \tag{A.4}$$

That is, the coupling of the spins to the x_1 mode will generally be highly non-resonant and its effect negligible. This justifies the use of a one dimensional gradient in the analysis provided in the main text.

A.2 Decoherence Between $\kappa^{\rm th}$ and $\kappa'^{\rm th}$ Wave Packet

In this section, we want to find an expression for $\mathrm{tr}\{\hat{\rho}_{\kappa,\kappa'}(T_{\rm tot})\}$ in the presence of the CSL model. Using Eq. (7.18), together with Eq. (7.9), the master equation governing the time evolution of $\rho_{\kappa,\kappa'}(q',q'') = \langle q'|\,\hat{\rho}_{\kappa,\kappa'}\,|q''\rangle$ is given by

$$\langle q'|\,\dot{\hat{\rho}}_{\kappa,\kappa'}\,|q''\rangle = -\frac{i}{\hbar}\,\langle q'|\,\hat{H}_\kappa\hat{\rho}_{\kappa,\kappa'} - \hat{\rho}_{\kappa,\kappa'}\hat{H}_{\kappa'} + \eta_{\kappa,\kappa'}\hat{\rho}_{\kappa,\kappa'}\,|q''\rangle \\ -\xi\left(1 - e^{-\frac{(q'-q'')^2}{4r_{\rm CSL}^2}}\right)\rho_{\kappa,\kappa'}(q',q''). \tag{A.5}$$

It can be easily shown that

$$e^{-\frac{(q'-q'')^2}{4r_{\rm CSL}^2}}\,\rho(q',q'') = \frac{1}{\sqrt{\pi}r_{\rm CSL}}\,\langle q'|\int_{-\infty}^{\infty}\mathrm{d}x\,e^{-\frac{(\hat{q}-x)^2}{2r_{\rm CSL}^2}}\,\hat{\rho}e^{-\frac{(\hat{q}-x)^2}{2r_{\rm CSL}^2}}\,|q''\rangle\,. \tag{A.6}$$

We define

$$T[\hat{\rho}] \equiv \frac{1}{\sqrt{\pi}r_{\rm CSL}}\int_{-\infty}^{\infty}\mathrm{d}x\,e^{-\frac{(\hat{q}-x)^2}{2r_{\rm CSL}^2}}\,\hat{\rho}e^{-\frac{(\hat{q}-x)^2}{2r_{\rm CSL}^2}} \tag{A.7}$$

and write the master equation as

$$\langle q'|\,\dot{\hat{\rho}}_{\kappa,\kappa'}\,|q''\rangle = -\frac{i}{\hbar}\,\langle q'|\,\hat{H}_\kappa\hat{\rho}_{\kappa,\kappa'} - \hat{\rho}_{\kappa,\kappa'}\hat{H}_{\kappa'} + \eta_{\kappa,\kappa'}\hat{\rho}_{\kappa,\kappa'} - \xi\,(\hat{\rho} - T[\hat{\rho}])\,|q''\rangle\,. \tag{A.8}$$

First, we go into the rotating picture to eliminate the unitary time evolution by defining

$$\hat{\rho}^S_{\kappa,\kappa'} = \hat{U}^\dagger_\kappa(t)\hat{\rho}_{\kappa,\kappa'}\hat{U}_{\kappa'}(t)e^{\frac{i}{\hbar}\eta_{\kappa,\kappa'}}. \tag{A.9}$$

With

$$\hat{U}_\kappa(t) = e^{-\frac{i}{\hbar}\hat{H}_k t} \tag{A.10}$$

the equation governing the evolution of $\hat{\rho}^S_{\kappa,\kappa'}$ is given by

$$\dot{\hat{\rho}}^S_{\kappa,\kappa'} = -\xi\left(\hat{\rho}^S_{\kappa,\kappa'} - T^S[\hat{\rho}^S_{\kappa,\kappa'}]\right)$$

where

$$T^S[\hat{\rho}^S_{\kappa,\kappa'}] = \hat{U}^\dagger_\kappa(t)T[\hat{\rho}_{\kappa,\kappa'}]\hat{U}_{\kappa'}(t).$$

$T^S[\hat{\rho}^S_{\kappa,\kappa'}]$ can be further simplified by using the unitary nature of $\hat{U}_\kappa(t)$. With $\hat{q}_\kappa \equiv \hat{U}^\dagger_\kappa(t)\hat{q}\hat{U}_\kappa(t)$ we find

$$T^S[\hat{\rho}^S_{\kappa,\kappa'}] = \frac{1}{\sqrt{\pi}r_{\mathrm{CSL}}}\int_{-\infty}^{\infty}\mathrm{d}x\, e^{-\frac{(\hat{q}_\kappa - x)^2}{2r^2_{\mathrm{CSL}}}}\,\hat{\rho}^S_{\kappa,\kappa'}e^{-\frac{(\hat{q}_{\kappa'} - x)^2}{2r^2_{\mathrm{CSL}}}}. \tag{A.11}$$

To evaluate $\hat{q}_\kappa$, one first has to find an expression for the time evolution of the κ^{th} wave packet. We realize that we can write $\hat{H}_\kappa$ in terms of the ladder operators $\hat{a}, \hat{a}^\dagger$ defined by $\hat{q} = x_0(\hat{a}^\dagger + \hat{a})$ and $\hat{p} = ip_0(\hat{a}^\dagger - \hat{a})$. x_0 and p_0 are given by $x_0 = \sqrt{\hbar/(2m\Omega)}$ and $p_0 = \sqrt{\hbar m\Omega/2}$. By using the properties of the displacement operator $\hat{D}(\zeta) = \exp\bigl(\zeta\hat{a}^\dagger - \zeta^*\hat{a}\bigr)$, we can write

$$e^{-\frac{i}{\hbar}\hat{H}_\kappa t} = e^{i\Omega t\hat{a}^\dagger\hat{a}}\hat{D}\left(\frac{\chi}{2x_0}(2\kappa - N)\right)e^{-i\Omega t\hat{a}^\dagger\hat{a}}. \tag{A.12}$$

Each π pulse flips all spins, therefore κ goes to $N-\kappa$. We can use the properties of the displacement operator to find the full-time evolution along the κ^{th} trajectory, which can be written as

$$\hat{U}_\kappa(t) = e^{-i\left(\frac{\chi}{2x_0}\right)^2\phi_\kappa(t)}\hat{D}\left(\frac{\chi}{2x_0}\zeta_\kappa(t)\right)e^{-i\Omega t\hat{a}^\dagger\hat{a}}. \tag{A.13}$$

$\zeta_\kappa(t)$ represents the classical phase space trajectory of the κ^{th} wave packet. The

position of the center of this wave packet is given by $\mathcal{X}_\kappa(t) = \chi\,\mathrm{Re}[\zeta_\kappa(t)]$. $\phi_\kappa(t) = \phi'_\kappa + (2\kappa - N)^2\eta T_{\mathrm{tot}}/\hbar$ as well as $\zeta_\kappa(t)$ are given by

$$\zeta_\kappa = (2\kappa - N)\begin{cases} 1 - e^{-i\Omega t} & 0 \le t < t_1 \\ e^{-i\Omega(t_1+t)} - 2e^{-it_1\Omega} + 1 & t_1 \le t < t_1 + t_2 \\ 2e^{-i\Omega(t_1+t_2)} - e^{-i\Omega(t_1+t_2+t)} - 2e^{-it_1\Omega} + 1 & t_1 + t_2 \le t < T_{\mathrm{tot}} \end{cases} \tag{A.14}$$

and

$$\phi'_\kappa(t) = -\,(2\kappa - N)^2\begin{cases} \sin(t\Omega) & 0 \le t < t_1 \\ 2\left[\sin(t\Omega) + \sin(t_2\Omega)\right] - \sin(\Omega(t_1 + t)) & t_1 \le t < t_1 + t_2 \\ 2\sin(t\Omega) + 2\sin(t_1\Omega) + 4\sin(t_2\Omega) - & \\ \quad 2\big[\sin((t + t_2)\Omega) + \sin((t_1 + t_2)\Omega)\big] & \\ \quad + \sin((t + t_1 + t_2)\Omega) & t_1 + t_2 \le t < T_{\mathrm{tot}} \end{cases}. \tag{A.15}$$

By using the properties of the displacement operator and the Baker–Campbell–Hausdorff formula, $\hat{q}_\kappa$ can be written as

$$\hat{U}^\dagger_\kappa(t)\hat{q}\hat{U}_\kappa(t) = \cos(\Omega t)\hat{q} + \sin(\Omega t)\hat{p}\frac{x_0}{p_0} + \mathcal{X}_\kappa(t). \tag{A.16}$$

As we are interested in $\mathrm{tr}(\hat{\rho}_{\kappa,\kappa'})$, we use the linearity and the cyclic properties of the trace and $[\hat{q}_\kappa, \hat{q}_{\kappa'}] = 0$ to find

$$\mathrm{tr}\big\{T^S[\hat{\rho}^S]\big\} = \frac{1}{\sqrt{\pi}r_{\mathrm{CSL}}}\,\mathrm{tr}\left\{\int_{-\infty}^{\infty}\mathrm{d}x\, e^{\frac{(\hat{q}_\kappa - x)^2 - (\hat{q}_{\kappa'} - x)^2}{2r^2_{\mathrm{CSL}}}}\hat{\rho}^S\right\} = \mathrm{tr}\left\{e^{-\frac{(\hat{q}_\kappa - \hat{q}_{\kappa'})^2}{4r^2_{\mathrm{CSL}}}}\hat{\rho}^S\right\}. \tag{A.17}$$

When plugging Eq. (A.16) into Eq. (A.17), all terms involving $\hat{q}$ and $\hat{p}$ cancel out and one finds

$$\frac{\partial\,\mathrm{tr}\big\{\hat{\rho}^S_{\kappa,\kappa'}\big\}}{\partial t} = -\xi\left[1 - e^{-\frac{(\mathcal{X}_\kappa(t) - \mathcal{X}_{\kappa'}(t))^2}{4r^2_{\mathrm{CSL}}}}\right]\mathrm{tr}\big\{\hat{\rho}^S_{\kappa,\kappa'}\big\}. \tag{A.18}$$

This differential equation can be easily solved by

$$\mathrm{tr}\big\{\hat{\rho}^S_{\kappa,\kappa'}(T_{\mathrm{tot}})\big\} = e^{-\Lambda_{\kappa,\kappa'}}\,\mathrm{tr}\big\{\hat{\rho}^S_{\kappa,\kappa'}(0)\big\} \tag{A.19}$$

with

$$\Lambda_{\kappa,\kappa'} = \xi \int_0^{T_{\text{tot}}} (1 - e^{-\frac{[\mathcal{X}_\kappa(t') - \mathcal{X}_{\kappa'}(t')]^2}{4r_{\text{CSL}}^2}}) \, \mathrm{d}t'. \tag{A.20}$$

The protocol is designed such that the κ^{th} and the κ'^{th} wave packets overlap, meaning that $\zeta_\kappa(T_{\text{tot}}) = \zeta_{\kappa'}(T_{\text{tot}})$. Hence, $\hat{U}_\kappa(T_{\text{tot}})$ and $\hat{U}_{\kappa'}(T_{\text{tot}})$ are the same up to a phase. Therefore, $\text{tr}\{\hat{\rho}^S_{\kappa,\kappa'}(T_{\text{tot}})\} = \text{tr}\{\hat{\rho}_{\kappa,\kappa'}(T_{\text{tot}})\} \exp(-i\Delta\phi_{\kappa,\kappa'}(T_{\text{tot}}))$ holds true, where we defined $\Delta\phi_{\kappa,\kappa'} \equiv \phi_\kappa(T_{\text{tot}}) - \phi_{\kappa'}(T_{\text{tot}})$. At $t = 0$, the wave packets did not split up yet. Therefore, we know $\text{tr}\{\hat{\rho}_{\kappa,\kappa'}(0)\} = \text{tr}\{\hat{\rho}(0)\} = 1$. $\text{tr}\{\hat{\rho}_{\kappa,\kappa'}(T_{\text{tot}})\}$ is then given by

$$\text{tr}\{\hat{\rho}_{\kappa,\kappa'}\} = e^{-i\Delta\phi_{\kappa,\kappa'}} e^{-\Lambda_{\kappa,\kappa'}}. \tag{A.21}$$

If $(\mathcal{X}_\kappa(t') - \mathcal{X}_{\kappa'}(t')) \ll r_{\text{CSL}}$, $\Lambda_{\kappa,\kappa'}$ simplifies to

$$\Lambda_{\kappa,\kappa'} \approx (T_{\text{tot}}) \frac{\xi}{4r_{\text{CSL}}^2} \int_0^{T_{\text{tot}}} (\mathcal{X}_\kappa(t') - \mathcal{X}_{\kappa'}(t'))^2 \, \mathrm{d}t'. \tag{A.22}$$

A.3 Expectation Value of $\langle \hat{M} \rangle$

We want to find the expectation value of $\langle \hat{M} \rangle(T_{\text{tot}}) = \text{tr}\Big\{\hat{U}^{\otimes N}_{\pi/2} \hat{\rho}_{\text{s}}(T_{\text{tot}}) \hat{U}^{\dagger \otimes N}_{\pi/2} \hat{M}\Big\}$, where $\hat{U}_{\pi/2}$ is a $\pi/2$ pulse acting on the spins and $\hat{\rho}_{\text{S}}$ is given by Eq. (7.20). Due to the cyclic properties of the trace and since $\hat{U}_{\pi/2} \hat{\sigma}_z \hat{U}^\dagger_{\pi/2} = \hat{\sigma}_x$, $\langle \hat{M} \rangle(T_{\text{tot}})$ is given by

$$\langle \hat{M} \rangle(T_{\text{tot}}) = \frac{\hbar\gamma_p}{2^{N+1}} \sum_{\kappa,\kappa'=0}^{N} \sqrt{\binom{N}{\kappa}\binom{N}{\kappa'}} e^{-i\Delta\phi_{\kappa,\kappa'}} e^{-\Lambda_{\kappa,\kappa'}} \ \text{tr}\Big\{\hat{X} \left|\kappa\right\rangle \left\langle\kappa'\right|\Big\}. \tag{A.23}$$

Here, $\hat{X} = \sum_{n=1}^{N} \hat{\sigma}_x^{(n)}$ is the sum over all $\hat{\sigma}_x$ operators.

To find an expression for $\hat{X} \left|\kappa\right\rangle$, one can use combinatorics and the relation $\hat{\sigma}_x \left|\uparrow / \downarrow\right\rangle = \left|\downarrow / \uparrow\right\rangle$. It can be shown that

$$\sqrt{\binom{N}{\kappa}} \hat{X} \left|\kappa\right\rangle = [N - (\kappa - 1)] \sqrt{\binom{N}{\kappa - 1}} \left|\kappa - 1\right\rangle + (\kappa + 1) \sqrt{\binom{N}{\kappa + 1}} \left|\kappa + 1\right\rangle. \tag{A.24}$$

Since Dicke states are orthonormal, we find that for $\langle \hat{M} \rangle(T_{\text{tot}})$ only terms like $\kappa' = \kappa \pm 1$ contribute to the double sum. Furthermore, $\mathcal{X}_\kappa(t)$ is linear in κ, therefore only the nearest neighbours' decoherences contribute and $\mathcal{X}_\kappa(t') - \mathcal{X}_{\kappa\pm1}(t')$ is independent of κ and can be taken out of the sum. The left sum has a closed form

solution that is given by

$$\langle \hat{M} \rangle (T_{\text{tot}}) = \langle \hat{M} \rangle (0) e^{-\gamma} \cos^{N-1}(4\phi) \tag{A.25}$$

with

$$\phi = (\chi/2x_0)^2 \sin(\Omega t_1) + \eta T_{\text{tot}}/\hbar, \quad \gamma = \Lambda_{\kappa,\kappa\pm1}. \tag{A.26}$$

If $\mathcal{X}_{\kappa,\kappa\pm1}(t') \ll r_{\text{CSL}}$ at all times γ simplifies to $\gamma = \xi/(2r_{\text{CSL}}^2) \int_0^{T_{\text{tot}}} \mathcal{X}_{\kappa,\kappa\pm1}(t')^2 \, \mathrm{d}t'$, which has a closed form solution given by

$$\begin{aligned}
\gamma = \frac{\xi}{4r_{\text{CSL}}^2} \frac{\chi^2}{4\Omega} \Big\{ & 14\Omega(2t_1 + t_2) - 8\Omega(t_1 + t_2)\cos(\Omega t_1) + 8\Omega t_1 \big[-2\cos(\Omega t_2) \\
& + \cos(\Omega(t_1 + t_2)) \big] + 8\sin(\Omega t_1) - 11\sin(2\Omega t_1) + 4\sin(3\Omega t_1) \\
& - \sin(4\Omega t_1) + 24\sin(2\Omega(t_1 + t_2)) - 4\sin(3\Omega(t_1 + t_2)) \\
& + 3\sin(4\Omega(t_1 + t_2)) - 8\sin(\Omega(2t_1 + t_2)) + 5\sin(2\Omega(2t_1 + t_2)) \\
& - 16\sin(\Omega(t_1 + 2t_2)) - 4\sin(2\Omega(t_1 + 2t_2)) \\
& - 12\sin(3\Omega t_1 + 2\Omega t_2) + 8\sin(2\Omega t_1 + 3\Omega t_2) - 8\sin(4\Omega t_1 + 3\Omega t_2) \\
& + 4\sin(5\Omega t_1 + 3\Omega t_2) + 4\sin(3\Omega t_1 + 4\Omega t_2) - 4\sin(5\Omega t_1 + 4\Omega t_2) \\
& + \sin(6\Omega t_1 + 4\Omega t_2) \Big\}.
\end{aligned} \tag{A.27}$$

A.4 $\pi/2$ Pulse in Dicke Basis

To write down the explicit expression for $\langle \hat{M} \rangle (T_{\text{tot}}) / \langle \hat{M} \rangle (0)$ for the modified protocol, the matrix elements of a $\pi/2$ and $3\pi/2$ pulse in the Dicke basis are needed.

To do that, we first look at the closely related Hadamard gate, i.e., we want to know what $H^{\otimes N} |\kappa\rangle$ looks like on the Dicke basis. To do so, let us look at the eigenvectors of the Hadamard gate H on the spin basis. In this section, ket vectors in the spin basis will be denoted by $|\cdot\rangle_S$

$$H^{\otimes N} |k\rangle_S = \frac{1}{2^{N/2}} \sum_{a \in \{0,1\}} (-1)^{a \cdot k} |a\rangle_S \tag{A.28}$$

where "1" corresponds to "↑" and "0" corresponds to "↓". By definition, the Dicke state $|\kappa\rangle$ can be written in the spin basis as

$$\sqrt{\binom{N}{\kappa}} |\kappa\rangle = \sum_{k \in \pi(\underbrace{1, \ldots, 1}_{\kappa} \underbrace{0, \ldots, 0}_{N-\kappa})} |k\rangle_S = \sum_{k \in \pi(k_0)} |k\rangle_S \tag{A.29}$$

where π is the permutation operator and k_0 is the vector $k_0 = \{1\}^{\otimes \kappa} \{0\}^{\otimes (N-\kappa)}$.

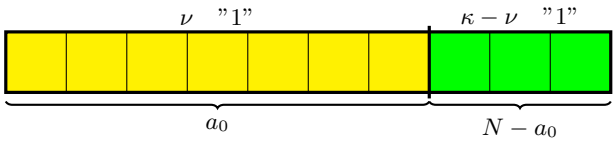


Figure 1: There are $\binom{a_0}{\nu}$ possibilities to place ν ones in the yellow entries of k' and $\binom{N-a_0}{\kappa-\nu}$ possibilities to place $\kappa-\nu$ ones in the green entries.

Hence, $H^{\otimes N}|\kappa\rangle$ can be written as

$$H^{\otimes N}|\kappa\rangle = \frac{1}{2^{\frac{N}{2}}\sqrt{\binom{N}{\kappa}}} \sum_{a\in\{0,1\}} \sum_{k\in\pi(k_0)} (-1)^{k\cdot a}|a\rangle_S\,. \tag{A.30}$$

Let's look at the vectors of the form $|a_0\rangle_S = \left|\{1\}^{\otimes a_0}\{0\}^{\otimes(N-a_0)}\right\rangle$ and find the weighting factor of $|a_0\rangle_S$ i.e. $\sum_{k\in\pi(k_0)}(-1)^{k\cdot a_0}$. More explicitly, we want to find an expression for

$$\sum_{k\in\pi(k_0)} (-1)^{k\cdot a_0} = \sum_{k\in\pi(k_0)} (-1)^{\sum_{i=1}^{a_0} k_i}\,. \tag{A.31}$$

To evaluate this expression, let us look at Fig. 1. We sum over all permutations of k_0 that contain κ ones in total. For a given permutation that contains ν ones in the first a_0 entries, there are $\kappa-\nu$ ones in the last $N-a_0$ entries. There are $\binom{a_0}{\nu}\binom{N-a_0}{\kappa-\nu}$ possibilities to distribute the ν and $N-\nu$ ones that way. Now, ν goes from zero to κ. Hence, we find

$$\sum_{k\in\pi(k_0)} (-1)^{\sum_{i=1}^{a_0} k_i} = \sum_{\nu=0}^{\kappa}(-1)^{\nu}\binom{a_0}{\nu}\binom{N-a_0}{\kappa-\nu}. \tag{A.32}$$

Since we sum over all permutations of k_0, the weighting factor of all $|a\rangle_S$ with the same number of spins up will be the same. We can summarise all $|a\rangle_S$ with same numbers of spin up in the Dicke state $\sqrt{\binom{N}{\alpha}}|\alpha\rangle$ and find

$$H^{\otimes N}|\kappa\rangle = \frac{1}{2^{\frac{N}{2}}}\sum_{\alpha=0}^{N}\sqrt{\frac{\binom{N}{\alpha}}{\binom{N}{\kappa}}}\sum_{\nu=0}^{\kappa}(-1)^{\nu}\binom{\alpha}{\nu}\binom{N-\alpha}{\kappa-\nu}|\alpha\rangle\,. \tag{A.33}$$

The N-particle Hadamard gate in Dicke basis is therefore given by

$$H^{\otimes N}_{\kappa,\alpha} = \frac{1}{2^{\frac{N}{2}}}\sqrt{\frac{\binom{N}{\alpha}}{\binom{N}{\kappa}}}\sum_{\nu=0}^{\kappa}(-1)^{\nu}\binom{\alpha}{\nu}\binom{N-\alpha}{\kappa-\nu}. \tag{A.34}$$

What is left is to retrieve the $\pi/2$ pulse from the Hadamard gate. We can do that by applying the X operator on the Hadamard gate as one can check easily for the

one spin case

$$XH = \frac{1}{\sqrt{2}} \begin{pmatrix} 0 & 1 \\ 1 & 0 \end{pmatrix} \begin{pmatrix} 1 & 1 \\ 1 & -1 \end{pmatrix} = \frac{1}{\sqrt{2}} \begin{pmatrix} 1 & -1 \\ 1 & 1 \end{pmatrix} = \left(\frac{\pi}{2}\right). \tag{A.35}$$

A X gate flips $|\uparrow\rangle_S$ to $|\downarrow\rangle_S$ and the other way around. Therefore, $X^{\otimes N}$ acts on a Dicke state like $X^{\otimes N}|\alpha\rangle = |N-\alpha\rangle$. We find with a few arithmetic transformations

$$U_{\pi/2}^{\otimes N}|\kappa\rangle = X^{\otimes N} H^{\otimes N}|\kappa\rangle = \frac{1}{2^{\frac{N}{2}}} \sum_{\alpha=0}^{N} \sqrt{\frac{\binom{N}{\alpha}}{\binom{N}{\kappa}}} \sum_{\nu=0}^{\kappa} (-1)^{\nu} \binom{N-\alpha}{\nu} \binom{\alpha}{\kappa-\nu} |\alpha\rangle . \tag{A.36}$$

Therefore, the matrix elements of $U_{\pi/2}^{\otimes N}|\kappa\rangle$ in Dicke basis are

$$\left(\frac{\pi}{2}\right)_{\kappa,\alpha}^{\otimes N} = \langle\alpha| U_{\pi/2}^{\otimes N}|\kappa\rangle = \frac{1}{2^{\frac{N}{2}}} \sqrt{\frac{\binom{N}{\alpha}}{\binom{N}{\kappa}}} \sum_{\nu=0}^{\kappa} (-1)^{\nu} \binom{N-\alpha}{\nu} \binom{\alpha}{\kappa-\nu}. \tag{A.37}$$

Furthermore, a $3\pi/2$ pulse is given by $U_{3\pi/2} = U_\pi U_{\pi/2}$. One can easily convince oneself, that $U_\pi|\alpha\rangle = (-1)^{\alpha+1}|N-\alpha\rangle$. Therefore, we find

$$\left(\frac{3\pi}{2}\right)_{\kappa,\alpha}^{\otimes N} = \frac{(-1)^{\alpha+1}}{2^{\frac{N}{2}}} \sqrt{\frac{\binom{N}{\alpha}}{\binom{N}{\kappa}}} \sum_{\nu=0}^{\kappa} (-1)^{\nu} \binom{\alpha}{\nu} \binom{N-\alpha}{\kappa-\nu}. \tag{A.38}$$

A.5 Expectation Value of $\langle\hat{M}\rangle$, Modified Protocol

For the protocol as depicted in Fig. 7.4, the classical trajectories of the $(\kappa,\alpha,\beta)^{\text{th}}$ trajectory is given by

$$\zeta_{\kappa,\alpha,\beta}(t) = \begin{cases} \zeta^{(1)}_{\kappa,\alpha,\beta}(t) & T_1 \le t < T_{2,1} \\ \zeta^{(2)}_{\kappa,\alpha,\beta}(t) & T_{2,1} \le t < T_{2,2} \\ \zeta^{(3)}_{\kappa,\alpha,\beta}(t) & T_{2,2} \le t < T_{2,3} \\ \zeta^{(4)}_{\kappa,\alpha,\beta}(t) & T_{2,3} \le t < T_{\text{tot}} \end{cases} \tag{A.39}$$

with

$$
\begin{aligned}
\zeta^{(1)}_{\kappa,\alpha,\beta}(t) &= \tilde{\kappa}\left(1-e^{-i\Omega t}\right)\\
\zeta^{(2)}_{\kappa,\alpha,\beta}(t) &= \tilde{\alpha}\left(1-e^{-i(t-T_1)\Omega}\right)-\tilde{\kappa}e^{-it\Omega}\left(-1+e^{iT_1\Omega}\right)\\
\zeta^{(3)}_{\kappa,\alpha,\beta}(t) &= \tilde{\alpha}e^{-it\Omega}\left(e^{it\Omega}+e^{iT_1\Omega}-2e^{iT_{2,1}\Omega}\right)-\tilde{\kappa}e^{-it\Omega}\left(-1+e^{iT_1\Omega}\right)\\
\zeta^{(4)}_{\kappa,\alpha,\beta}(t) &= \tilde{\alpha}e^{-it\Omega}\big(e^{it\Omega}-e^{iT_1\Omega}+2\,e^{iT_{2,1}\Omega}-2\,e^{iT_{2,2}\Omega}\big)\\
&\quad-\tilde{\kappa}e^{-it\Omega}\big(-1+e^{iT_1\Omega}\big)\\
\zeta^{(5)}_{\kappa,\alpha,\beta}(t) &= \tilde{\beta}\left(-1+e^{-i(t-T_{2,3})\Omega}\right)+\tilde{\kappa}e^{-it\Omega}\left(1-e^{iT_1\Omega}\right).
\end{aligned}
\tag{A.40}
$$

Here, we defined $\tilde{\kappa}=2\kappa-N$, $\tilde{\alpha}=2\alpha-N$, $\tilde{\beta}=2\beta-N$, $T_1=t_1$, $T_{2,1}=t_1+t_{2,1}$, $T_{2,2}=t_1+t_{2,1}+t_{2,2}$, $T_{2,3}=t_1+2t_{2,1}+t_{2,2}$ and $T_{\mathrm{tot}}=2t_1+2t_{2,1}+t_{2,2}$. The phase each trajectory accumulates is given by

$$
\phi_{\kappa,\alpha,\beta}(t)=\begin{cases}\phi^{(1)}_{\kappa,\alpha,\beta}(t) & 0\le t<T_1\\ \phi^{(2)}_{\kappa,\alpha,\beta}(t) & T_1\le t<T_{2,1}\\ \phi^{(3)}_{\kappa,\alpha,\beta}(t) & T_{2,1}\le t<T_{2,2}\\ \phi^{(4)}_{\kappa,\alpha,\beta}(t) & T_{2,2}\le t<T_{2,3}\\ \phi^{(5)}_{\kappa,\alpha,\beta}(t) & T_{2,3}\le t<T_{\mathrm{tot}}\end{cases}
\tag{A.41}
$$

with

$$
\begin{aligned}
\phi^{(1)}_{\kappa,\alpha,\beta}(t) &= \tilde{\kappa}^2\sin(t\Omega)+\tilde{\kappa}^2\frac{\eta}{\hbar}t\\
\phi^{(2)}_{\kappa,\alpha,\beta}(t) &= \tilde{\alpha}^2\sin\left((t-T_1)\Omega\right)+\tilde{\kappa}^2\sin\left(T_1\Omega\right)\\
&\quad+\tilde{\alpha}\tilde{\kappa}\big[-\sin(t\Omega)+\sin\left((t-T_1)\Omega\right)+\sin\left(T_1\Omega\right)\big]\\
&\quad+\frac{\eta}{\hbar}\left[\tilde{\kappa}^2T_1+\tilde{\alpha}^2(t-T_1)\right]\\
\phi^{(3)}_{\kappa,\alpha,\beta}(t) &= \tilde{\kappa}^2\sin(T_1\Omega)+\tilde{\alpha}^2\big\{-\sin((t-T_1)\Omega)+2\big[\sin((t-T_{2,1})\Omega)\\
&\quad+\sin(t_{2,1}\Omega)\big]\big\}+\tilde{\alpha}\tilde{\kappa}\big[\sin(t\Omega)-\sin((t-T_1)\Omega)+\sin(T_1\Omega)\\
&\quad+2\sin(t_{21}\Omega)-2\sin(T_{21}\Omega)\big]+\frac{\eta}{\hbar}\left[\tilde{\kappa}^2T_1+\tilde{\alpha}^2(t-T_1)\right]\\
\phi^{(4)}_{\kappa,\alpha,\beta}(t) &= \tilde{\kappa}^2\sin(t_1\Omega)+\tilde{\alpha}^2\{\sin((t-T_1)\Omega)+2[-\sin((t-T_{2,1})\Omega)\\
&\quad+\sin(t_{2,1}\Omega)+\sin((t-T_{2,2})\Omega)+2\sin(t_{2,2}\Omega)\\
&\quad-\sin((t_{2,1}+t_{2,2})\Omega)]\}+\tilde{\alpha}\tilde{\kappa}\{-\sin(t\Omega)+\sin((t-t_1)\Omega)+\sin(t_1\Omega)\\
&\quad+2[\sin(t_{21}\Omega)-\sin((T_{2,1})\Omega)-\sin((t_{21}+t_{22})\Omega)+\sin((T_{2,2})\Omega)]\}\\
&\quad+\frac{\eta}{\hbar}\left[\tilde{\kappa}^2T_1+\tilde{\alpha}^2(t-T_1)\right]
\end{aligned}
\tag{A.42}
$$

and

$$\begin{aligned}\phi^{(5)}_{\kappa,\alpha,\beta}(t) = {} & \tilde{\beta}^2 \frac{(-5\sin(t\Omega) + 2\sin(t\Omega - t_{2,1}\Omega) + 2\sin(t\Omega + t_{2,1}\Omega))}{-5 + 4\cos(t_{2,1}\Omega)} \\ & + \tilde{\kappa}^2 \frac{(-5\sin(t_1\Omega) + 2\sin((t_1 - t_{2,1})\Omega) + 2\sin((t_1 + t_{2,1})\Omega))}{-5 + 4\cos(t_{2,1}\Omega)} \\ & + 4\tilde{\alpha}^2 \sin(t_{2,1}\Omega) + \frac{\tilde{\beta}\tilde{\kappa}}{-5 + 4\cos(t_{2,1}\Omega)} [b\sin(t\Omega) + \sin(t_1\Omega) \\ & + 4\sin(t_{2,1}\Omega) - 4\sin(2t_{2,1}\Omega) - \sin((t + t_1)\Omega) - 4\sin((t + t_{2,1})\Omega) \\ & - 4\sin((t_1 + t_{2,1})\Omega) + 4\sin((t + T_{2,1})\Omega) + 4\sin((t + 2t_{2,1})\Omega) \\ & + 4\sin((t_1 + 2t_{2,1})\Omega) - 4\sin((t + t_1 + 2t_{2,1})\Omega)] \\ & \frac{\eta}{\hbar}\left[\tilde{\kappa}^2 T_1 + \tilde{\alpha}^2(T_{2,3} - T_1) + \tilde{\beta}^2(t - T_{2,3})\right]. \end{aligned} \tag{A.43}$$

As one can easily check, the phase each trajectory accumulates for all $(\kappa, \alpha, \beta = \kappa)$ is a multiple of π if the parameters are chosen according to Table 10.1. For an initial state as in Eq. (7.6) and

$$\hat{\rho}_{\kappa,\kappa\prime,\alpha,\alpha',\beta,\beta'} = \hat{U}_{\kappa,\alpha,\beta}\hat{\rho}_{\mathrm{th}}\hat{U}^{\dagger}_{\kappa',\alpha',\beta'}, \tag{A.44}$$

the final spin state is given by

$$\begin{aligned}\hat{\rho}_{\mathrm{S}} = \frac{1}{2^N} \sum_{\kappa,\kappa'=0}^{N} \sum_{\alpha,\alpha'=0}^{N} \sum_{\beta,\beta'=0}^{N} & \sqrt{\binom{N}{\kappa}}\sqrt{\binom{N}{\kappa'}} \left(\frac{\pi}{2}\right)^{\otimes N}_{\kappa,\alpha} \left(\frac{3\pi}{2}\right)^{\otimes N}_{\alpha,\beta} \left(\frac{\pi}{2}\right)^{\otimes N}_{\alpha',\kappa'} \left(\frac{3\pi}{2}\right)^{\otimes N}_{\beta',\alpha'} \\ & \times \mathrm{tr}\{\hat{\rho}_{\kappa,\kappa\prime,\alpha,\alpha',\beta,\beta'}(T_{\mathrm{tot}})\} \left|\beta\right\rangle \left\langle\beta\right|. \end{aligned} \tag{A.45}$$

For the trajectories that recombine, the trace over $\hat{\rho}_{\kappa,\kappa\prime,\alpha,\alpha',\beta,\beta'}(T_{\mathrm{tot}})$ is given by

$$e^{-\xi \int_0^T [1 - e^{-[\mathcal{X}_{\kappa,\alpha,\beta}(t') - \mathcal{X}_{\kappa',\alpha',\beta'}(t')]^2/(4r^2_{\mathbf{CSL}})}]\,\mathrm{d}t'}, \tag{A.46}$$

where $\mathcal{X}_{\kappa,\alpha,\beta}(t)$ is given by $\mathcal{X}_{\kappa,\alpha,\beta}(t) = \chi\ \mathrm{Re}[\zeta_{\kappa,\alpha,\beta}(t)]$.

If the trajectories do not recombine, the trace over $\hat{\rho}_{\kappa,\kappa\prime,\alpha,\alpha',\beta,\beta'}(T_{\mathrm{tot}})$ goes to zero mainly because the wave packets do not perfectly overlap. The overlap between two thermal states, where one is displaced by ζ_i and the other by ζ_j, is given by $\mathrm{tr}\Big\{\hat{D}(\zeta_i)\hat{\rho}_{\mathrm{th}}\hat{D}^{\dagger}(\zeta_j)\Big\}$. To find an expression for this overlap, we expand $\hat{\rho}_{\mathrm{th}}$ in coherent states

$$\hat{\rho}_{\mathrm{th}} = \int \frac{\mathrm{d}\alpha^2}{\pi} \frac{e^{-\frac{|\alpha|^2}{\bar{n}}}}{\bar{n}} \left|\alpha\right\rangle \left\langle\alpha\right| \tag{A.47}$$

where $\bar{n}$ is the occupation number. To evaluate the trace, we use the definition of a coherent state $\left|\alpha\right\rangle = \hat{D}(\alpha)\left|0\right\rangle$ and the properties of the displacement operator.

One then finds

$$\mathrm{tr}\Big\{\hat{D}(\zeta_i)\left|\alpha\right\rangle\left\langle\alpha\right|\hat{D}^\dagger(\zeta_j)\Big\} = e^{\phi}e^{\Delta\zeta\alpha^*-\Delta\zeta^*\alpha}e^{\frac{-|\Delta\zeta|^2}{2}} \tag{A.48}$$

with $\Delta\zeta = \zeta_i - \zeta_j$ and $\phi = (\zeta_j^*\zeta_i - \zeta_j\zeta_i^*)/2$. All that's left is solving the integral to find

$$\mathrm{tr}\Big[\hat{D}(\zeta_i)\hat{\rho}_{\mathrm{th}}\hat{D}^\dagger(\zeta_j)\Big] = e^{\phi-|\Delta\zeta|^2(\frac{1}{2}+\bar{n})}. \tag{A.49}$$

As the overlap goes with $\exp(-\bar{n})$, it goes to zero very quickly for large occupation numbers.

A.6 Analysis of Wave Functions Structure

Initially, the wave packet is prepared in a thermal state. After applying the first $\pi/2$ pulse, the wave packet will split up into $N+1$ Gaussian wave packets, which we numerate with $\kappa \in 0, N$, where κ denotes how many spins point up. The position of the $\kappa^{\mathbf{th}}$ trajectory is proportional to κ at any time and the probability for it to be realised is given by a binomial distribution $\binom{N}{k}$. When the second $\pi/2$ pulse is applied, the structure of the wave packet becomes significantly more complex. Each trajectory again splits into $N+1$ trajectories. Therefore, each trajectory is denoted by (κ, α), where α is in $[0, N]$. The probability for the $(\kappa, \alpha)^{\mathrm{th}}$ to be realised is now given by

$$P(\alpha, \kappa) = \binom{N}{\kappa}\left[\left(\frac{\pi}{2}\right)_{\kappa,\alpha}^{\otimes N}\right]^2. \tag{A.50}$$

The position of the $(\kappa, \alpha)^{\mathrm{th}}$ trajectory is at all times of the form $c_\kappa\kappa + c_\alpha\alpha$, where $c_{\kappa,\alpha}$ depends on the time and the parameters of the experiment. As we are limited in the number of spins, we analyse the behaviour with the wave packets width for a limited number of spins and different c_κ, c_α in order to later extrapolate the wave function's width for larger N.
For some arbitrary numbers, the position distribution of the wave function is shown in Fig. 2, as well as how the width Δx grows with N for c_κ and x_α. We define the width as

$$\Delta x^2(t) = \sum_{\kappa,\alpha}^{N}\chi_{\kappa,\alpha}^2(t)P(\kappa,\alpha) = \sum_{\kappa,\alpha}^{N}\left(c_\kappa(t)\kappa + c_\alpha(t)\alpha\right)^2 P(\kappa,\alpha) \tag{A.51}$$

where $\chi_{\kappa,\alpha}(t)$ is the position of the $(\kappa, \alpha)^{\mathrm{th}}$ trajectories at time t. As expected, for $c_\alpha = 0$, the wave function is distributed according to a binomial distribution and $\Delta x^2(t)$ grows with N. For $c_\kappa = 0$ on the other hand, the wave function exhibits two distinct peaks and $\Delta x^2(t)$ grows like $N + N^2$. Therefore, we expect that the

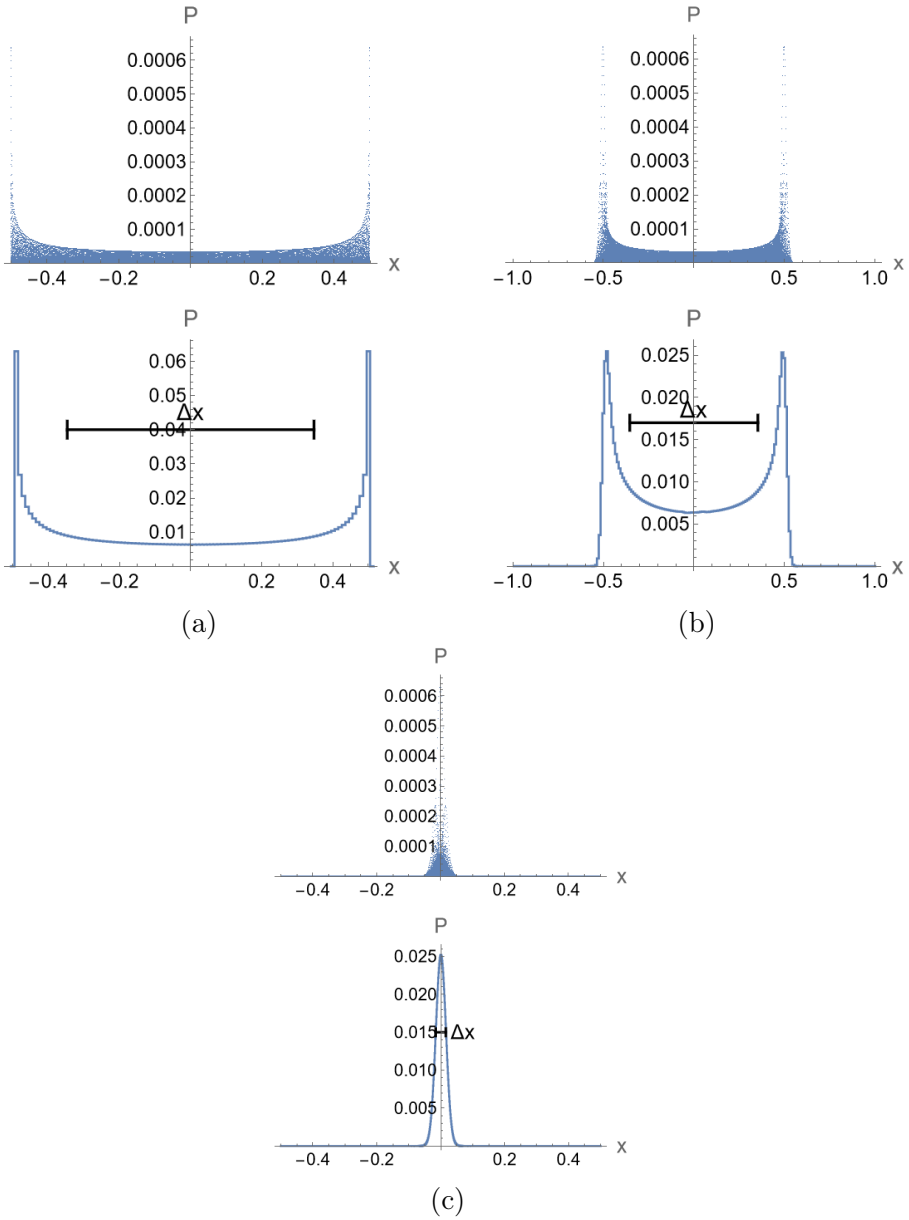


Figure 2: Here, the position distribution of the wave packet after the second $\pi/2$ pulse for some arbitrary numbers is given. In (a) one can see the wave packet for $c_\kappa = 0$, which shows two distinct peaks at the very end of the wave function, in (b) for $c_\kappa = c_\alpha$ and in (c) for $c_\alpha = 0$. For $c_\alpha \ll c_\kappa$, the peaks wander towards the middle and approach the Gaussian one expects for $c_\alpha = 0$. In the top plots, each dot represents the position and probability of one trajectory (κ, α). To understand the probability distribution better, in the bottom plot, one sees the corresponding histogram, where all probabilities in a given position range have been added up. $\Delta x = \sqrt{\Delta x^2}$ is the width of the wave function as defined in Eq. (A.51).

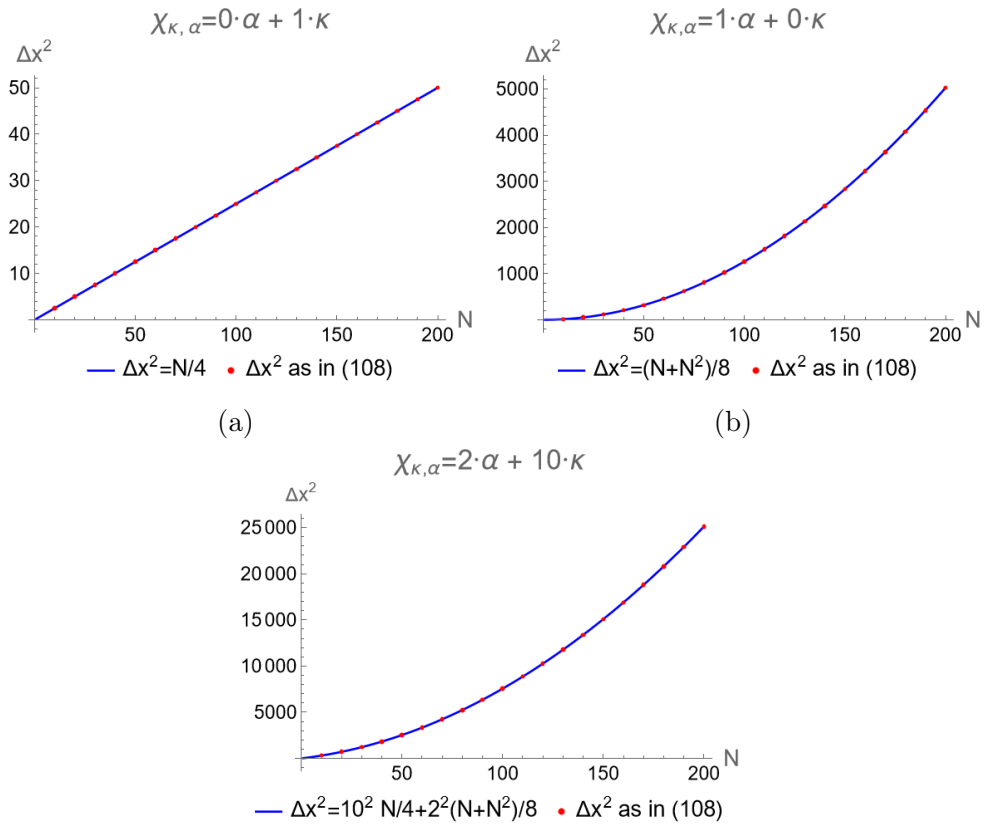


Figure 3: Dependence of the wave-function width on N. As can be seen in (a), the width grows linearly with N as $\Delta x_\kappa = N/4$ when $c_\alpha = 0$ and $c_\kappa = 1$, while for $c_\kappa = 0$ and $c_\alpha = 1$ the width grows as $\Delta x_\alpha = (N + N^2)/8$, as shown in (b). For a general superposition $\chi_{\kappa,\alpha} = c_\kappa \kappa + c_\alpha \alpha$, the width behaves as $\Delta x^2 = c_\kappa^2 \Delta x_\kappa^2 + c_\alpha^2 \Delta x_\alpha^2$, as shown in (c). Although we are not able to prove this analytically, it is consistent with all parameter sets we have tested.

wave function's width $\Delta x(t) = \sqrt{\Delta x^2(t)}$ grows with $\sqrt{N}$ for small N and for large N, the width eventually grows linearly in N. In order to find an expression of the variance in dependence of c_α, c_κ and N, we define

$$\Delta x_\kappa^2 = \sum_{\kappa,\alpha}^{N} \kappa^2 P(\kappa,\alpha) = \frac{N}{4}, \quad \Delta x_\alpha^2 = \sum_{\kappa,\alpha}^{N} \alpha^2 P(\kappa,\alpha) = \frac{N+N^2}{8} \tag{A.52}$$

and then use the Ansatz $\Delta x^2(t) = c_\kappa^2(t)\Delta x_\kappa^2 + c_\alpha^2(t)\Delta x_\alpha^2$, which fits perfectly as shown in Fig. 3. While we were not able to prove this relation, it fits with all parameters we tested.

A.7 Possible Noise Sources - Spin Flips

The T_1 time gives a time scale, at which a nuclear spin statistically flips. In this subsection, we want to analyse how such a flip affects the time evolution of the levitated nanoparticle. For that we split the time evolution into the time evolution before and after the spin flip. If the spins are initially fully polarised, the state is given by

$$\hat{\rho}(0) = \frac{1}{2^N} \sum_{\kappa=0}^{N} \sqrt{\binom{N}{\kappa}} \left|\kappa\right\rangle \otimes \hat{\rho}_x. \tag{A.53}$$

Until time τ, the nanoparticle evolves undisturbed according to the given protocol. The time evolution of the κ^{th} branch is then given by

$$\hat{U}_\kappa(\tau) = e^{-i\phi_\kappa(\tau)} \hat{D}\left(\frac{\chi}{2x_0}\zeta_\kappa(\tau)\right) e^{-i\tau\hat{a}^\dagger\hat{a}}. \tag{A.54}$$

If one spin flips, a Dicke state transforms like

$$\sqrt{\binom{N}{\kappa}} \left|\kappa\right\rangle_N \to \sqrt{\binom{N-1}{\kappa-1}} \left|0\right\rangle_1 \otimes \left|\kappa-1\right\rangle_{N-1} + \sqrt{\binom{N-1}{\kappa+1}} \left|1\right\rangle_1 \otimes \left|\kappa+1\right\rangle_{N-1}. \tag{A.55}$$

Therefore, each branch in turn splits into an incoherent superposition of two branches. One with $\kappa - 1$ spins up and one with $\kappa + 1$ spins up. The time evolution for the full protocol along the κ^{th} trajectory is therefore given by

$$\begin{aligned}\hat{U}_\kappa^\pm(T_{\text{tot}}, \tau) =& e^{-i\phi_{\kappa\pm1}(T_{\text{tot}}-\tau)} \hat{D}\left(\frac{\chi}{2x_0}\zeta_{\kappa\pm1}(T_{\text{tot}}-\tau)\right) e^{-i(T_{\text{tot}}-\tau)\hat{a}^\dagger\hat{a}} \\ &\times e^{-i\phi_\kappa(\tau)} \hat{D}\left(\frac{\chi}{2x_0}\zeta_\kappa(\tau)\right) e^{-i\tau\hat{a}^\dagger\hat{a}}.\end{aligned} \tag{A.56}$$

As ζ_κ is linear in $(2\kappa - N)$, we can write it as $\zeta_\kappa(t) = (2\kappa - N)\tilde{\zeta}(t)$. $\zeta_{\kappa\pm1}$ can therefore be rewritten as $\zeta_{\kappa\pm1} = \zeta_\kappa(t) \pm 2\tilde{\zeta}$. The effect of the spin-flip can be separated from the undisturbed time evolution, by rewriting the displacement operator like

$$\hat{D}\left(\frac{\chi}{2x_0}\zeta_{\kappa\pm1}(T_{\text{tot}}-\tau)\right) = \hat{D}\left(\pm\frac{\chi}{x_0}\tilde{\zeta}(T_{\text{tot}}-\tau)\right) \hat{D}\left(\frac{\chi}{2x_0}\zeta_\kappa(T_{\text{tot}}-\tau)\right). \tag{A.57}$$

We therefore find

$$\hat{U}_\kappa^\pm(T_{\text{tot}}, \tau) = e^{-i\tilde{\phi}_\kappa(T_{\text{tot}},\tau)} \hat{D}\left(\pm\frac{\chi}{x_0}\tilde{\zeta}(T_{\text{tot}}-\tau)\right) e^{-i\phi_\kappa(T_{\text{tot}})} \hat{D}\left(\frac{\chi}{2x_0}\zeta_\kappa(T_{\text{tot}})\right) e^{-iT_{\text{tot}}\hat{a}^\dagger\hat{a}}. \tag{A.58}$$

The second line describes the unperturbed evolution, while the first line describes the effect of the flip. The flip induces an additional phase $\tilde{\phi}_\kappa(T_{\rm tot},\tau) = \phi_{\kappa\pm1}(T_{\rm tot}-\tau)-\phi_\kappa(T_{\rm tot}-\tau)$. The protocol is designed such that, if the initial state is a thermal state, all trajectories recombine in the centre. The displacement operator in the first line indicates that, when a flip happens, the trajectories either recombine in $\hat{D}(\frac{\chi}{x_0}\tilde{\zeta}(T_{\rm tot}-\tau))$ or in $\hat{D}(-\frac{\chi}{x_0}\tilde{\zeta}(T_{\rm tot}-\tau))$, each with a probability of 50 %. The distance in phase space is given by $|\Delta\zeta(\tau)| = 2\chi/x_0|\tilde{\zeta}(T_{\rm tot}-\tau)|$. For the first protocol described here, $|\tilde{\zeta}(T_{\rm tot}-\tau)|$ is bounded by two. This bound is realised if the flip happens while the wave function is maximally spread at $\tau = \pi/\Omega$. The maximal displacement is therefore given by $|\Delta\zeta(\tau)| < 4\chi/x_0$.

B The Nuclear Einstein-de Haas and Barnett Effect with Levitated Nanoparticles

B.1 Friction

The particle might be subjected to friction from surrounding gas, damping its rotation. The equation describing the rotational angular momentum of the nanoparticle with drag due to friction is given by

$$\frac{\mathrm{d}}{\mathrm{d}t}L(t) = \tau(t) + \tau_{\rm drag}(t). \tag{B.59}$$

The drag torque, $\tau_{\rm drag}$, cannot be derived analytically for arbitrary shapes. Nevertheless, for $r\omega \ll v_{\rm sound}$, where ω is the angular velocity, r the typical length scale of the particle and $v_{\rm sound}$ is the speed of sound in the gas, $\tau_{\rm drag}$ can be described [289]. The criterion $r\omega \ll v_{\rm sound}$ ensures that the surface velocity of the rotating particle remains far below the speed of sound (low Mach number), such that compressibility effects can be neglected. For an ideal gas, the speed of sound in a gas is given by $v_{\rm sound} = \sqrt{\gamma R_{\rm spec} T}$ which is essentially independent of pressure at fixed temperature. $\gamma \approx 1.4$ is the adiabatic index and $R_{\rm spec} \approx 287\,\mathrm{Jkg^{-1}K^{-1}}$ is the specific gas constant. Hence, reducing the background pressure does not significantly change $v_{\rm sound}$. In order to keep naphthalene from evaporating, its bulk temperature should be around 100 K [1]. The speed of sound in air for an ideal gas at $100\,K$ is approximately 200 m/s. For a particle of a typical size of $10\,\mu$m, we find that $r\omega \ll v_{\rm sound}$ is valid as long as $\omega \ll 3\cdot(2\pi)$ MHz, which will always be the case here.

The friction torque due to the ellipsoid's rotation in a viscous gas can be calculated using the formalism presented in [289] and is given by

$$\tau_{\rm drag} = -\rho_g v_{\rm th} \sum_{i=x,y,z} \gamma_i \left(\boldsymbol{\omega}\cdot\mathbf{e}_i\right)\mathbf{e}_i, \tag{B.60}$$

where ρ_g is the mass density and $v_\mathrm{th} = \sqrt{8k_\mathrm{B}T/(\pi m_\mathrm{g})}$ is the mean thermal velocity of the surrounding gas. $m_\mathrm{g} \approx 29\,\mathrm{u}$ is the mass of one air molecule. Using $P = k_\mathrm{B}T\rho_\mathrm{g}/m_\mathrm{g}$, where P is the gas pressure, we find $\rho_\mathrm{g} v_\mathrm{th} = P\sqrt{8m_\mathrm{g}/(k_\mathrm{B}T\pi)}$, therefore the drag torque goes linearly with the gas pressure. The coefficients γ_μ determine the drag torque when the angular velocity ω of the rotating ellipsoid points along the μ^th semi-axis of the ellipsoid. These coefficients depend on the accommodation factor α, which describes the energy transfer between the gas molecules and the crystal, and varies between zero and one. For simplicity, it is assumed that the energy transfer between the incident air molecules and the naphthalene is fully inelastic, resulting in $\alpha = 1$. This also constitutes an upper bound for τ_drag.

In the previous section we assumed the particle to be rotating around the axis which is shortest to get a worst case estimate on the angular velocity $\boldsymbol{\omega}$. Hence, we assume $\boldsymbol{\omega} = \omega \mathbf{e}_z$ from here onward as well. The rotational angular momentum $L(t)$ can then be written in terms of the angular velocity by $L(t) = I_z\omega(t)$. The differential equation is therefore given by $I_z \mathrm{d}\omega(t)/\mathrm{d}t = S(0)/T_1 \exp(-t/T_1) - I_z\Gamma\omega(t)$ where the damping rate is defined as $\Gamma = \rho v_\mathrm{th}\gamma_z/I_z$. This differential equation is solved as

$$\omega(t) = \frac{S(0)}{I_z}\frac{e^{-t\Gamma} - e^{-\frac{t}{T_1}}}{1 - T_1\Gamma} \xrightarrow[t\Gamma \ll 1]{T_1\Gamma \ll 1} \frac{S(0)}{I_z}\left(1 - e^{-\frac{t}{T_1}}\right). \tag{B.61}$$

For $t\Gamma \ll 1, T_1\Gamma \ll 1$, ω will initially increase quickly with a rate of T_1^{-1} until air friction becomes relevant. After that, the rate of increase of ω slows down until the rotation of the ellipsoid eventually decreases slowly. The maximum value of ω_max is reached at time t_max, and these are given by

$$\omega_\mathrm{max} = \omega(t_\mathrm{max}) = \frac{S(0)}{I_z}\left(T_1\Gamma\right)^{\frac{1}{1-T_1\Gamma}-1} t_\mathrm{max} = \frac{T_1 \ln(T_1\Gamma)}{T_1\Gamma - 1}. \tag{B.62}$$

At 100 K, atmospheric pressure of $P = 101\,\mathrm{kPa} = 1\,\mathrm{Bar}$ and for $a = 150\,\mathrm{nm}$, $b = 100\,\mathrm{nm}$ and $c = 10\,\mathrm{nm}$, $\Gamma^{-1} = 0.1\,\mathrm{ms}$ is found. Nevertheless, already at a moderate vacuum of $10^{-3}\,\mathrm{mbar}$, Γ would be reduced by a factor 10^6, in which case Γ^{-1} reaches the order of minutes. For even better vacuums, the drag torque eventually becomes negligible.

In Fig. 4 the expected maximal rotation frequency ω_max and t' are shown for an elliptic naphthalene particle of varying sizes and gas pressures, where t' is the time at which $(1 - e^{-1})$ of the rotation speed is reached. As shown in Appendix B.3, with one patch charge, a static electric field of roughly $300\,\mathrm{V/m}$ suffices to move a particle of 100 nm radius to a regime where the bias field B_0 is zero. We hence expect the T_1 to drop drastically into the minute regime [250].

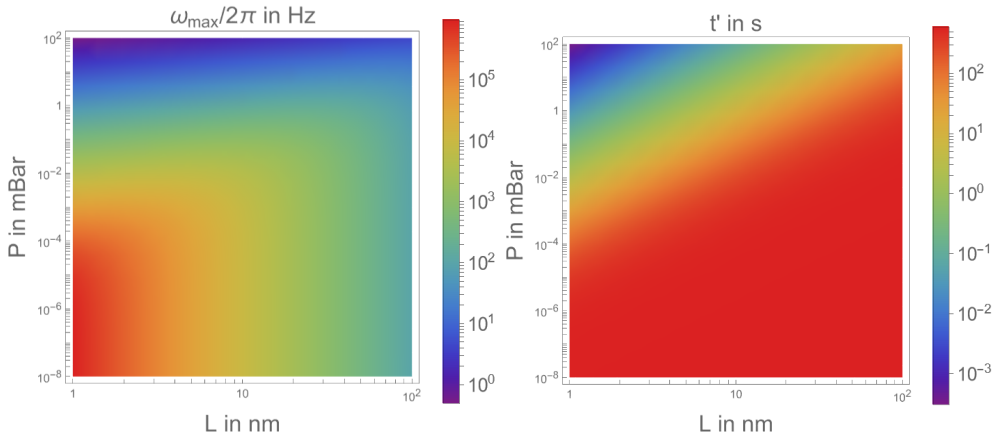


Figure 4: In (a), the expected maximum rotation frequency $\omega_{\max}$ due to the Einstein–de Haas effect is shown for different air pressures at $T = 100\,\mathrm{K}$ and various particle sizes with an initial nuclear spin polarisation of 10 % and a T_1 relaxation time of 10 minutes=600 s. L is the characteristic size of the particle with $a = 15\,L, b = 10\,L$ and $c = L$. (b) The time t' at which $\omega_{\max}(1 - 1/e)$ of the rotation speed is reached.

B.2 Friction Torque of a Rotating Ellipsoid in Gas

The friction torque of a rotating object in gas is given by [289]

$$\boldsymbol{\tau}_{\mathrm{drag}} = -\rho v_{\mathrm{th}} \Big[\frac{\alpha}{4} \int \mathbf{x} \times (\boldsymbol{\Omega} \times \mathbf{x})\, \mathrm{d}S + \left(1 - \frac{6-\pi}{8}\alpha\right) \int (\mathbf{x} \times \mathbf{n}) \boldsymbol{\Omega} \cdot (\mathbf{x} \times \mathbf{n})\, \mathrm{d}S \Big] \tag{B.63}$$

where $\boldsymbol{\Omega}$ is the angular velocity of the particle, ρ is the mass density, $v_{\mathrm{th}} = (8k_{\mathrm{B}}T/(\pi m))^{1/2}$ is the mean thermal velocity of the surrounding gas and α is the accommodation coefficient. $\mathbf{x}$ is a point on the surface of the ellipsoid and is given by

$$\mathbf{x} = \begin{pmatrix} a \sin\vartheta \cos\varphi \\ b \sin\vartheta \sin\varphi \\ c \cos\vartheta \end{pmatrix} \tag{B.64}$$

with $\vartheta \in [0, \pi]$, $\varphi \in [0, 2\pi)$ and the three semi-axes a, b and c. The surface normal $\mathbf{n}$ is given by

$$\mathbf{n} = \frac{1}{\sqrt{\frac{\sin^2\vartheta\cos^2\varphi}{a^2} + \frac{\sin^2\vartheta\sin^2\varphi}{b^2} + \frac{\cos^2\vartheta}{c^2}}} \begin{pmatrix} \sin\vartheta\cos\varphi/a \\ \sin\vartheta\sin\varphi/b \\ \cos\vartheta/c \end{pmatrix}. \tag{B.65}$$

This equation is valid as long as $L\Omega \ll v_{\mathrm{th}}$, where L is of the order of the linear dimension of the rotating body. The surface element $\mathrm{d}S$ is given by

$$\mathrm{d}S = abc \sin\vartheta \sqrt{\frac{\sin^2\vartheta\cos^2\varphi}{a^2} + \frac{\sin^2\vartheta\sin^2\varphi}{b^2} + \frac{\cos^2\vartheta}{c^2}}\mathrm{d}\vartheta\mathrm{d}\varphi. \tag{B.66}$$

To evaluate Eq. (B.63), we first notice that integrands $\cos\varphi, \sin\varphi$ and $\cos\varphi\sin\varphi$ integrate to zero over $[0, 2\pi]$, since each function has zero mean over a full period. As the first summand in Eq. (B.63) only involves integrals of the form $\int x_\mu x_\nu \,\mathrm{d}S$, all terms with $\mu \neq \nu$ evaluate to zero and we find

$$\int \mathbf{x} \times (\boldsymbol{\Omega} \times \mathbf{x})|_\mu \,\mathrm{d}S = \int (\mathbf{x}^2 - x_\mu^2)\,\mathrm{d}S\,\Omega_\mu. \tag{B.67}$$

The second summand in Eq. (B.63) only involves integrals of the form $\int(\mathbf{x} \times \mathbf{n})_\mu(\mathbf{x} \times \mathbf{n})_\nu \,\mathrm{d}S$. As before, all terms with $\mu \neq \nu$ evaluate to zero and we find

$$\int (\mathbf{x} \times \mathbf{n})\boldsymbol{\Omega} \cdot (\mathbf{x} \times \mathbf{n})|_\mu \,\mathrm{d}S = \int [(\mathbf{x} \times \mathbf{n})|_\mu]^2 \,\mathrm{d}S\,\Omega_\mu. \tag{B.68}$$

The friction torque is then given by

$$\boldsymbol{\tau}_{\mathrm{drag}} = -\rho v_{\mathrm{th}} \sum_{\mu\in\{x,y,z\}} \gamma_\mu(\omega \cdot \mathbf{e}_\mu)\mathbf{e}_\mu \tag{B.69}$$

with

$$\gamma_\mu = \frac{\alpha}{4}\int (\mathbf{x}^2 - x_\mu^2)\,\mathrm{d}S + \left(1 - \frac{6-\pi}{8}\alpha\right)\int [(\mathbf{x} \times \mathbf{n})|_\mu]^2 \,\mathrm{d}S. \tag{B.70}$$

For $a = b$, γ_μ has a closed form solution which is given in [289].

B.3 Rotation Under Confinement

The nanoparticle may not be free to rotate but instead experiences rotational confinement. Assuming the restoring potential is given by

$$U_{\mathrm{res}} = -U_0 \cos(\theta), \tag{B.71}$$

with $U_0 > 0$, the restoring torque is

$$\tau_{\mathrm{res}} = -\frac{\partial U_{\mathrm{res}}}{\partial\theta} = -U_0 \sin(\theta). \tag{B.72}$$

The equation governing θ is therefore

$$\frac{\mathrm{d}}{\mathrm{d}t}L(t) = I\ddot{\theta} = -U_0 \sin(\theta) + \frac{S_0}{T_1}e^{-t/T_1}. \tag{B.73}$$

This differential equation has two sets of solutions: one where the particle escapes confinement, and another one where it starts to oscillate but stays trapped. Here, we focus on the first case and show that, for sufficiently weak confinement, the confinement can be neglected during the angular-momentum transfer. For early times at which

$$|U_0| \ll \left|\frac{S_0}{T_1}e^{-t/T_1}\right|, \tag{B.74}$$

the restoring torque can be neglected. This approximation breaks down at approximately

$$t' \approx T_1 \log\left(\frac{|S_0|}{|U_0|T_1}\right), \tag{B.75}$$

which only exists if $|S_0|/(|U_0|T_1) > 1$. Until this time, the differential equation can be approximated as

$$I\ddot{\theta} = I\dot{\omega} = \frac{S_0}{T_1}e^{-t/T_1}, \tag{B.76}$$

and for $\omega(0) = 0$ one finds

$$\omega(t) = \frac{S_0}{I}\left(1 - e^{-t/T_1}\right). \tag{B.77}$$

Around t', this gives

$$\omega(t') = \frac{S_0}{I}\left(1 - \frac{U_0 T_1}{S_0}\right). \tag{B.78}$$

Under the assumption that

$$\left|\frac{U_0 T_1}{S_0}\right| \ll 1, \tag{B.79}$$

almost all angular momentum of the nuclei is transferred to the mechanical rotation before the rotational confinement begins to play a role. After the driving torque has become negligible, the equation of motion is

$$I\ddot{\theta} = -U_0 \sin\theta. \tag{B.80}$$

Multiplying by $\dot{\theta}$ yields the conserved energy

$$\frac{I}{2}\dot{\theta}^2 - U_0 \cos\theta = E, \qquad E = \text{const.} \tag{B.81}$$

Since the potential minimum is $-U_0$ at $\theta = 0$ and the maximum is $+U_0$ at $\theta = \pi$, the barrier height is $2U_0$. Escape from confinement requires $E > U_0$. For a particle starting near the bottom of the potential, $\theta(0) \approx 0$, so that $E = \frac{I}{2}\omega(t')^2 - U_0$, and

the escape condition becomes

$$\frac{I}{2}\omega(t')^2 \gtrsim 2U_0. \tag{B.82}$$

For a general initial angle θ_0, the required kinetic energy for escape is $U_0(1+\cos\theta_0)$, which is maximised at $\theta_0 = 0$ and vanishes at $\theta_0 = \pi$. Thus, as a scaling condition, escape is guaranteed when

$$\frac{S_0^2}{4I} \gg U_0. \tag{B.83}$$

In summary, the two conditions for the spin angular momentum to be transferred before confinement becomes relevant, and for the particle to escape confinement afterwards, are

$$\left|\frac{U_0 T_1}{S_0}\right| \ll 1 \qquad \text{and} \qquad \frac{S_0^2}{4I} \gg U_0. \tag{B.84}$$

For a potential of the form $U_{\rm res} = -U_0\cos(2\theta)$, the restoring torque is $-2U_0\sin(2\theta)$, modifying the short-pulse condition to $|2U_0T_1/S_0| \ll 1$. Upon integration, the factor of two is reabsorbed upon integration and the potential still oscillates between $-U_0$ and $+U_0$, giving a barrier height of $2U_0$, identical to the $\cos\theta$ case. The escape condition $S_0^2/(4I) \gg U_0$ is therefore unchanged.

Tilt confinement does not directly affect the spin dynamics to leading order, but must be checked separately for stability against tilt perturbations, which are characterized by the tilt libration frequency $\omega_{\rm lib}$, the small-angle oscillation frequency for tilts of the spin axis away from the field direction. For a fully asymmetric particle, coupling to the remaining rotational degrees of freedom can occur. If the principal moments of inertia are unequal, $I_x \neq I_y \neq I_z$, torque-free Euler dynamics can induce wobble of the spin axis, characterized by $\omega_{\rm wobble}$. Linearising the Euler equations around ω_z (with $\omega_x, \omega_y \ll \Omega$) gives the coupled system

$$\frac{\mathrm{d}}{\mathrm{d}t}\begin{pmatrix}\omega_x\\ \omega_y\end{pmatrix} = \omega_z \begin{pmatrix}0 & (I_y - I_z)/I_x\\ (I_z - I_x)/I_y & 0\end{pmatrix}\begin{pmatrix}\omega_x\\ \omega_y\end{pmatrix}. \tag{B.85}$$

Differentiating the first row and substituting the second eliminates ω_y and yields

$$\ddot{\omega}_i = \frac{(I_j - I_z)(I_z - I_i)}{I_i I_j}\,\omega_z^2\,\omega_i \tag{B.86}$$

with $i, j \in \{x, y\}$. The characteristic equation $r^2 = C\omega_z^2$, where

$$C = \frac{(I_j - I_z)(I_z - I_i)}{I_i I_j}, \tag{B.87}$$

has roots $r = \pm\omega_z\sqrt{C}$, whose character depends on the sign of C:

- If the spin axis z carries the largest or smallest moment of inertia, $C < 0$ and $r = \pm \mathrm{i}\,\omega_{\mathrm{wobble}}$ is purely imaginary, giving bounded oscillation. Here ω_{wobble} is the body-frame precession (wobble) frequency of the transverse angular-velocity components, it is defined by

$$\omega_{\mathrm{wobble}} = \omega_z \sqrt{\frac{(I_z - I_i)(I_z - I_j)}{I_i I_j}}. \tag{B.88}$$

- If the spin axis z carries the intermediate moment of inertia, $C > 0$ and $r = \pm\sigma$ is real, giving exponential growth (Dzhanibekov instability or tennis racket theorem) at rate

$$\sigma = \omega_z \sqrt{\frac{(I_z - I_{\min})(I_{\max} - I_z)}{I_{\min} I_{\max}}}. \tag{B.89}$$

Stability with librational confinement. When the particle is librationally confined, restoring torques act on the two tilt modes and can suppress the Dzhanibekov instability. For a fully asymmetric particle the two tilt directions have, in general, different libration frequencies $\omega_{\mathrm{lib},y}$ and $\omega_{\mathrm{lib},x}$: we derive the stability condition by extending the Euler equations to include these torques. Let θ_y denote the small tilt of the spin axis toward $\hat{x}$ (rotation about y) and θ_x the tilt toward $\hat{y}$ (rotation about x). For small tilts the rates of change are related to the transverse angular-velocity components by

$$\dot{\theta}_x = \omega_x, \qquad \dot{\theta}_y = \omega_y, \tag{B.90}$$

to leading order. Adding restoring torques $\tau_y = -I_y\,\omega_{\mathrm{lib},y}^2\,\theta_y$ and $\tau_x = -I_x\,\omega_{\mathrm{lib},x}^2\,\theta_x$ to Eq. (B.85) gives

$$I_x \dot{\omega}_x = (I_y - I_z)\,\omega_z\,\omega_y - I_x\,\omega_{\mathrm{lib},x}^2\,\theta_x, \tag{B.91}$$

$$I_y \dot{\omega}_y = (I_z - I_x)\,\omega_z\,\omega_x - I_y\,\omega_{\mathrm{lib},y}^2\,\theta_y. \tag{B.92}$$

Dividing by I_x and I_y respectively and using Eq. (B.90) to replace $\omega_{x,y}$ by $\dot{\theta}_{x,y}$ yields two coupled second-order equations for the tilt angles:

$$\ddot{\theta}_x + \omega_{\mathrm{lib},x}^2\,\theta_x = \frac{I_y - I_z}{I_x}\,\omega_z\,\dot{\theta}_y, \tag{B.93}$$

$$\ddot{\theta}_y + \omega_{\mathrm{lib},y}^2\,\theta_y = \frac{I_z - I_x}{I_y}\,\omega_z\,\dot{\theta}_x. \tag{B.94}$$

Inserting the ansatz $(\theta_x, \theta_y) \propto e^{\lambda t}$ turns Eqs. (B.93) and (B.94) into two algebraic equations:

$$(\lambda^2 + \omega_{\mathrm{lib},x}^2)\,\theta_x = \frac{I_y - I_z}{I_x}\,\omega_z \lambda\,\theta_y, \qquad (\lambda^2 + \omega_{\mathrm{lib},y}^2)\,\theta_y = \frac{I_z - I_x}{I_y}\,\omega_z \lambda\,\theta_x. \tag{B.95}$$

Multiplying these two equations eliminates θ_y and θ_x and gives the characteristic equation

$$\lambda^4 + \left(\omega_{\mathrm{lib},x}^2 + \omega_{\mathrm{lib},y}^2 - C\omega_z^2\right)\lambda^2 + \omega_{\mathrm{lib},x}^2\,\omega_{\mathrm{lib},y}^2 = 0. \tag{B.96}$$

For all four roots λ to be purely imaginary (bounded motion), both roots of the quadratic in λ^2 must be real and negative. The product of the two roots equals $\omega_{\mathrm{lib},x}^2\omega_{\mathrm{lib},y}^2 > 0$, which is automatically satisfied. Their sum equals

$$-(\omega_{\mathrm{lib},x}^2 + \omega_{\mathrm{lib},y}^2 - C\omega_z^2) \tag{B.97}$$

, which is negative if and only if

$$\omega_{\mathrm{lib},x}^2 + \omega_{\mathrm{lib},y}^2 > C\omega_z^2. \tag{B.98}$$

The discriminant of the quadratic in λ^2 factorizes as

$$\Delta = \left[(\omega_{\mathrm{lib},x} - \omega_{\mathrm{lib},y})^2 - C\omega_z^2\right]\left[(\omega_{\mathrm{lib},x} + \omega_{\mathrm{lib},y})^2 - C\omega_z^2\right]. \tag{B.99}$$

For $\Delta \geq 0$ both factors must have the same sign. Both negative would require $(\omega_{\mathrm{lib},x} + \omega_{\mathrm{lib},y})^2 < C\omega_z^2$, which contradicts Eq. (B.98), so stability requires both factors to be non-negative. Since $\omega_{\mathrm{lib},x} + \omega_{\mathrm{lib},y} > |\omega_{\mathrm{lib},x} - \omega_{\mathrm{lib},y}|$, the binding condition is

$$|\omega_{\mathrm{lib},x} - \omega_{\mathrm{lib},y}| > \sigma = \sqrt{C}\,\omega_z. \tag{B.100}$$

It is the splitting of the two tilt libration frequencies, not their individual values, that must exceed the Dzhanibekov rate. When the two tilt frequencies are degenerate ($\omega_{\mathrm{lib},x} = \omega_{\mathrm{lib},y}$) with $C > 0$, Eq. (B.100) is never satisfied for $\omega_z \neq 0$: the degenerate modes are resonantly driven by the Euler coupling and no amount of libration frequency (only splitting) can stabilize the spin. For $C \leq 0$ (spin about $I_{\max}$ or $I_{\min}$), all coefficients in Eq. (B.96) are positive for any $\omega_{\mathrm{lib},x}^2, \omega_{\mathrm{lib},y}^2 > 0$ and the motion is unconditionally stable. In addition, direct resonances of the form $\omega_{\mathrm{wobble}} \approx \omega_{\mathrm{lib}}$ should be avoided, since they can transfer energy from the spin degree of freedom into tilt modes. Beyond direct resonance, parametric instabilities can arise when $\omega_{\mathrm{wobble}} \approx 2\,\omega_{\mathrm{lib}}$, or more generally at sub-harmonic ratios $\omega_{\mathrm{wobble}} \approx (n/m)\,\omega_{\mathrm{lib}}$ for integers n, m. In this work, we will focus on avoiding the unstable rotation regime.

Diamagnetic trapping. For a diamagnetic asymmetric particle in a quadrupole field, the abstract quantities introduced above take explicit forms. Consider a particle of characteristic size r, volume V, and anisotropic diamagnetic susceptibility

$\chi_x \neq \chi_y \neq \chi_z$, with all components negative, translationally confined at the origin of the quadrupole field

$$\mathbf{B} = (B'_x x,\, B'_y y,\, B'_z z + B_0). \tag{B.101}$$

The magnetic energy of a finite-size particle can be written, to leading order in the field expansion over the particle volume, as

$$U = -\frac{1}{2}\int_V \mathbf{M}_{\rm dia}\cdot\mathbf{B}\,\mathrm{d}V = -\frac{VB_0^2}{2\mu_0}\chi_{zz}^{(\rm lab)}(\tilde{\Omega}) - \frac{1}{2\mu_0}\sum_{ij}\chi_{ij}^{(\rm lab)}(\tilde{\Omega})B'_iB'_j\,\mathcal{I}_{ij}, \tag{B.102}$$

where $\mathcal{I}_{ij} = \int_V r_i r_j\,\mathrm{d}V$ is the second-moment tensor of the particle volume and $\tilde{\Omega}$ denotes the particle orientation. The first term is set by the homogeneous bias field B_0, the second is set by the field gradient across the finite particle extent. For tilt modes (rotations around x and y), the B_0 term dominates when $B_0 \gg B'r$, where r is the characteristic length of the particle. Otherwise, the gradients would determine the particles orientation. For a small tilt θ of the body z-axis away from $\mathbf{e}_z$, the relevant susceptibility component is $\chi_{zz}^{(\rm lab)} = \chi_z\cos^2\theta + \chi_\perp\sin^2\theta$, giving

$$U_\theta \approx -\frac{VB_0^2}{2\mu_0}\big[\chi_z + (\chi_\perp - \chi_z)\theta^2\big]. \tag{B.103}$$

The equation of motion $I_\perp\ddot{\theta} = -\partial U_\theta/\partial\theta$ then yields

$$I_\perp\ddot{\theta} = \frac{VB_0^2(\chi_\perp - \chi_z)}{\mu_0}\,\theta = -\frac{VB_0^2\,\Delta\chi}{\mu_0}\,\theta, \qquad \Delta\chi \equiv \chi_z - \chi_\perp. \tag{B.104}$$

Since $\chi < 0$, the magnetic energy is minimised when the axis of smallest susceptibility magnitude aligns with the strongest field direction. In the bias-dominated limit $B_0 \gg B'r$, this is $\mathbf{e}_z$, so stability requires $\Delta\chi \equiv \chi_z - \chi_\perp > 0$, i.e. $|\chi_z| < |\chi_\perp|$. When the gradient term dominates the equilibrium shifts, and in general the preferred orientation depends on the full field configuration, throughout this analysis we assume the bias-dominated case. The tilt libration frequency is

$$\omega_{\rm lib}^2 = \frac{VB_0^2\,\Delta\chi}{\mu_0 I_\perp}, \qquad \Delta\chi = \chi_z - \chi_\perp > 0, \tag{B.105}$$

with the gradient term contributing a relative correction of order $(B'r/B_0)^2$. Eq. (B.105) gives the libration frequency for small tilts of the spin axis $\hat{z}$ toward one specific transverse direction, say $\mathbf{e}_x$; here $\chi_\perp = \chi_e$ is the body-frame susceptibility along that direction and $I_\perp$ is the moment of inertia about the corresponding rotation axis $\mathbf{e}_y$. For a fully asymmetric particle ($\chi_x \neq \chi_y$), a second distinct libration frequency arises for tilts toward $\mathbf{e}_y$, as given explicitly in Eq. (B.124).

For the spin mode (rotation around $\mathbf{e}_z$), the B_0 term gives no restoring torque

because it does not change $\chi_{zz}^{(\mathrm{lab})}$, spin confinement hence originates entirely from the gradient term. Spin confinement therefore arises entirely from the gradient term,

$$U_\varphi = -\frac{1}{2\mu_0} \sum_{i,j\in\{x,y\}} \chi_{ij}^{(\mathrm{lab})}(\varphi)\, B'_i B'_j\, \mathcal{I}_{ij}(\varphi) + \mathrm{const}, \tag{B.106}$$

where the z-components vanish for ellipsoidal particles and a rotation about $\hat{z}$. Under this rotation the transverse susceptibility components are

$$\begin{aligned}
\chi_{xx}^{(\mathrm{lab})} &= \frac{\chi_x + \chi_y}{2} + \frac{\chi_x - \chi_y}{2}\cos 2\varphi, \\
\chi_{yy}^{(\mathrm{lab})} &= \frac{\chi_x + \chi_y}{2} - \frac{\chi_x - \chi_y}{2}\cos 2\varphi, \\
\chi_{xy}^{(\mathrm{lab})} &= \frac{\chi_x - \chi_y}{2}\sin 2\varphi,
\end{aligned} \tag{B.107}$$

and the tensor $\mathcal{I}_{ij}$, with body-frame moments $J_i = \int_V r_i^2 \,\mathrm{d}V$, transforms as

$$\begin{aligned}
\mathcal{I}_{xx} &= \frac{J_x + J_y}{2} + \frac{J_x - J_y}{2}\cos 2\varphi, \\
\mathcal{I}_{yy} &= \frac{J_x + J_y}{2} - \frac{J_x - J_y}{2}\cos 2\varphi \\
\mathcal{I}_{xy} &= \frac{J_x - J_y}{2}\sin 2\varphi.
\end{aligned} \tag{B.108}$$

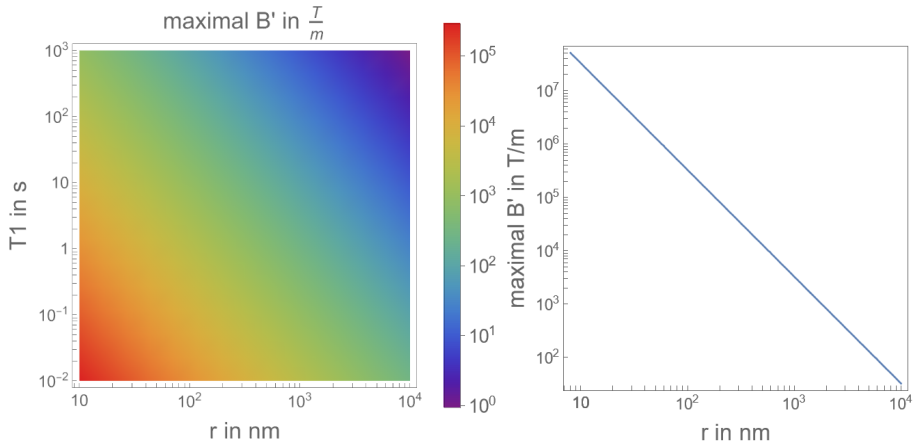
Substituting and collecting the $\cos(2\varphi)$ terms, the $B'_x B'_y$ cross term produces only $\sin^2 2\varphi$, contributing a constant and a subleading $\cos(4\varphi)$ correction, gives the leading-order spin-confinement potential

$$U_\varphi = -\frac{V\left(B_x'^2 - B_y'^2\right)\left(\chi_x a_x^2 - \chi_y a_y^2\right)}{20\mu_0}\cos(2\varphi), \tag{B.109}$$

where we evaluated J_i for an ellipsoid.

Three consequences follow immediately: a sphere ($J_x = J_y$) with susceptibility anisotropy is confined even without shape anisotropy; an ellipsoid with isotropic susceptibility ($\chi_x = \chi_y$) is confined by shape alone; and a symmetric trap ($B'_x = B'_y$) produces no spin confinement regardless of particle properties. The libration frequency is $\omega_\varphi^2 = 4U_0/I_z$.

The magnetic susceptibility of naphthalene is $\boldsymbol{\chi}_V = -\mathrm{diag}(7.9, 4.4, 17.8)\cdot 10^{-6}$ [209]. The geometry of the particle can in principle modify this through the



(a) (b)

Figure 5: To escape the diamagnetic rotational confinement, $\Delta U_{\text{dia}} = U_0$ has to be small enough to ensure $|U_0 T_1/S_0| \ll 1$ and $S_0^2/(4I) \gg U_0$. In (a), the T_1 time at which $|U_0 T_1/S_0|$ is maximally 0.1 for a spherical naphthalene particle with 10 % polarization is shown. In (b), the maximal B'_y at which $S_0^2/(4I)/U_0 > 10$ for a spherical particle with 10 % polarization and a given radius r is shown.

demagnetization tensor $\mathcal{N}$ [290]: the effective susceptibility is then given by

$$\boldsymbol{\chi}_{V,\text{eff}} = (1 + \boldsymbol{\chi}_V \mathcal{N})^{-1} \boldsymbol{\chi}_V. \tag{B.110}$$

In the principal frame of $\mathcal{N}$, the constraint $\mathcal{N}_x + \mathcal{N}_y + \mathcal{N}_z = 1$ holds. Since $|\boldsymbol{\chi}_V| \sim 10^{-5}$, one has $\boldsymbol{\chi}_V \mathcal{N} \ll 1$ and therefore $\boldsymbol{\chi}_{V,\text{eff}} \approx \boldsymbol{\chi}_V$ for any particle geometry, the shape correction is negligible and we henceforth use $\boldsymbol{\chi}_V$ directly.

To analyze $U_0 T_1/S_0$, we assume a particle with a strongly asymmetric trapping field of $B'_y = 0$ and $B_x = B'$ and a particle of typical size r. The confinement energy then scales like

$$U_\varphi \sim -\frac{\pi B'^2 \Delta\chi r^5}{15\mu_0} \tag{B.111}$$

Here, the potential depends on $\cos(2\varphi)$ as well, hence the short-pulse condition has to be adapted accordingly. In Fig. 5, the required T_1 is shown to ensure at least $|2U_0 T_1/S_0| < 0.1$ for different B' and r of a naphthalene particle with 10 % polarization. In Fig. 5b, the maximal B' at which $S_0^2/(4I)/U_0 > 10$ for a given r is shown. Note that for symmetric traps, the particles will be way less confined in its rotation round $\mathbf{e}_z$ and here a worst case scenario is presented. Alternatively, the particle could be manufactured in a way that $\chi_x/\chi_y = a_x^2/a_y^2$.

Electrical confinement. In the presence of electric fields, whether intentionally applied to displace the particle within the trap or arising as uncontrolled stray fields, the abstract quantities U_0 and ω_φ take explicit forms from two independent mechanisms: a permanent electric dipole due to a localised surface charge, and the dielectric anisotropy of the particle body. Consider first the effect of a static field $\mathbf{E} = E_0\mathbf{e}_z$ applied along the trapping axis. A net charge Q on the particle produces a force $F_{\mathrm{e},z} = QE_0$ that shifts the translational equilibrium, the local bias field at the new equilibrium is

$$B_0 = \frac{\mu_0}{B_z'\chi_V}\left(g\rho - \frac{QE_0}{V}\right). \tag{B.112}$$

For naphthalene ($\rho = 1145\,\mathrm{kg/m^3}$, $B_z' = 10^3\,\mathrm{T/m}$) this gives $B_0 \approx 1.4\,\mathrm{T}$ at zero field. A field of

$$E_0 = \left(47.050 \times 10^3\,\frac{\mathrm{J}}{\mathrm{m}^4}\right)\frac{r^3}{Q} \tag{B.113}$$

is required to move the particle to a field-free point, for a 100 nm sphere carrying one elementary charge, this corresponds to approximately $300\,\mathrm{V/m}$. An axial field of this type does not break the azimuthal symmetry around $\mathbf{e}_z$ and therefore does not confine the spin degree of freedom, the analysis below concerns transverse fields. The dominant electrical confinement mechanism is a localized patch charge Q fixed on the particle surface at distance r from the center of mass, creating a permanent electric dipole

$$\mathbf{p}_0 = Qr\,\hat{\mathbf{n}}, \tag{B.114}$$

where $\hat{\mathbf{n}}$ is the orientation of the charge in the body frame. In an external field $\mathbf{E} = E_0\hat{x}$ perpendicular to the spin axis, the orientational energy is

$$U_{\mathrm{Q}}(\theta) = -\mathbf{p}_0 \cdot \mathbf{E} = -p_0E_0\cos\theta, \tag{B.115}$$

where θ is the angle between $\hat{\mathbf{n}}$ and $\hat{x}$. This is the standard form (B.73) with $U_0 = p_0E_0 = QrE_0$. The corresponding tilt libration frequency is

$$\omega_{\mathrm{lib,Q}}^2 = \frac{p_0E_0}{I} = \frac{QrE_0}{I}, \tag{B.116}$$

and the escape conditions (B.84) become

$$\frac{QrE_0\,T_1}{S_0} \ll 1 \qquad \text{and} \qquad \frac{S_0^2}{4I} \gg QrE_0. \tag{B.117}$$

For a naphthalene sphere with 10 % nuclear polarization carrying a single surface charge in the equatorial plane, $p_0 = er$, and

$$\frac{U_{\mathrm{Q},0}\,T_1}{S_0} = \frac{eE_0rT_1}{N\hbar/2 \cdot 0.1} \approx \left(1.7 \times 10^{-13}\,\frac{\mathrm{m}^3}{\mathrm{V\,s}}\right)\frac{E_0T_1}{r^2}. \tag{B.118}$$

Stray fields without shielding are typically tens of V/m, a Faraday cage (typical transmission $\sim 10^{-7}$ [291]) suppresses them sufficiently. The weaker constraint $S_0^2/(4I)/U_{\mathrm{Q},0} > 10$ is satisfied for fields up to 74 V/m.

Even if the charge is placed on the particle in such a way, that it does not confine the particle's rotation, for example by being fully delocalized over the extent of the particle, the particle's rotation around $\mathbf{e}_z$ might be constrained by a transverse electric field due to the dielectric anisotropy. The electrostatic interaction energy of an induced dipole is

$$U_{\mathrm{el}} = -\frac{\varepsilon_0 V}{2}\mathbf{E}^{\mathsf{T}}\boldsymbol{\chi}_{\mathrm{el}}\mathbf{E}, \tag{B.119}$$

where $\boldsymbol{\chi}_{\mathrm{el}}$ is the body-frame electric susceptibility tensor. For a rotation φ about $\mathbf{e}_z$ in the field $\mathbf{E} = E_0\hat{x}$, using $\cos^2\varphi = (1+\cos 2\varphi)/2$ and discarding the constant offset, the φ-dependent part is

$$U_{\mathrm{el},\varphi} = -\frac{\varepsilon_0 V}{4}E_0^2\,\Delta\chi_{\mathrm{el}}\cos(2\varphi), \qquad \Delta\chi_{\mathrm{el}} = \chi_{\mathrm{el},\parallel} - \chi_{\mathrm{el},\perp}. \tag{B.120}$$

Here, the potential depends on $\cos(2\varphi)$, hence the short-pulse condition has to be adapted accordingly. The corresponding libration frequency is given by

$$\omega_{\mathrm{lib,el}}^2 = \frac{\varepsilon_0 V E_0^2 \Delta\chi_{\mathrm{el}}}{I} \tag{B.121}$$

The dielectric tensor of naphthalene is $\boldsymbol{\varepsilon}_r = \mathrm{diag}(2.25, 2.87, 3.43)$ [292], giving $\boldsymbol{\chi}_{\mathrm{el}} = \boldsymbol{\varepsilon}_r - \mathbf{1} = \mathrm{diag}(1.25, 1.87, 2.43)$. The worst-case anisotropy is $\Delta\chi_{\mathrm{el}} = \chi_{\mathrm{el,max}} - \chi_{\mathrm{el,min}} = 1.18$. As with the diamagnetic case, the particle geometry modifies the effective susceptibility through the depolarization tensor $\mathcal{N}$ (with $\mathcal{N}_x + \mathcal{N}_y + \mathcal{N}_z = 1$):

$$\chi_{\mathrm{el,eff},i} = \frac{\chi_{\mathrm{el},i}}{1 + \mathcal{N}_i\chi_{\mathrm{el},i}}, \qquad i \in \{x, y, z\}. \tag{B.122}$$

Even in the extreme disc limit ($\mathcal{N}_x \approx 1$, $\mathcal{N}_{y,z} \approx 0$), which yields $\boldsymbol{\chi}_{\mathrm{el,eff}} = \mathrm{diag}(0.56, 1.87, 2.43)$, the anisotropy $\Delta\chi_{\mathrm{el}}$ increases by at most a factor of 1.5, leaving the scaling of the results unchanged. In Fig. 6a, $|2U_{\mathrm{Q},0}T_1/S_0|$ is shown for different E_0 and T_1 for a spherical naphthalene particle with 10 % polarization carrying a single surface charge. In Fig. 6b, $|2U_{\mathrm{el},0}T_1/S_0|$ for the dielectric mechanism is shown, in Fig. 6c, the maximal E_0 for which $S_0^2/(4I)/U_{\mathrm{el},0} > 10$ is given as a function of r.

Coupling to other rotational modes: bias-field trap ($B_0 \gg B'r$). The analysis above treats tilt and spin as independent degrees of freedom. For a fully asymmetric particle they are coupled through the Euler dynamics, we now establish the conditions under which this coupling is negligible, specializing to the naphthalene ellipsoid with semi-axes $a = 15L$, $b = 10L$, $c = L$. If no electric charge is used to move the particle into a regime where $B_0 \gg B'r$ to shorten the T_1 time,

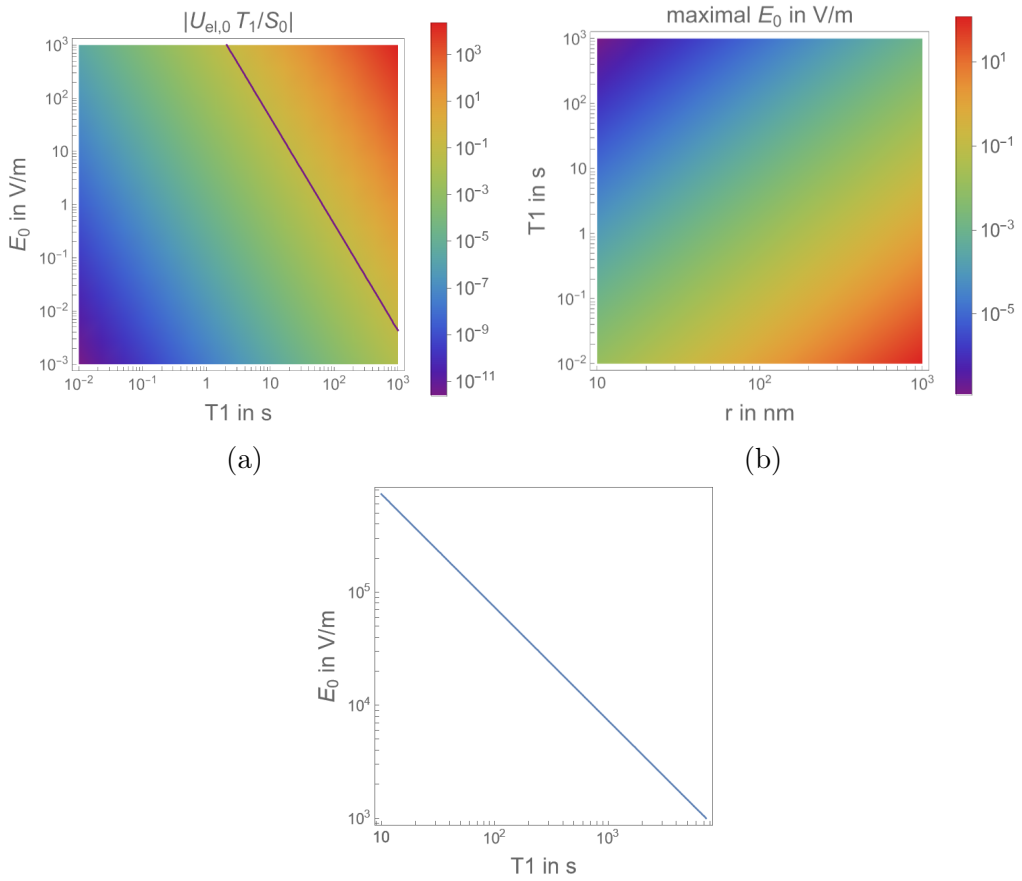


Figure 6: To escape electrical rotational confinement, U_0 must be small enough to ensure $|U_0 T_1/S_0| \ll 1$ and $S_0^2/(4I) \gg U_0$. (a) $|U_{\mathrm{el},0} T_1/S_0|$ for a spherical naphthalene particle with 10 % polarization carrying a single surface charge in a transverse stray field, the black contour marks $|U_{\mathrm{el},0} T_1/S_0| = 0.1$. (b) Maximal E_0 to ensure $|U_{\mathrm{Q},0} T_1/S_0| < 0.1$ for the confinement due to dielectric anisotropy. (c) Maximal E_0 for which $S_0^2/(4I)/U_{\mathrm{el},0} > 10$ as a function of r and T_1. To satisfy $|S_0^2/(4I)/U_{\mathrm{Q},0}| > 10$ for a naphthalene particle carrying one charge, fields up to 74 V/m can be tolerated.

we are in the regime where E_0 and $B_0 \gg B'r$. With the bias-dominated field and $\boldsymbol{\chi}_V = -\mathrm{diag}(17.8, 7.9, 4.4) \times 10^{-6}$, we assume the worst case in which the largest magnetic susceptibility axis coincides with the intermediate rotation axis ($10L$, $|\chi_z| = 4.4 \times 10^{-6}$ smallest) aligns with $\mathbf{e}_z$. The spin axis is therefore b, with moment of inertia $I_b = \frac{m}{5}(a^2+c^2) = 226\frac{mL^2}{5}$. Since $I_a = 101\frac{mL^2}{5} < I_b < I_c = 325\frac{mL^2}{5}$, this is the intermediate principal axis, so the torque-free Euler dynamics are unstable (Dzhanibekov instability) with exponential growth rate

$$\sigma = \sqrt{C}\,\omega_z, \qquad C = \frac{(I_c - I_b)(I_b - I_a)}{I_a I_c} \approx 0.377, \tag{B.123}$$

where ω_z is the final spin rate.

Two distinct tilt libration frequencies. Because $I_a \neq I_c$, the two tilt modes have different moments of inertia and different magnetic susceptibilities, leading to two distinct libration frequencies. Applying Eq. (B.105) separately to each tilt direction:

$$\omega_{\mathrm{lib},ba}^2 = \frac{V B_0^2\,(\chi_b - \chi_a)}{\mu_0 I_c}, \qquad \omega_{\mathrm{lib},bc}^2 = \frac{V B_0^2\,(\chi_b - \chi_c)}{\mu_0 I_a}, \tag{B.124}$$

where $\omega_{\mathrm{lib},ba}$ corresponds to tilting b toward a (rotation about c, moment I_c) and $\omega_{\mathrm{lib},bc}$ to tilting b toward c (rotation about a, moment I_a). At $B_0 = 1\,\mathrm{T}$ and $L = 100\,\mathrm{nm}$:

$$\omega_{\mathrm{lib},ba} \approx 9.7(2\pi)\,\mathrm{kHz}, \qquad \omega_{\mathrm{lib},bc} \approx 34.2(2\pi)\,\mathrm{kHz}, \tag{B.125}$$

both scaling as B_0/L.

Stability condition. Identifying $\omega_{\mathrm{lib},y} = \omega_{\mathrm{lib},ba}$ and $\omega_{\mathrm{lib},x} = \omega_{\mathrm{lib},bc}$, the general condition Eq. (B.100) requires

$$|\omega_{\mathrm{lib},ba} - \omega_{\mathrm{lib},bc}| > \sigma = \sqrt{C}\,\omega_z. \tag{B.126}$$

This condition is only relevant when $C > 0$, which requires the spin axis to carry the *intermediate* moment of inertia and therefore $I_a \neq I_c$. When $I_a = I_c$ (axially symmetric particle), the Euler coefficient satisfies $C = -(I_a - I_b)^2/(I_a^2) \leq 0$: the spin axis b is automatically the maximum or minimum principal axis, the two tilt frequencies are equal, and the rotation is unconditionally stable — the Dzhanibekov instability cannot arise.

Numerical evaluation. The final spin rate for b-axis spin is $\omega_{z,\infty} = S_0/I_b \approx 4.39\times10^{-12}/L^2$ (in SI), giving $\omega_{z,\infty} \approx 70(2\pi)\,\mathrm{Hz}$ and $\sigma \approx 43(2\pi)\,\mathrm{Hz}$ at $L = 100\,\mathrm{nm}$.

Condition (B.126) then reads

$$|\omega_{\mathrm{lib},ba} - \omega_{\mathrm{lib},bc}| = 24.5(2\pi)\,\mathrm{kHz} \gg \sigma = 43(2\pi)\,\mathrm{Hz}, \tag{B.127}$$

satisfied by a factor of ≈ 570. Because $|\omega_{\mathrm{lib},ba} - \omega_{\mathrm{lib},bc}| \propto B_0/L$ while $\sigma \propto \omega_{z,\infty} \propto 1/L^2$, the margin grows as $B_0 L$ and improves for larger particles. Equating both sides gives a critical size $L_{\mathrm{crit}} = 0.18\,\mathrm{nm}$ — below the bond length — so condition (B.126) holds for any physical naphthalene particle.

Coupling to other rotational modes: gradient trap with electric alignment ($B_0 = 0$). We now consider $B_0 = 0$, so that the particle sits at the field zero of $\mathbf{B} = (B'_x x,\, B'_y y,\, B'_z z)$, with orientation set by a static electric field $\mathbf{E} = E_0 \mathbf{e}_z = 300\,\mathrm{V/m}\,\mathbf{e}_z$. Here we assume that the charge on the particle used to move the particle to a low-magnetic field regime does not influence its orientation, for example if the charge is fully delocalized over the particle.

Axis alignment. The Maxwell relation $\chi_{\mathrm{el},i} = n_i^2 - 1$ applied to the principal-axis refractive indices of naphthalene [209] shows that $\boldsymbol{\chi}_V$ and $\boldsymbol{\chi}_{\mathrm{el}}$ are diagonal in the same crystal frame. The ordering is anti-correlated: the axis with the largest diamagnetic susceptibility magnitude carries the smallest electric susceptibility, and vice versa. Consequently the electric field $E_0 \mathbf{e}_z$ aligns the axis of smallest $|\chi_V|$ with $\mathbf{e}_z$.

Orientation equilibrium. At $B_0 = 0$ the bias-field torque vanishes, the equilibrium orientation is determined by the competition between the electric orientation energy

$$\Delta U_{\mathrm{el}} = \frac{\varepsilon_0 V E_0^2\, \Delta\chi_{\mathrm{el}}}{2} \tag{B.128}$$

and the magnetic-gradient orientation energy, which for a particle of typical radius r scales as

$$\Delta U_{\mathrm{mag}} \sim \frac{V (B'r)^2\, |\Delta\chi_V|}{2\mu_0}. \tag{B.129}$$

Their ratio is

$$\frac{\Delta U_{\mathrm{el}}}{\Delta U_{\mathrm{mag}}} = \frac{\varepsilon_0 \mu_0\, E_0^2\, \Delta\chi_{\mathrm{el}}}{(B'r)^2\, |\Delta\chi_V|} = \frac{E_0^2\, \Delta\chi_{\mathrm{el}}}{c^2 (B'r)^2\, |\Delta\chi_V|}. \tag{B.130}$$

For $E_0 = 300\,\mathrm{V/m}$, $B' = 10^3\,\mathrm{T/m}$, $\Delta\chi_{\mathrm{el}} = 1.18$, and $|\Delta\chi_V| = 13.4 \times 10^{-6}$:

$$\frac{\Delta U_{\mathrm{el}}}{\Delta U_{\mathrm{mag}}} \approx \frac{8.8 \times 10^{-14}\,\mathrm{m}^2}{r^2}, \tag{B.131}$$

which equals unity at the crossover radius

$$r_{\rm cross} = \frac{E_0}{B'}\sqrt{\frac{\varepsilon_0\mu_0\,\Delta\chi_{\rm el}}{|\Delta\chi_V|}} \approx 300\,\text{nm}. \tag{B.132}$$

For $r \gtrsim r_{\rm cross}$ the magnetic gradient dominates, for $r \lesssim r_{\rm cross}$ the electric field sets the orientation. At $r = 100\,\text{nm}$ the electric interaction dominates by a factor of ≈ 9, so the spin-axis orientation is primarily set by $\boldsymbol{\chi}_{\rm el}$.

Tilt libration frequencies. For $B_0 = 0$, the libration frequencies yield

$$\begin{aligned}\omega^2_{{\rm lib,grad},ba} &= \frac{(B'r)^2\,V(\chi_{V,b}-\chi_{V,a})}{5\,\mu_0\,I_c},\\ \omega^2_{{\rm lib,grad},bc} &= \frac{(B'r)^2\,V(\chi_{V,b}-\chi_{V,c})}{5\,\mu_0\,I_a},\end{aligned} \tag{B.133}$$

Notice, that $B'r$ here gives the order of magnitude for the difference of the gradient times the particle radius along the respective axis. For a fully symmetrical particle in a fully symmetrical trap, the libration frequencies are zero. With $B'r = 10^3\,\text{T/m} \times 100\,\text{nm} = 10^{-4}\,\text{T}$ at $r = 100\,\text{nm}$:

$$\omega_{{\rm lib,grad},ba} \approx 0.43(2\pi)\,\text{Hz}, \qquad \omega_{{\rm lib,grad},bc} \approx 1.53(2\pi)\,\text{Hz}, \tag{B.134}$$

four to five orders of magnitude smaller than the bias-field values (B.125). The electric contribution to the tilt libration is

$$\begin{aligned}\omega_{{\rm lib,el},ba} &= \sqrt{\frac{\varepsilon_0 V E_0^2\,(\chi_{{\rm el},b}-\chi_{{\rm el},a})}{I_c}} \approx 3.9(2\pi)\,\text{Hz},\\ \omega_{{\rm lib,el},bc} &= \sqrt{\frac{\varepsilon_0 V E_0^2\,(\chi_{{\rm el},b}-\chi_{{\rm el},c})}{I_a}} \approx 10.1(2\pi)\,\text{Hz},\end{aligned} \tag{B.135}$$

with $\chi_{{\rm el},b} = 2.43$, $\chi_{{\rm el},a} = 1.87$, $\chi_{{\rm el},c} = 1.25$.

Dzhanibekov stability. The stability condition Eq. (B.100) requires $|\omega_{{\rm lib},x} - \omega_{{\rm lib},y}| > \sigma = \sqrt{C}\,\omega_z$, where ω_z is the particle's spin rate. The two contributions to the splitting scale differently with r, leading to qualitatively different stability inequalities.

Electric splitting: Because $V \propto r^3$ and $I_{a,c} \propto \rho r^5$, one has $\sqrt{V/I} \propto r^{-1}$, so the

electric splitting

$$\begin{aligned}\Delta\omega_{\rm el} &\equiv \omega_{{\rm lib,el},bc} - \omega_{{\rm lib,el},ba} \\ &= E_0\sqrt{\varepsilon_0}\left(\sqrt{\frac{V\,\Delta\chi_{\rm el,bc}}{I_a}} - \sqrt{\frac{V\,\Delta\chi_{\rm el,ba}}{I_c}}\right) \equiv \frac{\beta_{\rm el}\,E_0}{r}\end{aligned} \tag{B.136}$$

defines a material/shape constant $\beta_{\rm el} = r\,\Delta\omega_{\rm el}/E_0$. Numerically, $\beta_{\rm el}$ is of the order of $\approx 1.3\cdot 10^{-8}\,{\rm m}^2/({\rm Vs})$. The stability condition $\Delta\omega_{\rm el} > \sigma$ gives directly

$$r < r_{\rm Dzh,el} \equiv \frac{\beta_{\rm el}\,E_0}{\sqrt{C}\,\omega_z} \approx \frac{1.3\cdot 10^{-8}\,{\rm m}\times 300\,{\rm V\,m^{-1}}}{0.61\times\omega_z} \approx \frac{6.4\,\mu{\rm m\,rad\,s^{-1}}}{\omega_z}. \tag{B.137}$$

The electric field thus stabilizes particles smaller than $r_{\rm Dzh,el}$. At $\omega_z = 70(2\pi)\,{\rm Hz}$ this requires $r \lesssim 15\,{\rm nm}$, far below $r_{\rm cross}$, so the electric field alone cannot stabilize particles in the experimentally relevant size range.

Gradient splitting: The factor $(B'r)^2$ in (B.133) is canceled by $V/I \propto r^{-2}$, so the gradient splitting

$$\begin{aligned}\Delta\omega_{\rm grad} &\equiv \omega_{{\rm lib,grad},bc} - \omega_{{\rm lib,grad},ba} \\ &= B'r\sqrt{\frac{V}{\mu_0}}\left(\sqrt{\frac{\Delta\chi_{V,bc}}{5\,I_a}} - \sqrt{\frac{\Delta\chi_{V,ba}}{5\,I_c}}\right) \equiv \beta_{\rm grad}\,B'\end{aligned} \tag{B.138}$$

is independent of r , with $\beta_{\rm grad} \approx 6.9\times 10^{-3}\,{\rm rad\,s^{-1}\,m\,T^{-1}}$ ($\Delta\omega_{\rm grad} = 1.1(2\pi)\,{\rm Hz}$ at $B' = 10^3\,{\rm T\,m^{-1}}$). The stability condition $\Delta\omega_{\rm grad} > \sigma$ gives

$$B' > B'_{\rm Dzh} \equiv \frac{\sqrt{C}\,\omega_z}{\beta_{\rm grad}} \approx \frac{0.61\times\omega_z}{6.9\times 10^{-3}\,{\rm rad\,s^{-1}\,m\,T^{-1}}} \approx 89\,\omega_z\,{\rm T\,m^{-1}\,rad^{-1}\,s}, \tag{B.139}$$

independent of r. At $\omega_z = 70(2\pi)\,{\rm Hz}$ this requires $B' \gtrsim 3.9\times 10^4\,{\rm T\,m^{-1}}$, about 40 times the reference gradient. The electric field contributes a small additional splitting at any r but does not qualitatively change the gradient condition.

Compared with the bias-field case ($L_{\rm crit} = 0.18\,{\rm nm}$), the $B_0 = 0$ trap is far more susceptible to Dzhanibekov instability. For the gradient trap to suppress the spin-flip instability at spin rate ω_z, the field gradient must exceed $B'_{\rm Dzh} \approx 89\,\omega_z\,{\rm T\,m^{-1}\,rad^{-1}\,s}$, regardless of particle size, which might in general not be possible.

Note that this is a worst case estimation. If the particle is manufactured in a way that either the first or third principal axis is aligned with the rotation axis or if the particle is manufactured in a more symmetric manner, the Dzhanibekov effect vanishes.

Coupling to other rotational modes: charge-stabilized b-axis rotation ($B_0 = 0$). We now consider $B_0 = 0$ with a single net charge Q localized at the surface of the particle along the body b-axis, at distance $d = b_{\mathrm{semi}} = 10L$ from the center of mass. This constitutes a worst case scenario, where the charge locks the particle to the most unfavorable rotation axis with intermediate moment of inertia. The resulting permanent electric dipole $\mathbf{p}_0 = Qd\,\hat{b}$ couples to a static field $\mathbf{E} = E_0\mathbf{e}_z$, giving the orientational energy $U_{\mathrm{tilt}}(\theta) = -QdE_0\cos\theta$, where θ is the polar tilt of $\hat{b}$ from $\mathbf{e}_z$. This aligns the spin axis with $\mathbf{e}_z$ independently of the particle's dielectric or diamagnetic anisotropy. Crucially, rotating the particle around $\hat{b}$ leaves the dipole position unchanged in the lab frame, so this configuration provides tilt confinement without imposing any spin confinement ($U_{0,\mathrm{spin}} = 0$); the angular-momentum-transfer conditions (B.84) are therefore trivially satisfied for the spin degree of freedom.

Tilt libration frequencies. Because U_{tilt} depends only on the polar angle θ and not on the azimuthal direction of the tilt, both tilt modes experience the same restoring-torque amplitude QdE_0. Their libration frequencies therefore differ only through their moments of inertia:

$$\omega^2_{\mathrm{lib,ch},ba} = \frac{QdE_0}{I_c}, \qquad \omega^2_{\mathrm{lib,ch},bc} = \frac{QdE_0}{I_a}, \tag{B.140}$$

where $\omega_{\mathrm{lib,ch},ba}$ corresponds to tilting b toward a (rotation about c, moment I_c) and $\omega_{\mathrm{lib,ch},bc}$ to tilting b toward c (rotation about a, moment I_a).

At $L = 100\,\mathrm{nm}$, $Q = e$, $d = 10L$, and $E_0 = 300\,\mathrm{V/m}$:

$$\omega_{\mathrm{lib,ch},ba} \approx 51\,(2\pi)\,\mathrm{Hz}, \qquad \omega_{\mathrm{lib,ch},bc} \approx 92\,(2\pi)\,\mathrm{Hz}. \tag{B.141}$$

These are orders of magnitude larger than the gradient-dominated values (B.133) ($\lesssim 2\,(2\pi)\,\mathrm{Hz}$) and the electric-alignment values from dielectric anisotropy ($\approx$4–$10\,(2\pi)\,\mathrm{Hz}$), but still far below the bias-field values (B.125) ($\sim$10–$34\,(2\pi)\,\mathrm{kHz}$).

Dzhanibekov stability. Since both libration frequencies share the same QdE_0, their splitting is

$$\Delta\omega_{\mathrm{ch}} \equiv \omega_{\mathrm{lib,ch},bc} - \omega_{\mathrm{lib,ch},ba} = \sqrt{QdE_0}\left(\frac{1}{\sqrt{I_a}} - \frac{1}{\sqrt{I_c}}\right), \tag{B.142}$$

controlled entirely by the inertia asymmetry of the particle. The stability condition Eq. (B.100), $\Delta\omega_{\mathrm{ch}} > \sigma = \sqrt{C}\,\omega_z$, is equivalent to a lower bound on the electric field:

$$E_0 > E_{0,\mathrm{Dzh,ch}} \equiv \frac{C\,\omega_z^2}{Qd\left(\frac{1}{\sqrt{I_a}} - \frac{1}{\sqrt{I_c}}\right)^2}. \tag{B.143}$$

With $d \propto L$, $I_{a,c} \propto \rho L^5$, and $\omega_z = S_0/I_b \propto L^{-2}$, one finds $\Delta\omega_{\mathrm{ch}} \propto L^{-2}$ and $\sigma \propto L^{-2}$, so their ratio is independent of particle size. The critical field $E_{0,\mathrm{Dzh,ch}}$ depends on ω_z, Q, and shape, but not on L. For $a = 15L, b = 10L, c = L$ and $Q = eA$, we find $E_{0,\mathrm{Dzh,ch}} = 340\,\mathrm{V/m}$. E_0 is depends on V according to Eq. (B.112), a larger particle is favorable in this case. To find an $E_0 \gg E_{0,\mathrm{Dzh,ch}}$, a minimal particle size of $L \gg 20\,\mathrm{nm}$ is necessary, which is feasible. As before, if this condition cannot be fulfilled, a particle has to be manufactured to be a sphere or in such a way, that it rotates either around the major or minor rotation axis.

B.4 Statistical Rotational Uncertainty

Another important point to consider is that, due to the particle's small moment of inertia, the statistical uncertainty in its rotational states is significant at 100 K. At a given temperature T, the probability distribution of ω follows the Boltzmann distribution: $P(\omega) = \sqrt{\beta I/(2\pi)}\exp(-\beta E)$, where $\beta = (k_B T)^{-1}$ and $E = I\omega^2/2$. The variance of ω is then given by $\Delta\omega = \sqrt{k_B T/I}$, which is approximately 500 kHz at room temperature and a spherical particle with 100 nm radius. To gain an intuitive understanding, we consider very low pressures, neglect friction effects, and compare $\Delta\omega$ to the maximum angular momentum the particle can theoretically acquire via the Einstein–de Haas effect:

$$\frac{S(0)/I}{\Delta\omega} = \sqrt{\frac{5\pi}{6}}\frac{\hbar\rho_N p\sqrt{r}}{\sqrt{\rho k_B T}} \approx 58400 \cdot p\sqrt{\frac{r}{T}} \tag{B.144}$$

where $\rho_N = N/\rho$ is the spin density within the particle. For a 100 nm sphere with 10 % of the nuclear spins hyperpolarized and at 100 K, this ratio is approximately 0.2. One could boost the signal by using a larger particle, cooling the environment, or cooling the rotational degrees of freedom. Nevertheless, $\Delta\omega > \omega_{\max}$ does not fundamentally prevent the effect from being observed but does increase the number of measurements required to resolve the rotation. Note, that, if the particle is in thermal equilibrium with its environment, $\Delta\omega$ is also an upper limit on the rotational uncertainty induced by scattering with air molecules and black body radiation.

B.5 Mechanical Back Action of Nuclear Spin Relaxation

We assume the particle to be in a magnetic field gradient of the form $\mathbf{B} = (B'_x x, B'_y y, B'_z z + B_0)$. If a nuclear spin with magnetic moment $\boldsymbol{\mu}$ flips while located at $\mathbf{x}$, it induces a torque on the particle of the form

$$\boldsymbol{\tau} = \mathbf{x} \times \nabla(\boldsymbol{\mu} \cdot \mathbf{B}). \tag{B.145}$$

This torque is, in general, non-zero if $\mathbf{x}$ is displaced from the particle's center of mass. Furthermore, we assume the nuclei to be aligned with the external magnetic field and that $B_0 \gg B'_x x, B'_y y, B'_z z$.

First-Order Torque from Gradient Forces

The magnetic potential energy stored in the nuclear spin is given by

$$U_{\text{grad}} = -\boldsymbol{\mu} \cdot \mathbf{B}(\mathbf{x}). \tag{B.146}$$

As we assume the spins to be aligned with the magnetic field, the energy released when a spin flips is given by

$$\Delta U_{\text{grad}} = 2\mu|\mathbf{B}(\mathbf{x})| = 2\mu\sqrt{(B'_x x)^2 + (B'_y y)^2 + (B'_z z + B_0)^2}. \tag{B.147}$$

In the limit $B_0 \gg B'_x x, B'_y y, B' z z$, this expression can be expanded as

$$\Delta U\text{grad} \approx 2\mu \left(B_0 + B'_z z + O\left(\frac{B'^2_i x_i^2}{B_0} \right) \right). \tag{B.148}$$

In this limit, there are two distinct contributions to this expression:

(i) $U_{\text{grad,const}} = 2\mu B_0$, the homogeneous Zeeman energy, which is identical for every spin regardless of position and therefore does not couple to rotation, and

(ii) $U_{\text{grad,rot}} = 2\mu B'_z z$ (together with the transverse gradient terms), which is position dependent and therefore gives rise to the non-zero torque $\boldsymbol{\tau} = \mathbf{x} \times \nabla(\boldsymbol{\mu} \cdot \mathbf{B})$. This contribution is what drives the rotational motion.

To leading order in the gradient, we therefore obtain

$$\Delta U_{\text{grad,rot}} \approx 2\mu B'_z z. \tag{B.149}$$

As each spin flip is independent, the rotational energy deposited into the particle can be written as

$$E_{\text{rot}} = \sum_{i=1}^{N_{\text{flip}}} \Delta U_{\text{grad,rot}}(\mathbf{x}_i). \tag{B.150}$$

Since the $\mathbf{x}i$ are independent and identically distributed, we find for a symmetric particle

$$\langle E_{\text{rot}} \rangle = 2N_{\text{flip}}\mu B' z \langle z \rangle = 0, \tag{B.151}$$

meaning that, averaged over many realizations, the mean contribution of the mechanical back action to the rotational energy vanishes. Nevertheless, it introduces

fluctuations in the rotational energy, which for a symmetric particle are given by

$$\sigma^2_{E,\text{torque}} = N_{\text{flip}} \langle E^2_{\text{rot}} \rangle = 4 N_{\text{flip}} \mu^2 B'^2_z \langle z^2 \rangle. \tag{B.152}$$

Assuming a spherical particle with $\langle z^2 \rangle = r^2/5$, and that number of flips in the same order of magnitude of the N spins, we obtain

$$\sigma_{E,\text{torque}} = 2\mu |B'_z| r \sqrt{\frac{N}{5}}. \tag{B.153}$$

Comparison to the Einstein–de Haas Effect

In contrast, the rotational energy contributed by the Einstein-de Haas effect is correlated. For a particle with N spins and polarization fraction p, only the net polarized fraction contributes coherently, so the total angular momentum transferred to the particle is

$$L = N p \hbar. \tag{B.154}$$

The corresponding rotational energy is then given by

$$E_{\text{EdH}} = \frac{L^2}{2I} = \frac{N^2 p^2 \hbar^2}{2I}. \tag{B.155}$$

The ratio between the rotational energy associated with the Einstein-de Haas effect and the spread in rotational energy due to the mechanical back action is therefore

$$\frac{E_{\text{EdH}}}{\sigma_{E,\text{torque}}} = \frac{N^2 p^2 \hbar^2/(2I)}{2\mu B'_z r \sqrt{N/5}} = \sqrt{\frac{5\pi}{3}} \frac{5 p^2 \hbar^2}{4 B'_z \mu \rho} \left(\frac{\rho_N}{r}\right)^{3/2}, \tag{B.156}$$

where we assumed a spherical particle.

Hence, for sufficiently small particles, the Einstein–de Haas effect dominates, whereas for larger particles the spread caused by the mechanical back action may eventually become large enough to obscure the Einstein–de Haas signal. In Fig. 7, the maximal particle radius for which $E_{\text{EdH}}/\sigma_{E,\text{torque}} > 1$ is shown. As can be seen, the relevant particle sizes lie well within the range considered throughout this thesis. Note also that this constitutes a conservative upper bound, since we assumed that the entire potential energy associated with the interaction between the nuclear spins is converted into rotational energy along the z axis, which will generally not be the case. Furthermore, we neglected any rotational confinement, which would further reduce σ_E.

B.6 Commutator of Dipole-Dipole Hamiltonian with Angular Momentum

Let's look at the case, where N spins are fixed in a lattice and are interacting with each other via dipole-dipole coupling. While this model does not account

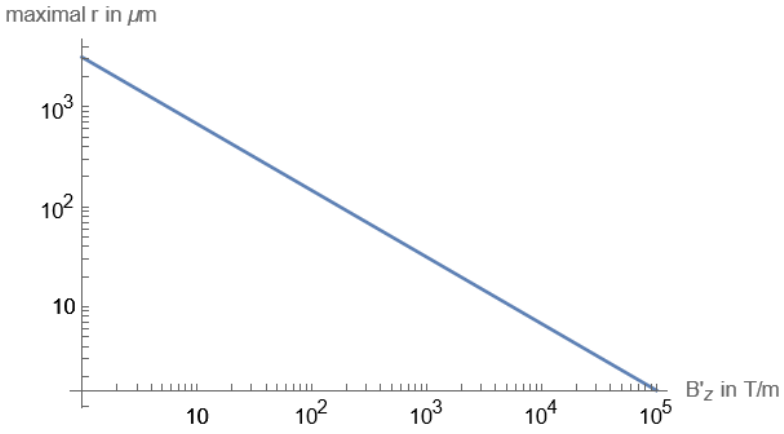


Figure 7: Here, the maximal radius particle r for which $E_{\mathrm{EdH}}/\sigma_{E,\mathrm{torque}} > 1$

for all contributions to the Einstein–de Haas effect, it nevertheless demonstrates that, in principle, dipole-dipole coupling can mediate an interaction between the rotational degrees of freedom of the rigid body and the nuclear spin degrees of freedom. The dipole-dipole coupling between two of the N spins is denoted $\hat{DD}_{\mu\nu}$ and the total dipole-dipole coupling is then given by

$$\begin{aligned}\hat{DD} &= -\frac{1}{2}\sum_{\mu\neq\nu}\Gamma_{\mu,\nu}\left[3(\hat{\mathbf{S}}_\mu\cdot\hat{\vec{e}}_{\mu\nu})(\hat{\mathbf{S}}_\nu\cdot\hat{\vec{e}}_{\mu\nu})-\hat{\mathbf{S}}_\mu\cdot\hat{\mathbf{S}}_\nu\right]\\ &= -\frac{\hbar}{2}\left(\hat{DD}_1-\hat{DD}_2\right)\end{aligned} \tag{B.157}$$

where $\mu,\nu\in[1,N]$ denote the different spins. For convenience, we defined

$$\begin{aligned}\hat{DD}_1 &= \frac{\hbar}{4}\sum_{\mu\neq\nu}\frac{3\Gamma_{\mu\nu}}{L_{\mu\nu}^2}\hat{\sigma}_{\mu,n}\hat{\sigma}_{\nu,m}(\hat{r}_{\mu,n}-\hat{r}_{\nu,n})(\hat{r}_{\mu,m}-\hat{r}_{\nu,m}),\\ \hat{DD}_2 &= \frac{\hbar}{4}\sum_{\mu\neq\nu}\Gamma_{\mu\nu}\hat{\sigma}_{\mu,n}\hat{\sigma}_{\nu,n}.\end{aligned} \tag{B.158}$$

$n,m\in x,y,z$ denote the dimensions and we used Einstein's sum convention. $\Gamma_{\mu,\nu}$ is the coupling strength between the μ^{th} and ν^{th} spin and is given by $\Gamma_{\mu,\nu}=\mu_0\gamma_1\gamma_2\hbar/(4\pi L_{\mu\nu}^3)$ and $\hat{\vec{e}}_{\mu\nu}=(\hat{\mathbf{r}}_\mu-\hat{\mathbf{r}}_\nu)/L_{\mu\nu}$ is the unit vector pointing from spin ν to μ, where $L_{\mu\nu}$ is the distance between the two spins.
The total angular momentum is given by

$$\hat{J}_k=\sum_\lambda\hat{J}_{\lambda,k}=\hat{S}_{\mathrm{tot},k}+\hat{L}_{\mathrm{tot},k}=\sum_\lambda\left(\frac{\hbar}{2}\hat{\sigma}_{\lambda,k}+\hat{r}_{\lambda,i}\,\hat{p}_{\lambda,j}\varepsilon_{ijk}\right) \tag{B.159}$$

where $\hat{S}_{\mathrm{tot},k}$ is the k^{th} component of the spin angular momentum all nuclear spins carry and $\hat{L}_{\mathrm{tot},k}$ the k^{th} component of the angular momentum of the rigid body.

We want to show that

$$[\hat{DD}, \hat{J}_k] = 0 \tag{B.160}$$

for all k.
As a first intermediate step, we calculate

$$\begin{aligned}\frac{\hbar}{2}[\hat{\sigma}_{\mu,n}\hat{\sigma}_{\nu,n}, \hat{\sigma}_{\lambda,k}] &= \frac{\hbar}{2}\left([\hat{\sigma}_{\mu,n}, \hat{\sigma}_{\lambda,k}]\hat{\sigma}_{\nu,n} + \hat{\sigma}_{\mu,n}[\hat{\sigma}_{\nu,n}, \hat{\sigma}_{\lambda,k}]\right) \\ &= i\hbar\left(\hat{\sigma}_{\mu,l}\hat{\sigma}_{\nu,n}\varepsilon_{nkl}\delta_{\mu\lambda} + \hat{\sigma}_{\mu,n}\hat{\sigma}_{\nu,l}\varepsilon_{nkl}\delta_{\nu\lambda}\right)\end{aligned} \tag{B.161}$$

and therefore find

$$\begin{aligned}\left[\hat{DD}_2, \hat{J}_k\right] =& i\frac{\hbar^2}{4}\sum_{\mu\neq\nu}\sum_{\lambda}\Gamma_{\mu\nu}\left(\hat{\sigma}_{\mu,l}\hat{\sigma}_{\nu,n}\varepsilon_{nkl}\delta_{\mu\lambda} + \hat{\sigma}_{\mu,n}\hat{\sigma}_{\nu,l}\varepsilon_{nkl}\delta_{\nu\lambda}\right) \\ =& i\frac{\hbar^2}{4}\sum_{\mu\neq\nu}\Gamma_{\mu\nu}\left(\hat{\sigma}_{\mu,l}\hat{\sigma}_{\nu,n}\varepsilon_{nkl} + \hat{\sigma}_{\mu,n}\hat{\sigma}_{\nu,l}\varepsilon_{nkl}\right) \\ =& i\frac{\hbar^2}{4}\sum_{\mu\neq\nu}\Gamma_{\mu\nu}\hat{\sigma}_{\mu,l}\hat{\sigma}_{\nu,n}(\varepsilon_{nkl} + \varepsilon_{lkn}) = 0\end{aligned} \tag{B.162}$$

where in the penultimate step, we renamed the summation indices $n \leftrightarrow l$ and used the asymmetry of the Levi-Civita symbol.
Next, we want to find $[\hat{DD}_1, \hat{J}_k]$. For that we calculate as an intermediate step

$$\begin{aligned}[\hat{\sigma}_{\mu,n}\hat{\sigma}_{\nu,m}, \hat{\sigma}_{\lambda,k}] &= [\hat{\sigma}_{\mu,n}, \hat{\sigma}_{\lambda,k}]\hat{\sigma}_{\nu,m} + \hat{\sigma}_{\mu,n}[\hat{\sigma}_{\nu,m}, \hat{\sigma}_{\lambda,k}] \\ &= 2i(\hat{\sigma}_{\mu,l}\hat{\sigma}_{\nu,m}\varepsilon_{nkl}\delta_{\mu,\lambda} + \hat{\sigma}_{\mu,n}\hat{\sigma}_{\nu,l}\varepsilon_{mkl}\delta_{\nu\lambda}).\end{aligned} \tag{B.163}$$

We therefore find

$$\begin{aligned}[\hat{DD}_1, \hat{S}_k] &= \sum_{\mu\neq\nu}\sum_{\lambda}\frac{3\Gamma_{\mu\nu}}{L_{\mu\nu}^2}\frac{\hbar^2}{8}[\hat{\sigma}_{\mu,n}\hat{\sigma}_{\nu,m}, \hat{\sigma}_{\lambda,k}](\hat{r}_{\mu,n} - \hat{r}_{\nu,n})(\hat{r}_{\mu,m} - \hat{r}_{\nu,m}) \\ &= \sum_{\mu\neq\nu}\frac{3i\hbar^2\Gamma_{\mu\nu}}{4L_{\mu\nu}^2}(\hat{\sigma}_{\mu,l}\hat{\sigma}_{\nu,m}\varepsilon_{nkl} + \hat{\sigma}_{\mu,n}\hat{\sigma}_{\nu,l}\varepsilon_{mkl})(\hat{r}_{\mu,n} - \hat{r}_{\nu,n})(\hat{r}_{\mu,m} - \hat{r}_{\nu,m})\end{aligned} \tag{B.164}$$

Next, we calculate

$$
\begin{aligned}
&[(\hat{r}_{\mu,n}-\hat{r}_{\nu,n})(\hat{r}_{\mu,m}-\hat{r}_{\nu,m}),\hat{r}_{\lambda,i}\,\hat{p}_{\lambda,j}\varepsilon_{ijk}]\\
&=\hat{r}_{\lambda,i}\Big([\hat{r}_{\mu,n}\hat{r}_{\mu,m},\hat{p}_{\lambda,j}]-[\hat{r}_{\mu,n}\hat{r}_{\nu,m},\hat{p}_{\lambda,j}]\\
&\quad-[\hat{r}_{\nu,n}\hat{r}_{\mu,m},\hat{p}_{\lambda,j}]+[\hat{r}_{\nu,n}\hat{r}_{\nu,m},\hat{p}_{\lambda,j}]\Big)\varepsilon_{ijk}\\
&=\hat{r}_{\lambda,i}\Big([\hat{r}_{\mu,n},\hat{p}_{\lambda,j}]\hat{r}_{\mu,m}+\hat{r}_{\mu,n}[\hat{r}_{\mu,m},\hat{p}_{\lambda,j}]\\
&\quad-[\hat{r}_{\mu,n},\hat{p}_{\lambda,j}]\hat{r}_{\nu,m}-\hat{r}_{\mu,n}[\hat{r}_{\nu,m},\hat{p}_{\lambda,j}]\\
&\quad-[\hat{r}_{\nu,n},\hat{p}_{\lambda,j}]\hat{r}_{\mu,m}-\hat{r}_{\nu,n}[\hat{r}_{\mu,m},\hat{p}_{\lambda,j}]\\
&\quad+[\hat{r}_{\nu,n},\hat{p}_{\lambda,j}]\hat{r}_{\nu,m}+\hat{r}_{\nu,n}[\hat{r}_{\nu,m},\hat{p}_{\lambda,j}]\Big)\varepsilon_{ijk}\\
&=i\hbar\hat{r}_{\lambda,i}\Big(\delta_{\mu,\lambda}\delta_{n,j}\hat{r}_{\mu,m}+\hat{r}_{\mu,n}\delta_{\mu,\lambda}\delta_{mj}-\delta_{\mu,\lambda}\delta_{n,j}\hat{r}_{\nu,m}-\hat{r}_{\mu,n}\delta_{\nu,\lambda}\delta_{m,j}\\
&\quad-\delta_{\nu,\lambda}\delta_{n,j}\hat{r}_{\mu,m}-\hat{r}_{\nu,n}\delta_{\mu,\lambda}\delta_{m,j}+\delta_{\nu,\lambda}\delta_{n,j}\hat{r}_{\nu,m}+\hat{r}_{\nu,n}\delta_{\nu,\lambda}\delta_{m,j}\Big)\varepsilon_{ijk}
\end{aligned}
\tag{B.165}
$$

Plugging this into $[\hat{DD_1},\hat{L}_k]$ we find

$$
\begin{aligned}
[\hat{DD_1},\hat{L}_k]&=\sum_{\mu\neq\nu}\sum_{\lambda}\frac{3i\hbar^2\Gamma_{\mu\nu}}{4L_{\mu\nu}^2}\hat{\sigma}_{\mu,n}\hat{\sigma}_{\nu,m}\hat{r}_{\lambda,i}\\
&\quad\Big(\delta_{\mu,\lambda}\delta_{n,j}\hat{r}_{\mu,m}+\hat{r}_{\mu,n}\delta_{\mu,\lambda}\delta_{mj}-\delta_{\mu,\lambda}\delta_{n,j}\hat{r}_{\nu,m}-\hat{r}_{\mu,n}\delta_{\nu,\lambda}\delta_{m,j}\\
&\quad-\delta_{\nu,\lambda}\delta_{n,j}\hat{r}_{\mu,m}-\hat{r}_{\nu,n}\delta_{\mu,\lambda}\delta_{m,j}+\delta_{\nu,\lambda}\delta_{n,j}\hat{r}_{\nu,m}+\hat{r}_{\nu,n}\delta_{\nu,\lambda}\delta_{m,j}\Big)\varepsilon_{ijk}\\
&=\sum_{\mu\neq\nu}\frac{3i\hbar^2\Gamma_{\mu\nu}}{4L_{\mu\nu}^2}\hat{\sigma}_{\mu,n}\hat{\sigma}_{\nu,m}\\
&\quad\Big(\varepsilon_{ink}\hat{r}_{\mu,i}\hat{r}_{\mu,m}+\varepsilon_{imk}\hat{r}_{\mu,i}\hat{r}_{\mu,n}-\varepsilon_{ink}\hat{r}_{\mu,i}\hat{r}_{\nu,m}-\varepsilon_{imk}\hat{r}_{\nu,i}\hat{r}_{\mu,n}\\
&\quad-\varepsilon_{ink}\hat{r}_{\nu,i}\hat{r}_{\mu,m}-\varepsilon_{imk}\hat{r}_{\mu,i}\hat{r}_{\nu,n}+\varepsilon_{ink}\hat{r}_{\nu,i}\hat{r}_{\nu,m}+\varepsilon_{imk}\hat{r}_{\nu,i}\hat{r}_{\nu,n}\Big)\\
&=\sum_{\mu\neq\nu}\frac{3i\hbar^2\Gamma_{\mu\nu}}{4L_{\mu\nu}^2}\hat{\sigma}_{\mu,n}\hat{\sigma}_{\nu,m}\\
&\quad\Big[\varepsilon_{ink}\Big(\hat{r}_{\mu,i}\hat{r}_{\mu,m}-\hat{r}_{\mu,i}\hat{r}_{\nu,m}-\hat{r}_{\nu,i}\hat{r}_{\mu,m}+\hat{r}_{\nu,i}\hat{r}_{\nu,m}\Big)\\
&\quad+\varepsilon_{imk}\Big(\hat{r}_{\mu,i}\hat{r}_{\mu,n}-\hat{r}_{\nu,i}\hat{r}_{\mu,n}-\hat{r}_{\mu,i}\hat{r}_{\nu,n}+\hat{r}_{\nu,i}\hat{r}_{\nu,n}\Big)\Big]\\
&=\sum_{\mu\neq\nu}\frac{3i\hbar^2\Gamma_{\mu\nu}}{4L_{\mu\nu}^2}\hat{\sigma}_{\mu,n}\hat{\sigma}_{\nu,m}\\
&\quad\Big[\varepsilon_{ink}(\hat{r}_{\mu,i}-\hat{r}_{\nu,i})(\hat{r}_{\mu,m}-\hat{r}_{\nu,m})+\varepsilon_{imk}(\hat{r}_{\mu,i}-\hat{r}_{\nu,i})(\hat{r}_{\mu,n}-\hat{r}_{\nu,n})\Big]
\end{aligned}
\tag{B.166}
$$

By renaming in the first term $i\to n, n\to l$ and in the second term $i\to m, m\to l$,

we find

$$
\begin{aligned}
[\hat{DD}_1, \hat{L}_k] = \sum_{\mu\neq\nu} \frac{3i\hbar^2\Gamma_{\mu\nu}}{4L_{\mu\nu}^2} \Big[& \hat{\sigma}_{\mu,l}\hat{\sigma}_{\nu,m}\varepsilon_{nlk}(\hat{r}_{\mu,n} - \hat{r}_{\nu,n})(\hat{r}_{\mu,m} - \hat{r}_{\nu,m}) \\
& + \hat{\sigma}_{\mu,n}\hat{\sigma}_{\nu,l}\varepsilon_{mlk}(\hat{r}_{\mu,m} - \hat{r}_{\nu,m})(\hat{r}_{\mu,n} - \hat{r}_{\nu,n}) \Big] \\
= \sum_{\mu\neq\nu} \frac{3i\hbar^2\Gamma_{\mu\nu}}{4L_{\mu\nu}^2} & (\hat{\sigma}_{\mu,l}\hat{\sigma}_{\nu,m}\varepsilon_{nlk} + \hat{\sigma}_{\mu,n}\hat{\sigma}_{\nu,l}\varepsilon_{mlk}) \\
& (\hat{r}_{\mu,n} - \hat{r}_{\nu,n})(\hat{r}_{\mu,m} - \hat{r}_{\nu,m})
\end{aligned} \tag{B.167}
$$

We therefore find for $[\hat{DD}_1, \hat{J}_k] = [\hat{DD}_1, \hat{S}_k + \hat{L}_k]$

$$
\begin{aligned}
[\hat{DD}_1, \hat{J}_k] = & \sum_{\mu\neq\nu} \frac{3i\hbar^2\Gamma_{\mu\nu}}{4L_{\mu\nu}^2} (\hat{\sigma}_{\mu,l}\hat{\sigma}_{\nu,m}\varepsilon_{nkl} + \hat{\sigma}_{\mu,n}\hat{\sigma}_{\nu,l}\varepsilon_{mkl}) \\
& \qquad (\hat{r}_{\mu,n} - \hat{r}_{\nu,n})(\hat{r}_{\mu,m} - \hat{r}_{\nu,m}) \\
& + \sum_{\mu\neq\nu} \frac{3i\hbar^2\Gamma_{\mu\nu}}{4L_{\mu\nu}^2} (\hat{\sigma}_{\mu,l}\hat{\sigma}_{\nu,m}\varepsilon_{nlk} + \hat{\sigma}_{\mu,n}\hat{\sigma}_{\nu,l}\varepsilon_{mlk}) \\
& \qquad (\hat{r}_{\mu,n} - \hat{r}_{\nu,n})(\hat{r}_{\mu,m} - \hat{r}_{\nu,m}) \\
= & \, 0
\end{aligned} \tag{B.168}
$$

Ultimately we can conclude that $[\hat{DD}, \hat{J}_k] = [\hat{DD}_1, \hat{J}_k] + [\hat{DD}_2, \hat{J}_k] = 0$.

B.7 Magnetization in Magnetic Field Gradient

If an irregularly shaped particle is placed in a magnetic field gradient $\mathbf{B} = (B'_x x, B'_y y, B'_z z) + \mathbf{B}_0$, the spins will thermalize after some time $T \gg T_1$. If the interaction between the nuclear spins is small compared to the interaction between the spins and the magnetic field, the spins will align with the magnetic field according to Boltzmann's distribution. Only the hydrogen atoms in naphthalene carry nuclear spins whose position can be deducted from scattering experiments. From the position, the coupling between the nuclear spins in naphthalene can be found, which is in the order of kHz [1]. Already for a magnetic field of 3 mT we find $\gamma_p B = 130 \cdot (2\pi)$ kHz, For a magnetic field gradient of $B' = 10^3$ T/m and a particle with radius 500 nm, the change of B along the particle is 0.5 mT, therefore if B_0 is a few mT or larger, one can neglect the coupling between the spins at this point.

Under this assumption, the contribution of the nuclear spins to the magnetization of the particle can be found as follows: A spin sitting at the point $\mathbf{r} = (x, y, z)$ sees the local magnetic field $\mathbf{B}$ with the amplitude $B = |B|$. The magnetic moment of

this spin is given by $\mu_p = \hbar\gamma_p \tanh(\hbar\gamma_p B/(2k_\mathrm{B}T))/2 \approx \hbar^2\gamma_p^2 B/(4k_\mathrm{B}T)$, where the last approximation holds true for moderate temperatures and magnetic fields as assumed here. The vector magnetic moment is then given by

$$\boldsymbol{\mu}_p = \mu_p \frac{\mathbf{B}}{B} = \frac{\hbar^2\gamma_p^2}{4k_\mathrm{B}T}\mathbf{B}. \tag{B.169}$$

The spins are assumed to be distributed evenly throughout the particle with a spin density ρ_S. The net magnetic moment of the nanoparticle is then given by

$$\mathbf{M} = \rho_S \frac{\hbar^2\gamma_p^2}{4k_\mathrm{B}T} \int_V \mathbf{B}\,\mathrm{d}V \tag{B.170}$$

By defining $\langle r_i \rangle = V^{-1}\int_V r_i\,\mathrm{d}V$ the components of $\mathbf{M}$ can be written as

$$M_i = N\frac{\hbar^2\gamma_p^2}{4k_\mathrm{B}T}\left(B_i' \langle r_i\rangle + B_{0,i}\right) \tag{B.171}$$

there $N = \rho_S V$ is the total number of nuclear spins within the particle. As one can see, whether B_i' contributes to the net magnetization highly depends on the symmetry of the particle as well as its orientation within the magnetic field. For highly symmetric particles such as spheres or ellipsoids, one finds $\langle x\rangle = \langle y\rangle = \langle z\rangle = 0$. The same holds true for cylinders, parallelepipeds or dumbbells.

B.8 Magnetization of a Rotating Particle

The magnetic field that a individual spin, which is initially at (x,0,z), sees when the host particle rotates around the z-axis is given by

$$\mathbf{B}(t) = (B_x'\, x\cos(\omega_r t), -B_y'\, x\sin(\omega_r t), B_z'\, z) + \mathbf{B}_0. \tag{B.172}$$

The coordinate system can always be chosen in a way that $\mathbf{B}_0 = (0, 0, B_0)$. By defining the quantities $\Omega_x = \gamma_p B_x'\, x$ and $\omega_z = \gamma_p(B'z + B_0) + \omega_r$, one can write the Hamiltonian governing one spins dynamics as

$$\hat{H} = \frac{\hbar}{2}[\Omega_x \cos(\omega_r t)\sigma_x + \hbar\Omega_y \sin(\omega_r t)\sigma_y + \omega_z\sigma_z] \tag{B.173}$$

ω_z is composed of the contribution of the magnetic field as well as the contribution due to the rotation of the nano particle ω_r which is exactly the Barnett effect. In principle, the rotation of the nano particle could induce transitions of the nuclear spins, even though the nuclear spins are always off resonant by $\gamma_p(B'z + B_0)$. In order to induce transitions, the Rabi frequencies $\Omega_{x,y}$ have to be larger than the detuning. For $B' = 10^3\,\mathrm{T/m}$ and a particle with 200 nm radius, one finds $\Omega_{x/y} = B' r_{x/y} \leq 9(2\pi)\,\mathrm{kHz}$. In contrast, for $B_0 = 5\,\mathrm{mT}$, one finds $\gamma_p(B'z + B_0) \approx$

$\gamma_p B_0 = 210(2\pi)\,\mathrm{kHz}$. Therefore, for magnetic fields of 5 mT and stronger, the nuclear spins are far detuned and one cannot expect any transitions due to the rotation of the nano particle.

In order to measure M, one needs to apply a π pulse. As the eigenfrequency of the nuclear spins depends on z, all nuclear spins within the particle have a different eigenfrequency. For a 200 nm particle and a field gradient of $10^3\,\mathrm{T/m}$, the maximal detuning is about $9(2\pi)\,\mathrm{kHz}$. As Rabi frequencies of $100\,\mathrm{kHz} \gg 9\,\mathrm{kHz}$ have been achieved, one can compensate for this detuning by applying strong pulses.

B.9 Alternative Materials

In principle, this test of the nuclear Barnett effect could be performed with any diamagnetic particle containing nuclear spins. Another example is ^{13}C-enriched diamond, where each ^{13}C nucleus carries a nuclear spin. The gyromagnetic ratio of ^{13}C is $\gamma_{^{13}\mathrm{C}} = 67.2828 \cdot 10^6, \mathrm{s}^{-1}\mathrm{T}^{-1}$, while for ^{29}Si it is $\gamma_{^{29}\mathrm{Si}} = -52.19 \cdot 10^6, \mathrm{s}^{-1}\mathrm{T}^{-1}$. The negative sign of $\gamma_{^{29}\mathrm{Si}}$ implies that the nuclear spins in silica align antiparallel to the rotation axis, in contrast to ^{13}C and ^{1}H, whose spins align parallel to the rotation axis.

The magnetic susceptibility of diamond is $\chi_V = -2.2 \cdot 10^{-5}$, allowing for larger trapping frequencies compared to naphthalene. Given the natural abundance of ^{13}C at only 1.1 %, isotopically pure diamonds composed entirely of ^{13}C can, in principle, be synthesized. In this analysis, a ^{13}C content of 30 % is considered. Another alternative would be silica with a magnetic susceptibility of $\chi_V = -1.2 \cdot 10^{-5}$. The natural abundance of the spin carrying ^{29}Si is just 4.67 %, so like for diamond, ^{29}Si enriched silica can be synthesized.

For a diamond with 30 % ^{13}C, the spin density is $\rho_{^{13}C} = 5.15 \cdot 10^{28}\mathrm{m}^{-3}$ and for silica with 30 % ^{29}Si, the spin density is $\rho_{^{29}\mathrm{Si}} = 6.62 \cdot 10^{27}\mathrm{m}^{-3}$. As shown in Fig. 8a, Fig. 8b, and Fig. 8c and Fig. 8d, the results for diamond, silica and naphthalene are similar.

Furthermore, the longitudinal relaxation time T_1 must be sufficiently long to allow measurement of the displacement signal $x(t)$ after the spins are flipped. A T_1 time on the order of seconds should be sufficient for this purpose. For ^{13}C enriched diamond, T_1 times of seconds have been reported for sub-micron diamond particles [293, 294]. The T_1 of ^{29}Si spins in silica glass has been reported to be seconds to hours [295, 296]. Hence, both materials are suitable for testing the nuclear Barnett effect.

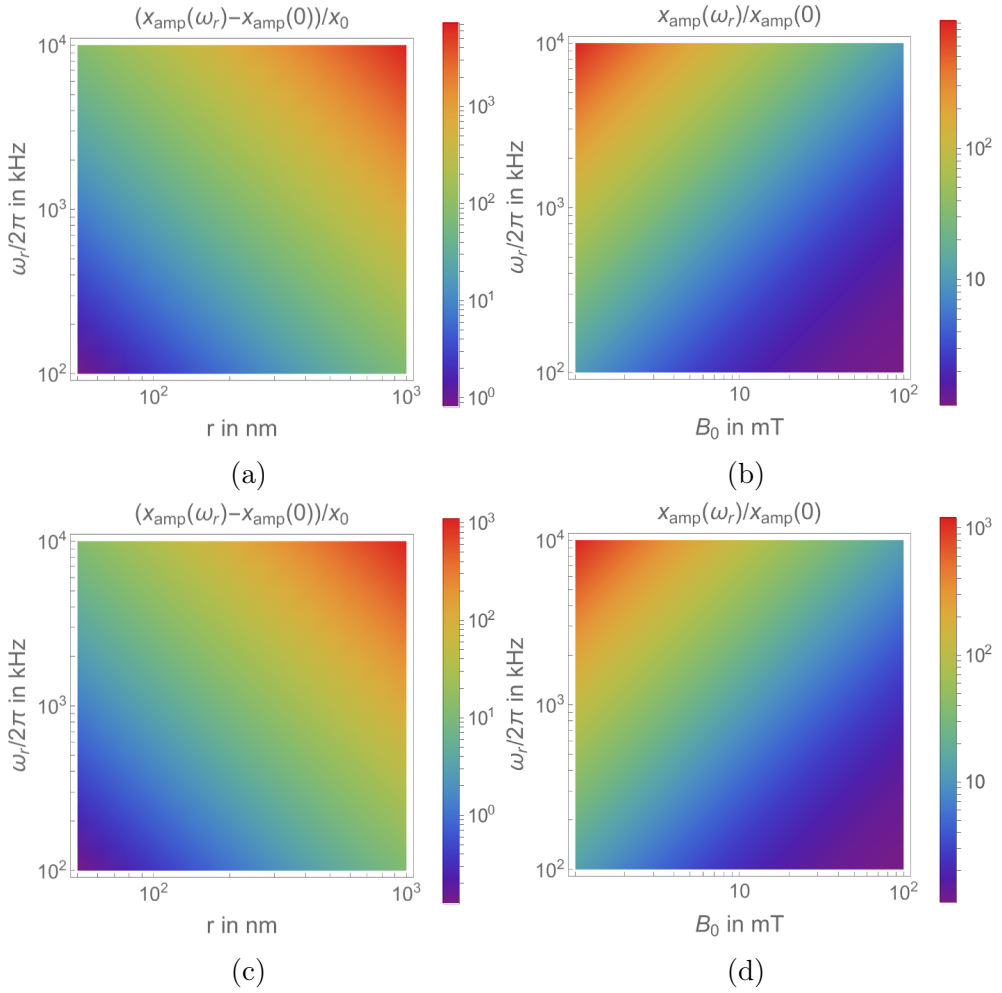


Figure 8: In (a), the difference in oscillation amplitude for a rotating, 30 % ^{13}C-enriched nanodiamonds is shown as a function of its radius and rotation frequency, in units of x_0, for $T = 100\,\mathrm{K}$ and $B' = 10^3\,\mathrm{T/m}$. In (b), the relative gain in x_{amp} compared to the oscillation amplitude expected for a non-rotating diamonds particle is depicted. In (c) and (d), the corresponding plots for 30 % ^{29}Si-enriched silica are shown. The tensile strength of both materials also exceeds that of naphthalene.

C Stability Thresholds for Gravitationally Induced Entanglement in Shielded Setups

C.1 Size and Thickness of the Shield

Thickness Estimations

The shield is used to screen direct non-gravitational interactions between the two particles. It can either be a conductive Faraday shield to screen electrostatic- and Casimir interactions, which impose dominant noise in GIE experiments with silica nanospheres or a superconducting Meissner shield for dominant magnetic dipole interactions in GIE experiments with magnetically levitated superconducting lead particles.

We focus mainly on Coulomb interactions (if both particles carry a net charge $q_{A/B}$), electric and magnetic dipole-dipole interactions (either through intrinsic dipole moments or externally induced by stray fields, patch potentials or the trapping mechanism) and mutual Casimir interactions. The transmission of the electromagnetic field through a conductor of thickness d_s and conductivity σ (with $\sigma_{\text{Copper}} \approx 1.5 \times 10^{10}\text{S/m}$ at low temperatures [297]) is approximated by $\mathcal{T} = 2/(Z_0 \sigma d_s)$, where $Z_0 = 377\Omega$ is the impedance of free space [291]. Demanding that the entanglement rate $\Gamma_{\text{ent.}} = \mathrm{d}E_N/\mathrm{d}t\big|_{t=0} = 2\Delta x_A \Delta x_B \big\|\partial_r^2 V\big|_{r=2L}\big\|/(\hbar \log 2)$ due to gravitational interactions (see Eq. (11.6) or Ref. [74]) is strictly larger (ideally by a constant factor) than other direct interactions $V(r)$, the thickness of the shield can be estimated.

The corresponding entanglement rates for each interaction are given by:

$$\Gamma_{\text{Gravity}} = \frac{G}{2\hbar \log 2} \frac{M_A M_B \Delta x_A \Delta x_B}{L^3} \tag{C.174}$$

$$\Gamma_{\text{Casimir}} = \mathcal{T}^2 \frac{161c}{128\pi \log 2} \frac{R^6 \Delta x_A \Delta x_B}{L^9} \left(\frac{\varepsilon_r - 1}{\varepsilon_r + 2}\right)^2$$
$$\text{for} \quad V(r) = -\frac{23\hbar c R^6}{4\pi r^7} \left(\frac{\varepsilon_r - 1}{\varepsilon_r + 2}\right)^2 \tag{C.175}$$

$$\Gamma_{\text{Coulomb}} = \mathcal{T} \frac{1}{8\pi\varepsilon_0 \hbar \log 2} \frac{|q_A q_B| \Delta x_A \Delta x_B}{L^3}$$
$$\text{for} \quad V(r) = \frac{1}{4\pi\varepsilon_0} \frac{q_A q_B}{r} \tag{C.176}$$

$$\Gamma_{\text{elec. Dipole}} = \mathcal{T}^2 \frac{3}{8\pi\varepsilon_0 \hbar \log 2} \frac{|p_A p_B| \Delta x_A \Delta x_B}{L^5}$$
$$\text{for} \quad V(r) = -\frac{2}{4\pi\varepsilon_0} \frac{p_A p_B}{r^3}, \text{ (linear dipole alignment)} \tag{C.177}$$

where the potential corresponding to Γ_{Casimir} was taken from [298]. The entanglement rate is suppressed by a factor of $\mathcal{T}$ for Coulomb interactions and by a factor of $\mathcal{T}^2$ for dipole-dipole and Casimir interactions, as their coupling arises from field correlations that require two transmissions through the shield (from $B \to A$ and back $A \to B$). The resulting estimated minimum thickness of the shield for the different interactions are summarised in Table 1. One has to note, that these values are very thin. The requirement, that the shield has to act as a perfect mirror for the electromagnetic modes over all relevant frequencies (around $\lambda \sim 2L$, see e.g. chapter 12 in Ref. [261] for the relevance to Casimir interactions) is much more stringent. The skin depth at these frequencies is usually around 20nm [257] and facilitates a more realistic lower bound on the thickness. The thickness for a conducting Faraday shield is therefore mainly dictated by mechanical rigidity and ease of fabrication rather than by fundamental physical limits.

Table 1: Size and thickness estimations of the shield (either conductive Faraday- or superconducting Meissner shielding) to effectively shield different forms of direct particle-particle interactions below the gravitational coupling strength. Optical skin depth ($\sim$ 20nm [257]), mechanical rigidity and ease of fabrication ultimately impose realistic lower bounds on the shields thickness of around $1 - 10\mu$m. For the magnetic Dipole interaction, $B_{\text{ext.}} \lesssim 71\mu$T must hold for silica and $B_{\text{ext.}} \lesssim 2.83\,$nT must hold for superconducting lead. the coulomb interaction, it was assumed that each particle is charged with $q_{\text{A/B}} = e$. For the electric dipole interaction, an intrinsic dipole moment of $p \approx 10^{-2} e\,$cm and an induced dipole moment (e.g. via patch potentials) of $p \lesssim 10^{-3} e\,$cm was assumed.

Interaction	type of shielding	min. thickness d_s	min. radius r_s [1]
Casimir	cond. Faraday	0.3 nm	50μm
mag. Dipole	none / mu-metal		
	supercond.	455nm [2]	7.7mm
Coulomb	cond. Faraday	20 nm	66cm
elec. Dipole	cond. Faraday	0.5 nm	1.2mm
		0.05 nm	180μm

Static magnetic fields are usually shielded very poorly by a Faraday shield and require either Mu-metal shields or, as focused on here, superconducting Meissner shielding. For an induced magnetic dipole with $\vec{m} = 4\pi R^3 \chi_V \vec{B}/[\mu_0(3+\chi_V)]$ (χ_V being the volume susceptibility with $\chi_{V,\text{SiO}_2} \approx -1.4 \times 10^{-5}$ [263] and $\chi_{V,\text{supercond.}} = -1$), the entanglement rate between both particles in the absence of magnetic

shielding is given by

$$\Gamma_{\text{mag. Dipole}} = \frac{3\mu_0}{8\pi\hbar\log 2}\frac{|m_A m_B|\Delta x_A \Delta x_B}{L^5}$$
$$\text{for} \quad V(r) = -\frac{2\mu_0}{4\pi}\frac{m_A m_B}{r^3}, \text{ for linear dipole alignment.} \tag{C.178}$$

Estimating the upper limit of external magnetic fields before these dipole interactions exceed gravitational entanglement generation, we find $B \lesssim 71\mu\text{T}$ for silica particles and $B \lesssim 2.83\,\text{nT}$ for superconducting lead. A superconducting Niobium shield with London penetration depth $\lambda_L \approx 40\text{nm}$ [266] would suppress a trap field of $B_{\text{trap}} \sim 250\mu\text{T}$ to the allowed values for a thickness of

$$d_s \geq \lambda_L \log\left(\frac{B_{\text{trap}}}{B}\right) \approx 455\text{nm}. \tag{C.179}$$

Lateral Size Estimations

The lateral dimension r_s of the shield can be estimated by considering fringe fields and diffraction around the shield. If a fraction $\kappa \in [0,1]$ of the electromagnetic modes can leak around the edges of the shield and re-establish a direct non-gravitational coupling. Geometric considerations yield that for a potential $V \sim L^{-d}$ ($d = 1$ for the Coulomb potential, $d = 3$ for dipole-dipole coupling and $d = 7$ for Casimir interactions), a shield of radius

$$r_s \geq L\tan\left(\arccos\left(\kappa^{1/d}\right)\right) = L\sqrt{\kappa^{-2/d} - 1} \tag{C.180}$$

is required. Since the entanglement rate is proportional to the underlying interaction potential, one can simply demand $|V_{\text{Gravity}}| > \kappa|V_{\text{non-gravitational}}|$ to estimate the radius of the shield such that the gravitational interaction dominates. The resulting values for the different interactions are summarised in Table 1.

C.2 Gravitational and Non-Gravitational Interactions

Gravitational Interaction

The gravitational interaction between two particles is given by

$$\hat{H}_{\text{Gravity}} = -\frac{GM_A M_B}{|\hat{d}_{AB}|}, \tag{C.181}$$

where G is the gravitational constant, $M_{A/B}$ are the masses of the two particles, and $\left|\hat{d}_{AB}\right|$ is the canonically quantised distance between them, defined as

$$\hat{d}_{AB} = \sqrt{(\hat{x}'_A - \hat{x}'_B)^2 + (\hat{y}'_A - \hat{y}'_B)^2}. \tag{C.182}$$

Here, $\hat{x}'_{A/B}$ and $\hat{y}'_{A/B}$ are the absolute position operators in the lab frame of the respective particles. As the particles' wave functions are centreed around ($x'_{A/B} = \pm L, y'_{A/B} = 0$) and their principal axes of delocalisation are tilted by an angle $\theta_{A/B}$ with respect to shield, the particles positions can be expressed in their local position operators $\hat{x}_{A/B}$, $\hat{y}_{A/B}$ as

$$\begin{pmatrix} \hat{x}'_{A/B} \\ \hat{y}'_{A/B} \end{pmatrix} = \begin{pmatrix} \pm L + \hat{x}_{A/B} \sin\theta_{A/B} - \hat{y}_{A/B} \cos\theta_{A/B} \\ \hat{x}_{A/B} \cos\theta_{A/B} + \hat{y}_{A/B} \sin\theta_{A/B} \end{pmatrix}. \tag{C.183}$$

Since $\Delta x, \Delta y \ll L$, $\hat{H}_{\text{Gravity}}$ can be expanded up to second order in $\hat{x}$ and $\hat{y}$. For simplicity, we restrict ourselves to the parallel configuration with $\theta_{A/B} = 0$ and the linear configuration with $\theta_{A/B} = \pi/2$, obtaining

$$\begin{aligned} \hat{H}_{\text{Gravity, parall.}} \approx \lambda\Big(& - L\hat{y}_A - \tfrac{1}{2}\hat{y}_A^2 + L\hat{y}_B - \tfrac{1}{2}\hat{y}_B^2 + \hat{y}_A\hat{y}_B + \tfrac{1}{4}\hat{x}_A^2 + \tfrac{1}{4}\hat{x}_B^2 \\ & - \tfrac{1}{2}\hat{x}_A\hat{x}_B\Big), \end{aligned} \tag{C.184}$$

$$\begin{aligned} \hat{H}_{\text{Gravity, linear}} \approx \lambda\Big(& L\hat{x}_A - \tfrac{1}{2}\hat{x}_A^2 - L\hat{x}_B - \tfrac{1}{2}\hat{x}_B^2 + \hat{x}_A\hat{x}_B + \tfrac{1}{4}\hat{y}_A^2 + \tfrac{1}{4}\hat{y}_B^2 \\ & - \tfrac{1}{2}\hat{y}_A\hat{y}_B\Big). \end{aligned} \tag{C.185}$$

Here, the parameter

$$\lambda = \frac{GM_AM_B}{4L^3}, \tag{C.186}$$

with units J/m^2 has been introduced. Entanglement is generated by the terms coupling the position of particle A with particle B, i.e. terms proportional to $\hat{x}_A\hat{x}_B$ and $\hat{y}_A\hat{y}_B$.

For simplicity, we neglect variations in L and θ in the gravitational interaction. The associated gravitational fluctuations are suppressed by $\lambda/\eta \sim 10^{-7}$ relative to the Casimir coupling η for silica particles (defined later in Eq. (C.193)) and suppressed by a factor of $\lambda/\delta \sim 10^{-11}$ relative to magnetic dipole interactions in superconducting lead particles (δ defined in Eq. (C.198)). Furthermore, numerical simulations confirm that entanglement degradation is driven almost entirely by non-gravitational interactions.

Closed-form expressions for this potential across all distances are not known, however approximations in the two limiting regimes for small and large distances exists. For small surface-to-surface separations $L - R - \frac{d_s}{2} \ll R$, the interaction can be described by the proximity-force-approximation (PFA) [258, 259]

$$V_{\mathrm{PFA}} = -\frac{\hbar c \pi^3 R}{720(L - R - d_s/2)^2}\varphi(\varepsilon_r) \tag{C.187}$$

where L is the distance from the sphere's centre to the plane, $\hbar$ is Plank's constant, c the speed of light and $\varphi(\varepsilon_r)$ accounts for dielectric properties. It is given by $\varphi(\varepsilon_r) = (\varepsilon_r - 1)/(\varepsilon_r + 1)\chi(\varepsilon_r)$ with $\chi(\varepsilon_r \to \infty) \to 1$, $\chi(\varepsilon_r = 1) \approx 0.46$ and $\chi(\varepsilon_{r,\mathrm{Silica}}) \approx 0.5$ being a tabulated function [260]. In the large separation limit (LSL) $L \gg R$, the interaction reduces to the well-known Casimir-Polder potential [299] in leading order [259, 300], i.e.

$$V_{\mathrm{LSL}} = -\frac{3\hbar c}{8\pi L^4}\alpha \quad \text{with } \alpha = \left(\frac{\varepsilon_r - 1}{\varepsilon_r + 2}\right) R^3\,, \tag{C.188}$$

where α is the electric polarisability of a sphere. As shown in Figure 7 of Ref. [300], the PFA consistently predicts stronger interactions for a sphere-plate geometry and thus provides a conservative worst-case estimate of their influence throughout the whole range of $L/R \in [1, \infty)$. We therefore use the PFA in all subsequent calculations, as it provides an upper bound on the noise induced on the particles. For the parameters in Table 10.1 (i.e. $L/R = 2$), the Casimir energy is overestimated roughly by a factor of 2.4.

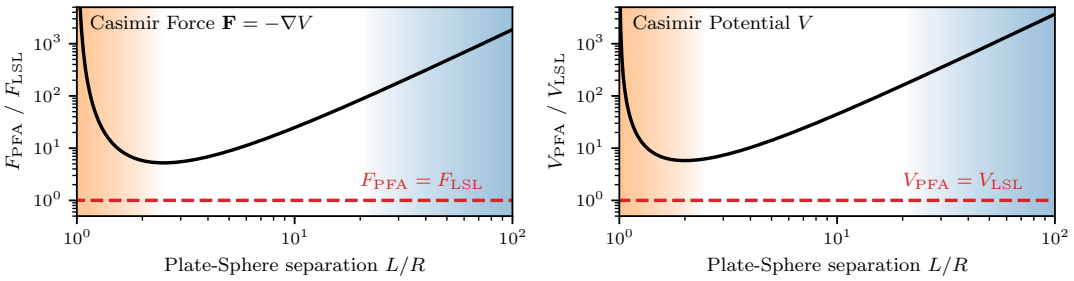


Figure 9: **Comparison of Casimir interaction models.** The Proximity-Force Approximation (PFA, validity region shaded orange), valid in short-distance regimes $L \lesssim 2R$, consistently predicts a larger Casimir potential and attraction force $\vec{F} = -\nabla V$ than the large-separation limit (LSL, shaded blue), which applies for $L \gg R$. Here, L is the centre-surface separation and R the spheres radius. Because the PFA exceeds the LSL for all ratios L/R, it provides a conservative upper bound on the Casimir interaction strength and is thus used throughout this work.

The corresponding Hamiltonian between one particle and the shield is given by

$$\hat{H}_{\text{Casimir}} = -\frac{\hbar c \pi^3 R}{720}\varphi(\varepsilon_r)\frac{1}{|\hat{d}|^2} \tag{C.189}$$

where $\hat{d}$ is the surface-to-surface separation between particle and shield. Including variations in L and θ, it is given by

$$\hat{d} = d_0 + \xi^{(L)}_{A/B} \mp \left[\hat{x}\sin\left(\theta_{A/B} + \xi^{(\theta)}_{A/B}\right) - \hat{y}\cos\left(\theta_{A/B} + \xi^{(\theta)}_{A/B}\right)\right] \tag{C.190}$$

where the "$\pm$" distinguishes between particle A and B and $d_0 = L - R - \frac{d_s}{2}$. Expanding Eq. (C.189) in $\hat{x}, \hat{y}$ (since $\Delta x, \Delta y \ll L - R - d_s/2$) as well as in the variations $\xi^{(L)} \ll L - R - d_s/2$ and $\xi^{(\theta)} \ll (L - R - d_s/2)/\Delta x$, we find

$$\begin{aligned}\hat{H}_{\text{Casimir, parall.}} \approx \eta\Big[&\pm 2d_0\hat{y} - 3\hat{y}^2 \mp 6\xi^{(L)}\hat{y} + \frac{12\xi^{(L)}\hat{y}^2}{d_0} \pm \frac{12\xi^{(L)\,2}\hat{y}}{d_0} \\ &- \frac{30\xi^{(L)\,2}\hat{y}^2}{d_0^2} \mp 2d_0\xi^{(\theta)}\hat{x} + 6\xi^{(\theta)}\hat{x}\hat{y} - 3\xi^{(\theta)\,2}\hat{x}^2 \mp d_0\xi^{(\theta)\,2}\hat{y} + 3\xi^{(\theta)\,2}\hat{y}^2\Big]\end{aligned} \tag{C.191}$$

$$\begin{aligned}\hat{H}_{\text{Casimir, linear.}} \approx \eta\Big[&\mp 2d_0\hat{x} - 3\hat{x}^2 \pm 6\xi^{(L)}\hat{x} + \frac{12\xi^{(L)}\hat{x}^2}{d_0} \mp \frac{12\xi^{(L)\,2}\hat{x}}{d_0} \\ &- \frac{30\xi^{(L)\,2}\hat{x}^2}{d_0^2} \mp 2d_0\xi^{(\theta)}\hat{y} - 6\xi^{(\theta)}\hat{x}\hat{y} + 3\xi^{(\theta)\,2}\hat{x}^2 \pm d_0\xi^{(\theta)\,2}\hat{x} - 3\xi^{(\theta)\,2}\hat{y}^2\Big]\end{aligned} \tag{C.192}$$

As before, we restricted ourselves to the linear and parallel case only and introduced a parameter η with dimensions of energy over length squared which is given by

$$\eta = \frac{\hbar c \pi^3 R}{720(L - R - d_s/2)^4}\varphi(\varepsilon_r). \tag{C.193}$$

Magnetic Dipole Interactions

The interaction Hamiltonian between a sphere of radius R with magnetic volume susceptibility χ_V in the presence of an external field $\vec{B}_{\text{ext.}}$ with a superconducting shield is given by

$$\hat{H}_{\text{mag. Dipole}} = -\frac{|\vec{m}|^2\mu_0}{32\pi|\hat{d}|^3}\left(1 + \cos^2\phi\right) \tag{C.194}$$

with the magnetic dipole moment $\vec{m} = 4\pi R^3\chi_V\vec{B}_{\text{ext.}}/[\mu_0(3 + \chi_V)]$ and vacuum permeability μ_0. The angle ϕ is measured between the dipole orientation and the shield's normal. We take $\phi = 0$ for a worst-case estimate. The particle-shield

separation $\hat{d}$ is given by

$$\hat{d} = d_0 \pm \xi^{(L)} \mp \left[\hat{x}\sin\left(\theta_{A/B} + \xi^{(\theta)}\right) - \hat{y}\cos\left(\theta_{A/B} + \xi^{(\theta)}\right)\right] \tag{C.195}$$

where the $\pm$ distinguishes between particle A and B and $d_0 = L - \frac{d_s}{2}$. As done previously for Casimir interactions, we can expand the Hamiltonian in second order in $x_{A/B}$, $y_{A/B}$ and in the variations $\xi^{(L)}, \xi^{(\theta)}$ for the parallel and linear orientation:

$$\begin{aligned}\hat{H}_{\text{mag. Dipole, parall.}} \approx \delta\Big[&\pm 3d_0\hat{y} - 6\hat{y}^2 \mp 12\xi^{(L)}\hat{y} + \frac{30\xi^{(L)}\hat{y}^2}{d_0} \pm \frac{30\xi^{(L)\,2}\hat{y}}{d_0} \\ &- \frac{90\xi^{(L)\,2}\hat{y}^2}{d_0^2} \mp 3d_0\xi^{(\theta)}\hat{x} + 12\xi^{(\theta)}\hat{x}\hat{y} - 6\xi^{(\theta)\,2}\hat{x}^2 \mp \frac{3}{2}d_0\xi^{(\theta)\,2}\hat{y} + 6\xi^{(\theta)\,2}\hat{y}^2\Big]\end{aligned} \tag{C.196}$$

$$\begin{aligned}\hat{H}_{\text{mag. Dipole, linear}} \approx \delta\Big[&\mp 3d_0\hat{x} - 6\hat{x}^2 \pm 12\xi^{(L)}\hat{x} + \frac{30\xi^{(L)}\hat{x}^2}{d_0} \mp \frac{30\xi^{(L)\,2}\hat{x}}{d_0} \\ &- \frac{90\xi^{(L)\,2}\hat{x}^2}{d_0^2} \mp 3d_0\xi^{(\theta)}\hat{y} - 12\xi^{(\theta)}\hat{x}\hat{y} + 6\xi^{(\theta)\,2}\hat{x}^2 \pm \frac{3}{2}d_0\xi^{(\theta)\,2}\hat{x} - 6\xi^{(\theta)\,2}\hat{y}^2\Big]\end{aligned} \tag{C.197}$$

Here, we defined the coupling strength with units $\mathrm{J/m^2}$ as

$$\delta = \frac{2|\vec{m}|^2\mu_0}{32\pi(L - d_s/2)^5}. \tag{C.198}$$

Dynamical Shield

The shapes of the vibrational eigenmodes, labelled by integers (k, l) with $k \in [1, \infty)$ and $l \in [0, \infty)$, can be expressed as [301]

$$u_{kl}(r, \vartheta, t) = \left[J_l(\beta_k r) - \frac{J_l(\beta_k r_s)}{I_l(\beta_k r_s)} I_l(\beta_k r)\right] \cos(l\vartheta)\sin(\omega_{kl} t), \tag{C.199}$$

where $\beta_k := \tilde{r}_k / r_s$, and the eigenfrequencies are given by

$$\omega_{kl} = \tilde{r}_k^2 \frac{d_s}{r_s^2}\sqrt{\frac{E}{12\rho(1-\nu^2)}}. \tag{C.200}$$

Here, E is the Young's modulus (with $E_{\mathrm{Cu}} = 110\mathrm{GPa}$ for a Copper shield and $E_{\mathrm{Nb}} = 105\mathrm{GPa}$ for Niobium), ν the Poisson ratio ($\nu_{\mathrm{Cu}} = 1/3$ and $\nu_{\mathrm{Nb}} = 0.40$), and ρ the mass density of the shield's material ($\rho_{\mathrm{Cu}} = 8960\mathrm{kg/m^3}$ and $\rho_{\mathrm{Nb}} = 8582\mathrm{kg/m^3}$). The quantity $\tilde{r}_k$ denotes the k-th root of the characteristic equation

$$J_l(\tilde{r}_k)I_{l+1}(\tilde{r}_k) + I_l(\tilde{r}_k)J_{l+1}(\tilde{r}_k) = 0, \tag{C.201}$$

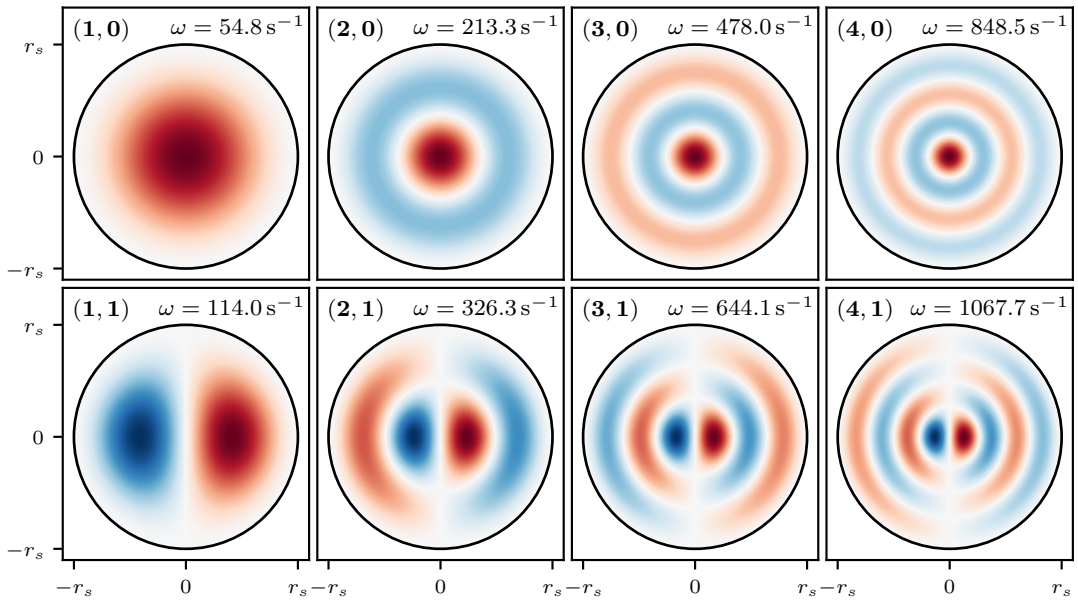


Figure 10: **Selected vibrational modes of a circular shield.** Spatial profiles $u_{kl}(r, \vartheta)$ of the lowest vibrational modes, together with their corresponding eigenfrequencies, computed for a Copper shield with the parameters given in Table 10.1. For a conservative estimation of shield-induced decoherence, the particle is assumed to be located at the centre of the shield ($r = 0$), where the displacements of the $(k, 0)$-modes are maximal and where the radial gradients $\partial_r u_{kl}\big|_{r=0}$ of the $(k, 1)$-modes attains their largest value for $\vartheta = 0$.

with J_l and I_l being the Bessel- and modified Bessel functions of the first kind, respectively. For a worst-case estimate, we set $r = 0$ and $\vartheta = 0$ (see Fig. 10 and main text). If the spatial extend of the superposition is small compared to the scale over which the mode-profile varies (i.e. if $\Delta x \partial_r u_{kl},\ \Delta y \partial_r u_{kl} \ll 1$), the mode can be linearised around the particles' delocalisation, spanning $\hat{r} = (\hat{x}\cos\theta - \hat{y}\sin\theta)$, as

$$u_{kl}(\hat{r}) \approx u_{kl}(0) + \hat{r}\partial_r u_{kl}\big|_{r=0}. \tag{C.202}$$

The distance between the particle and the shield, $\hat{d}_{kl}$, depends on u_{kl} and is thus given by

$$\begin{aligned}\hat{d}_{kl} = d_0 &\pm (\hat{x}\sin\theta_{A/B} + \hat{y}\cos\theta_{A/B}) \\ &\mp \hat{q}_{kl}\Big[u_{kl}(0) \mp \big(\hat{x}\cos\theta_{A/B} - \hat{y}\sin\theta_{A/B}\big)\,\partial_r u_{kl}\big|_{r=0}\Big],\end{aligned} \tag{C.203}$$

where $\hat{q}_{kl}$ is the shield's position operator. For Casimir interactions between silica particles, we find $d_0 = L - R - \frac{d_s}{2}$. For $\Delta x, \Delta y \ll d_0$, the Hamiltonian Eq. (C.189)

can be expanded in $\hat{x}$, $\hat{y}$ and $\hat{q}_{kl}$ to yield

$$\begin{aligned}\hat{H}_{kl,\text{Casimir, parall.}} \approx \eta\Big[&\mp 2d_0 u_{kl}(0)\hat{q}_{kl} \pm 2d_0\hat{y} - 3u_{kl}(0)^2\hat{q}_{kl}^2 \\ &+ 6u_{kl}(0)\hat{q}_{kl}\hat{y} - 3\hat{y}^2 + 2d_0\partial_r u_{kl}\big|_{r=0}\hat{q}_{kl}\hat{x}\Big], \qquad \text{(C.204)}\\ \hat{H}_{kl,\text{Casimir, linear}} \approx \eta\Big[&\mp 2d_0 u_{kl}(0)\hat{q}_{kl} \pm 2d_0\hat{x} - 3u_{kl}(0)^2\hat{q}_{kl}^2 \\ &+ 6u_{kl}(0)\hat{q}_{kl}\hat{x} - 3\hat{x}^2 - 2d_0\partial_r u_{kl}\big|_{r=0}\hat{q}_{kl}\hat{y}\Big]. \qquad \text{(C.205)}\end{aligned}$$

For magnetic dipole interactions between superconducting lead particles, d_0 is simply given by $d_0 = L - d_s/2$. Similar to above, the Hamiltonian Eq. (C.194) can be expanded like

$$\begin{aligned}\hat{H}_{kl,\text{mag. Dipole, parall}} \approx \delta\Big[&\mp 3d_0 u_{kl}(0)\hat{q}_{kl} \pm 3d_0\hat{y} - 6u_{kl}(0)^2\hat{q}_{kl}^2 + 12u_{kl}(0)\hat{q}_{kl}\hat{y} \\ &- 6\hat{y}^2 + 3d_0\partial_r u_{kl}\big|_{r=0}\hat{q}_{kl}\hat{x}\Big], \qquad \text{(C.206)}\\ \hat{H}_{kl,\text{mag. Dipole, linear}} \approx \delta\Big[&\mp 3d_0 u_{kl}(0)\hat{q}_{kl} \pm 3d_0\hat{x} - 6u_{kl}(0)^2\hat{q}_{kl}^2 + 12u_{kl}(0)\hat{q}_{kl}\hat{x} \\ &- 6\hat{x}^2 - 3d_0\partial_r u_{kl}\big|_{r=0}\hat{q}_{kl}\hat{y}\Big]. \qquad \text{(C.207)}\end{aligned}$$

C.3 Gaussian States

Time Evolution of the Covariance Matrix

For a system described by the quadrature operators $\mathbf{r} = (x_1, p_1, \ldots, x_N, p_N)^\intercal$ obeying the canonical commutation relations

$$[\mathbf{r}, \mathbf{r}^\intercal] = i\hbar\Omega, \qquad \Omega := \begin{pmatrix} 0 & 1 \\ -1 & 0 \end{pmatrix}^{\oplus N} \qquad \text{(C.208)}$$

the statistical properties of a Gaussian state are fully determined by its first and second moments

$$d_i = \langle r_i \rangle, \quad V_{ij} = \frac{1}{2}\langle r_i r_j + r_j r_i \rangle, \qquad \text{(C.209)}$$

where $\langle \cdot \rangle = \mathrm{tr}\{\cdot\,\rho\}$ denotes the expectation value. Gaussianity is preserved under a time evolution of a quadratic Hamiltonian in the form

$$\hat{H} = \tfrac{1}{2}\mathbf{r}^\intercal G\mathbf{r} + \mathbf{g}^\intercal\mathbf{r}. \qquad \text{(C.210)}$$

and linear Lindblad operators

$$L_k = \mathbf{l}_k^\intercal\mathbf{r}, \quad \mathbf{l}_k \in \mathbb{C}^{2N} \quad \text{with Kossakowski matrix} \quad C \equiv \sum_k \mathbf{l}_k\mathbf{l}_k^\intercal. \qquad \text{(C.211)}$$

The (adjoint) Heisenberg generator of the dynamics for an operator $\hat{O}$ is then given by

$$\frac{\mathrm{d}}{\mathrm{d}t}\hat{O} = \frac{i}{\hbar}[\hat{H}, \hat{O}] + \sum_k \left(L_k^\dagger \hat{O} L_k - \frac{1}{2}\left\{ L_K^\dagger L_K, \hat{O} \right\} \right). \tag{C.212}$$

This results in the following dynamics of $\mathbf{r}$ and $\mathbf{r}\mathbf{r}^\intercal$:

$$\dot{\mathbf{r}} = K\mathbf{r} + \Omega\mathbf{g}, \qquad \text{with} \qquad K = \Omega G - \Omega\,\mathrm{Im}(C) \tag{C.213}$$

$$\frac{\mathrm{d}}{\mathrm{d}t}(\mathbf{r}\mathbf{r}^\intercal) = \dot{\mathbf{r}}\mathbf{r}^\intercal + \mathbf{r}\dot{\mathbf{r}}^\intercal + \mathcal{D} \qquad \text{with} \qquad \mathcal{D} = \hbar^2 \Omega\,\mathrm{Re}(C)\Omega^\intercal. \tag{C.214}$$

The dynamics for $\mathbf{d}$ and V follow directly as

$$\dot{\mathbf{d}} = K\mathbf{d} + \Omega\mathbf{g} \qquad \text{with solution} \qquad \mathbf{d}(t) = S(t)\mathbf{d}(0) + \mathbf{h}(t) \tag{C.215}$$

and

$$\dot{V} = KV + VK^\intercal + \Omega\mathbf{g}\mathbf{d}^\intercal + \mathbf{d}(\Omega\mathbf{g})^\intercal + \mathcal{D} \tag{C.216}$$

which, in general, is solved by

$$\begin{aligned} V(t) =& S(t)V(0)S(t)^\intercal + S(t)\mathbf{d}(0)\mathbf{h}(t)^\intercal + \mathbf{h}(t)(S(t)\mathbf{d}(0))^\intercal + \mathbf{h}(t)\mathbf{h}(t)^\intercal \\ &+ \int_0^t \mathrm{d}s\, S(t-s)\mathcal{D}S(t-s)^\intercal. \end{aligned} \tag{C.217}$$

The covariance matrix $\sigma = V - \mathbf{d}\mathbf{d}^\intercal$ then satisfies

$$\dot{\sigma} = K\sigma + \sigma K^\intercal + \mathcal{D} \tag{C.218}$$

which is solved by

$$\sigma(t) = S(t)\sigma(0)S(t)^\intercal + \int_0^t \mathrm{d}s\, S(t-s)\mathcal{D}S(t-s)^\intercal. \tag{C.219}$$

Here we have defined

$$S(t) = e^{Kt} \qquad \text{and} \qquad \mathbf{h}(t) = \int_0^t \mathrm{d}s\, S(t-s)\Omega\mathbf{g}. \tag{C.220}$$

Stochastic Noise in the Trapping

Using that the noise has vanishing mean, i.e. $\langle \xi_i(t) \rangle = 0$, we find that the dynamics are given by

$$\langle \mathbf{d}(t) \rangle_\xi = S(t)\mathbf{d}(0) \tag{C.221}$$

$$\langle V(t) \rangle_\xi = S(t)V(0)S(t)^\intercal + \langle \mathbf{h}(t)\mathbf{h}(t) \rangle_\xi . \tag{C.222}$$

The covariance $\mathrm{Cov}_\xi[\mathbf{d}] = \langle \mathbf{d}\mathbf{d}^\intercal \rangle_\xi - \langle \mathbf{d} \rangle_\xi \langle \mathbf{d} \rangle_\xi^\intercal$ is given by

$$\mathrm{Cov}_\xi[\mathbf{d}] = \int_0^t \mathrm{d}s \int_0^t \mathrm{d}s'\, S(t-s) B\, C(s-s')\, B^\intercal S(t-s')^\intercal \tag{C.223}$$

where B includes the linear interaction and is defined by $\mathbf{g} = B\,\xi$. For the Hamiltonian given by Eq. (12.2), it is given by

$$B = \begin{pmatrix} 0 & 0 \\ 1 & 0 \\ 0 & 0 \\ 0 & 1 \end{pmatrix} \qquad \text{with correlator} \qquad C(\tau) = \begin{pmatrix} C_A(\tau) & 0 \\ 0 & C_B(\tau) \end{pmatrix} \tag{C.224}$$

Quasi-Static limit ($t_c \gg t$)

The correlator is approximately constant $C_i(\tau) = \Delta\xi^2$ over an entire single-run dynamics. Only classical variations between runs induce noise and $\xi_i(t) = \text{const.}$ over the entire run. Eq. (C.223) becomes

$$\mathrm{Cov}_\xi[\mathbf{d}] = \Delta\xi^2 \sum_{i=A,B} \left(\int_0^t \mathrm{d}s\, S(t-s) B_i \right) \left(\int_0^t \mathrm{d}s'\, S(t-s) B_i \right)^\intercal \tag{C.225}$$

with $B_A = (0,1,0,0)^\intercal$ and $B_B = (0,0,0,1)^\intercal$.

Markovian limit ($t_c \to 0$)

By taking $C_i(\tau) = 2D_i\delta(\tau)$, we find

$$\mathrm{Cov}_\xi[\mathbf{d}] = \int_0^t \mathrm{d}s\, S(t-s) \mathcal{D} S(t-s)^\intercal \quad \text{with} \quad \mathcal{D} = \bigoplus_i \begin{pmatrix} 0 & 0 \\ 0 & 2D_i \end{pmatrix}. \tag{C.226}$$

Differentiating Eq. (11.4), we find the following Markovian master equation governing the evolution

$$\frac{\mathrm{d}\sigma}{\mathrm{d}t} = K\sigma + \sigma K^\intercal + \mathcal{D}. \tag{C.227}$$

This is equivalent to the Lindblad equation

$$\frac{\mathrm{d}\rho}{\mathrm{d}t} = -\frac{i}{\hbar}[\hat{H}, \rho] - \sum_i \frac{D_i}{\hbar^2} [\hat{x}_i, [\hat{x}_i, \rho]]. \tag{C.228}$$

The Lindblad operators of this can be rewritten like

$$L_i = \sqrt{\frac{2D_i}{\hbar^2}} x_i = \mathbf{l}_i^\intercal \mathbf{r}, \quad \mathbf{l}_i = \sqrt{2D_i/\hbar^2}\, \mathbf{e}_{x_i}, \tag{C.229}$$

where $\mathbf{e}_{x_i}$ picks out the x_i component. The Kossakowski matrix $C = \sum_i \mathbf{l}_i \mathbf{l}_i^\intercal$ is purely real and the diffusion matrix $\mathcal{D}$ is given by

$$\mathcal{D} = \hbar^2 \Omega \left(\sum_i \frac{2D_i}{\hbar^2} \mathbf{e}_{x_i} \mathbf{e}_{x_i}^\intercal \right) \Omega^\intercal = 2 \sum_i D_i \mathbf{e}_{p_i} \mathbf{e}_{p_i}^\intercal = 2 \bigoplus_i \begin{pmatrix} 0 & 0 \\ 0 & D_i \end{pmatrix}. \tag{C.230}$$

Entanglement Dynamics for Gaussian States

Starting from the quadratically expanded gravitational Hamiltonian Eq. (C.181) with $\theta_A = \theta_B \equiv \theta$:

$$\begin{aligned} \hat{H}_{\text{Gravity}} \approx \lambda \Big[& \left(\sin^2\theta - \frac{1}{2}\cos^2\theta \right) \hat{x}_A \hat{x}_B + \left(\cos^2\theta - \frac{1}{2}\sin^2\theta \right) \hat{y}_A \hat{y}_B \\ & - \left(\frac{3}{2} \cos\theta \sin\theta \right) (\hat{x}_A \hat{y}_B + \hat{x}_B \hat{y}_A) \Big]. \end{aligned} \tag{C.231}$$

To simplify the calculation, we only take terms coupling both particles A and B, as all other terms cannot influence the bipartite entanglement generation. A more sophisticated analysis and numerical data show, that in fact, this is true. We can construct the Gaussianity-preserving Hamiltonian $\hat{H} = \frac{1}{2}\mathbf{r}^\intercal G \mathbf{r}$, where G is given in block-matrix form as

$$G = \begin{pmatrix} 0 & \tilde{G} \\ \tilde{G} & 0 \end{pmatrix} \quad \text{where} \quad \tilde{G} = \begin{pmatrix} A & 0 & C & 0 \\ 0 & 0 & 0 & 0 \\ C & 0 & B & 0 \\ 0 & 0 & 0 & 0 \end{pmatrix}. \tag{C.232}$$

Here, we denote $A = \lambda(\sin^2\theta - \frac{1}{2}\cos^2\theta)$, $B = \lambda(\cos^2\theta - \frac{1}{2}\sin^2\theta)$ and $C = -\frac{3\lambda}{2}\sin\theta\cos\theta$. Computing $\sigma(t) = e^{Kt}\sigma_0 e^{K^\intercal t}$ with σ_0 given by Eq. (11.2) and Eq. (11.3) and partially transposing the covariance matrix to $\sigma(t)^\Gamma = P\sigma(t)P$ with $P = \text{diag}\{1,1,1,1,1,-1,1,-1\}$, we are left with a block-matrix in the form of

$$\sigma(t)^\Gamma = \begin{pmatrix} \sigma_1 & \sigma_2 \\ -\sigma_2 & \sigma_1 \end{pmatrix}, \tag{C.233}$$

whose eigenvalues are given by $\{\lambda_i, \lambda_i^*\}$, when λ_i is an eigenvalue of the 4×4 matrix $\sigma_1 + i\sigma_2$. The symplectic eigenvalues of $\sigma(t)^\Gamma$ are (in linear order in t) given by

$$\left\{ \left| At\Delta x_A \Delta x_B (1 + 2\bar{n}_x) \pm \frac{1}{2}(1 + 2\bar{n}_x) \right|, \left| Bt\Delta y_A \Delta y_B \pm \frac{1}{2} \right| \right\} \tag{C.234}$$

with multiplicity 2 for each eigenvalue. This is independent of the parameter C for all θ. The logarithmic negativity can be computed with Eq. (11.5) and is given in linear order in t at zero temperature by

$$E_N = \frac{2t}{\hbar \log 2}\big(|A|\Delta x_A \Delta x_B + |B|\Delta y_A \Delta y_B\big). \tag{C.235}$$

Corrections to Non-Gaussianity

After classical averaging, the resulting state $\langle\rho\rangle \equiv \rho$ is in general no longer Gaussian. In lowest order, the deviation from the Gaussian reference state ρ_G can be written as

$$\rho = \rho_G + \Delta\rho \quad \text{with} \quad \Delta\rho = \int \mathrm{d}\xi\, p(\xi)\left(D(\xi)\rho_G D^\dagger(\xi) - \rho_G\right). \tag{C.236}$$

Using the reverse triangle inequality for the trace norm,

$$\|\rho\|_1 \geq \|\rho_G\|_1 - \|\Delta\rho\|_1. \tag{C.237}$$

and applying the monotonicity of the logarithm, we obtain the following lower bound on the logarithmic negativity:

$$\begin{aligned} E_N(\rho) &= \log_2 \left\|\rho^\Gamma\right\|_1 \geq \log_2(\left\|\rho_G^\Gamma\right\|_1 - \left\|\Delta\rho^\Gamma\right\|_1) \\ &= \log_2 \left\|\rho_G^\Gamma\right\|_1 - \frac{\left\|\Delta\rho^\Gamma\right\|_1}{\log 2 \|\rho_G^\Gamma\|_1} + \mathcal{O}(\|\Delta\rho\|_1^2). \end{aligned} \tag{C.238}$$

Here, we have expanded the logarithm to first order for small deviations $\|\Delta\rho\|_1 \ll \|\rho_G\|_1$. The random displacement channel given by $D(\xi)$ is LOCC and the logarithmic negativity is non-increasing under LOCC channels as shown in Ref. [272], thus $E_N(\rho) \leq E_N(\rho_G)$. Combining both bounds, the deviation from the Gaussian logarithmic negativity is bounded by

$$\Delta E_N = E_N(\rho_G) - E_N(\rho) \leq \frac{\left\|\Delta\rho^\Gamma\right\|_1}{\log 2 \|\rho_G^\Gamma\|_1} = \frac{\left\|\Delta\rho^\Gamma\right\|_1}{\log 2} 2^{-E_N(\rho_G)} + \mathcal{O}(\|\Delta\rho\|_1^2). \tag{C.239}$$

To estimate the magnitude of the non-Gaussian correction $\Delta\rho$, we express it in terms of the characteristic function of the quadrature operators $\hat{x}$ and $\hat{p}$ by

$$\Delta\rho = \frac{1}{(2\pi)^n} \int \mathrm{d}^{2n}\lambda\, \Delta\chi(\lambda) e^{-i\lambda^\intercal \Omega \mathbf{r}}, \tag{C.240}$$

where $\Delta\chi(\lambda) = \chi(\lambda) - \chi_G(\lambda)$ denotes the difference between the characteristic function $\chi(\lambda) = \int \mathrm{d}\xi\, p(\xi)\chi_\xi(\lambda)$ and and its Gaussian counterpart $\chi_G(\lambda)$. The

characteristic function can be written as a cumulant expansion

$$\chi(\lambda) = \left\langle e^{f(\xi;\lambda)} \right\rangle_\xi = \exp\left\{ \sum_{n=0}^{\infty} \frac{\kappa^{(n)}(f)}{n!} \right\} \quad \text{with} \quad f(\xi;\lambda) = -\frac{1}{2}\lambda^\intercal \Omega^\intercal \sigma(\xi) \Omega \lambda + i\lambda^\intercal \Omega d(\xi). \tag{C.241}$$

Expanding $f = f_0 + f_1\xi + f_2\xi^2 + \mathcal{O}(\xi^3)$ in powers of the classical variable ξ and assuming a Gaussian distribution $\xi \sim \mathcal{N}(0, \Delta\xi^2)$, Wick's theorem yields $\langle \xi^{2m+1} \rangle = 0$ and $\langle \xi^{2m} \rangle = (2m-1)!!(\Delta\xi^2)^m$. Consequently, the cumulants scale as $\kappa^{(n)} \sim \mathcal{O}(\Delta\xi^{2\lceil n/2 \rceil})$ where the lowest order is explicitly given by

$$\begin{aligned} \chi(\lambda) &= \chi_G(\lambda) \exp\left\{ \frac{\Delta\xi^2}{2}(2f_1^2 + f_2) + \mathcal{O}(\Delta\xi^4) \right\} \\ &\approx \chi_G(\lambda) \left(1 + \frac{\Delta\xi^2}{2}(2f_1^2 + f_2) \right) + \mathcal{O}(\Delta\xi^4). \end{aligned} \tag{C.242}$$

Thus, the non-Gaussian correction $\|\Delta\rho\|_1 \sim \Delta\xi^2 \|\rho_G\|_1$, with a pre-factor determined by $2f_1(\lambda)^2 + f_2(\lambda)$ and the integral expression from Eq. (C.240). For small variations, the state is therefore almost Gaussian with a small correction to the logarithmic negativity

$$\Delta E_N \sim \Delta\xi^2 + \mathcal{O}(\Delta\xi^4). \tag{C.243}$$

C.4 Cat-States

Entanglement Dynamics for Two-Level Cat-States

Starting from the Hamiltonian Eq. (C.181), we take the limit $\hat{y} \to 0$ and expand to second order in $\hat{x}$ to find

$$\begin{aligned} \hat{H}_{\text{Gravity}} \approx & \frac{GM_AM_B}{2L} + \lambda \Bigg(\hat{x}_A \hat{x}_B \sin\theta_A \sin\theta_B - \frac{1}{2}\hat{x}_A \hat{x}_B \cos\theta_A \cos\theta_B \\ & - \frac{1}{2}\left(\hat{x}_A^2 + \hat{x}_B^2\right) + \frac{3}{4}\left(\hat{x}_A^2 \cos^2\theta_A + \hat{x}_B^2 \cos^2\theta_B\right) \\ & + L\hat{x}_A \sin\theta_A - L\hat{x}_B \sin\theta_B \Bigg). \end{aligned} \tag{C.244}$$

Upon discretising the position operator by $\hat{x} \to \Delta x \sigma_z$ with σ_z being the Pauli matrix, the interaction reduces to an effective two-level Hamiltonian acting on the Hilbert-space spanned by $\left\{ \left|\psi^{(1)}\right\rangle, \left|\psi^{(2)}\right\rangle \right\}^{\otimes 2}$. For the initial product state

$\rho_{\text{Particles}} = \frac{1}{4}(\text{id} + \sigma_x)^{\otimes 2}$, the evolution under $\hat{H}_{\text{Gravity}}$ takes the analytic form

$$\rho_{\text{Gravity}}(t) = \frac{1}{4}\begin{pmatrix} 1 & e^{-it\frac{A-B_B}{\hbar}} & e^{-it\frac{A+B_A}{\hbar}} & e^{-it\frac{B_A-B_B}{\hbar}} \\ e^{it\frac{A-B_B}{\hbar}} & 1 & e^{-it\frac{B_A+B_B}{\hbar}} & e^{it\frac{A-B_A}{\hbar}} \\ e^{it\frac{A+B_A}{\hbar}} & e^{it\frac{B_A+B_B}{\hbar}} & 1 & e^{it\frac{A+B_B}{\hbar}} \\ e^{it\frac{B_A-B_B}{\hbar}} & e^{-it\frac{A-B_A}{\hbar}} & e^{-it\frac{A+B_B}{\hbar}} & 1 \end{pmatrix}, \tag{C.245}$$

with $A = 2\lambda\Delta x_A \Delta x_B \left(\sin\theta_A \sin\theta_B - \frac{1}{2}\cos\theta_A \cos\theta_B\right)$ and $B_i = 2L\lambda\Delta x_i \sin\theta_i$. The eigenvalues of the partial transposed state ρ^Γ are given by

$$\left\{\frac{1}{2}\sin\left(\frac{tA}{\hbar}\right), -\frac{1}{2}\sin\left(\frac{tA}{\hbar}\right), \sin^2\left(\frac{tA}{2\hbar}\right), \cos^2\left(\frac{tA}{2\hbar}\right)\right\}, \tag{C.246}$$

thus resulting in a logarithmic negativity of

$$E_N = \log_2\left(1 + |\sin(\phi t)|\right) \tag{C.247}$$

with

$$\phi = \frac{A}{\hbar} = \frac{\lambda\Delta x_A \Delta x_B}{\hbar}\left(2\sin\theta_A \sin\theta_B - \cos\theta_A \cos\theta_B\right). \tag{C.248}$$

Stochastic Placement Variations for Two-Level Cat-States

In addition to the gravitational interaction Eq. (C.244), we include Casimir and magnetic dipole interactions from Eq. (C.189) and Eq. (C.194) at arbitrary orientations. In the limit $\hat{y} \to 0$, we can expand to *first order* in the variations and find

$$\begin{aligned} \hat{H} = \hat{H}_{\text{Gravity}} + \eta\Big[&6\hat{x}_A\xi_A^{(L)}\sin\theta_A - 2(L - R - \tfrac{d_s}{2})\hat{x}_A\xi_A^{(\theta)}\cos\theta_A \\ &+ \frac{12\hat{x}_A^2\xi_A^{(L)}\sin^2\theta_A}{L - R - d_s/2} - 6\hat{x}_A^2\xi_A^{(\theta)}\sin\theta_A\cos\theta_A\Big] \qquad \text{(C.249)} \\ + \eta\Big[&-6\hat{x}_B\xi_B^{(L)}\sin\theta_B + 2(L - R - \tfrac{d_s}{2})\hat{x}_B\xi_B^{(\theta)}\cos\theta_B \\ &+ \frac{12\hat{x}_B^2\xi_B^{(L)}\sin^2\theta_B}{L - R - d_s/2} - 6\hat{x}_B^2\xi_B^{(\theta)}\sin\theta_B\cos\theta_B\Big] \qquad \text{(C.250)} \end{aligned}$$

for Casimir interactions and

$$\begin{aligned}\hat{H} = \hat{H}_{\text{Gravity}} + \delta\Big[&12\hat{x}_A\xi_A^{(L)}\sin\theta_A - 3(L-\tfrac{d_s}{2})\hat{x}_A\xi_A^{(\theta)}\cos\theta_A \\ &+ \frac{30\hat{x}_A^2\xi_A^{(L)}\sin^2\theta_A}{L-d_s/2} - 12\hat{x}_A^2\xi_A^{(\theta)}\sin\theta_A\cos\theta_A\Big] \\ + \delta\Big[&-12\hat{x}_B\xi_B^{(L)}\sin\theta_B + 3(L-\tfrac{d_s}{2})\hat{x}_B\xi_B^{(\theta)}\cos\theta_B \\ &+ \frac{30\hat{x}_B^2\xi_B^{(L)}\sin^2\theta_B}{L-d_s/2} - 12\hat{x}_B^2\xi_B^{(\theta)}\sin\theta_B\cos\theta_B\Big]\end{aligned} \tag{C.251}$$

for magnetic dipole interactions.

After replacing $\hat{x} \to \Delta x\sigma_z$ to project into the two-dimensional Hilbert-space for the two-level cat-states, the time evolved and averaged state can be obtained analytically. Here, we again distinguish between the general case, where the detectors move from run to run and the case, where the shield moves and thus $\xi_A^{(L)} = -\xi_B^{(L)}$ and $\xi_A^{(\theta)} = \xi_B^{(\theta)}$:

Detector movement

In the general case with uncorrelated $\xi_{A/B}$, the averaged density matrix can be written in the form

$$\langle\rho\rangle = \rho_{\text{Gravity}}(t)\odot \begin{pmatrix} 1 & e^{-\sum_k\gamma_{B,k}^2} & e^{-\sum_k\gamma_{A,k}^2} & e^{-\sum_k(\gamma_{A,k}^2+\gamma_{B,k}^2)} \\ e^{-\sum_k\gamma_{B,k}^2} & 1 & e^{-\sum_k(\gamma_{A,k}^2+\gamma_{B,k}^2)} & e^{-\sum_k\gamma_{A,k}^2} \\ e^{-\sum_k\gamma_{A,k}^2} & e^{-\sum_k(\gamma_{A,k}^2+\gamma_{B,k}^2)} & 1 & e^{-\sum_k\gamma_{B,k}^2} \\ e^{-\sum_k(\gamma_{A,k}^2+\gamma_{B,k}^2)} & e^{-\sum_k\gamma_{A,k}^2} & e^{-\sum_k\gamma_{B,k}^2} & 1 \end{pmatrix} \tag{C.252}$$

where $k \in \{L,\theta\}\times\{\text{Casimir},\ \text{mag. Dipole}\}$ iterates over all considered interactions and variations with

$$\begin{aligned}\gamma_{i,\,\theta,\,\text{Casimir}} &= \sqrt{8}(L-R-\frac{d_s}{2})\eta\Delta\theta\cos\theta_i\,\Delta x_i\,t\,/\,\hbar, \\ \gamma_{i,\,L,\,\text{Casimir}} &= \pm\sqrt{72}\eta\Delta L\sin\theta_i\,\Delta x_i\,t\,/\,\hbar\end{aligned} \tag{C.253}$$

$$\begin{aligned}\gamma_{i,\,\theta,\,\text{mag. Dipole}} &= \sqrt{18}(L-\frac{d_s}{2})\delta\Delta\theta_i\cos\theta_i\,\Delta x_i\,t\,/\,\hbar, \\ \gamma_{i,\,L,\,\text{mag. Dipole}} &= \pm\sqrt{288}\delta\Delta L\sin\theta_i\,\Delta x_i\,t\,/\,\hbar\end{aligned} \tag{C.254}$$

The $\pm$ distinguishes between particles A and B and $\odot$ denotes the element-wise Hadamard product of the two matrices, where $\rho_{\text{Gravity}}(t)$ is given by Eq. (C.245) and is the evolved state with only gravitational interactions included. Denoting

$\gamma_i^2 \equiv \sum_k \gamma_{i,k}^2$, the logarithmic negativity of this state is given by

$$E_N = \max\left\{0, \log_2\left[\frac{1}{2}\Big(1 + e^{-\gamma_A^2-\gamma_B^2} + \sqrt{e^{-2\gamma_A^2} + e^{-2\gamma_B^2} - 2e^{-\gamma_A^2-\gamma_B^2}\cos(2\phi t)}\Big)\right]\right\}. \tag{C.255}$$

In the special case of $\gamma_A = \gamma_B := \gamma$, corresponding to two identical delocalisations, the logarithmic negativity can be expressed in the form

$$E_N = \max\left\{0, \log_2\left(e^{-\gamma^2}(\cosh(\gamma^2) + |\sin\phi t|)\right)\right\} \tag{C.256}$$

$$= \log_2\left\{\frac{1}{2}e^{-\gamma^2}\Big(\big|\sin\phi t - \sinh(\gamma^2)\big| + \big|\sin\phi t + \sinh(\gamma^2)\big| + 2\cosh(\gamma^2)\Big)\right\}. \tag{C.257}$$

Shield movement

If $\xi_{A/B}$ are correlated due to the shield movement affecting the couplings of both particles with the shield in the same way, the averaged density matrix is given by

$$\langle\rho\rangle = \rho_{\text{Gravity}}(t) \odot \begin{pmatrix} 1 & e^{-\sum_k \gamma_{B,k}^2} & e^{-\sum_k \gamma_{A,k}^2} & e^{-\sum_k (\gamma_{A,k}-\gamma_{B,k})^2} \\ e^{-\sum_k \gamma_{B,k}^2} & 1 & e^{-\sum_k (\gamma_{A,k}+\gamma_{B,k})^2} & e^{-\sum_k \gamma_{A,k}^2} \\ e^{-\sum_k \gamma_{A,k}^2} & e^{-\sum_k (\gamma_{A,k}+\gamma_{B,k})^2} & 1 & e^{-\sum_k \gamma_{B,k}^2} \\ e^{-\sum_k (\gamma_{A,k}-\gamma_{B,k})^2} & e^{-\sum_k \gamma_{A,k}^2} & e^{-\sum_k \gamma_{B,k}^2} & 1 \end{pmatrix} \tag{C.258}$$

with $\gamma_{i,k}$ given from before. A compact expression for the logarithmic negativity of the state cannot be given here. For only one considered interaction, however, it is given by

$$E_N = \max\left\{0, \log_2\left[\frac{1}{2}\Big(1 + e^{-\gamma_A^2-\gamma_B^2}\cosh(2\gamma_A\gamma_B) + \sqrt{e^{-2(\gamma_A^2+\gamma_B^2)}\sinh(2\gamma_A\gamma_B) + e^{-2\gamma_A^2} + e^{-2\gamma_B^2} - 2e^{-\gamma_A^2-\gamma_B^2}\cos(2\phi t)}\Big)\right]\right\} \tag{C.259}$$

In the special case $\gamma_A = \gamma_B := \gamma$, this reduces to

$$E_N = \max\left\{0, \log_2\left[\frac{1}{4}\Big(3 + e^{-4\gamma^2} + 2e^{-2\gamma^2} \times \sqrt{4e^{2\gamma^2}\sin^2(\phi t) + \sinh^2(2\gamma^2)}\Big)\right]\right\} \tag{C.260}$$

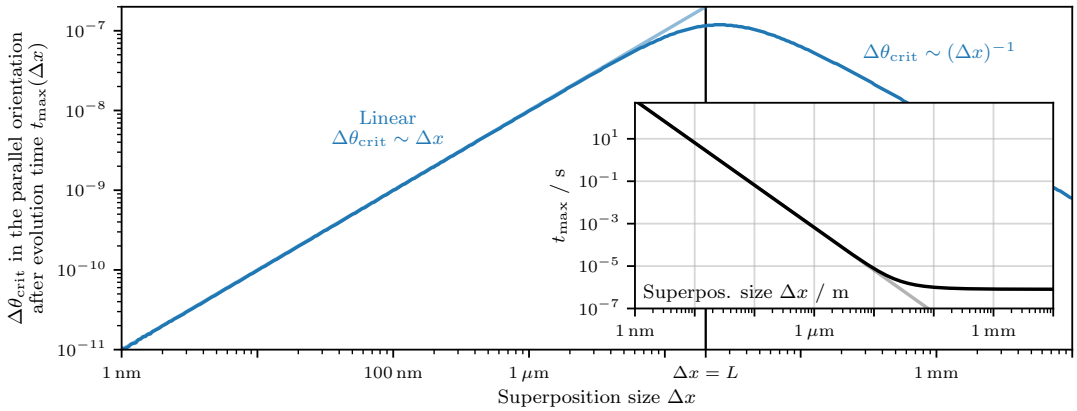


Figure 11: **Stability for large spatial superpositions.** Numerically determined critical angular variations $\Delta\theta_{\mathrm{crit}}$ as a function of the superposition size Δx, evaluated at the interaction time $t_{\mathrm{max}}(\Delta x)$ at which the entanglement is maximal. For $\Delta\theta > \Delta\theta_{\mathrm{crit}}$ the logarithmic negativity vanishes. The inset shows the corresponding times t_{max}. A qualitative change in stability occurs for $\Delta x \gtrsim L$, where decoherence starts to dominate. This analysis was exemplarily performed for silica particles prepared in idealised two-level cat-states.

Throughout this work, we always employ the approximation $\Delta x \ll L$, which allows for the interaction potentials to be expanded up to second order in the position operators (see e.g. Apx. C.2). For superposition sizes approaching the micrometer scale, however, this approximation breaks down and the analytical treatment is no longer valid. To assess the robustness of entanglement generation beyond this regime, we therefore perform a full numerical analysis for arbitrary superposition sizes Δx. Fig. 11 shows the numerically determined critical angular standard deviation $\Delta\theta_{\mathrm{crit}}$ as a function of Δx. For angular fluctuations exceeding $\Delta\theta > \Delta\theta_{\mathrm{crit}}$, the logarithmic negativity vanishes and no bipartite entanglement is present in the averaged state. The entire analysis is exemplarily performed for silica particles prepared in idealised two-level cat-states interacting with the shield via Casimir interactions. The data is evaluated at an evolution time $t_{\mathrm{max}}(\Delta x)$, defined as the time at which the entanglement reaches its maximal value of $E_N(t_{\mathrm{max}}) = 1$ in the absence of noise. This time is shown in the inset of Fig. 11 as a function of Δx.

For small superposition sizes $\Delta x \ll L$, this time scales as $t_{\mathrm{max}} \sim \Delta x^{-2}$, in agreement with the analytical results in Eq. (11.7). From Eq. (11.8), we find that at critical variations $\gamma_{\mathrm{crit}}(t_{\mathrm{max}})$, it has to hold that $\Delta\theta_{\mathrm{crit}} \propto 1/(\Delta x\, t_{\mathrm{max}})$, such that the reduction in the interaction time overcompensates the increased sensitivity. As a result, the critical angular tolerance *increases* linearly with Δx, leading to

more stability. This behaviour changes qualitatively once the superposition site exceeds the particle separation $\Delta x \gtrsim L$. Here, the time $t_{\max}$ saturates and no longer decreases with Δx. Consequently, decoherence continues to grow with Δx, resulting in a loss of stability.

While increasing the spatially delocalisation can, within our model, enhance robustness against placement-induced decoherence, large superpositions are nevertheless known to be fragile under other decoherence mechanisms. In particular, Ref. [302] shows that Coulomb-induced decoherence from nearby conducting surfaces increases rapidly with growing Δx. This limitation is rooted in a different physical mechanism than the placement-induced dephasing considered here and therefore, one might not be able to fully exploit the parametric regime in which larger Δx would otherwise improve robustness. More generally, for scattering processes such as collisions with air molecules or photons, the decoherence rate typically to increase with Δx^2 [131].

Cat-States in Front of a Vibrating Thermal Shield

The Hamiltonian

$$\hat{H}_{\text{Shield}} = \sum_{(k,l)} \hat{H}_{kl} + \hbar\omega_{kl}(\hat{a}_{kl}^\dagger \hat{a}_{kl} + 1/2) \tag{C.261}$$

describes the vibrating shield modes labelled by (k, l) and their interaction with the particles. As gravity couples only through position operators, $\hat{H}_{\text{Gravity}}$ commutes with $\hat{H}_{\text{Shield}}$. As the time evolution generated by $\hat{H}_{\text{Gravity}}$ has already been analysed in Appendix C.4, it remains only to determine the evolution under $\hat{H}_{\text{Shield}}$. In the interaction picture w.r.t. $\hat{H}_0 = \sum_{(k,l)} \hbar\omega_{kl}(\hat{a}_{kl}^\dagger \hat{a}_{kl} + 1/2)$ it is given by

$$\hat{H}_{\text{Shield,int}} = \sum_{(k,l)} \hat{G}_{kl}(\hat{a}_{kl} e^{-i\omega_{kl}t} + \hat{a}_{kl}^\dagger e^{i\omega_{kl}t}), \tag{C.262}$$

where $\hat{G}_{\text{kl}} = \text{diag}(g_1, \ldots, g_4)$ incorporates the interaction of the delocalised particles with the shield. It can be derived by making the replacements $\hat{x} \to \Delta x \sigma_z$ and $\hat{y} \to 0$ in Eq. (C.204) and Eq. (C.205) and it thus given by

$$\begin{aligned}\hat{G}_{kl,\text{Casimir, parallel}} =& 4\eta\Delta x(L - R - \tfrac{d_s}{2})\, \partial_r u_{kl}\big|_{r=0} \\ &\times \sqrt{\frac{\hbar}{2m_{\text{eff}}\omega_{kl}}}\, \text{diag}(0, -1, 1, 0)\,, \end{aligned} \tag{C.263}$$

$$\hat{G}_{kl,\text{Casimir linear}} = 12\eta\Delta x\, u_{kl}(r=0)\sqrt{\frac{\hbar}{2m_{\text{eff}}\omega_{kl}}}\, \text{diag}(1, 0, 0, -1) \tag{C.264}$$

for Casimir interactions and by

$$\hat{G}_{kl,\text{mag. dipole, parall.}} = 6\delta\Delta x(L - \tfrac{d_s}{2})\,\partial_r u_{kl}\big|_{r=0}\sqrt{\frac{\hbar}{2m_{\text{eff}}\omega_{kl}}}\,\text{diag}(0,-1,1,0)\,, \tag{C.265}$$

$$\hat{G}_{kl,\text{mag. dipole, linear}} = 24\delta\Delta x\,u_{kl}(r=0)\sqrt{\frac{\hbar}{2m_{\text{eff}}\omega_{kl}}}\,\text{diag}(1,0,0,-1) \tag{C.266}$$

for magnetic dipole interactions.

As the Magnus expansion breaks off in second order, the time evolution can be found exactly and is given by

$$\hat{U}(t) = \exp\Big\{-\frac{i}{\hbar}\int_0^t \mathrm{d}t_1\,\hat{H}(t_1) - \frac{1}{2\hbar^2}\int_0^t \mathrm{d}t_1\int_0^{t_1}\mathrm{d}t_2\,[\hat{H}(t_1),\hat{H}(t_2)]\Big\} \tag{C.267}$$

$$= \exp\Big\{\hat{G}(f_1\hat{a}^\dagger - f_1^*\hat{a}) + i\hat{G}^2 f_2\Big\} \tag{C.268}$$

$$= \text{diag}\left(\hat{D}(f_1 g_1)e^{if_2 g_1^2}, \hat{D}(f_1 g_2)e^{if_2 g_2^2}, \hat{D}(f_1 g_3)e^{if_2 g_3^2}, \hat{D}(f_1 g_4)e^{if_2 g_4^2}\right) \tag{C.269}$$

with

$$f_1 = \frac{(1-e^{i\omega_{kl}t})}{\hbar\omega_{kl}} \quad \text{and} \quad f_2 = \frac{t\omega_{kl} - \sin(t\omega_{kl})}{\hbar^2\omega_{kl}^2}. \tag{C.270}$$

The displacement operator is defined by $\hat{D}(\alpha) = \exp\{\alpha\hat{a}^\dagger - \alpha^*\hat{a}\}$. The time evolved density matrix $\rho(t) = \hat{U}(t)\rho_0\hat{U}^\dagger(t)$ of $\rho_0 = \bigotimes_{(k,l)}\rho_{\text{th},kl}\otimes\rho_{\text{Particles}}$ is therefore given by

$$\rho_{ij}(t) = \left[\bigotimes_{(k,l)}\hat{D}(f_1 g_i)\rho_{\text{th},kl}\hat{D}^\dagger(f_1 g_j)\right] e^{if_2(g_i^2 - g_j^2)}\rho_{\text{particles},ij} \tag{C.271}$$

where the indices i,j of the resulting block-matrix $\rho(t)$ label the basis states of the particles. Tracing out the shield and using $\text{tr}\{A\otimes B\} = \text{tr}\,A\,\text{tr}\,B$ one finds for the time evolution of both particles

$$\rho_{\text{particles},ij}(t) = \prod_{(k,l)}\text{tr}\Big\{\hat{D}(f_1 g_i)\rho_{\text{th},kl}\hat{D}^\dagger(f_1 g_j)\Big\}e^{if_2(g_i^2-g_j^2)}\rho_{\text{Particles},ij}. \tag{C.272}$$

Using that $\text{tr}\Big\{\hat{D}(\zeta_i)\rho_{\text{th}}\hat{D}^\dagger(\zeta_j)\Big\} = \exp\Big\{\tilde{\zeta} - |\Delta\zeta|^2\left(\frac{1}{2}+\bar{n}\right)\Big\}$ where $\Delta\zeta = \zeta_i - \zeta_j$ and $\tilde{\zeta} = (\zeta_j^*\zeta_i - \zeta_j\zeta_i^*)/2 = 0$ [1], the elements of the evolved density matrix are finally

given by

$$\rho_{\text{particles},ij}(t) = \exp\left\{-\sum_{(k,l)} |g_{i,kl} - g_{j,kl}|^2 f_1 f_1^* \left(\frac{1}{2} + \bar{n}\right)\right\} e^{if_2(g_{i,kl}^2 - g_{j,kl}^2)} \rho_{\text{particles},ij}(0)\,. \tag{C.273}$$

Crucially, ground-state fluctuations of the shield give rise to additional decoherence even at $T = 0$.

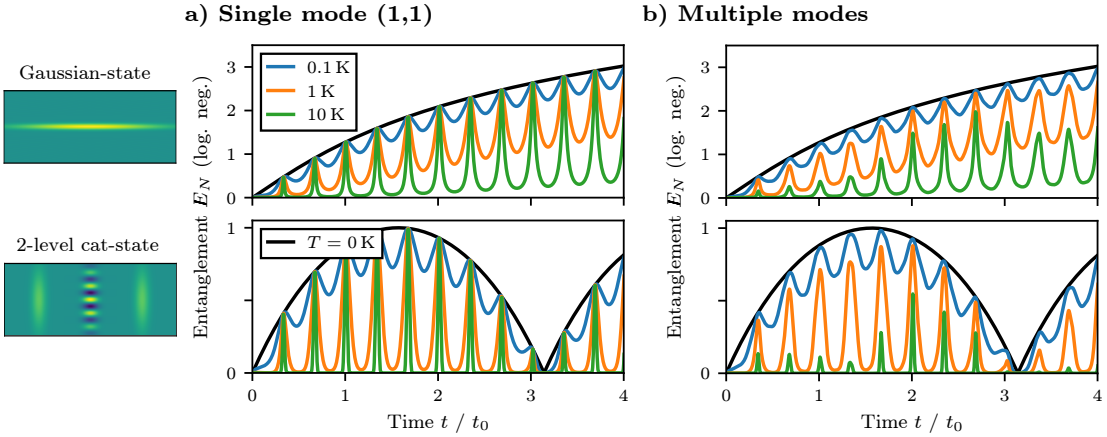


Figure 12: **Entanglement dynamics in a GIE setup in the presence of a quantum shield.** Results are shown for delocalised silica particles in the parallel orientation ($\theta = 0$). This figure is quantitatively the same as Fig. 13.1 but with weaker Casimir interactions between the particles and the shield. Here, the particle parameters from Table 10.1 were used with a Copper shield of size $d_s = 500$nm and $r_s = 1$cm. The thinner thickness compared to Fig. 13.1 was chosen to better visualize the underlying dynamics for the much weaker gravitational coupling between the silica particles. **a,** Entanglement dynamics for Gaussian states (**top**) and two-level cat-states (**bottom**) with the shield dynamics restricted to the dominant $(1,1)$-mode only. **b,** Corresponding dynamics where multiple shield modes are included (here: lowest 64 modes).

Bibliography

[1] Marit O. E. Steiner, Julen S. Pedernales, and Martin B. Plenio. Optically Hyperpolarized Materials for Levitated Optomechanics. *Quantum*, 9:1928, December 2025.

[2] Jan Bulling, Marit O. E. Steiner, Julen S. Pedernales, and Martin B. Plenio. Stability thresholds for gravitationally induced entanglement in shielded setups, 2026. arXiv:2604.22593 [quant-ph].

[3] Kenneth G. Libbrecht and Eric D. Black. Toward quantum-limited position measurements using optically levitated microspheres. *Physics Letters A*, 321(2):99–102, 2004.

[4] C. Gonzalez-Ballestero, M. Aspelmeyer, L. Novotny, R. Quidant, and O. Romero-Isart. Levitodynamics levitation and control of microscopic objects in vacuum. *Science*, 374(6564), October 2021.

[5] A. Ashkin. Acceleration and trapping of particles by radiation pressure. *Phys. Rev. Lett.*, 24:156–159, January 1970.

[6] Oriol Romero-Isart, Mathieu L. Juan, Romain Quidant, and J. Ignacio Cirac. Toward quantum superposition of living organisms. *New Journal of Physics*, 12:033015, 2010.

[7] D. E. Chang, C. A. Regal, S. B. Papp, D. J. Wilson, J. Ye, O. Painter, H. J. Kimble, and P. Zoller. Cavity opto-mechanics using an optically levitated nanosphere. *Proceedings of the National Academy of Sciences*, 107(3):1005–1010, 2010.

[8] P. F. Barker and M. N. Shneider. Cavity cooling of an optically trapped nanoparticle. *Phys. Rev. A*, 81:023826, February 2010.

[9] Urovs Deli'c, Manuel Reisenbauer, Kahan Dare, David Grass, Vladan Vuleti'c, Nikolai Kiesel, and Markus Aspelmeyer. Cooling of a levitated nanoparticle to the motional quantum ground state. *Science*, 367(6480):892–895, February 2020.

[10] Lorenzo Magrini, Philipp Rosenzweig, Constanze Bach, Andreas Deutschmann-Olek, Sebastian G. Hofer, Sungkun Hong, Nikolai Kiesel, Andreas Kugi, and Markus Aspelmeyer. Real-time optimal quantum control of mechanical motion at room temperature. *Nature*, 595(7867):373–377, 2021.

[11] Felix Tebbenjohanns, M. Luisa Mattana, Massimiliano Rossi, Martin Frimmer, and Lukas Novotny. Quantum control of a nanoparticle optically levitated in cryogenic free space. *Nature*, 595(7867):378–382, 2021.

[12] Stefan Kuhn, Alon Kosloff, Benjamin A. Stickler, Fernando Patolsky, Klaus Hornberger, Markus Arndt, and James Millen. Full rotational control of levitated silicon nanorods. *Optica*, 4(3):356–360, March 2017.

[13] Benjamin A. Stickler, Klaus Hornberger, and M. S. Kim. Quantum rotations of nanoparticles. *Nature Reviews Physics*, 3(8):589–597, 2021.

[14] J. S. Pedernales, F. Cosco, and M. B. Plenio. Decoherence-free rotational degrees of freedom for quantum applications. *Phys. Rev. Lett.*, 125:090501, August 2020.

[15] René Reimann, Michael Doderer, Erik Hebestreit, Rozenn Diehl, Martin Frimmer, Dominik Windey, Felix Tebbenjohanns, and Lukas Novotny. Ghz rotation of an optically trapped nanoparticle in vacuum. *Physical Review Letters*, 121(3):033602, July 2018.

[16] Jonghoon Ahn, Zhujing Xu, Jaehoon Bang, Yu-Hao Deng, Thai M. Hoang, Qinkai Han, Ren-Min Ma, and Tongcang Li. Optically levitated nanodumbbell torsion balance and ghz nanomechanical rotor. *Phys. Rev. Lett.*, 121:033603, July 2018.

[17] Jonghoon Ahn, Zhujing Xu, Jaehoon Bang, Peng Ju, Xingyu Gao, and Tongcang Li. Ultrasensitive torque detection with an optically levitated nanorotor. *Nature Nanotechnology*, 15(2):89–93, 2020.

[18] Markus Aspelmeyer, Tobias J. Kippenberg, and Florian Marquardt. Cavity optomechanics. *Rev. Mod. Phys.*, 86:1391–1452, December 2014.

[19] Yair Margalit, Or Dobkowski, Zhifan Zhou, Omer Amit, Yonathan Japha, Samuel Moukouri, Daniel Rohrlich, Anupam Mazumdar, Sougato Bose, Carsten Henkel, and Ron Folman. Realization of a complete stern-gerlach interferometer: Toward a test of quantum gravity. *Science Advances*, 7(22), May 2021.

[20] T. Delord, P. Huillery, L. Nicolas, and G. H'etet. Spin-cooling of the motion of a trapped diamond. *Nature*, 580(7801):56–59, 2020.

[21] C. Pellet-Mary, P. Huillery, M. Perdriat, and G. H'etet. Magnetic torque enhanced by tunable dipolar interactions. *Phys. Rev. B*, 104:L100411, September 2021.

[22] M. Perdriat, P. Huillery, C. Pellet-Mary, and G. H'etet. Angle locking of a levitating diamond using spin diamagnetism. *Phys. Rev. Lett.*, 128:117203, March 2022.

[23] Kirill Streltsov, Julen S. Pedernales, and Martin B. Plenio. Ground-state cooling of levitated magnets in low-frequency traps. *Phys. Rev. Lett.*, 126:193602, May 2021.

[24] Levi P. Neukirch, Eva von Haartman, Jessica M. Rosenholm, and A. Nick Vamivakas. Multi-dimensional single-spin nano-optomechanics with a levitated nanodiamond. *Nature Photonics*, 9(10):653–657, 2015.

[25] Thai M. Hoang, Jonghoon Ahn, Jaehoon Bang, and Tongcang Li. Electron spin control of optically levitated nanodiamonds in vacuum. *Nature Communications*, 7(1):12250, 2016.

[26] Gerard P. Conangla, Andreas W. Schell, Ra'ul A. Rica, and Romain Quidant. Motion control and optical interrogation of a levitating single nitrogen vacancy in vacuum. *Nano Letters*, 18(6):3956–3961, 06 2018.

[27] M. Scala, M. S. Kim, G. W. Morley, P. F. Barker, and S. Bose. Matter-wave interferometry of a levitated thermal nano-oscillator induced and probed by a spin. *Phys. Rev. Lett.*, 111:180403, October 2013.

[28] C. Wan, M. Scala, G. W. Morley, ATM. A. Rahman, H. Ulbricht, J. Bateman, P. F. Barker, S. Bose, and M. S. Kim. Free nano-object ramsey interferometry for large quantum superpositions. *Phys. Rev. Lett.*, 117:143003, September 2016.

[29] Julen S. Pedernales, Gavin W. Morley, and Martin B. Plenio. Motional dynamical decoupling for interferometry with macroscopic particles. *Physical Review Letters*, 125(2):023602, July 2020.

[30] Julen S. Pedernales, Kirill Streltsov, and Martin B. Plenio. Enhancing Gravitational Interaction between Quantum Systems by a Massive Mediator. *Phys. Rev. Lett.*, 128:110401, March 2022.

[31] James E March, Benjamin D Wood, Colin J Stephen, Laura Dur'an Fervenza, Ben G Breeze, Soumen Mandal, Andrew M Edmonds, Daniel J Twitchen, Matthew L Markham, Oliver A Williams, et al. Long spin coherence and relaxation times in nanodiamonds milled from polycrystalline 12c diamond. *Physical Review Applied*, 20(4):044045, 2023.

[32] A. Henstra, T.-S. Lin, J. Schmidt, and W.Th. Wenckebach. High dynamic nuclear polarization at room temperature. *Chemical Physics Letters*, 165(1):6–10, January 1990.

[33] T. R. Eichhorn, M. Haag, B. van den Brandt, P. Hautle, and W. Th. Wenckebach. High proton spin polarization with dnp using the triplet state of pentacene-d14. *Chemical Physics Letters*, 555:296–299, January 2013.

[34] T. R. Eichhorn, B. van den Brandt, P. Hautle, A. Henstra, and W. Th. Wenckebach. Dynamic nuclear polarisation via the integrated solid effect ii experiments on naphthalene-h8 doped with pentacene-d14. *Molecular Physics*, 112(13):1773–1782, December 2013.

[35] T. V. Can, Q.Z. Ni, and R.G. Griffin. Mechanisms of dynamic nuclear polarization in insulating solids. *Journal of Magnetic Resonance*, 253:23–35, April 2015.

[36] Y. Quan, B. van den Brandt, J. Kohlbrecher, W.Th. Wenckebach, and P. Hautle. A transportable neutron spin filter. *Nuclear Instruments and Methods in Physics Research Section A*, 921:22–26, March 2019.

[37] M. Haag, B. van den Brandt, T. R. Eichhorn, P. Hautle, and W.Th. Wenckebach. Spin filtering neutrons with a proton target dynamically polarized using photo-excited triplet states. *Nuclear Instruments and Methods in Physics Research Section A*, 678:91–97, June 2012.

[38] Tim R. Eichhorn, Anna J. Parker, Felix Josten, Christoph Müller, Jochen Scheuer, Jakob M. Steiner, Martin Gierse, Jonas Handwerker, Michael Keim, Sebastian Lucas, Mohammad Usman Qureshi, Alastair Marshall, Alon Salhov, Yifan Quan, Jan Binder, Kay D. Jahnke, Philipp Neumann, Stephan Knecht, John W. Blanchard, Martin B. Plenio, Fedor Jelezko, Lyndon Emsley, Christophoros C. Vassiliou, Patrick Hautle, and Ilai Schwartz. Hyperpolarized solution-state nmr spectroscopy with optically polarized crystals. *Journal of the American Chemical Society*, 144(6):2511–2519, February 2022.

[39] Angelo Bassi, Kinjalk Lochan, Seema Satin, Tejinder P. Singh, and Hendrik Ulbricht. Models of wave-function collapse, underlying theories, and experimental tests. *Rev. Mod. Phys.*, 85(2):471–527, April 2013.

[40] Vanessa Wachter, Silvia Viola Kusminskiy, Gabriel Hétet, and Benjamin A. Stickler. Gyroscopically stabilized quantum spin rotors. *Phys. Rev. Lett.*, 136:073604, February 2026.

[41] C. C. Rusconi, V. Pöchhacker, J. I. Cirac, and O. Romero-Isart. Linear stability analysis of a levitated nanomagnet in a static magnetic field quantum spin stabilized magnetic levitation. *Physical Review B*, 96(13):134419, October 2017.

[42] Yue Ma, M. S. Kim, and Benjamin A. Stickler. Torque-free manipulation of nanoparticle rotations via embedded spins. *Physical Review B*, 104(13):134310, October 2021.

[43] A. Einstein. Experimenteller nachweis der ampéreschen molekularströme. *Die Naturwissenschaften*, 3(19):237–238, May 1915.

[44] S. J. Barnett. Magnetization by rotation. *Physical Review*, 6(4):239–270, October 1915.

[45] O. W. Richardson. A mechanical effect accompanying magnetization. *Physical Review (Series I)*, 26(3):248–253, March 1908.

[46] Marc Ganzhorn, Svetlana Klyatskaya, Mario Ruben, and Wolfgang Wernsdorfer. Quantum einstein-de haas effect. *Nature Communications*, 7(1), April 2016.

[47] Mohsen Arabgol and Tycho Sleator. Observation of the nuclear barnett effect. *Physical Review Letters*, 122(17):177202, May 2019.

[48] Hiroyuki Chudo, Masao Ono, Kazuya Harii, Mamoru Matsuo, Jun'ichi Ieda, Rie Haruki, Satoru Okayasu, Sadamichi Maekawa, Hiroshi Yasuoka, and Eiji Saitoh. Observation of barnett fields in solids by nuclear magnetic resonance. *Applied Physics Express*, 7(6):063004, May 2014.

[49] H. Chudo, M. Matsuo, S. Maekawa, and E. Saitoh. Barnett field, rotational doppler effect, and berry phase studied by nuclear quadrupole resonance with rotation. *Physical Review B*, 103(17):174308, May 2021.

[50] A. A. Wood, E. Lilette, Y. Y. Fein, V. S. Perunicic, L. C. L. Hollenberg, R. E. Scholten, and A. M. Martin. Magnetic pseudo-fields in a rotating electron–nuclear spin system. *Nature Physics*, 13(11):1070–1073, August 2017.

[51] Cécile DeWitt-Morette and Dean Rickles. *The role of gravitation in physics: Report from the 1957 Chapel Hill Conference*. Edition Open Access, 2011.

[52] Netanel H. Lindner and Asher Peres. Testing quantum superpositions of the gravitational field with bose-einstein condensates. *Physical Review A*, 71(2):024101, February 2005.

[53] Dvir Kafri and J. M. Taylor. A noise inequality for classical forces, 11 2013. arXiv:1311.4558 [quant-ph].

[54] Marios Christodoulou, Andrea Di Biagio, Markus Aspelmeyer, Časlav Brukner, Carlo Rovelli, and Richard Howl. Locally mediated entanglement in linearized quantum gravity. *Physical Review Letters*, 130(10):100202, March 2023.

[55] M.B. Plenio and S. Virmani. An introduction to entanglement measures. *Quantum Information and Computation*, 7(1&2):1–51, January 2007.

[56] M. Kamba and K. Aikawa. Revealing the velocity uncertainties of a levitated particle in the quantum ground state. *Physical Review Letters*, 131(18):183602, October 2023.

[57] Johannes Piotrowski, Dominik Windey, Jayadev Vijayan, Carlos Gonzalez-Ballestero, Andrés de los Ríos Sommer, Nadine Meyer, Romain Quidant, Oriol Romero-Isart, René Reimann, and Lukas Novotny. Simultaneous ground-state cooling of two mechanical modes of a levitated nanoparticle. *Nature Physics*, 19(7):1009–1013, March 2023.

[58] A. Ranfagni, K. Børkje, F. Marino, and F. Marin. Two-dimensional quantum motion of a levitated nanosphere. *Physical Review Research*, 4(3):033051, July 2022.

[59] Lorenzo Dania, Oscar Schmitt Kremer, Johannes Piotrowski, Davide Candoli, Jayadev Vijayan, Oriol Romero-Isart, Carlos Gonzalez-Ballestero, Lukas Novotny, and Martin Frimmer. High-purity quantum optomechanics at room temperature. *Nature Physics*, 21(10):1603–1608, August 2025.

[60] Lorenzo Magrini, Philipp Rosenzweig, Constanze Bach, Andreas Deutschmann-Olek, Sebastian G. Hofer, Sungkun Hong, Nikolai Kiesel, Andreas Kugi, and Markus Aspelmeyer. Real-time optimal quantum control of mechanical motion at room temperature. *Nature*, 595(7867):373–377, July 2021.

[61] Felix Tebbenjohanns, M. Luisa Mattana, Massimiliano Rossi, Martin Frimmer, and Lukas Novotny. Quantum control of a nanoparticle optically levitated in cryogenic free space. *Nature*, 595(7867):378–382, July 2021.

[62] Mitsuyoshi Kamba, Naoki Hara, and Kiyotaka Aikawa. Quantum squeezing of a levitated nanomechanical oscillator. *Science*, 389(6766):1225–1228, September 2025.

[63] Stephan Troyer, Florian Fechtel, Lorenz Hummer, Henning Rudolph, Benjamin A. Stickler, Uroš Delić, and Markus Arndt. Quantum ground-state cooling of two librational modes of a nanorotor. *Nature Physics*, 22:584—-590, April 2026.

[64] Tobias Westphal, Hans Hepach, Jeremias Pfaff, and Markus Aspelmeyer. Measurement of gravitational coupling between millimetre-sized masses. *Nature*, 591(7849):225–228, March 2021.

[65] J. G. Lee, E. G. Adelberger, T. S. Cook, S. M. Fleischer, and B. R. Heckel. New test of the gravitational $1/r^2$ law at separations down to 52 μm. *Physical Review Letters*, 124(10):101101, March 2020.

[66] Sougato Bose, Anupam Mazumdar, Gavin W. Morley, Hendrik Ulbricht, Marko Toroš, Mauro Paternostro, Andrew A. Geraci, Peter F. Barker, M. S. Kim, and Gerard Milburn. Spin entanglement witness for quantum gravity. *Physical Review Letters*, 119(24):240401, December 2017.

[67] C. Marletto and V. Vedral. Gravitationally induced entanglement between two massive particles is sufficient evidence of quantum effects in gravity. *Physical Review Letters*, 119(24):240402, December 2017.

[68] H. Pino, J. Prat-Camps, K. Sinha, B. Prasanna Venkatesh, and O. Romero-Isart. On-chip quantum interference of a superconducting microsphere. *Quantum Science and Technology*, 3(2):025001, January 2018.

[69] Ludovico Lami, Julen S. Pedernales, and Martin B. Plenio. Testing the quantumness of gravity without entanglement. *Phys. Rev. X*, 14:021022, May 2024.

[70] Kai Li, Yi Ling, and Zhangping Yu. Gravity induced entanglement of multiple massive particles with large spin. *Classical and Quantum Gravity*, 42(22):225003, November 2025.

[71] Richard Howl, Roger Penrose, and Ivette Fuentes. Exploring the unification of quantum theory and general relativity with a bose–einstein condensate. *New Journal of Physics*, 21(4):043047, April 2019.

[72] Richard Howl, Vlatko Vedral, Devang Naik, Marios Christodoulou, Carlo Rovelli, and Aditya Iyer. Non-gaussianity as a signature of a quantum theory of gravity. *PRX Quantum*, 2(1):010325, February 2021.

[73] Jonathan Oppenheim, Carlo Sparaciari, Barbara Šoda, and Zachary Weller-Davies. Gravitationally induced decoherence vs space-time diffusion: testing the quantum nature of gravity. *Nature Communications*, 14(1):7910, December 2023.

[74] Julen S. Pedernales and Martin B. Plenio. On the origin of force sensitivity in tests of quantum gravity with delocalised mechanical systems. *Contemporary Physics*, 64(2):147–163, 2023.

[75] Trinidad B. Lantaño, Luciano Petruzziello, Susana F. Huelga, and Martin B. Plenio. Angular momentum entanglement mediated by general relativistic frame dragging. *Quantum*, 10:2042, 2025.

[76] Rainer Kaltenbaek, Gerald Hechenblaikner, Nikolai Kiesel, Oriol Romero-Isart, Keith C. Schwab, Ulrich Johann, and Markus Aspelmeyer. Macroscopic quantum resonators (maqro): Testing quantum and gravitational physics with massive mechanical resonators. *Experimental Astronomy*, 34(2):123–164, March 2012.

[77] Yuka Shiomatsu, Youka Kaku, Akira Matsumura, and Tomohiro Fujita. Boosting gravity-induced entanglement through parametric resonance. *Phys. Rev. D*, 113:124002, June 2026.

[78] Luciano Petruzziello, Trinidad B. Lantaño Pinto, Susana F. Huelga, and Martin B. Plenio. Experimental witness for general relativistic effects in quantum mechanics. *International Journal of Modern Physics D*, 34(16):2544026, October 2025.

[79] J. Schmöle, M. Dragosits, H. Hepach, and M. Aspelmeyer. A micromechanical proof-of-principle experiment for measuring the gravitational force of milligram masses. *Classical and Quantum Gravity*, 33:125031, 2016.

[80] Thomas W. van de Kamp, Ryan J. Marshman, Sougato Bose, and Anupam Mazumdar. Quantum Gravity Witness via Entanglement of Masses: Casimir Screening. *Physical Review A*, 102(6):062807, December 2020.

[81] Marit O. E. Steiner, Julen S. Pedernales, and Martin B. Plenio. The nuclear einstein-de haas and barnett effect with levitated nanoparticles. In preparation, 2026.

[82] T. Delord, P. Huillery, L. Schwab, L. Nicolas, L. Lecordier, and G. Hétet. Ramsey interferences and spin echoes from electron spins inside a levitating macroscopic particle. *Physical Review Letters*, 121(5):053602, July 2018.

[83] Dmitry S. Bykov, Pau Mestres, Lorenzo Dania, Lisa Schmöger, and Tracy E. Northup. Direct loading of nanoparticles under high vacuum into a paul trap for levitodynamical experiments. *Applied Physics Letters*, 115(3), July 2019.

[84] Stefan Lindner, Paul Juschitz, Jakob Rieser, Yaakov Y. Fein, Maxime Debiossac, Mario A. Ciampini, Markus Aspelmeyer, and Nikolai Kiesel. Hollow-core fiber loading of nanoparticles into ultra-high vacuum. *Applied Physics Letters*, 124(14), April 2024.

[85] Jan Gieseler, Bradley Deutsch, Romain Quidant, and Lukas Novotny. Subkelvin parametric feedback cooling of a laser-trapped nanoparticle. *Physical Review Letters*, 109(10):103603, September 2012.

[86] Peng Ju, Yuanbin Jin, Kunhong Shen, Yao Duan, Zhujing Xu, Xingyu Gao, Xingjie Ni, and Tongcang Li. Near-field ghz rotation and sensing with an optically levitated nanodumbbell. *Nano Letters*, 23(22):10157–10163, November 2023.

[87] J. Gieseler, A. Kabcenell, E. Rosenfeld, J. D. Schaefer, A. Safira, M. J. A. Schuetz, C. Gonzalez-Ballestero, C. C. Rusconi, O. Romero-Isart, and M. D. Lukin. Single-spin magnetomechanics with levitated micromagnets. *Phys. Rev. Lett.*, 124:163604, April 2020.

[88] A. Vinante, P. Falferi, G. Gasbarri, A. Setter, C. Timberlake, and H. Ulbricht. Ultralow mechanical damping with meissner-levitated ferromagnetic microparticles. *Phys. Rev. Appl.*, 13:064027, June 2020.

[89] Yuanbin Jin, Kunhong Shen, Peng Ju, Xingyu Gao, Chong Zu, Alejandro J. Grine, and Tongcang Li. Quantum control and berry phase of electron spins in rotating levitated diamonds in high vacuum. *Nature Communications*, 15(1), June 2024.

[90] J. Millen, T. Deesuwan, P. Barker, and J. Anders. Nanoscale temperature measurements using non-equilibrium brownian dynamics of a levitated nanosphere. *Nature Nanotechnology*, 9(6):425–429, May 2014.

[91] Loïc Rondin, Jan Gieseler, Francesco Ricci, Romain Quidant, Christoph Dellago, and Lukas Novotny. Direct measurement of kramers turnover with a levitated nanoparticle. *Nature Nanotechnology*, 12(12):1130–1133, October 2017.

[92] Jan Gieseler and James Millen. Levitated nanoparticles for microscopic thermodynamics—a review. *Entropy*, 20(5):326, April 2018.

[93] Yu Zheng, Lyu-Hang Liu, Xiang-Dong Chen, Guang-Can Guo, and Fang-Wen Sun. Arbitrary nonequilibrium steady-state construction with a levitated nanoparticle. *Physical Review Research*, 5(3):033101, August 2023.

[94] Erik Hebestreit, Ren'e Reimann, Martin Frimmer, and Lukas Novotny. Measuring the internal temperature of a levitated nanoparticle in high vacuum. *Physical Review A*, 97(4):043803, April 2018.

[95] Jonghoon Ahn, Zhujing Xu, Jaehoon Bang, Yu-Hao Deng, Thai M. Hoang, Qinkai Han, Ren-Min Ma, and Tongcang Li. Optically levitated nanodumbbell torsion balance and ghz nanomechanical rotor. *Physical Review Letters*, 121(3):033603, July 2018.

[96] C. D. Brown, Y. Wang, M. Namazi, G. I. Harris, M. T. Uysal, and J. G. E. Harris. Superfluid helium drops levitated in high vacuum. *Physical Review Letters*, 130:216001, 2023.

[97] Francesco Ricci, Marc T. Cuairan, Andreas W. Schell, Erik Hebestreit, Raúl A. Rica, Nadine Meyer, and Romain Quidant. A chemical nanoreactor based on a levitated nanoparticle in vacuum. *ACS Nano*, 16(6):8677–8683, May 2022.

[98] Gambhir Ranjit, Mark Cunningham, Kirsten Casey, and Andrew A. Geraci. Zeptonewton force sensing with nanospheres in an optical lattice. *Physical Review A*, 93(5):053801, May 2016.

[99] Chris Timberlake, Giulio Gasbarri, Andrea Vinante, Ashley Setter, and Hendrik Ulbricht. Acceleration sensing with magnetically levitated oscillators above a superconductor. *Applied Physics Letters*, 115(22), November 2019.

[100] Joel K. Jose, Andrea Marchese, Marion Cromb, Hendrik Ulbricht, Andrejs Cebers, Ping Koy Lam, Tao Wang, and Andrea Vinante. Cryogenic pressure sensing with an ultrafast meissner-levitated microrotor, 2025. arXiv:2509.24964 [quant-ph].

[101] David C. Moore, Alexander D. Rider, and Giorgio Gratta. Search for millicharged particles using optically levitated microspheres. *Physical Review Letters*, 113(25):251801, December 2014.

[102] Alexander D. Rider, David C. Moore, Charles P. Blakemore, Maxime Louis, Marie Lu, and Giorgio Gratta. Search for Screened Interactions Associated with Dark Energy below the 100 μm Length Scale. *Physical Review Letters*, 117(10):101101, August 2016.

[103] Fernando Monteiro, Wenqiang Li, Gadi Afek, Chang-ling Li, Michael Mossman, and David C. Moore. Force and acceleration sensing with optically levitated nanogram masses at microkelvin temperatures. *Physical Review A*, 101(5):053835, May 2020.

[104] Yu-Han Tseng, T. W. Penny, Benjamin Siegel, Jiaxiang Wang, and David C. Moore. Search for dark matter scattering from optically levitated nanoparticles. *PRX Quantum*, 6(4), December 2025.

[105] Wolfgang Paul and Helmut Steinwedel. Notizen: Ein neues massenspektrometer ohne magnetfeld. *Zeitschrift für Naturforschung A*, 8(7):448–450, July 1953.

[106] Dirk Nolting, Robert Malek, and Alexander Makarov. Ion traps in modern mass spectrometry. *Mass Spectrometry Reviews*, 38(2):150–168, October 2017.

[107] Colin D. Bruzewicz, John Chiaverini, Robert McConnell, and Jeremy M. Sage. Trapped-ion quantum computing: Progress and challenges. *Applied Physics Reviews*, 6(2), May 2019.

[108] D. Leibfried, R. Blatt, C. Monroe, and D. Wineland. Quantum dynamics of single trapped ions. *Reviews of Modern Physics*, 75(1):281–324, March 2003.

[109] A. Ashkin and J. M. Dziedzic. Optical trapping and manipulation of viruses and bacteria. *Science*, 235(4795):1517–1520, March 1987.

[110] Steven Chu, J. E. Bjorkholm, A. Ashkin, and A. Cable. Experimental observation of optically trapped atoms. *Physical Review Letters*, 57(3):314–317, July 1986.

[111] P. F. Barker. Doppler cooling a microsphere. *Physical Review Letters*, 105(7):073002, August 2010.

[112] O. Romero-Isart, A. C. Pflanzer, M. L. Juan, R. Quidant, N. Kiesel, M. Aspelmeyer, and J. I. Cirac. Optically levitating dielectrics in the quantum regime: Theory and protocols. *Physical Review A*, 83(1):013803, January 2011.

[113] Lukas Novotny and Bert Hecht. *Principles of Nano-Optics*. Cambridge University Press, September 2012.

[114] A. T. M. A. Rahman, A. C. Frangeskou, M. S. Kim, S. Bose, G. W. Morley, and P. F. Barker. Burning and graphitization of optically levitated nanodiamonds in vacuum. *Scientific Reports*, 6(1), February 2016.

[115] William M. Haynes, editor. *CRC Handbook of Chemistry and Physics*. CRC Press, June 2014.

[116] Tomoya Naito, Tomoaki Suzuki, and Yasuhiro Ikezoe. Diamagnetic levitation of water realized with a simple device consisting of ordinary permanent magnets. *Applied Physics Letters*, 125(26), December 2024.

[117] F. London and H. London. The electromagnetic equations of the supraconductor. *Proceedings of the Royal Society of London. Series A - Mathematical and Physical Sciences*, 149(866):71–88, March 1935.

[118] Andrea Vinante, Chris Timberlake, and Hendrik Ulbricht. Levitated micromagnets in superconducting traps: A new platform for tabletop fundamental physics experiments. *Entropy*, 24(11):1642, November 2022.

[119] J. Gieseler, A. Kabcenell, E. Rosenfeld, J. D. Schaefer, A. Safira, M. J. A. Schuetz, C. Gonzalez-Ballestero, C. C. Rusconi, O. Romero-Isart, and M. D. Lukin. Single-spin magnetomechanics with levitated micromagnets. *Physical Review Letters*, 124(16):163604, April 2020.

[120] A. Vinante, P. Falferi, G. Gasbarri, A. Setter, C. Timberlake, and H. Ulbricht. Ultralow mechanical damping with meissner-levitated ferromagnetic microparticles. *Physical Review Applied*, 13(6):064027, June 2020.

[121] Tao Wang, Sean Lourette, Sean R. O'Kelley, Metin Kayci, Y.B. Band, Derek F. Jackson Kimball, Alexander O. Sushkov, and Dmitry Budker. Dynamics of a ferromagnetic particle levitated over a superconductor. *Physical Review Applied*, 11(4):044041, April 2019.

[122] Charles W. Lewandowski, William R. Babbitt, and Brian D'Urso. Comparison of magneto-gravitational and optical trapping for levitated optomechanics. In Kishan Dholakia and Gabriel C. Spalding, editors, *Optical Trapping and Optical Micromanipulation XVI*, page 48. SPIE, September 2019.

[123] J. A. Zielińska, F. van der Laan, A. Norrman, R. Reimann, M. Frimmer, and L. Novotny. Long-axis spinning of an optically levitated particle: A levitated spinning top. *Physical Review Letters*, 132(25):253601, June 2024.

[124] David Hempston, Jamie Vovrosh, Marko Toroš, George Winstone, Muddassar Rashid, and Hendrik Ulbricht. Force sensing with an optically levitated charged nanoparticle. *Applied Physics Letters*, 111(13), September 2017.

[125] Hendrik Ulbricht. *Testing Fundamental Physics by Using Levitated Mechanical Systems*, pages 303–332. Springer International Publishing, 2021.

[126] Peiran Yin, Rui Li, Chengjiang Yin, Xiangyu Xu, Xiang Bian, Han Xie, Chang-Kui Duan, Pu Huang, Jian-hua He, and Jiangfeng Du. Experiments with levitated force sensor challenge theories of dark energy. *Nature Physics*, 18(10):1181–1185, August 2022.

[127] Dorian W. P. Amaral, Tim M. Fuchs, Hendrik Ulbricht, and Christopher D. Tunnell. Magnetic levitation as a new probe of non-newtonian gravity. *Physical Review D*, 113(2), January 2026.

[128] Nancy Aggarwal, Odylio D. Aguiar, Diego Blas, Andreas Bauswein, Giancarlo Cella, Sebastian Clesse, Adrian Michael Cruise, Valerie Domcke, Sebastian Ellis, Daniel G. Figueroa, Gabriele Franciolini, Camilo García-Cely, Andrew Geraci, Maxim Goryachev, Hartmut Grote, Mark Hindmarsh, Asuka Ito, Joachim Kopp, Sung Mook Lee, Killian Martineau, Jamie McDonald, Francesco Muia, Nikhil Mukund, David Ottaway, Marco Peloso, Krisztian Peters, Fernando Quevedo, Angelo Ricciardone, Andreas Ringwald, Jessica Steinlechner, Sebastian Steinlechner, Sichun Sun, Carlos Tamarit, Michael E. Tobar, Francisco Torrenti, Caner Ünal, and Graham White. Challenges and opportunities of gravitational-wave searches above 10 khz. *Living Reviews in Relativity*, 28(1), November 2025.

[129] Eva Kilian, Markus Rademacher, Jonathan M. H. Gosling, Julian H. Iacoponi, Fiona Alder, Marko Toroš, Antonio Pontin, Chamkaur Ghag, Sougato Bose, Tania S. Monteiro, and P. F. Barker. Dark matter searches with levitated sensors. *AVS Quantum Science*, 6(3), September 2024.

[130] M. Rossi, A. Militaru, N. Carlon Zambon, A. Riera-Campeny, O. Romero-Isart, M. Frimmer, and L. Novotny. Quantum delocalization of a levitated nanoparticle. *Physical Review Letters*, 135(8), August 2025.

[131] Maximilian A. Schlosshauer. *Decoherence*. Springer Berlin Heidelberg, November 2010.

[132] Oriol Romero-Isart. Quantum superposition of massive objects and collapse models. *Physical Review A*, 84(5):052121, November 2011.

[133] A. O. Caldeira and A. J. Leggett. Quantum tunnelling in a dissipative system. *Annals of Physics*, 149(2):374–456, September 1983.

[134] Heinz-Peter Breuer and Francesco Petruccione. *The Theory of Open Quantum Systems*. Oxford University Press, New York, 2002.

[135] Bassano Vacchini and Klaus Hornberger. Quantum linear boltzmann equation. *Physics Reports*, 478(4-6):71–120, July 2009.

[136] Markus Arndt and Klaus Hornberger. Testing the limits of quantum mechanical superpositions. *Nature Physics*, 10(4):271–277, April 2014.

[137] Björn Schrinski, Stefan Nimmrichter, and Klaus Hornberger. Quantum-classical hypothesis tests in macroscopic matter-wave interferometry. *Physical Review Research*, 2(3):033034, July 2020.

[138] Sebastian Pedalino, Bruno E. Ramírez-Galindo, Richard Ferstl, Klaus Hornberger, Markus Arndt, and Stefan Gerlich. Probing quantum mechanics with nanoparticle matter-wave interferometry. *Nature*, 649(8098):866–870, January 2026.

[139] G. C. Ghirardi, A. Rimini, and T. Weber. Unified dynamics for microscopic and macroscopic systems. *Physical Review D*, 34(2):470–491, July 1986.

[140] L. Diósi. A universal master equation for the gravitational violation of quantum mechanics. *Physics Letters A*, 120(8):377–381, March 1987.

[141] Roger Penrose. On gravity's role in quantum state reduction. *General Relativity and Gravitation*, 28(5):581–600, May 1996.

[142] Gian Carlo Ghirardi, Philip Pearle, and Alberto Rimini. Markov processes in hilbert space and continuous spontaneous localization of systems of identical particles. *Physical Review A*, 42(1):78–89, July 1990.

[143] Philip Pearle. Combining stochastic dynamical state-vector reduction with spontaneous localization. *Physical Review A*, 39(5):2277–2289, March 1989.

[144] Angelo Bassi and GianCarlo Ghirardi. Dynamical reduction models. *Physics Reports*, 379(5-6):257–426, June 2003.

[145] Brian Collett and Philip Pearle. Wavefunction collapse and random walk. *Foundations of Physics*, 33(10):1495–1541, 2003.

[146] Stefan Nimmrichter, Klaus Hornberger, and Klemens Hammerer. Optomechanical sensing of spontaneous wave-function collapse. *Physical Review Letters*, 113(2):020405, July 2014.

[147] Stephen L Adler. Lower and upper bounds on CSL parameters from latent image formation and IGMtextasciitildeheating. *Journal of Physics A Mathematical and Theoretical*, 40(44):13501–13501, October 2007.

[148] A. Vinante, M. Bahrami, A. Bassi, O. Usenko, G. Wijts, and T. H. Oosterkamp. Upper bounds on spontaneous wave-function collapse models using millikelvin-cooled nanocantilevers. *Physical Review Letters*, 116(9):090402, March 2016.

[149] Di Zheng, Yingchun Leng, Xi Kong, Rui Li, Zizhe Wang, Xiaohui Luo, Jie Zhao, Chang-Kui Duan, Pu Huang, Jiangfeng Du, Matteo Carlesso, and Angelo Bassi. Room temperature test of the continuous spontaneous localization model using a levitated micro-oscillator. *Physical Review Research*, 2(1):013057, January 2020.

[150] Marko Torovs, Giulio Gasbarri, and Angelo Bassi. Colored and dissipative continuous spontaneous localization model and bounds from matter-wave interferometry. *Physics Letters A*, 381(47):3921–3927, December 2017.

[151] Yaakov Y. Fein, Philipp Geyer, Patrick Zwick, Filip Kialka, Sebastian Pedalino, Marcel Mayor, Stefan Gerlich, and Markus Arndt. Quantum superposition of molecules beyond 25 kDa. *Nature Physics*, 15(12):1242–1245, September 2019.

[152] Andrea Smirne and Angelo Bassi. Dissipative continuous spontaneous localization (csl) model. *Scientific Reports*, 5(1), August 2015.

[153] A. Vinante, R. Mezzena, P. Falferi, M. Carlesso, and A. Bassi. Improved noninterferometric test of collapse models using ultracold cantilevers. *Physical Review Letters*, 119(11):110401, September 2017.

[154] Angelo Bassi, Mauro Dorato, and Hendrik Ulbricht. Collapse models: A theoretical, experimental and philosophical review. *Entropy*, 25(4):645, April 2023.

[155] Matteo Carlesso, Mauro Paternostro, Hendrik Ulbricht, Andrea Vinante, and Angelo Bassi. Non-interferometric test of the continuous spontaneous localization model based on rotational optomechanics. *New Journal of Physics*, 20(8):083022, August 2018.

[156] Matteo Carlesso, Angelo Bassi, Paolo Falferi, and Andrea Vinante. Experimental bounds on collapse models from gravitational wave detectors. *Physical Review D*, 94(12):124036, December 2016.

[157] Kristian Piscicchia, Angelo Bassi, Catalina Curceanu, Raffaele Grande, Sandro Donadi, Beatrix Hiesmayr, and Andreas Pichler. Csl collapse model mapped with the spontaneous radiation. *Entropy*, 19(7):319, June 2017.

[158] Sandro Donadi, Kristian Piscicchia, Raffaele Del Grande, Catalina Curceanu, Matthias Laubenstein, and Angelo Bassi. Novel csl bounds from the noise-induced radiation emission from atoms. *The European Physical Journal C*, 81(8):773, August 2021.

[159] L. Diósi. Models for universal reduction of macroscopic quantum fluctuations. *Physical Review A*, 40(3):1165–1174, August 1989.

[160] Philip Pearle. Ways to describe dynamical state-vector reduction. *Physical Review A*, 48(2):913–923, August 1993.

[161] Stephen L Adler and Angelo Bassi. Collapse models with non-white noises: Ii. particle-density coupled noises. *Journal of Physics A: Mathematical and Theoretical*, 41(39):395308, September 2008.

[162] G. 't Hoofd and M. Veltman. *One-loop divergencies in the theory of gravitation*, pages 3–28. WORLD SCIENTIFIC, May 1993.

[163] Marc H. Goroff and Augusto Sagnotti. The ultraviolet behavior of einstein gravity. *Nuclear Physics B*, 266(3-4):709–736, March 1986.

[164] Dean Rickles and Cécile M. DeWitt. *The Role of Gravitation in Physics: Reportfrom the 1957 Chapel Hill Conference*. Max-Planck-Gesellschaft zur Förderung der Wissenschaften, 2011.

[165] D. Kafri, J. M. Taylor, and G. J. Milburn. A classical channel model for gravitational decoherence. *New Journal of Physics*, 16(6):065020, June 2014.

[166] N. D. Birrell and P. C. W. Davies. *Quantum Fields in Curved Space*. Cambridge University Press, February 1982.

[167] Claus Lämmerzahl Domenico J. W. Giulini, Claus Kiefer. *Quantum Gravity: From Theory to Experimental Search*. Springer Berlin Heidelberg, 2003.

[168] Michael B. Green, John H. Schwarz, and Edward Witten. *Superstring Theory: 25th Anniversary Edition*. Cambridge University Press, July 2012.

[169] Carlo Rovelli. *Quantum Gravity*. Cambridge University Press, November 2004.

[170] Ryszard Horodecki, Paweł Horodecki, Michał Horodecki, and Karol Horodecki. Quantum entanglement. *Reviews of Modern Physics*, 81(2):865–942, June 2009.

[171] Chiara Marletto and Vlatko Vedral. When can gravity path-entangle two spatially superposed masses? *Physical Review D*, 98(4):046001, August 2018.

[172] Thomas D. Galley, Flaminia Giacomini, and John H. Selby. A no-go theorem on the nature of the gravitational field beyond quantum theory. *Quantum*, 6:779, August 2022.

[173] Soham Pal, Priya Batra, Tanjung Krisnanda, Tomasz Paterek, and T. S. Mahesh. Experimental localisation of quantum entanglement through monitored classical mediator. *Quantum*, 5:478, June 2021.

[174] Chiara Marletto and Vlatko Vedral. Witnessing nonclassicality beyond quantum theory. *Physical Review D*, 102(8):086012, October 2020.

[175] Jonathan Oppenheim. A postquantum theory of classical gravity? *Physical Review X*, 13(4):041040, December 2023.

[176] S Carlip. Is quantum gravity necessary? *Classical and Quantum Gravity*, 25(15):154010, July 2008.

[177] David Trillo and Miguel Navascués. Diósi-penrose model of classical gravity predicts gravitationally induced entanglement. *Physical Review D*, 111(12):l121101, June 2025.

[178] Michael J W Hall and Marcel Reginatto. On two recent proposals for witnessing nonclassical gravity. *Journal of Physics A: Mathematical and Theoretical*, 51(8):085303, January 2018.

[179] C. Anastopoulos and B. L. Hu. Probing a gravitational cat state. *Classical and Quantum Gravity*, 32(16):165022, July 2015.

[180] Charis Anastopoulos, Michalis Lagouvardos, and Konstantina Savvidou. Gravitational effects in macroscopic quantum systems: a first-principles analysis. *Classical and Quantum Gravity*, 38(15):155012, July 2021.

[181] Joseph Aziz and Richard Howl. Classical theories of gravity produce entanglement. *Nature*, 646(8086):813–817, October 2025.

[182] Eduardo Martín-Martínez and T. Rick Perche. What gravity mediated entanglement can really tell us about quantum gravity. *Physical Review D*, 108(10):l101702, November 2023.

[183] Vasileios Fragkos, Michael Kopp, and Igor Pikovski. On inference of quantization from gravitationally induced entanglement. *AVS Quantum Science*, 4(4), November 2022.

[184] Daniel Carney. Newton, entanglement, and the graviton. *Physical Review D*, 105(2):024029, January 2022.

[185] John F. Donoghue. General relativity as an effective field theory: The leading quantum corrections. *Physical Review D*, 50(6):3874–3888, September 1994.

[186] Freeman Dyson. Is a graviton detectable? *International Journal of Modern Physics A*, 28(25):1330041, October 2013.

[187] Germain Tobar, Sreenath K. Manikandan, Thomas Beitel, and Igor Pikovski. Detecting single gravitons with quantum sensing. *Nature Communications*, 15(1), August 2024.

[188] Daniel Carney, Valerie Domcke, and Nicholas L. Rodd. Graviton detection and the quantization of gravity. *Physical Review D*, 109(4):044009, February 2024.

[189] Daniel Carney. Comments on graviton detection, 2024. arXiv:2408.00094 [quant-ph].

[190] Giovanni Spaventa, Ludovico Lami, and Martin B. Plenio. On tests of the quantum nature of gravitational interactions in presence of non-linear corrections to quantum mechanics. *Quantum*, 7:1157, October 2023.

[191] G. G. Scott. Review of gyromagnetic ratio experiments. *Reviews of Modern Physics*, 34(1):102–109, January 1962.

[192] Viktor Ya Frenkel'. On the history of the einstein–de haas effect. *Soviet Physics Uspekhi*, 22(7):580–587, July 1979.

[193] Felix Ahrens and Andrea Vinante. Observation of gyroscopic coupling in a nonspinning levitated ferromagnet. *Physical Review Letters*, 136(14), April 2026.

[194] Andrea Vinante, Chris Timberlake, Dmitry Budker, Derek F. Jackson Kimball, Alexander O. Sushkov, and Hendrik Ulbricht. Surpassing the energy resolution limit with ferromagnetic torque sensors. *Physical Review Letters*, 127(7):070801, August 2021.

[195] K. R. Fast, J. E. Losby, G. Hajisalem, P. E. Barclay, and M. R. Freeman. Einstein–de haas torque as a discrete spectroscopic probe allows nanomechanical measurement of a magnetic resonance. *Physical Review B*, 109(6):064404, February 2024.

[196] S. J. Barnett. Magnetization and rotation. *American Journal of Physics*, 16(3):140–147, March 1948.

[197] Mamoru Matsuo, Jun'ichi Ieda, Kazuya Harii, Eiji Saitoh, and Sadamichi Maekawa. Mechanical generation of spin current by spin-rotation coupling. *Physical Review B*, 87(18):180402, May 2013.

[198] Atsufumi Hirohata, Yuji Baba, Benedict A. Murphy, Benny Ng, Yunqi Yao, Kazuki Nagao, and Jun-young Kim. Magneto-optical detection of spin accumulation under the influence of mechanical rotation. *Scientific Reports*, 8(1), January 2018.

[199] H Brunner, R. H. Fritsch, and K. H. Hausser. Notizen: Cross polarization in electron nuclear double resonance by satisfying the hartmann-hahn condition. *Zeitschrift für Naturforschung A*, 42(12):1456–1457, December 1987.

[200] A. Henstra, P. Dirksen, J. Schmidt, and W. Th. Wenckebach. Nuclear spin orientation via electron spin locking (novel). *Journal of Magnetic Resonance (1969)*, 77(2):389–393, April 1988.

[201] A. Henstra and W.Th. Wenckebach. Dynamic nuclear polarisation via the integrated solid effect i: theory. *Molecular Physics*, 112(13):1761–1772, November 2013.

[202] Ilai Schwartz, Jochen Scheuer, Benedikt Tratzmiller, Samuel Müller, Qiong Chen, Ish Dhand, Zhen-Yu Wang, Christoph Müller, Boris Naydenov, Fedor Jelezko, and Martin B. Plenio. Robust optical polarization of nuclear spin baths using hamiltonian engineering of nitrogen-vacancy center quantum dynamics. *Science Advances*, 4(8):eaat8978, 2018.

[203] A. J. Van Strien and J. Schmidt. An epr study of the triplet state of pentacene by electron spin-echo techniques and laser flash excitation. *Chemical Physics Letters*, 70(3):513–517, March 1980.

[204] Koichi Komatsu, Yasujiro Murata, Nobuyuki Sugita, Ken'ichi Takeuchi, and Terence S.M. Wan. Use of naphthalene as a solvent for selective formation of the 11 diels-alder adduct of c60 with anthracene. *Tetrahedron Letters*, 34(52):8473–8476, January 1993.

[205] Zerong Wang. *Comprehensive Organic Name Reactions and Reagents*. John Wiley & Sons, Inc, 2010.

[206] Smruti Rekha Dash, Ritwik Sarkar, and Santanu Bhattacharyya. Gel casting of hydroxyapatite with naphthalene as pore former. *Ceramics International*, 41(3):3775–3790, April 2015.

[207] Tim R. Eichhorn. *Dynamic Nuclear Polarization with Paramagnetic Centers Created by Photo-Excitation*. PhD thesis, École Polytechnique Fédérale de Lausanne, 2014.

[208] D. W. J. Cruickshank. A detailed refinement of the crystal and molecular structure of naphthalene. *Acta Crystallographica*, 10(8):504–508, August 1957.

[209] S. Bhagavantam. The magnetic anisotropy of naphthalene crystals. *Proceedings of the Royal Society of London. Series A*, 124(795):545–554, July 1929.

[210] Jacek W. Hennel and Jacek Klinowski. Magic-angle spinning a historical perspective. In *Topics in Current Chemistry*, pages 1–14. Springer Berlin Heidelberg, October 2004.

[211] Yoshihiko Arita, Michael Mazilu, and Kishan Dholakia. Laser-induced rotation and cooling of a trapped microgyroscope in vacuum. *Nature Communications*, 4(1):2374, August 2013.

[212] Fernando Monteiro, Sumita Ghosh, Elizabeth C. van Assendelft, and David C. Moore. Optical rotation of levitated spheres in high vacuum. *Phys. Rev. A*, 97:051802, May 2018.

[213] Yuanbin Jin, Jiangwei Yan, Shah Jee Rahman, Jie Li, Xudong Yu, and Jing Zhang. 6 ghz hyperfast rotation of an optically levitated nanoparticle in vacuum. *Photon. Res.*, 9(7):1344–1350, July 2021.

[214] Keita Sakamoto, Tomoyuki Hamachi, Katsuki Miyokawa, Kenichiro Tateishi, Tomohiro Uesaka, Yuki Kurashige, and Nobuhiro Yanai. Polarizing agents beyond pentacene for efficient triplet dynamic nuclear polarization in glass matrices. *Proceedings of the National Academy of Sciences*, 120(44):e2307926120, 2023.

[215] Vadim E. Zorin, Steven P. Brown, and Paul Hodgkinson. Origins of linewidth in h1 magic-angle spinning NMR. *The Journal of Chemical Physics*, 125(14):144508, October 2006.

[216] Jette Oddershede and Sine Larsen. Charge density study of naphthalene based on x-ray diffraction data at four different temperatures and theoretical calculations. *The Journal of Physical Chemistry A*, 108(6):1057–1063, January 2004.

[217] Lea Marti, Nergiz Şahin Solmaz, Michal Kern, Anh Chu, Reza Farsi, Philipp Hengel, Jialiang Gao, Nicholas Alaniva, Michael A. Urban, Ronny Gunzenhauser, Alexander Däpp, Daniel Klose, Jens Anders, Giovanni Boero, Lukas Novotny, Martin Frimmer, and Alexander B. Barnes. Towards optical mas magnetic resonance using optical traps. *Journal of Magnetic Resonance Open*, 18:100145, 2024.

[218] Yusuke Nishiyama, Guangjin Hou, Vipin Agarwal, Yongchao Su, and Ayyalusamy Ramamoorthy. Ultrafast magic angle spinning solid-state nmr spectroscopy advances in methodology and applications. *Chemical Reviews*, 123(3):918–988, 2023.

[219] Henning Rudolph, Jonas Schäfer, Benjamin A. Stickler, and Klaus Hornberger. Theory of nanoparticle cooling by elliptic coherent scattering. *Physical Review A*, 103(4):043514, April 2021.

[220] Marcel Schuck, Daniel Steinert, Thomas Nussbaumer, and Johann W. Kolar. Ultrafast rotation of magnetically levitated macroscopic steel spheres. *Science Advances*, 4(1):e170151, January 2018.

[221] P. S. Bassi, N. K. Sharma, and M. K. Sharma. Mode of solidification and strength properties(II). naphthalene-benzil binary system. *Crystal Research and Technology*, 18(9):1191–1197, 1983.

[222] Craig F. Bohren and Donald R. Huffman. *Absorption and Scattering of Light by Small Particles*. Wiley, April 1998.

[223] James Bateman, Stefan Nimmrichter, Klaus Hornberger, and Hendrik Ulbricht. Near-field interferometry of a free-falling nanoparticle from a point-like source. *Nature Communications*, 5(1):4788, September 2014.

[224] R. D. Chirico, S. E. Knipmeyer, and W. V. Steele. Heat capacities, enthalpy increments, and derived thermodynamic functions for naphthalene between the temperatures 5k and 440k. *The Journal of Chemical Thermodynamics*, 34(11):1873–1884, November 2002.

[225] Markus Schwoerer and Hans Christoph Wolf. *Organic Molecular Solids*. Wiley-VCH, Berlin, 2006. page 145.

[226] H. Port and D. Rund. High resolution excitation spectroscopy on triplet excitons in organic molecular crystals comparison of naphthalene and anthracene. *Journal of Molecular Structure*, 45:455–464, January 1978.

[227] Daniel Faltermeier, Bruno Gompf, Martin Dressel, Ashutosh K. Tripathi, and Jens Pflaum. Optical properties of pentacene thin films and single crystals. *Physical Review B*, 74(12):125416, September 2006.

[228] K. Tennakone and M. G. C. Peiris. Sublimation of moth balls. *American Journal of Physics*, 46(4):418–419, April 1978.

[229] Květoslav Růžička, Michal Fulem, and Vlastimil Růžička. Recommended vapor pressure of solid naphthalene. *Journal of Chemical & Engineering Data*, 50(6):1956–1970, 2005.

[230] F. Cosco, J. S. Pedernales, and M. B. Plenio. Enhanced force sensitivity and entanglement in periodically driven optomechanics. *Physical Review A*, 103(6):l061501, June 2021.

[231] T. Weiss, M. Roda-Llordes, E. Torrontegui, M. Aspelmeyer, and O. Romero-Isart. Large quantum delocalization of a levitated nanoparticle using optimal control applications for force sensing and entangling via weak forces. *Phys. Rev. Lett.*, 127(2):023601, July 2021.

[232] Zhang qi Yin, Tongcang Li, Xiang Zhang, and L. M. Duan. Large quantum superpositions of a levitated nanodiamond through spin-optomechanical coupling. *Physical Review A*, 88(3):033614, September 2013.

[233] B. D. Wood, S. Bose, and G. W. Morley. Spin dynamical decoupling for generating macroscopic superpositions of a free-falling nanodiamond. *Physical Review A*, 105:012824, 2021.

[234] Michael Victor Berry. The levitron an adiabatic trap for spins. *Proceedings of the Royal Society of London. Series A*, 452(1948):1207–1220, December 1996.

[235] S. Gov, S. Shtrikman, and H. Thomas. On the dynamical stability of the hovering magnetic top. *Physica D Nonlinear Phenomena*, 126(3–4):214–224, February 1999.

[236] Lukas Martinetz, Klaus Hornberger, James Millen, M. S. Kim, and Benjamin A. Stickler. Quantum electromechanics with levitated nanoparticles. *npj Quantum Information*, 6(1):101, 2020.

[237] D. Rugar, R. Budakian, H. J. Mamin, and B. W. Chui. Single spin detection by magnetic resonance force microscopy. *Nature*, 430(6997):329–332, July 2004.

[238] A. Vinante, M. Carlesso, A. Bassi, A. Chiasera, S. Varas, P. Falferi, B. Margesin, R. Mezzena, and H. Ulbricht. Narrowing the parameter space of collapse models with ultracold layered force sensors. *Physical Review Letters*, 125(10):100404, September 2020.

[239] Bassam Helou, B. J. J. Slagmolen, David E. McClelland, and Yanbei Chen. Lisa pathfinder appreciably constrains collapse models. *Physical Review D*, 95(8):084054, April 2017.

[240] I. J. Arnquist, F. T. Avignone, A. S. Barabash, C. J. Barton, K. H. Bhimani, E. Blalock, B. Bos, M. Busch, M. Buuck, T. S. Caldwell, Y-D. Chan, C. D. Christofferson, P.-H. Chu, M. L. Clark, C. Cuesta, J. A. Detwiler, Yu. Efremenko, H. Ejiri, S. R. Elliott, G. K. Giovanetti, M. P. Green, J. Gruszko, I. S. Guinn, V. E. Guiseppe, C. R. Haufe, R. Henning, D. Hervas Aguilar, E. W. Hoppe, A. Hostiuc, I. Kim, R. T. Kouzes, T. E. Lannen V., A. Li, A. M. Lopez, J. M. López-Castaño, E. L. Martin, R. D. Martin, R. Massarczyk, S. J. Meijer, T. K. Oli, G. Othman, L. S. Paudel, W. Pettus, A. W. P. Poon, D. C. Radford, A. L. Reine, K. Rielage, N. W. Ruof, D. Tedeschi, R. L. Varner, S. Vasilyev, J. F. Wilkerson, C. Wiseman, W. Xu, C.-H. Yu, and B. X. Zhu. Search for spontaneous radiation from wave function collapse in the majorana demonstrator. *Physical Review Letters*, 129(8):080401, August 2022.

[241] Lorenzo Dania, Katharina Heidegger, Dmitry S. Bykov, Giovanni Cerchiari, Gabriel Araneda, and Tracy E. Northup. Position measurement of a levitated nanoparticle via interference with its mirror image. *Physical Review Letters*, 129(1):013601, June 2022.

[242] A. K. Vershovskii and A. K. Dmitriev. A weak magnetic field sensor based on nitrogen-vacancy color centers in a diamond crystal. *Technical Physics*, 65(8):1301–1306, August 2020.

[243] Malcolm H. Levitt. Composite pulses. *Progress in Nuclear Magnetic Resonance Spectroscopy*, 18(2):61–122, January 1986.

[244] Malcolm H. Levitt. Composite pulses, March 2007.

[245] Sambeda Sarkar, Rudra N. Purusottam, Ashutosh Kumar, and Navin Khaneja. Chirp pulse sequences for broadband *pi* rotation. *Journal of Magnetic Resonance*, 328:107002, July 2021.

[246] S. Sellner, M. Besirli, M. Bohman, M. J. Borchert, J. Harrington, T. Higuchi, A. Mooser, H. Nagahama, G. Schneider, C. Smorra, T. Tanaka, K. Blaum, Y. Matsuda, C. Ospelkaus, W. Quint, J. Walz, Y. Yamazaki, and S. Ulmer. Improved limit on the directly measured antiproton lifetime. *New Journal of Physics*, 19(8):083023, August 2017.

[247] René Reimann, Michael Doderer, Erik Hebestreit, Rozenn Diehl, Martin Frimmer, Dominik Windey, Felix Tebbenjohanns, and Lukas Novotny. Ghz rotation of an optically trapped nanoparticle in vacuum. *Physical Review Letters*, 121(3):033602, July 2018.

[248] Kai Zeng, Yulie Wu, Xuezhong Wu, and Dingbang Xiao. Polarization-modulation-based orientation metrology of optically levitated rotating birefringent particles. *Physical Review Research*, 6(1):013160, February 2024.

[249] Thai M. Hoang, Yue Ma, Jonghoon Ahn, Jaehoon Bang, F. Robicheaux, Zhang-Qi Yin, and Tongcang Li. Torsional optomechanics of a levitated nonspherical nanoparticle. *Physical Review Letters*, 117(12):123604, September 2016.

[250] H. Kolb and H. C . Wolf. Protonen-relaxation durch triplett-excitonen in naphthalin-und anthracen-kristallen. *Zeitschrift für Naturforschung A*, 27(1):51–55, January 1972.

[251] A. Abragam. *The principles of nuclear magnetism*. Oxford, Clarendon Press, 1962.

[252] Martin Frimmer, Karol Luszcz, Sandra Ferreiro, Vijay Jain, Erik Hebestreit, and Lukas Novotny. Controlling the net charge on a nanoparticle optically levitated in vacuum. *Physical Review A*, 95(6):061801, June 2017.

[253] Jen-Feng Hsu, Peng Ji, Charles W. Lewandowski, and Brian D'Urso. Cooling the motion of diamond nanocrystals in a magneto-gravitational trap in high vacuum. *Scientific Reports*, 6(1):30125, July 2016.

[254] Martine Schut, Alexey Grinin, Andrew Dana, Sougato Bose, Andrew Geraci, and Anupam Mazumdar. Relaxation of experimental parameters in a Quantum-Gravity Induced Entanglement of Masses Protocol using electromagnetic screening. *Physical Review Research*, 5(4):043170, November 2023.

[255] Christos Pavlou, Maria Giovanna Pastore Carbone, Anastasios C. Manikas, George Trakakis, Can Koral, Gianpaolo Papari, Antonello Andreone, and Costas Galiotis. Effective EMI shielding behaviour of thin graphene/PMMA nanolaminates in the THz range. *Nature Communications*, 12(1):4655, August 2021.

[256] H. B. G. Casimir. On the attraction between two perfectly conducting plates. *Proc. Kon. Ned. Akad. Wet.*, 51:793–795, 1948.

[257] S. Roberts. Optical Properties of Copper. *Phys. Rev.*, 118:1509–1518, June 1960.

[258] Aurel Bulgac, Piotr Magierski, and Andreas Wirzba. Scalar Casimir effect between Dirichlet spheres or a plate and a sphere. *Phys. Rev. D*, 73:025007, January 2006.

[259] Irina G. Pirozhenko and Michael Bordag. Casimir repulsion in sphere-plate geometry. *Phys. Rev. D*, 87:085031, April 2013.

[260] E.M. Lifshitz and M. Hamermesh. 26 - The theory of molecular attractive forces between solids - Reprinted from Soviet Physics JETP 2, Part 1, 73, 1956. In L. P. Pitaevski, editor, *Perspectives in Theoretical Physics*, pages 329–349. Pergamon, Amsterdam, 1992.

[261] Michael Bordag, Galina Leonidovna Klimchitskaya, Umar Mohideen, and Vladimir Mikhaylovich Mostepanenko. *Advances in the Casimir Effect*. Oxford University Press, 05 2009.

[262] John David Jackson. *Classical electrodynamics*. Wiley, New York, NY, 3rd ed. edition, 1999.

[263] W. M. Haynes. *Handbook of Chemistry and Physics*. CRC Press, 97 edition, 2017.

[264] Jen-Feng Hsu, Peng Ji, Charles W. Lewandowski, and Brian D'Urso. Cooling the Motion of Diamond Nanocrystals in a Magneto-Gravitational Trap in High Vacuum. *Sci. Rep.*, 6:30125, July 2016.

[265] David Jiles. *Introduction to Magnetism and Magnetic Materials*. CRC Press, 3 edition, September 2015.

[266] B. W. Maxfield and W. L. McLean. Superconducting penetration depth of niobium. *Phys. Rev.*, 139:A1515–A1522, August 1965.

[267] Nadav Priel, Alexander Fieguth, Charles P. Blakemore, Emmett Hough, Akio Kawasaki, Denzal Martin, Gautam Venugopalan, and Giorgio Gratta. Dipole moment background measurement and suppression for levitated charge sensors. *Science Advances*, 8(41):eabo2361, 2022.

[268] Norna A Robertson. Kelvin Probe Measurements of the Patch Effect. Technical Report LIGO - G070481-00-R, LIGO, July 2007.

[269] Joseph L. Garrett, Jongbum Kim, and Jeremy N. Munday. Measuring the effect of electrostatic patch potentials in Casimir force experiments. *Phys. Rev. Res.*, 2:023355, June 2020.

[270] J. Harms, F. Acernese, F. Barone, I. Bartos, M. Beker, J. F. J. van den Brand, N. Christensen, M. Coughlin, R. DeSalvo, S. Dorsher, J. Heise, S. Kandhasamy, V. Mandic, S. Márka, G. Mueller, L. Naticchioni, T. O'Keefe, D. S. Rabeling, A. Sajeva, T. Trancynger, and V. Wand. Characterization of the seismic environment at the sanford underground laboratory, south dakota. *Classical and Quantum Gravity*, 27(22):225011, October 2010.

[271] M. Armano, H. Audley, J. Baird, P. Binetruy, M. Born, D. Bortoluzzi, E. Castelli, A. Cavalleri, A. Cesarini, V. Chiavegato, A. M. Cruise, D. Dal Bosco, K. Danzmann, M. De Deus Silva, I. Diepholz, G. Dixon, R. Dolesi, L. Ferraioli, V. Ferroni, E. D. Fitzsimons, M. Freschi, L. Gesa, D. Giardini, F. Gibert, R. Giusteri, C. Grimani, J. Grzymisch, I. Harrison, M. S. Hartig, G. Heinzel, M. Hewitson, D. Hollington, D. Hoyland, M. Hueller, H. Inchauspé, O. Jennrich, P. Jetzer, B. Johlander, N. Karnesis, B. Kaune, N. Korsakova, C. J. Killow, J. A. Lobo, J. P. López-Zaragoza, R. Maarschalkerweerd, D. Mance, V. Martín, L. Martin-Polo, F. Martin-Porqueras, J. Martino, P. W. McNamara, J. Mendes, L. Mendes, N. Meshksar, M. Nofrarias, S. Paczkowski, M. Perreur-Lloyd, A. Petiteau, E. Plagnol, J. Ramos-Castro, J. Reiche, F. Rivas, D. I. Robertson, G. Russano, L. Sala, J. Slutsky, C. F. Sopuerta, T. Sumner, D. Texier, J. I. Thorpe, D. Vetrugno, S. Vitale, G. Wanner, H. Ward, P. Wass, W. J. Weber, L. Wissel, A. Wittchen, C. Zanoni, and P. Zweifel. In-depth analysis of LISA Pathfinder performance results: Time evolution, noise projection, physical models, and implications for LISA. *Physical Review D*, 110(4):042004, August 2024.

[272] M. B. Plenio. Logarithmic Negativity: A Full Entanglement Monotone That is not Convex. *Phys. Rev. Lett.*, 95:090503, August 2005.

[273] Alessio Serafini. *Quantum continuous variables a primer of theoretical methods*. CRC Press, Taylor & Francis Group, Boca Raton, FL, 2017.

[274] Tanjung Krisnanda, Guo Yao Tham, Mauro Paternostro, and Tomasz Paterek. Observable quantum entanglement due to gravity. *npj Quantum Information*, 6(1):12, January 2020.

[275] C. U. Lei, A. J. Weinstein, J. Suh, E. E. Wollman, A. Kronwald, F. Marquardt, A. A. Clerk, and K. C. Schwab. Quantum nondemolition measurement of a quantum squeezed state beyond the 3 db limit. *Phys. Rev. Lett.*, 117:100801, August 2016.

[276] Giacomo Marocco, David C. Moore, and Daniel Carney. Three-dimensional squeezing of optically levitated nanospheres, 2026. arXiv:2601.22283 [quant-ph].

[277] Saad Zaheer, Sahand Jamal Rahi, Thorsten Emig, and Robert L. Jaffe. Casimir potential of a compact object enclosed by a spherical cavity. *Phys. Rev. A*, 82(5):052507, November 2010.

[278] Noah Graham, Alexander Shpunt, Thorsten Emig, Sahand Jamal Rahi, Robert L. Jaffe, and Mehran Kardar. Electromagnetic Casimir forces of parabolic cylinder and knife-edge geometries. *Phys. Rev. D*, 83(12):125007, June 2011.

[279] Masahiro Kitagawa and Masahito Ueda. Squeezed spin states. *Physical Review A*, 47(6):5138–5143, June 1993.

[280] D. J. Wineland, J. J. Bollinger, W. M. Itano, and D. J. Heinzen. Squeezed atomic states and projection noise in spectroscopy. *Physical Review A*, 50(1):67–88, July 1994.

[281] Jian Ma, Xiaoguang Wang, C.P. Sun, and Franco Nori. Quantum spin squeezing. *Physics Reports*, 509(2-3):89–165, December 2011.

[282] Luca Pezzè, Augusto Smerzi, Markus K. Oberthaler, Roman Schmied, and Philipp Treutlein. Quantum metrology with nonclassical states of atomic ensembles. *Reviews of Modern Physics*, 90(3):035005, September 2018.

[283] Dmitry Budker, Peter W. Graham, Micah Ledbetter, Surjeet Rajendran, and Alexander O. Sushkov. Proposal for a cosmic axion spin precession experiment (casper). *Physical Review X*, 4(2):021030, May 2014.

[284] M. Deimling, H. Brunner, K. P. Dinse, K. H. Hausser, and J. P. Colpa. Microwave-induced optical nuclear polarization (mi-onp). *Journal of Magnetic Resonance (1969)*, 39(2):185–202, May 1980.

[285] M. Iinuma, Y. Takahashi, I. Shaké, M. Oda, A. Masaike, T. Yabuzaki, and H. M. Shimizu. High proton polarization by microwave-induced optical nuclear polarization at 77 k. *Physical Review Letters*, 84(1):171–174, January 2000.

[286] Haocun Yu, L. McCuller, M. Tse, N. Kijbunchoo, L. Barsotti, and N. Mavalvala. Quantum correlations between light and the kilogram-mass mirrors of LIGO. *Nature*, 583(7814):43–47, 2020.

[287] Lukas Martinetz, Klaus Hornberger, and Benjamin A. Stickler. Surface-Induced Decoherence and Heating of Charged Particles. *PRX Quantum*, 3:030327, August 2022.

[288] M. Brownnutt, M. Kumph, P. Rabl, and R. Blatt. Ion-trap measurements of electric-field noise near surfaces. *Reviews of Modern Physics*, 87(4):1419–1482, December 2015.

[289] J. Halbritter. Torque on a rotating ellipsoid in a rarefied gas. *Zeitschrift für Naturforschung A*, 29(12):1717–1722, December 1974.

[290] J. A. Osborn. Demagnetizing factors of the general ellipsoid. *Physical Review*, 67(11–12):351–357, June 1945.

[291] Guy A. E. Vandenbosch. The basic concepts determining electromagnetic shielding. *American Journal of Physics*, 90(9):672–681, 09 2022.

[292] R. W. Munn and Digby F. Williams. Dielectric tensor and the local electric field in naphthalene. *The Journal of Chemical Physics*, 59(4):1742–1746, August 1973.

[293] Yuliya Mindarava, Rémi Blinder, Yan Liu, Jochen Scheuer, Johannes Lang, Viatcheslav Agafonov, Valery A. Davydov, Christian Laube, Wolfgang Knolle, Bernd Abel, Boris Naydenov, and Fedor Jelezko. Synthesis and coherent properties of 13c-enriched sub-micron diamond particles with nitrogen vacancy color centers. *Carbon*, 165:395–403, September 2020.

[294] Leah B. Casabianca, Alexander I. Shames, Alexander M. Panich, Olga Shenderova, and Lucio Frydman. Factors affecting dnp nmr in polycrystalline diamond samples. *The Journal of Physical Chemistry C*, 115(39):19041–19048, September 2011.

[295] Tonya M. Atkins, Maja C. Cassidy, Menyoung Lee, Shreyashi Ganguly, Charles M. Marcus, and Susan M. Kauzlarich. Synthesis of long t_1 silicon nanoparticles for hyperpolarized ^{29}si magnetic resonance imaging. *ACS Nano*, 7(2):1609–1617, February 2013.

[296] Mohamed Haouas, David P. Petry, Michael W. Anderson, and Francis Taulelle. ^{29}si nmr relaxation of silicated nanoparticles in tetraethoxysilane–tetrapropylammonium hydroxide–water system (teos–tpaoh–h_2o). *The Journal of Physical Chemistry C*, 113(25):10838–10841, May 2009.

[297] R. Berman and David Keith Chalmers Macdonald. The thermal and electrical conductivity of copper at low temperatures. *Proceedings of the Royal Society A*, 211:122, 1952.

[298] T. Emig, N. Graham, R. L. Jaffe, and M. Kardar. Casimir Forces between Arbitrary Compact Objects. *Phys. Rev. Lett.*, 99:170403, October 2007.

[299] H. B. G. Casimir and D. Polder. The Influence of Retardation on the London-van der Waals Forces. *Phys. Rev.*, 73:360–372, February 1948.

[300] T. Emig. Fluctuation-induced quantum interactions between compact objects and a plane mirror. *Journal of Statistical Mechanics: Theory and Experiment*, 2008(04):P04007, April 2008.

[301] Singiresu S. Rao. *Vibration of Continuous Systems*. John Wiley & Sons, Inc., 2 edition, January 2019.

[302] N. Kerker, R. Röpke, L. M. Steinert, A. Pooch, and A. Stibor. Quantum decoherence by Coulomb interaction. *New Journal of Physics*, 22(6):063039, June 2020.

[303] K. B. Moller, T. G. Jorgensen, and J. P. Dahl. Displaced squeezed number states position space representation, inner product, and some applications. *Physical Review A*, 54(6):5378–5385, December 1996.

[304] T. Golubeva and Yu. Golubev. Purity and covariance matrix. *Journal of Russian Laser Research*, 35(1):47–55, January 2014.

[305] Y. Itikawa Yukikazu Itikawa. *Molecular Processes in Plasmas*. Springer-Verlag GmbH, August 2007.

[306] William B. Case. Wigner functions and weyl transforms for pedestrians. *American Journal of Physics*, 76(10):937–946, October 2008.

[307] Simone Rijavec, Matteo Carlesso, Angelo Bassi, Vlatko Vedral, and Chiara Marletto. Decoherence effects in non-classicality tests of gravity. *New Journal of Physics*, 23(4):043040, April 2021.

[308] Wolfgang Nolting. *Grundkurs Theoretische Physik 51.* Springer-Verlag GmbH, September 2008.

[309] Aniello Lampo, Miguel Ángel García March, and Maciej Lewenstein. *Quantum Brownian Motion Revisited.* Springer-Verlag GmbH, April 2019.

[310] M. Armano, H. Audley, J. Baird, P. Binetruy, M. Born, D. Bortoluzzi, E. Castelli, A. Cavalleri, A. Cesarini, A.hspace0.167emM. Cruise, K. Danzmann, M. de Deus Silva, I. Diepholz, G. Dixon, R. Dolesi, L. Ferraioli, V. Ferroni, E.hspace0.167emD. Fitzsimons, M. Freschi, L. Gesa, F. Gibert, D. Giardini, R. Giusteri, C. Grimani, J. Grzymisch, I. Harrison, G. Heinzel, M. Hewitson, D. Hollington, D. Hoyland, M. Hueller, H. Inchausp'e, O. Jennrich, P. Jetzer, N. Karnesis, B. Kaune, N. Korsakova, C.hspace0.167emJ. Killow, J.hspace0.167emA. Lobo, I. Lloro, L. Liu, J.hspace0.167emP. L'opez-Zaragoza, R. Maarschalkerweerd, D. Mance, N. Meshksar, V. Mart'in, L. Martin-Polo, J. Martino, F. Martin-Porqueras, I. Mateos, P.hspace0.167emW. McNamara, J. Mendes, L. Mendes, M. Nofrarias, S. Paczkowski, M. Perreur-Lloyd, A. Petiteau, P. Pivato, E. Plagnol, J. Ramos-Castro, J. Reiche, D.hspace0.167emI. Robertson, F. Rivas, G. Russano, J. Slutsky, C.hspace0.167emF. Sopuerta, T. Sumner, D. Texier, J.hspace0.167emI. Thorpe, D. Vetrugno, S. Vitale, G. Wanner, H. Ward, P.hspace0.167emJ. Wass, W.hspace0.167emJ. Weber, L. Wissel, A. Wittchen, and P. Zweifel. Beyond the required LISA free-fall performance new LISA pathfinder results down to 20 μhz. *Phys. Rev. Lett.*, 120(6):061101, February 2018.

[311] J. Junca, A. Bertoldi, D.hspace0.167emO. Sabulsky, G. Lef'evre, X. Zou, J.-B. Decitre, R. Geiger, A. Landragin, S. Gaffet, P. Bouyer, and B. Canuel. Characterizing earth gravity field fluctuations with the MIGA antenna for future gravitational wave detectors. *Phys. Rev. D*, 99(10):104026, may 2019.

[312] Der einstein-elevator, unimagazin. hannover leibniz universität hannover, nr. 34, s. 14-17, 2018. issn 1616-4075.

[313] Matteo Carlesso and Sandro Donadi. Collapse models main properties and the state of art of the experimental tests. *Springer Proceedings in Physics 237, 1 (2019)*, July 2019.

[314] B. H. Bransden. *Physics of atoms and molecules.* Prentice Hall, Harlow, England New York, 2003.

[315] O. Carnal and J. Mlynek. Young's double-slit experiment with atoms a simple atom interferometer. *Phys. Rev. Lett.*, 66(21):2689–2692, may 1991.

[316] Michael S. Chapman, Christopher R. Ekstrom, Troy D. Hammond, Richard A. Rubenstein, Jörg Schmiedmayer, Stefan Wehinger, and David E. Pritchard. Optics and interferometry withNa2molecules. *Phys. Rev. Lett.*, 74(24):4783–4786, June 1995.

[317] Julen S. Pedernales and Martin B. Plenio. Robust macroscopic matter-wave interferometry with solids. *Phys. Rev. A*, 105:063313, June 2022.

[318] Jasper Chan, T. P. Mayer Alegre, Amir H. Safavi-Naeini, Jeff T. Hill, Alex Krause, Simon Gröblacher, Markus Aspelmeyer, and Oskar Painter. Laser cooling of a nanomechanical oscillator into its quantum ground state. *Nature*, 478(7367):89–92, October 2011.

[319] Kirill Streltsov, Julen S. Pedernales, and Martin B. Plenio. Ground-state cooling of levitated magnets in low-frequency traps. *Phys. Rev. Lett.*, 126(19):193602, may 2021.

[320] Chris Gerry, Peter Knight, and C. C. Gerry. *Introductory Quantum Optics*. Cambridge University Press, June 2010.

[321] Roger G. Newton. *Scattering Theory of Waves and Particles*. Springer Berlin Heidelberg, 1982.

[322] M. Scala, M. S. Kim, G. W. Morley, P. F. Barker, and S. Bose. Matter-wave interferometry of a levitated thermal nano-oscillator induced and probed by a spin. *Physical Review Letters*, 111(18):180403, October 2013.

[323] C. Wan, M. Scala, G.hspace0.167emW. Morley, ATM. A. Rahman, H. Ulbricht, J. Bateman, P.hspace0.167emF. Barker, S. Bose, and M.hspace0.167emS. Kim. Free nano-object ramsey interferometry for large quantum superpositions. *Physical Review Letters*, 117(14):143003, September 2016.

[324] A. T. M. Anishur Rahman. Large spatial schrödinger cat state using a levitated ferrimagnetic nanoparticle. *New Journal of Physics*, 21(11):113011, November 2019.

[325] Andrew Geraci and Hart Goldman. Sensing short range forces with a nanosphere matter-wave interferometer. *Physical Review D*, 92(6):062002, September 2015.

[326] Benjamin A. Stickler, Birthe Papendell, Stefan Kuhn, Björn Schrinski, James Millen, Markus Arndt, and Klaus Hornberger. Probing macroscopic quantum superpositions with nanorotors. *New Journal of Physics*, 20(12):122001, December 2018.

[327] William Haynes. *CRC handbook of chemistry and physics a ready-reference book of chemical and physical data*. CRC Press, Boca Raton, Florida, 2017.

[328] G. Gabrielse, X. Fei, L. Orozco, R. Tjoelker, J. Haas, H. Kalinowsky, T. Trainor, and W. Kells. Thousandfold improvement in the measured antiproton mass. *Physical Review Letters*, 65(11):1317–1320, September 1990.

[329] Jan Harms. Terrestrial gravity fluctuations. *Living Reviews in Relativity*, 22(1), October 2019.

[330] Marco Bilardello, Sandro Donadi, Andrea Vinante, and Angelo Bassi. Bounds on collapse models from cold-atom experiments. *Physica A Statistical Mechanics and its Applications*, 462:764–782, November 2016.

[331] E. R. Andrew, A. Bradbury, and R. G. Eades. Nuclear magnetic resonance spectra from a crystal rotated at high speed. *Nature*, 182(4650):1659–1659, December 1958.

[332] Yoshihiko Arita, Andrew W. McKinley, Michael Mazilu, Halina Rubinsztein-Dunlop, and Kishan Dholakia. Picoliter rheology of gaseous media using a rotating optically trapped birefringent microparticle. *Analytical Chemistry*, 83(23):8855–8858, November 2011.

[333] R. Pilevar Shahri, S. S. Mousavi, and M. R. Benam. The electronic and optical properties of pristine, fluorinatedand chlorinated pentacene molecules an ab-initio study. *International Journal of Nanoscience and Nanotechnology*, 16(1):49–58, 2020.

[334] G. P. Thomson and A. Reid. Diffraction of cathode rays by a thin film. *Nature*, 119(3007):890–890, June 1927.

[335] Helmut Rauch and Samuel A. Werner. *Neutron Interferometry 2nd Edn Lessons in Experimental Quantum Mechanics, Wave-Particle Duality, and Entanglement*. Oxford University Press, January 2015.

[336] Ernst M. Rasel, Markus K. Oberthaler, Herman Batelaan, Jörg Schmiedmayer, and Anton Zeilinger. Atom wave interferometry with diffraction gratings of light. *Physical Review Letters*, 75(14):2633–2637, October 1995.

[337] D. S. Hall, M. R. Matthews, C. E. Wieman, and E. A. Cornell. Measurements of relative phase in two-component bose-einstein condensates. *Physical Review Letters*, 81(8):1543–1546, August 1998.

[338] Markus Arndt, Olaf Nairz, Julian Vos-Andreae, Claudia Keller, Gerbrand van der Zouw, and Anton Zeilinger. Wave–particle duality of c60 molecules. *Nature*, 401(6754):680–682, October 1999.

[339] Sandra Eibenberger, Stefan Gerlich, Markus Arndt, Marcel Mayor, and Jens Tüxen. Matter–wave interference of particles selectedfrom a molecular library with masses exceeding 10000amu. *Physical Chemistry Chemical Physics*, 15(35):14696, 2013.

[340] James Millen, Tania S Monteiro, Robert Pettit, and A Nick Vamivakas. Optomechanics with levitated particles. *Reports on Progress in Physics*, 83(2):026401, January 2020.

[341] Markus Rademacher, James Millen, and Ying Lia Li. Quantum sensing with nanoparticles for gravimetry when bigger is better. *Advanced Optical Technologies*, 9(5):227–239, September 2019.

[342] Sofia Qvarfort, Alessio Serafini, P. F. Barker, and Sougato Bose. Gravimetry through non-linear optomechanics. *Nature Communications*, 9(1), September 2018.

[343] S. Mancini, V. I. Man'ko, and P. Tombesi. Ponderomotive control of quantum macroscopic coherence. *Physical Review A*, 55(4):3042–3050, April 1997.

[344] S. Bose, K. Jacobs, and P. L. Knight. Scheme to probe the decoherence of a macroscopic object. *Physical Review A*, 59(5):3204–3210, May 1999.

[345] William Marshall, Christoph Simon, Roger Penrose, and Dik Bouwmeester. Towards quantum superpositions of a mirror. *Physical Review Letters*, 91(13):130401, September 2003.

[346] Ryan J. Marshman, Anupam Mazumdar, Ron Folman, and Sougato Bose. Constructing nano-object quantum superpositions with a stern-gerlach interferometer. *Physical Review Research*, 4(2):023087, May 2022.

[347] C. R. Downs. Oxidation of aromatic hydrocarbons. *Industrial and Engineering Chemistry*, 32(10):1294–1298, October 1940.

[348] Lea Marti, Nergiz Şahin Solmaz, Michal Kern, Anh Chu, Reza Farsi, Philipp Hengel, Jialiang Gao, Nicholas Alaniva, Michael A. Urban, Ronny Gunzenhauser, Alexander Däpp, Daniel Klose, Jens Anders, Giovanni Boero, Lukas Novotny, Martin Frimmer, and Alexander B. Barnes. Towards optical mas magnetic resonance using optical traps. *Journal of Magnetic Resonance Open*, 18:100145, March 2024.

[349] J. F. G. Hicks. A low temperature calorimeter. the heat capacity and entropy of thallium from 14 to 300°k. low temperature studies. no. 3. *Journal of the American Chemical Society*, 60(5):1000–1004, May 1938.

[350] Markus Schwoerer and Hans Christoph Wolf. Heat capacities, enthalpy increments, and derived thermodynamic functions for naphthalene between the temperatures 5k and 440k. *The Journal of Chemical Thermodynamics*, 34(11):1873–1884, November 2002.

[351] James Eills, Dmitry Budker, Silvia Cavagnero, Eduard Y. Chekmenev, Stuart J. Elliott, Sami Jannin, Anne Lesage, Jörg Matysik, Thomas Meersmann, Thomas Prisner, Jeffrey A. Reimer, Hanming Yang, and Igor V. Koptyug. Spin hyperpolarization in modern magnetic resonance. *Chemical Reviews*, 123(4):1417–1551, January 2023.

[352] S. Sangtawesin, C. A. McLellan, B. A. Myers, A. C. Bleszynski Jayich, D. D. Awschalom, and J. R. Petta. Hyperfine-enhanced gyromagnetic ratio of a nuclear spin in diamond. *New Journal of Physics*, 18(8):083016, August 2016.

[353] Tao Wang, Sean Lourette, Sean R. O'Kelley, Metin Kayci, Y.B. Band, Derek F. Jackson Kimball, Alexander O. Sushkov, and Dmitry Budker. Dynamics of a ferromagnetic particle levitated over a superconductor. *Phys. Rev. Appl.*, 11:044041, April 2019.

[354] Andreas Albrecht, Alex Retzker, and Martin B Plenio. Testing quantum gravity by nanodiamond interferometry with nitrogen-vacancy centers. *Physical Review A*, 90(3):033834, 2014.

[355] Koji Tsuji and Haruka Yamada. Infrared optical constants and absorption intensities of naphthalene single crystal. *The Journal of Physical Chemistry*, 76(2):260–269, January 1972.

[356] Koichiro Miyanishi, Takuya F. Segawa, Kazuyuki Takeda, Izuru Ohki, Shinobu Onoda, Takeshi Ohshima, Hiroshi Abe, Hideaki Takashima, Shigeki Takeuchi, Alexander I. Shames, Kohki Morita, Yu Wang, Frederick T.-K. So, Daiki Terada, Ryuji Igarashi, Akinori Kagawa, Masahiro Kitagawa, Norikazu Mizuochi, Masahiro Shirakawa, and Makoto Negoro. Room-temperature hyperpolarization of polycrystalline samples with optically polarized triplet electrons pentacene or nitrogen-vacancy center in diamond. *Magnetic Resonance*, 2(1):33–48, February 2021.

[357] Michael R. Wasielewski, Malcolm D. E. Forbes, Natia L. Frank, Karol Kowalski, Gregory D. Scholes, Joel Yuen-Zhou, Marc A. Baldo, Danna E. Freedman, Randall H. Goldsmith, Theodore Goodson, Martin L. Kirk, James K. McCusker, Jennifer P. Ogilvie, David A. Shultz, Stefan Stoll, and K. Birgitta Whaley. Exploiting chemistry and molecular systems for quantum information science. *Nature Reviews Chemistry*, 4(9):490–504, July 2020.

[358] J. V. Nicholas. Vibrational mode interactions with the photoexcited triplet state of naphthalene. *Chemical Physics Letters*, 82(2):225–228, September 1981.

[359] Fouad G. Major, Viorica N. Gheorghe, and Günther Werth. *Charged Particle Traps*. Springer-Verlag, 2005.

[360] Uroš Delić, Manuel Reisenbauer, Kahan Dare, David Grass, Vladan Vuletić, Nikolai Kiesel, and Markus Aspelmeyer. Cooling of a levitated nanoparticle to the motional quantum ground state. *Science*, 367(6480):892–895, February 2020.

[361] Jaehoon Bang, T. Seberson, Peng Ju, Jonghoon Ahn, Zhujing Xu, Xingyu Gao, F. Robicheaux, and Tongcang Li. Five-dimensional cooling and nonlinear dynamics of an optically levitated nanodumbbell. *Physical Review Research*, 2(4):043054, October 2020.

[362] Daniel Carney, Kyle G. Leach, and David C. Moore. Searches for massive neutrinos with mechanical quantum sensors. *PRX Quantum*, 4(1):010315, February 2023.

[363] John Ellis, Subhendra Mohanty, and Dimitri V. Nanopoulos. Quantum gravity and the collapse of the wavefunction. *Physics Letters B*, 221(2):113–119, April 1989.

[364] Marko Toroš, Giulio Gasbarri, and Angelo Bassi. Colored and dissipative continuous spontaneous localization model and bounds from matter-wave interferometry. *Physics Letters A*, 381(47):3921–3927, December 2017.

[365] Stephen L. Adler and Angelo Bassi. Collapse models with non-white noises. *Journal of Physics A: Mathematical and Theoretical*, 40(50):15083–15098, November 2007.

[366] James Millen and Benjamin A. Stickler. Quantum experiments with microscale particles. *Contemporary Physics*, 61(3):155–168, July 2020.

[367] Julen S. Pedernales and Martin B. Plenio. Robust macroscopic matter-wave interferometry with solids. *Physical Review A*, 105(6):063313, June 2022.

[368] Sougato Bose, Anupam Mazumdar, Roger Penrose, et al. A Spin-Based Pathway to Testing the Quantum Nature of Gravity, 2025. arXiv:2509.01586 [quant-ph].

[369] Daniel Carney, Philip C E Stamp, and Jacob M Taylor. Tabletop experiments for quantum gravity: a user's manual. *Classical and Quantum Gravity*, 36(3):034001, January 2019.

[370] F. Cosco, J. S. Pedernales, and M. B. Plenio. Enhanced force sensitivity and entanglement in periodically driven optomechanics. *Phys. Rev. A*, 103:L061501, June 2021.

[371] Daine L. Danielson, Gautam Satishchandran, and Robert M. Wald. Gravitationally mediated entanglement: Newtonian field versus gravitons. *Physical Review D*, 105(8):086001, April 2022.

[372] Jens Eisert, Christoph Simon, and Martin B. Plenio. On the quantification of entanglement in infinite-dimensional quantum systems. *Journal of Physics A: Mathematical and General*, 35(17):3911, April 2002.

[373] Michael M. Wolf, Geza Giedke, and J. Ignacio Cirac. Extremality of Gaussian Quantum States. *Phys. Rev. Lett.*, 96:080502, March 2006.

[374] B. L. Hu, Juan Pablo Paz, and Yuhong Zhang. Quantum brownian motion in a general environment: Exact master equation with nonlocal dissipation and colored noise. *Physical Review D*, 45(8):2843–2861, April 1992.

[375] L Diósi. On high-temperature markovian equation for quantum brownian motion. *Europhysics Letters (EPL)*, 22(1):1–3, April 1993.

[376] T. Delord, P. Huillery, L. Nicolas, and G. Hétet. Spin-cooling of the motion of a trapped diamond. *Nature*, 580(7801):56–59, March 2020.

[377] Fernando Monteiro, Gadi Afek, Daniel Carney, Gordan Krnjaic, Jiaxiang Wang, and David C. Moore. Search for composite dark matter with optically levitated sensors. *Physical Review Letters*, 125(18):181102, October 2020.

[378] Lajos Diósi. Calderia-leggett master equation and medium temperatures. *Physica A: Statistical Mechanics and its Applications*, 199(3-4):517–526, November 1993.

Erklärung über die selbständige Anfertigung der Dissertation

Ich versichere hiermit, dass ich die Arbeit selbständig angefertigt habe und keine anderen als die angegebenen Quellen und Hilfsmittel benutzt sowie die wörtlich oder inhaltlich übernommenen Stellen als solche kenntlich gemacht habe und die Satzung der Universität Ulm zur Sicherung guter wissenschaftlicher Praxis in der jeweils gültigen Fassung beachtet habe.

Ich bin damit einverstanden, dass die Dissertation auch zum Zweck der Überprüfung der Einhaltung allgemein geltender wissenschaftlicher Standards benutzt wird, insbesondere auch unter Verwendung elektronischer Datenverarbeitungsprogramme.

Ulm, den 27. August 2026

Marit Ottilie Eva Steiner